Ultrashort Nonlinear Light-Matter Interactions in Two-Dimensional Quasirelativistic Systems

by

David Romeu Nave Carvalho

A thesis submitted in fulfilment of the requirements for the degree of doctor of philosophy

Heriot-Watt University
School of Engineering & Physical Sciences
Institute of Photonics & Quantum Sciences

May 2018

Abstract

An encompassing study of nonlinear optical properties of two-dimensional quasirelativistic systems is presented. The electrons in such systems may be adequately described by Dirac spinors, solutions to an equation formally equivalent to the Dirac equation in $(2+1)$ dimensions. In order to model the carrier dynamics as a consequence of optical excitations, the *Dirac-Bloch Equations* (DBEs) are derived, their framework explained and their predictions simulated in a wide range of excitation conditions. In particular, intense and ultrashort pulses, whose effect on media is oftentimes challenging to obtain, are used to study and analyse general optical features through a prediction of the non-perturbative current and respective spectrum. As a starting point, pristine graphene samples are analysed and it is shown that the DBEs predict previously-forbidden second-harmonic generation. This result is to be contrasted with predictions from the Semiconductor Bloch Equations, which are shown to be inadequate to model graphene in such an excitation regime. If a gap in the spectrum is opened, the carriers acquire a Berry phase and may also produce interband-mediated harmonics of any desired order upon appropriate tuning. The effects of lack of centrosymmetry, trigonal warping and spin-orbit coupling are also considered, and studied for transition metal dichalcogenides by applying the *generalised Dirac-Bloch Equations*. High even-harmonic generation, in accordance with recent experiments, is predicted, alongside anisotropic effects on the current. The results and methods outlined in this thesis help establish new techniques to understand and predict the nonlinear optical behaviour of a range of two-dimensional relativistic-like semiconductors admitting two effective bands, and help pave the way to predict quantitatively, in a generalised fashion, the effect of wide range of intrinsic or deliberate properties on nonlinear optical features of the media.

To my mother, Paula.

Acknowledgements

Firstly, I would like to express my sincere gratitude to my supervisor Prof. Fabio Biancalana for his continuous support throughout my PhD, for his patience, motivation, and immense knowledge in the area. The results and conclusions obtained in this work would not have been properly understood or present at all if not for his intuition and his sense of the big picture. Thank you for guiding me to become a better scientist. *Grazie mille, Fabio!*

I must also thank my mother, Paula, and sister, Laura, for their unconditional love and care. Mum, without your encouragement to help pursue my dream and your sheer belief in the power of education, I would certainly not have made it to this stage – *o meu obrigado do fundo do coração.*

To everyone whom I had the privilege to interact with when conducting my research: my fellow colleages in the Nonlinear Photonics Nanostructures group (in particular Leone for the insightful discussions and help), the professors and lecturers in the Institute, thank you. The countless coffee-breaks-turned-into-rants certainly kept my sanity afloat.

Finally, I acknowledge financial support received from the International Max-Planck International Partnership and SUPA for their impeccable training and development opportunities.

ACADEMIC REGISTRY

Research Thesis Submission

Name*:*			
School:			
Version: *(i.e. First, Resubmission, Final)*		Degree Sought:	

Declaration

In accordance with the appropriate regulations I hereby submit my thesis and I declare that:

1) the thesis embodies the results of my own work and has been composed by myself
2) where appropriate, I have made acknowledgement of the work of others and have made reference to work carried out in collaboration with other persons
3) the thesis is the correct version of the thesis for submission and is the same version as any electronic versions submitted*.
4) my thesis for the award referred to, deposited in the Heriot-Watt University Library, should be made available for loan or photocopying and be available via the Institutional Repository, subject to such conditions as the Librarian may require
5) I understand that as a student of the University I am required to abide by the Regulations of the University and to conform to its discipline.
6) I confirm that the thesis has been verified against plagiarism via an approved plagiarism detection application e.g. Turnitin.

* *Please note that it is the responsibility of the candidate to ensure that the correct version of the thesis is submitted.*

Signature of Candidate*:*		Date:	

Submission

Submitted By *(name in capitals):*	
Signature of Individual Submitting:	
Date Submitted:	

For Completion in the Student Service Centre (SSC)

Received in the SSC by *(name in capitals):*			
Method of Submission *(Handed in to SSC; posted through internal/external mail):*			
*E-thesis Submitted (**mandatory for final theses)***			
Signature:		Date:	

Please note this form should be bound into the submitted thesis.

Contents

List of Publications

& Conferences

Journal Publications

- Carvalho, D. N., Marini, A., & Biancalana, F. (2017). Dynamical centrosymmetry breaking — A novel mechanism for second harmonic generation in graphene. Annals of Physics, 378, 24-32.

Abstract:

We discover an unusual phenomenon that occurs when a graphene monolayer is illuminated by a short and intense pulse at normal incidence. Due to the pulse-induced oscillations of the Dirac cones, a dynamical breaking of the layer's centrosymmetry takes place, leading to the generation of second harmonic waves. We prove that this result can only be found by using the full Dirac equation and show that the widely used semiconductor Bloch equations fail to reproduce this and some other important physics of graphene. Our results open new windows in the understanding of nonlinear light-matter interactions in a wide variety of new 2D materials with a gapped or ungapped Dirac-like dispersion.

- Carvalho, D. N., Biancalana, F., & Marini, A. (2018). Nonlinear optical effects of opening a gap in graphene. Physical Review B, 97(19), 195123.

Abstract:

Graphene possesses remarkable electronic, optical and mechanical properties that have taken the research of two-dimensional relativistic condensed matter systems to prolific levels. However, the understanding of how its nonlinear optical properties are affected by relativistic-like effects has been broadly uncharted. It has been recently shown that highly-nontrivial currents can be generated in free-standing samples, notably leading to the generation of even harmonics. Since graphene monolayers are centrosymmetric media, for which such harmonic generation is deemed inaccessible, this light-driven phenomenon is both startling and promising. More realistically, graphene samples are often deposited on a dielectric substrate, leading to additional intricate interactions. Here, we present a treatment to study this instance by gapping the spectrum and we show this leads to the appearance of a Berry phase in the carrier dynamics. We analyse the role of such a phase in the generated nonlinear current and conclude that it suppresses odd-harmonic generation. The pump energy can be tuned to the energy gap to yield interference among odd harmonics mediated by interband transitions, allowing even harmonics to be generated. Our results and general methodology pave the way for understanding the role of gap-opening physical factors in the nonlinear optics of hexagonal two-dimensional lattices.

Conference Publications

- Carvalho, D. N., Biancalana, F., & Marini, A. (2017). Monolayer Graphene Can Emit SHG Waves. Optical Data Processing and Storage, 3(1), 47-53.

Abstract:

The usually-held notion that monolayer graphene, a centrosymmetric system, does not allow even-harmonic generation when illuminated at normal incidence is challenged by the discovery of a peculiar effect we term the dynamical centrosymmetry breaking

mechanism. This effect results in a global pulse-induced oscillation of the Dirac cones which in turn produces second harmonic waves. We prove that this result can only be found by using the full Dirac equation and show that the widely used semiconductor Bloch equations fail to reproduce this and some other important physics of graphene. These results clear the way for further investigation concerning nonlinear light-matter interactions in a wide range of two-dimensional materials admitting either a gapped or ungapped Dirac-like spectrum.

Conferences

- *Lake Como School of Advanced Studies on "Spatiotemporal Complexity in Nonlinear Optics"*, August 2015, Como, Italy (attended).
- 1st *International Conference on Optics, Photonics and Materials*, October 2016, Nice, France (presented a talk).
- *Summer School on "Data-Driven Methods for Multi-Scale Physics and Complex Systems"*, Summer 2017, Rome, Italy (presented a talk)
- *UK-China 2D Materials Conference*, January 2018, Manchester, United Kingdom (presented a poster).

List of Tables

List of Figures

Chapter 1

Introduction

It is hard to believe that any well-rounded scientist or science enthusiast, up-to-date with the latest developments in Physics, Technology and Nobel prize hysteria, has not heard of the word "graphene" in some form or another. "*Graphene is the name given to a single layer of carbon atoms densely packed into a benzene-ring structure*", as was described in the seminal paper reporting its experimental realisation [4].
As an atom-thick layer of carbon atoms arranged in a hexagonal structure, graphene provides the basis of many nanostructures of carbon (known by the jargon allotropes): carbon nanotubes can be thought as rolled-up sheets of graphene; graphite can be construed as a particular stacking of such layers. Buckminsterfullerene C_{60}, also known as a "buckyball", can also be thought of a spherical version of graphene.

These structures can now be produced in the laboratory but this was not the case until very recently. Long theoretically predicted by Wallace [5], who determined the energy spectrum of a single electron in graphene in 1947, graphene was thought to be an abstract artefact of Solid State Physics, never to be produced in the laboratory. Most notably, Physics heavyweights Landau [6], Peirls [7] and later Mermin [8] invoked thermodynamical arguments to dispute the notion that two-dimensional

crystals can be stable, due to a divergent contribution of thermal fluctuations in low-dimensional crystal lattices. The rest is history - Geim and Novoselov [4] were successful in producing the first sample that would be unequivocally characterised as graphene in 2004. For those efforts, they were bestowed the highest honorary award attributed to the advancement of Humanity - the Nobel prize in Physics in 2010. *Why exactly?*

The physics of graphene and related materials has attracted an ardent interest since the initial experimental realisation of graphene monolayers [4]. *What exactly is so special about this particular material? How come is the research output concerning graphene still so abundant fourteen years after its physical realisation?* Firstly, the electronic structure displayed by the carriers is remarkable: at relative low energies, graphene shows a unique Dirac-like band structure and this implies that quasielectrons behave as if they were massless Dirac fermions [9], akin to "charged photons" or neutrinos!

It is not surprising, by the title of this thesis, that under certain conditions, quasiparticles may also be *quasirelativistic*. Electrons in graphene are ballistic in the sense that their Fermi velocity is a whopping 0.3% of the speed of light! While it is true that they do not attain velocities compared to the speed of light, where relativistic effects take place, the absence of both a gap, a crucial aspect of semiconductors, and curvature in the energy dispersion for low-lying electronic states, suggest this tempting analogy, namely to model them with a relativistic equation.

Due to this special property, graphene electronics is quite different from conventional semiconductor electronics, and holds the promise of revolutionising the technological landscape in many different ways [9]. It is no surprise that graphene has been the spotlight in Material Science research and, involuntarily, shaped the direction of two-dimensional crystals research in many unrelated ways.

Furthermore, on the technological side, a tremendous effort to link novel effects and properties to new devices and related applications have reached so far as to use graphene as an "atomic sieve" and as a biosensor [10, 11]. Its mechanical properties truly are amazing. Reports that "establish graphene as the strongest material ever measured" [12] motivate this claim.

For the theorist, graphene provides a joyful playground for studying and idealising a myriad of theoretical concepts. Given its quasirelativistic nature, graphene is expected to show signatures of features found in (high-energy) Quantum Electrodynamics, such as the Klein tunelling [13], Zitterbewegung [14]. Furthermore, graphene eventually led the research community to a true paradigm change in an abundant scope of areas: a deeper understanding of universal electronic properties through a topological analysis of the underlying Hamiltonian, leading to the discovery of many novel topological states [15, 16]. With this understanding, the Quantum Hall effect has been established alongside experimental observations [17]. Reports of superconductivity in twisted bilayer graphen have been published this year [18]. Graphene has prominently kicked off a whole new ambition in Condensed Matter Physics to engineer systems with generalised topological properties to new realms [19]. Examples of this are given by the observation of (three-dimensional) Dirac semimetals [20, 21], Weyl semimetals [22, 23] and, very recently, to new quasiparticles known as type-II Dirac fermions, which seem to break Lorentz invariance [24, 25]. The future seems promising for the field.

This work is concerned with understanding the optical properties of Dirac fermions and it relies on a particular employment of methods to predict optical phenomena of graphene and, at large, two-dimensional quasirelativistic materials. It begs the question: *In what way are these quasirelativistic features present in the optical interactions?* Apart from their noteworthy electronic properties, *massless* Dirac fermions,

the term used to describe the carriers in monolayer graphene, have already been shown extraordinary optical features [26] which have already been employed in photonics for ultrafast photodetectors [27], optical modulation [28], molecular sensing [29], and several nonlinear applications [30, 31].The conical dispersion itself is known to induce highly nonlinear dynamics for light [32]. Graphene's optical response is characterized by a highly-saturated absorption at rather modest light intensities [33], a remarkable property which has already been exploited for mode-locking in ultrafast fiber-lasers [34]. The high nonlinear response of graphene leads to the efficient generation of higher harmonics [35, 36].

The understanding of how these fermions interact with light in extreme and ultrashort conditions remains, to a large extent, incomplete. The work presented in this thesis tries to address this point with the aid of a set of equations, termed the *Dirac-Bloch Equations* (DBEs), which will be derived precisely and analysed with realistic probing parameters typical of intense (high electric field amplitudes) and short (few pulse optical cycles).

Graphene is not the only medium for which this quasirelativistic treatment is warranted. In particular, transition metal dichalcogenides (TMDs) present an interesting platform to study such interactions in Dirac materials. In the framework of the Dirac-Bloch formalism, several generalisations will be obtained in order to make the treatment as general as possible. This will eventually lead to equations modelling a general two-dimensional quasirelativistic medium.

Thesis Structure

The work will be presented in the following sequence. In Chapter 2, the main ingredients that will allow a treatment of light-matter interactions are outlined. Firstly, a brief explanation underlying the theory of crystal lattices, notably within the tight-binding formalism, will allow for the electronics of the system to be characterised.

The "reduction" of the usual Schrödinger Equation, which describes electrons in such systems very accurately, to the Dirac equation will be made. Subsequently, the quantum-mechanical characterisation of the massless Dirac fermions will be obtained. After a brief review of the necessary concepts in Optics, these particles will be coupled to light and their properties compared with those of more conventional semiconductors.

In Chapter 3, a foundational concept, that of a *two-level system* will be introduced and, with it, the carrier dynamics of a semiconductor will be shown to be modelled by the *Semiconductor Bloch Equations* (SBEs). With them, the low-field excitation regime of graphene will be studied and several well-established results confirmed by the simulations.

The idea behind the main theoretical machinery of this work is presented in Chapter 4, where the dynamics of a two-level system described by the Dirac equation is shown to be modelled by the *Dirac-Bloch Equations* (DBEs). Many novel features will be presented. Subsequently, a comparison between both models will lead to the conclusion that the SBEs are an approximation of the DBEs and that they are unsuitable to understand optical features of graphene when ultrashort and intense pulses are used to probe it. In particular, such a difference is manifested in the *dynamical centrosymmetry breaking mechanism*, an effect which allows even harmonics to be generated in a centrosymmetric medium at normal incidence.

In the same spirit as the previous section, Section 5 is concerned with the generalisation of the methods used to obtain the DBEs for gapped Dirac-like dispersions, which are termed the *Massive Dirac-Bloch Equations*. Realistic samples prepared in the laboratory are normally deposited on a substrate or have defects in their arrange-

ments. These and related features can be satisfactorily accommodated in the theory precisely by gapping the spectrum. A nontrivial, momentum and time-dependent *Berry phase* in the carrier dynamics is found when doing so. When considering the output spectrum, this phase is seen to suppress odd harmonics. The opening of a gap in the spectrum leads to different results to gapless samples. In particular, a mechanism from Extreme Optics known as "*third- harmonic generation in disguise of second-harmonic generation*" leads to an harmonic enhancement of a particular order, dictated by tuning conditions between the energy gap and the photon energy.

Finally, in Chapter 6, an all-new class of two-dimensional crystals that has sparked attention in the field for their robust and efficient optoelectronic properties – *transition metal dichalcogenides* – will be studied within the Dirac-Bloch framework developed in the previous sections, leading to the *Generalised Dirac-Bloch Equations*. From an optics point of view, such monolayers are alluring due to their lack of centre of inversion in their underlying lattice, unlike graphene. This property is explored to probe nonlinearities in the system.

With these equations, it is possible to link the harmonic composition of the generated current to any effective two-band model described by the Dirac equation.

A conclusion, encompassing a summary of the results and an outline of prospective future work is given in Chapter 7.

Chapter 2

The Physics of Graphene

2.1 Overview

Graphene is simply a layered structure of carbon atoms. From this point of view, the standard theory of crystals and solids may be used to understand it as a quantum mechanical system. In this section, the basic theory that underpins most of how the electronic properties of crystals in a particular lattice arrangement are understood is introduced. Most tools to study such condensed matter systems revolve around the tight-binding approximation, introduced in Section 2.2.2.

With it, it will be shown that, for the particular case of a graphene monolayer, the conduction and valence bands depend linearly on the magnitude of the crystal momentum, touching each other at two special points in reciprocal space. Tied to this observation, a reduction of the usual scalar wavefunction describing the carriers, determined from the Schrödinger equation, to the two-component spinor described by a (2+1)-dimensional Dirac equation, is presented.

In order to fully appreciate the physicochemical reasons behind this unusual property, a brief explanation underlying the process of orbital hybridisation is given in Section 2.2.1. Ultimately, the orbital hybridisation leads to the rather strong hexago-

nal arrangement – known as a *honeycomb lattice*– that is responsible for its structural stability.

The consequences of such a geometrical disposition are deep. Such a real-space lattice is not a *Bravais* lattice although it can be decomposed into two Bravais triangular sublattices. As will be seen, this fact will allow such a decomposition to play the role of a degree of freedom, in turn allowing the quasiparticles describing the unhybridised electrons to be written in a relativistic fashion, leading to the celebrated Dirac Equation.

Once the relativistic analogy is set up, mimicking the electronic features of the carriers in the low-momentum regime, this framework yields startling features. For instance, the density of states of a graphene monolayer is, contrary to what is predicted of usual two-dimensional semiconductors, shown to be linear in Section 2.3.1, as a consequence of the linearity of the dispersion. Not surprisingly, its optical properties are expected to differ from a conventional semiconductor. A brief exposition of the tools and concepts necessary to understand them is given in Section 2.4.1. With them, the law of universal absorption, another astonishing feature of graphene, is derived. As will be discussed, this consideration leads to deep conclusions about the non-perturbative nature of graphene.

2.2 Electronic Band Structure

To start off, the concept of a quasiparticle must be framed. Dynamical phenomena in condensed matter systems, owing much to the system intrinsic geometrical configuration, may sometimes be idealised with the aid of particles. Depending on whether these obey fermionic or bosonic rules, they are termed *quasiparticles* or *collective excitations*, respectively. Examples of such dynamical phenomena may be a transfer of charge, energy, momentum or spin and are obviously a result of often complicated

and intricate many-body interactions across the system.

The quasiparticle picture is particularly helpful precisely because it can reduce these phenomena to effective free-like single-particle excitations. For these reasons, one must distinguish conceptually the idea of an electron dispersing in free space, and of one constrained in a particular atomic arrangement, interacting with many other constituent parts of the system (including other electrons). For brevity purposes, the mouthful "*quasielectron*", used to describe electronic quasiparticles, will not be used throughout this thesis. Any subsequent description of "electrons" is meant in this way.

2.2.1 Hybridisation

Before engaging in discussions about the structure of graphene, it is enlightening to understand how those particular geometric arrangements make themselves manifest. In the jargon of Chemical Physics (or Physical Chemistry), the quasiparticles of interest in graphene are known as π electrons. The fundamental reason why such electrons may be represented by 2-component states is related to the geometrical arrangements, which arises from the sp^2 hybridisation of the outer shell electrons of the carbon ions - conceptualised through its hexagonal, honeycomb lattice.

A carbon atom has six electrons in a configuration $1s^2 2s^2 2p^2$. The first shell is normally irrelevant to chemical bonding, leaving the second shell, containing 2 electrons in the $2s$ orbital and another 2 in the $|2p_x\rangle, |2p_y\rangle, |2p_z\rangle$, available to participate in bonding. As intuition tells, the $2s$ orbital is energetically more favourable than the remaining energy-degenerate $2p$ orbitals, being 4 eV lower [37].

However, while bonding with other elements, namely carbon itself, this argument breaks down. The energy gain can be even higher if one $2s$ electron is promoted to one of the $2p$ orbitals, so that the three of them have one unpaired electron. This entails the basic idea behind *hybridisation*: the electrons are to be understood as a

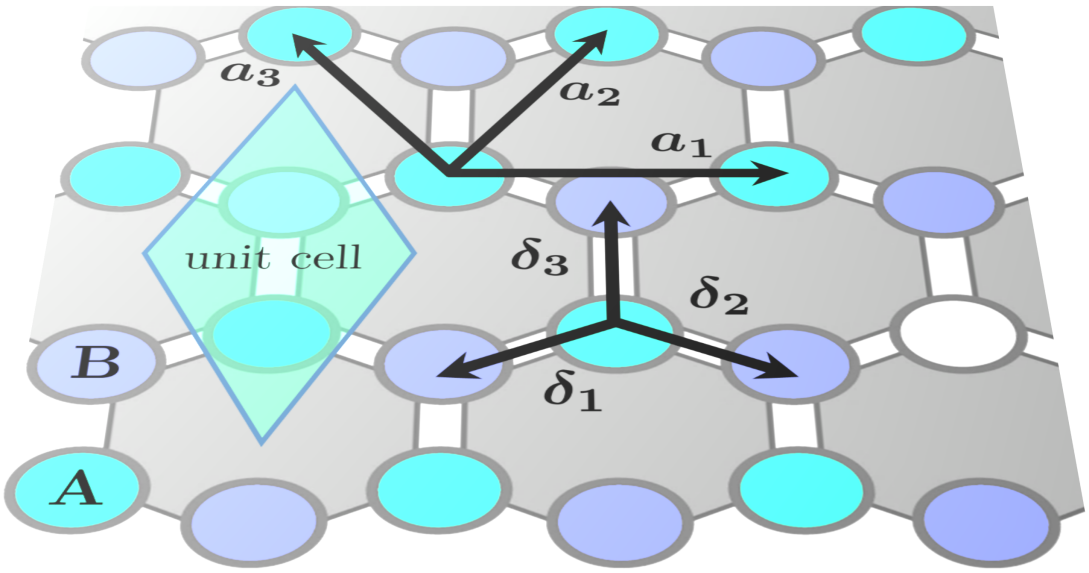

Figure 2.1: Diagram representation of the two sublattices – A (blue) and B (purple) – within the real lattice of graphene, including the next neighbour vectors δ_i and next-neighbour vectors $\boldsymbol{a}_i$. The unit cell is the turquoise rhombus.

superposition of the $|2s\rangle$ and $|2p\rangle$ states. It turns out that the planar configuration of the layer is obtained through sp^2 hybridisation, resulting in three new orbitals $|sp_i^2\rangle$ $(i = 1, 2, 3)$ comprised of linear combinations of the $|2s\rangle$ and two p orbitals, arbitrarily taken as $|2p_x\rangle$ and $|2p_y\rangle$.

Through this process, all orbitals in the $n = 2$ shell – the $|sp_i^2\rangle$ and the remaining $|2p\rangle$ – have one unpaired electron. The geometric shape of these new hybridised orbitals indeed reveals three (σ) carbon bonds along the horizontal plane, which are 120° apart and hence organise the atoms in a hexagonal, honeycomb arrangement. Moreover, the separation between the carbon atoms, dictated by these orbitals, is the lattice constant $a = 0.142$ nm. The unhybridised (π) orbital, $|2p_z\rangle$ has upper and lower symmetrical lobes and is perpendicular to the plane. The chemically-reactive electrons are the ones belonging to these orbitals and, any mention of "electrons" in graphene will be meant to denote these. π bonding between close-by π electrons is at the heart of the production of surface currents in graphene.

Even though all lattice sites, located at the corners of the hexagons, are composed

of identical carbon atoms, it is clear that the honeycomb lattice arrangement does not represent a Bravais lattice $\boldsymbol{T}$, a type of geometric arrangements where all lattice sites can be obtained through a suitable linear combination of a particular set of of vectors $\boldsymbol{a}_i$:

$$\boldsymbol{T} = \{n_1\boldsymbol{a}_1 + n_2\boldsymbol{a}_2 \mid n_1, n_2 \in \mathbb{Z}\} \tag{2.2.1}$$

where the basis of this space is known as the *primitive vectors*. The minimal area spanned by the basis is known as the *unit cell*.

This is a relevant observation. To see why the honeycomb lattice is not Bravais, consider Fig. 2.1. The vectors $\boldsymbol{\delta}_i$ connecting the nearest neighbours, all purple, to the blue site would have to also connect any purple site to all surrounding blue ones. However, it is clear that these vectors would have to be rotated by 60°. The blue and purple sites are hence not physically equivalent. If only alternate sites are considered, i.e. only the blue or purples sites, it can now be seen that the underlying triangular lattice $\boldsymbol{T}$ is indeed Bravais, leading to all sites to be related by a unique set of translational vectors and hence a Bravais lattice defined as Eq. (2.2.1) requires by taking, for instance, the primitive vectors $\boldsymbol{a}_1 = \sqrt{3}a(1, 0)$ and $\boldsymbol{a}_2 = \frac{\sqrt{3}a}{2}(1, \sqrt{3})$.

This construction holds for either colour of sites *separately*. This distinction of "species" is not made aimlessly: it is now clear that the honeycomb lattice can be decomposed into two Bravais *sublattices*, blue and purple, each containing one site per unit cell. Given that there is only one π electron per lattice site, the unit cell contains two valence electrons. This leads to the conclusion that the underlying lattice of graphene is a triangular with two sites per unit cell, which is depicted as the turquoise rhombus in Fig 2.1. As will be seen shortly, the physical meaning behind this decomposition is vital to understand the electronics of the π electrons.

These triangular sublattices are normally denoted by A and B. In this case, they are not *too* different: one is simply shifted by $\pm\boldsymbol{\delta}_3$ with respect to the other. Therefore, for a sublattice index j ($j = A, B$), a shift vector $\boldsymbol{\delta}_j$ can associate any point of the

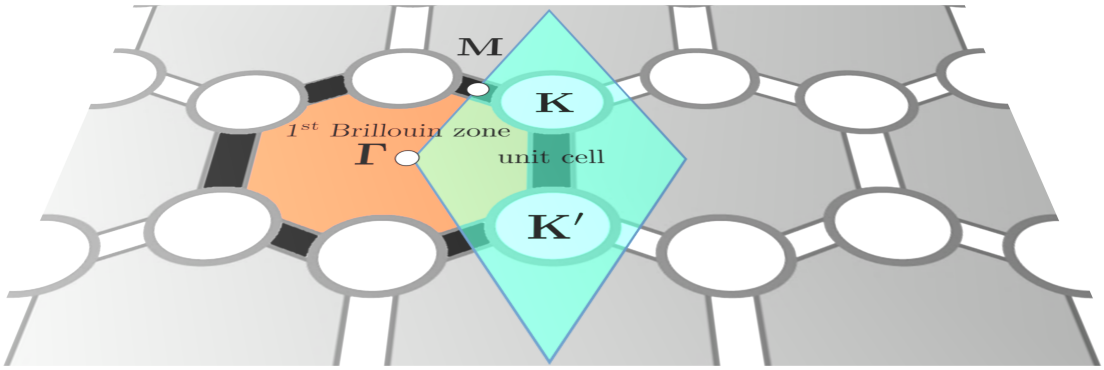

Figure 2.2: Depiction of the reciprocal lattice of the honeycomb lattice. Given the sublattice decomposition, two non-equivalent points in momentum space appear **K** and **K′**, contained in the reciprocal unit cell, the blue rhombus. All non-equivalent points are contained within the first Brillouin zone, depicted in orange.

honeycomb lattice to a point on that particular triangular sublattice j. Many choices for such shift vectors can be found although a rather simple choice is to fix one sublattice j with the honeycomb lattice (leading to $\boldsymbol{\delta}_j = 0$) and describe any other point in the other sublattice $i \neq j$ with a shift of $\boldsymbol{\delta}_i = \boldsymbol{\delta}_3$.

The reciprocal lattice of each triangular sublattice is also a triangular sublattice, but now spanned by the vectors $\boldsymbol{b}_1 = 2\pi/(\sqrt{3}a)(1, -1/\sqrt{3})$ and $\boldsymbol{b}_2 = 4\pi/(3a)(1, 0)$. If only inequivalent vectors are considered, i.e. vectors which cannot be obtained by a shift of any other vector in the reciprocal lattice, are considered, the Brillouin zone (BZ) is obtained. This region defines the *crystal momentum*: all possible lattice excitations must therefore be identifiable with one such vector.

Fig. (2.2) depicts the reciprocal lattice, with the Brillouin zone. It resembles a hexagon, bounded by six corners. These points cannot all belong to the interior, since four of them are related to the other two by a reciprocal vector shift. The two remaining, inequivalent points are termed the *Dirac points* and denoted by **K** and **K′**. Importantly, there is *one* unfilled π electron state per atom, as the three σ bonds that resulted from the sp^2 hybridisation of the orbitals leave the remaining π electron available for pairing. Therefore, the relevant dispersion to understand the electronic properties of graphene is the π bands, composed of the chemically and physically

reactive π electrons.

As will be shortly seen, the Dirac points are crucial in understanding the low-energy properties of the π electrons in graphene, i.e. far from the Γ point, located exactly in the centre of the hexagon. The next section will introduce methodologies to describe the electronic band of such electrons.

2.2.2 Tight-Binding Approximation

In order to calculate the electronic bands of the π electrons, the tight-binding formalism is used. In this method, the wavefunction of the overall many-body system is assumed to be a linear superposition of atomic wavefunctions, localised at a particular lattice site. The latter is calculated without any reference to the lattice, i.e. without accounting for any environmental interaction. For this reason, the atomic wavefunction is not a true eigenstate of the system. This difference is assumed to stem from overlaps of neighbouring atomic wavefunctions at different sites. Furthermore, the overlap is assumed to decay quickly given the localisation of the electron on its site – hence why it is *"tightly-bound"*.

To see this, an atomic Hamiltonian at a lattice site l in position $\mathbf{R}_l$ is considered:

$$H_l = -\frac{\hbar^2\nabla^2}{2m} + V_l(\mathbf{r} - \mathbf{R}_l) \tag{2.2.2}$$

where ∇^2 is the Laplacian, m the mass of the free electron and $V_l(\mathbf{r} - \mathbf{R}_l)$ is the potential at site l. The electron wavefunction at that site is the eigenfunction of the atomic Hamiltonian, satisfying:

$$H_l(\mathbf{r})\phi_n(\mathbf{r} - \mathbf{R}_l) = \mathcal{E}_n\phi_n(\mathbf{r} - \mathbf{R}_l) \tag{2.2.3}$$

where n is an index labelling the different orbitals composing the atom at site l and ϵ_n their energy. In a mean-field approach, the full Hamiltonian is composed of the single-particle contributions H_l, leading to an effective potential that may be treated as a perturbation $\Delta V(\mathbf{r})$:

$$H = \sum_l H_l = -\frac{\hbar^2\nabla^2}{2m} + \underbrace{\sum_{\mathbf{R}_l} V_l(\mathbf{r}-\mathbf{R}_l)}_{\Delta V(\mathbf{r})} \tag{2.2.4}$$

At this stage, the goal is to find the n eigenstates $\psi_{\mathbf{k}}(\mathbf{r})$ and their respective eigenvalues ϵ_n of this Hamiltonian. The atomic energies are categorically *not* the same as the band energies – that is the point!

Before one attempts to calculate them, an ansatz that solves Eq. (2.2.4) must be found. The symmetries of the underlying lattice constraint the wavefunction across the lattice itself.

The technicalities of such statement lie deep in what is known as *Bloch's theorem*. Given the physical invariance of the lattice sites in a Bravais lattice, the wavefunction must not behave differently when shifted by any lattice vector $\mathbf{R}$. In particular, this means that a suitable translation operator $\mathcal{T}(\mathbf{R})$ must commute with the Hamiltonian. Consequently, both operators share the same eigenfunctions:

$$\mathcal{T}(\mathbf{R})\psi_{\mathbf{k}} \equiv \psi_{\mathbf{k}}(\mathbf{r}+\mathbf{R}) = e^{i\mathbf{k}\cdot\mathbf{R}}\psi_{\mathbf{k}}(\mathbf{r}) \tag{2.2.5}$$

Given the Bravais decomposition of the honeycomb lattice just discussed, the wavefunction must in general be written as a linear combination of two components, one describing amplitudes from each sublattice:

$$\psi_{\mathbf{k}}(\mathbf{r}) = a_{\mathbf{k}}\psi^{(A)}_{\mathbf{k}}(\mathbf{r}) + b_{\mathbf{k}}\psi^{(B)}_{\mathbf{k}}(\mathbf{r}) \tag{2.2.6}$$

In this fashion, each component satisfies Bloch's Theorem, whenever $\mathbf{R}$ is a vector of each underlying triangular sublattice. The coefficients $\alpha(\mathbf{k})$ and $\beta(\mathbf{k})$ naturally quantify the probability of finding the electron in each sublattices.

Given the alternate nature of the lattice sites, the essence of the tight-binding philosophy becomes clear: an electron of momentum $\mathbf{k}$ is initially assumed to be fairly localised at an atomic site, belonging to a particular sublattice. The local site is itself composed of its atomic orbitals, dependent on the atomic character of the site. However, due to the overlap of the wavefunction sitting this particular lattice site with another electron wavefunction sitting on a adjacent lattice site, a non-zero probability of a transition into adjacent sites. Quantities pertaining to this mechanism are usually not easily reachable given the intrinsic complexities of the orbitals in question. In this instance, the p orbitals are not inherently challenging.

The Bloch functions $\psi_{\mathbf{k}}^{(j)}(\mathbf{r})$ of either sublattice are too general to compute. To attain an ansatz which satisfies Bloch's Theorem, the tight-binding assumption relies on constructing them using atomic wavefunctions $\phi^{(j)}$, eigenfunctions of the atomic Hamiltonian:

$$\psi_{\mathbf{k}}^{(j)}(\mathbf{r}) = \sum_{\mathbf{R}_l} e^{i\mathbf{k}\cdot\mathbf{R}_l}\phi^{(j)}(\mathbf{r} + \boldsymbol{\delta}_j - \mathbf{R}_l) \tag{2.2.7}$$

where the sum is performed over all Bravais lattice vectors. In the present case, these correspond to the $|p_z\rangle$ orbitals at each site. The connection to the sublattice index is now clear: the primitive unit cell in graphene contains two atoms (one per sublattice), as seen in Fig (2.1).

Precisely because the wavefunction $\Psi_{\mathbf{k}}(\mathbf{r})$ must comply with Bloch's Theorem, itself not warranted if the underlying lattice is not Bravais, a decomposition into Bravais sublattice must be found. This consideration alone leads to a decomposition of the wavefunction into two independent components, each pertaining to the different sublattices A and B and individually.

To obtain a matrix representation of the tight-binding Hamiltonian that will allow for the energy dispersion to be obtained, one must solve the Schrödinger equation $H\psi_{\mathbf{k}} = \epsilon_{\mathbf{k}}\psi_{\mathbf{k}}$. In the sublattice basis chosen in Eq. (2.2.6), the matrix elements must read:

$$H^{ij}_{\mathbf{k}} = \psi^{(i)*}_{\mathbf{k}} H \psi^{(j)}_{\mathbf{k}} \tag{2.2.8}$$

Given the expansion of each sublattice wavefunction in terms of the atomic orbitals of Eq. (2.2.7), this is generally a hugely difficult task. However, after a rather lengthy derivation which can be found in [37], the Hamiltonian elements are calculated more easily if the following decomposition of the Hamiltonian is performed:

$$H^{ij}_{\mathbf{k}} = N(\epsilon^{(i)} s^{ij}_{\mathbf{k}} + t^{ij}_{\mathbf{k}}) \tag{2.2.9}$$

In it, the first part contains the on-site energy ϵ^i of the orbital i, multiplied by what is known as the overlap matrix $s^{ij}_{\mathbf{k}} \equiv \psi^{(i)*}_{\mathbf{k}} \psi^{(j)}_{\mathbf{k}}$. This matrix accounts for the orthogonality between the orbital bases of each individual sublattice species:

$$s^{ij}_{\mathbf{k}}(\mathbf{r}) = \sum_{\mathbf{R}_l} e^{i\mathbf{k}\cdot\mathbf{R}_l} \int \phi^{(i)*}(\mathbf{r} + \boldsymbol{\delta}_i)\phi^{(j)}(\mathbf{r} + \boldsymbol{\delta}_j - \mathbf{R}_l) d^2\mathbf{r}. \tag{2.2.10}$$

Given the usual normalisation condition of the atomic orbitals, the diagonal entries of the overlap matrix are unity. The perturbation to the potential energy of Eq. (2.2.4) is fully expressed in the hopping matrix t which, not surprisingly, is related to the expectation value of the perturbation ΔV between sites i and j:

$$t^{ij}_{\mathbf{k}}(\mathbf{r}) = \sum_{\mathbf{R}_l} e^{i\mathbf{k}\cdot\mathbf{R}_l} \int \phi^{(i)*}(\mathbf{r} + \boldsymbol{\delta}_i)\Delta V(\mathbf{r})\phi^{(j)}(\mathbf{r} + \boldsymbol{\delta}_j - \mathbf{R}_l) d^2\mathbf{r}, \tag{2.2.11}$$

The factor of N accounts for the number of atoms per unit cell. As previously discussed, if one fixes the relative shifts as $\boldsymbol{\delta}_B = \boldsymbol{\delta}_3$ and $\boldsymbol{\delta}_A = \mathbf{0}$, the sum over the Bravais lattice vectors $\mathbf{R}_l$ is performed on the sublattice which has $\boldsymbol{\delta}_i = \mathbf{0}$. Keeping the con-

vention, the sublattice A is chosen as such. The space integrals in each matrix yield the amplitude of the process and are assumed a constant. Finally, the decomposition just presented allows for the energy dispersion $\epsilon_{\mathbf{k}}^{\lambda}$ to be obtained by solving the secular equation:

$$\det\left[H_{\mathbf{k}}^{ij} - \epsilon_{\mathbf{k}}^{\lambda} s_{\mathbf{k}}^{ij}\right] = 0 \tag{2.2.12}$$

leading to exactly N bands ($\lambda = 1, ..N$). With the sublattice basis, two bands are thus predicted.

Considering that the hopping matrix involves a challenging integral in space, summed over all lattice vectors, it is not surprising that the underlying calculation of its elements presents many difficulties. Further simplifications are often taken given the particular system.

Since both sublattices are comprised of the same atomic orbitals, the out-of-plane, vertically-oriented p_z orbitals contribute the same amount to the on-site energy and would yield an irrelevant shift in the dispersion given in Eq. (2.2.12). Furthermore, since it can be reasonably assumed that contributions from neighbouring atoms are more relevant, the sum over the lattice vectors may be performed by first considering the nearest neighbours, followed by the next-nearest neighbours and so on.

Given the alternate nature of the disposition of the sublattices, the nearest neighbours are always located at different sublattices. The amplitude of this particular element is known as the (nearest neighbour) hopping factor:

$$t = \int \phi^{A^*}(\mathbf{r}) \Delta V \phi^{B}(\mathbf{r} + \boldsymbol{\delta}_3) d^2\mathbf{r} \tag{2.2.13}$$

For graphene, it has a value $t = 2.8$ eV [2]. To compute the remaining phases in the hopping matrix t given in Eq. (2.2.11), the associated phases to each hopping are simply given by the appropriate triangular Bravais lattice vectors that connect an

arbitrary A site, at position r, to the nearest B sites –B_1, B_2, B_3, illustrated in Fig. 2.1. In order to find the shift in the position argument of the wavefunction at those points, one can use $\boldsymbol{a}_2 - \boldsymbol{\delta}_3$ for B_1, $\boldsymbol{a}_3 - \boldsymbol{\delta}_3$ for B_2 and $\mathbf{0} - \boldsymbol{\delta}_3$ for B_3. Therefore, the off-diagonal entries of the hopping matrix are simply $t_{\mathbf{k}}^{AB} = t_{\mathbf{k}}^{BA\,*} = t\gamma_{\mathbf{k}}$, where the phase acquired by each hopping is $\gamma_{\mathbf{k}}$:

$$\gamma_{\mathbf{k}} = 1 + e^{-i\mathbf{k}\cdot\boldsymbol{a}_2} + e^{-i\mathbf{k}\cdot\boldsymbol{a}_3} \tag{2.2.14}$$

The nearest-neighbour approximation assumes that the contribution to the atomic potential does not need to consider interactions between lattice sites farther away than the second smallest distance. Given the alternate nature of the honeycomb lattice, any contribution will come from sites separated by $\|\boldsymbol{a}_{1,2}\|$. This approximation already yields satisfactory results for most solids for which the tight-binding treatment applies and depends on the type of orbitals.

The addition of further sites to the calculation is similar in style: the next-nearest neighbours (nnn) are now of the same sublattice type:

$$t' = \int \phi^{A^*}(\mathbf{r})\Delta V \phi^A(\mathbf{r} + \mathbf{a}_1) d^2\mathbf{r} \tag{2.2.15}$$

where $\boldsymbol{a}_1$ is the vector connecting the amplitude of this nnn-hopping was obtained using the A sublattice but the B sublattice produces the same hopping factor. Again, from an arbitrary A sublattice site, six connections to other A sites are found, with the overall phase $\gamma'_{\mathbf{k}}$:

$$\begin{aligned} \gamma'_{\mathbf{k}} &= e^{i\mathbf{k}\cdot\boldsymbol{a}_1} + e^{i\mathbf{k}\cdot\boldsymbol{a}_2} + e^{i\mathbf{k}\cdot\boldsymbol{a}_3} + e^{-i\mathbf{k}\cdot\boldsymbol{a}_1} + e^{-i\mathbf{k}\cdot\boldsymbol{a}_2} + e^{-i\mathbf{k}\cdot\boldsymbol{a}_3} \\ &= 2\sum_{i=1}^{3} \cos(\mathbf{k}\cdot\boldsymbol{a}_i) \end{aligned} \tag{2.2.16}$$

Gathering all hopping terms leads to the hopping matrix:

$$t(\mathbf{k}) = \begin{pmatrix} t'\gamma'_{\mathbf{k}} & t\gamma_{\mathbf{k}} \\ t\gamma^*_{\mathbf{k}} & t'\gamma'_{\mathbf{k}} \end{pmatrix} \tag{2.2.17}$$

As one may expect, the contributions from the the overlap matrix s tend to be very small in comparison to their hopping counterparts. Going up to nearest-neighbours only, the sum is performed exactly like was performed for t. The normalisation of each sublattice Bloch wavefunction leads to the diagonal entries being 1. As for its off-diagonal entries, their amplitude is given by:

$$s = \int \phi^{A*}(\mathbf{r})\phi^B(\mathbf{r} + \boldsymbol{\delta}_3)d^2\mathbf{r} \tag{2.2.18}$$

and the overall phase exactly equal to t i.e. equal to $\gamma_{\mathbf{k}}$, leading to a matrix:

$$s(\mathbf{k}) = \begin{pmatrix} 1 & s\gamma_{\mathbf{k}} \\ s\gamma^*_{\mathbf{k}} & 1 \end{pmatrix} \tag{2.2.19}$$

finally allowing the tight-binding dispersion to be written to a great accuracy as:

$$\epsilon^\lambda_{\mathbf{k}} = \frac{t'\gamma'_{\mathbf{k}} + \lambda t|\gamma_{\mathbf{k}}|}{1 + \lambda s|\gamma_{\mathbf{k}}|} \tag{2.2.20}$$

where the secular equation of Eq. (2.2.12) was used. Given that the overlap amplitude s is much smaller than the others, the denominator can be Taylor-expanded as $1/(1+x) \approx 1 - x$, leading to:

$$\begin{aligned} \epsilon^\lambda_{\mathbf{k}} &\approx t'\gamma'_{\mathbf{k}} + \lambda\left(t - t's\gamma'_{\mathbf{k}}\right)|\gamma_{\mathbf{k}}| - ts|\gamma_{\mathbf{k}}|^2 \\ &\approx t'\gamma'_{\mathbf{k}} + \lambda t|\gamma_{\mathbf{k}}| - ts|\gamma_{\mathbf{k}}|^2 \end{aligned} \tag{2.2.21}$$

where the last step assumes $t' << t$. A bit of algebra yields a relation between the phases as $\gamma'_{\mathbf{k}} = |\gamma_{\mathbf{k}}|^2 - 3$, which allows the dispersion to be written as:

$$\epsilon^{\lambda}_{\mathbf{k}} = \underbrace{(t' - st)}_{t'_{\text{eff}}}|\gamma_{\mathbf{k}}|^2 + \lambda t|\gamma_{\mathbf{k}}| - 3t' \tag{2.2.22}$$

The factor $3t'$ corresponds to a constant shift and is therefore irrelevant. What is interesting is that the inclusion of the overlaps leads to a *renormalisation* of the nnn hopping amplitude. This effect is incredibly feeble in graphene, since t' is measured to be $t' \approx 0.01t = 0.028$ eV. As for the overlap amplitude, it is impossible to obtain given that measurements cannot differentiate t' from t'_{eff}.

It is now clear that if only the nn hoppings are considered, the dispersion is simply:

$$\epsilon^{\lambda}_{\mathbf{k}} = \lambda t|\gamma_{\mathbf{k}}| = \lambda t\sqrt{1 + 4\cos\left(\frac{\sqrt{3}k_x a}{2}\right)\cos\left(\frac{k_y a}{2}\right) + 4\cos^2\left(\frac{k_y a}{2}\right)} \tag{2.2.23}$$

where the explicit components of $\boldsymbol{a}_i$ were used. $\boldsymbol{a}_3$ is not part of the basis that was previously chosen: it is the combination $\boldsymbol{a}_3 = \boldsymbol{a}_2 - \boldsymbol{a}_1$. If this dispersion of Eq. (2.2.23) is now Taylor-expanded, for small $\mathbf{k}$, it becomes linear with the momentum, leading to the famous Dirac cones:

$$\epsilon^{\lambda}_{\mathbf{k}} = \lambda\hbar v_{\text{F}}\|\mathbf{k}\| \tag{2.2.24}$$

where the constant $v_{\text{F}} \equiv 3ta/(2\hbar) \approx c/300$ is known as the *Fermi velocity* and plays a crucial role in the reduction of the π electrons to two-dimensional Dirac spinors.

The applicability of this approximation holds up to energies of ≈ 1 eV, where a bending naturally arises so a peak is reached at the Γ point, as illustrated in Fig. 2.3.

This regime is nonetheless intriguing. Firstly, it indicates that graphene behaves like a zero-gap semiconductor. The positive and negative signs of Eq. (2.2.24) imply the existence of two symmetrical bands, naturally interpreted as the conduction and

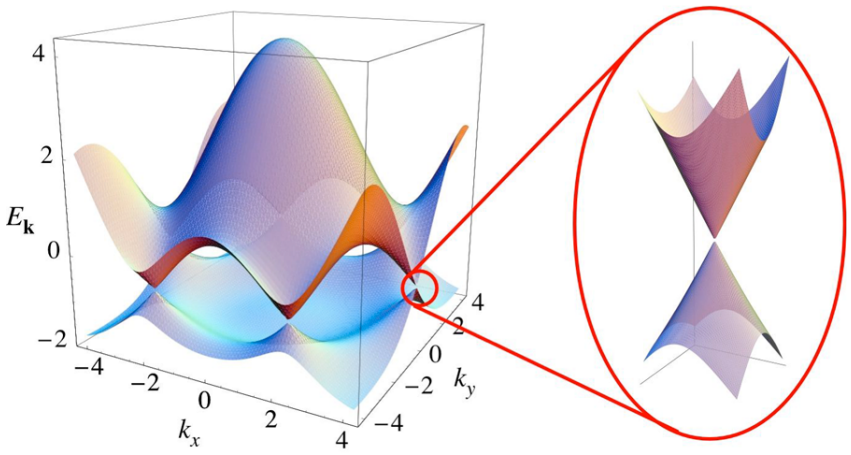

Figure 2.3: The energy dispersion of graphene using a Tight Binding model for the π electrons in the Brillouin zone. The inset shows the conical structure for small $\mathbf{k}$ described on the corners. Figure taken from [2].

valence bands, respectively. Furthermore, this symmetry imply something deeper, namely the equivalence between electron and hole states occupying each band. The Fermi energy lies at the band-touching.

In principle, the introduction of a next-nearest neighbour interactions breaks such symmetry, as seen in Eq. (2.2.22). The rather strong covalent bonding of the nearest neighbour corrections in graphene absolutely dominate the overall perburbation expansion. Indeed, as was previously discussed, measurements of the nnn hopping amplitude put this figure as $t' \approx 0.01$ eV, compared to its nn amplitude counterpart of $t \approx 2.8$ eV [2].

2.3 Massless Dirac Fermions

The previous section offered insightful clues to the adequacy of thinking of the carriers in graphene as massless Dirac fermions. In particular, the linear dispersion provides an exciting result since it mimics the dispersion found for massless quasiparticles notably neutrinos and photons, which are known to be ultra-relativistic. Many in the research community ponder the implication of such a connection. *Is it possible*

to probe high-energy physics concepts, adequate for such relativistic particles in a low-energy framework?

In this section, the quasirelativistic nature of the carriers is formalised. The connection between the Dirac equation in $(3+1)$ dimensions will be shown to model the plane-confined carriers in $(2+1)$ dimensions, allowing interesting analogies to be presented between both models.

The Dirac Equation was formulated by Dirac in 1928 [38] in the hope of reconciling Special Relativity with Quantum Mechanics for a spin 1/2 fermion. The particle, of rest mass m, is described with the aid of a 4-dimensional spinor Ψ and, in free-space, must satisfy:

$$(i\hbar\gamma^{\mu}\partial_{\mu} - mc)\Psi = 0 \tag{2.3.1}$$

where c is the speed of light. The γ matrices are 4-dimensional objects and not uniquely defined. A suitable representation for them must however satisfy the Clifford algebra:

$$\{\gamma^{\mu}, \gamma^{\nu}\} = 2\eta^{\mu\nu}\mathbb{I}_4 \tag{2.3.2}$$

where $\{\cdot,\cdot\}$ denotes the anti-commutator and $\mathbb{I}_4$ the identity operator. Additionally, they must satisfy the Hermicity condition:

$$(\gamma^0)^{\dagger} = \gamma^0 \quad (\gamma^i)^{\dagger} = -\gamma^i \tag{2.3.3}$$

If Eq. (2.3.1) is left-multiplied by γ^0 and the definition $\alpha^{\mu} \equiv \gamma^0\gamma^{\mu}$ applied:

$$(i\hbar\alpha^{\mu}\partial_{\mu} - mc\gamma^0)\Psi = 0 \tag{2.3.4}$$

The metric tensor is taken as $\eta^{\mu\nu} = \mathrm{diag}(1,-1,-1,-1)$. The differential 4-vector has covariant components $\partial_{\mu} = \{(1/c)\partial_t, \boldsymbol{\nabla}\}$ and contravariant components $\partial^{\mu} =$

$\{(1/c)\partial_t, -\boldsymbol{\nabla}\}$. The remaining dot product thus takes the form:

$$\alpha^\mu \partial_\mu = \eta_{\mu\nu}\alpha^\mu \partial^\nu = \alpha^0 \partial_0 + \boldsymbol{\alpha}\cdot\boldsymbol{\nabla} = \left(\frac{1}{c}\right)\partial_t + \boldsymbol{\alpha}\cdot\boldsymbol{\nabla} \tag{2.3.5}$$

Where $\alpha^0 = (\gamma^0)^2 = \mathbb{I}$ by the anticommutation relation.

This is a partial differential equation, depending on space. However, through the canonical relation $\mathbf{p} = -i\hbar\boldsymbol{\nabla}$, the equation is Fourier-transformed, becoming an ordinary differential equation in time. This form is, of course, reminiscent of the Schrödinger equation.

$$i\hbar\frac{d}{dt}\Psi = \underbrace{\left(c\boldsymbol{\alpha}\cdot\mathbf{p} + mc^2\gamma^0\right)}_{H_D}\Psi \tag{2.3.6}$$

The operator on the right-hand side becomes associated to the (Dirac) Hamiltonian H_D. For a massless fermion, $m = 0$ and γ_0 becomes irrelevant. As for a_i, and consequently γ_i, the Dirac representation can be constructed with the aid of the two-dimensional Pauli matrices:

$$\boldsymbol{\sigma}^1 = \begin{pmatrix} 0 & 1 \\ 1 & 0 \end{pmatrix} \quad \boldsymbol{\sigma}^2 = \begin{pmatrix} 0 & -i \\ i & 0 \end{pmatrix} \quad \boldsymbol{\sigma}^3 = \begin{pmatrix} 1 & 0 \\ 0 & -1 \end{pmatrix} \tag{2.3.7}$$

the Dirac representation of γ matrices is simply taken as:

$$\gamma^0 = \begin{pmatrix} \mathbb{I} & 0 \\ 0 & -\mathbb{I} \end{pmatrix} \quad \gamma^i = \begin{pmatrix} 0 & \boldsymbol{\sigma}^i \\ -\boldsymbol{\sigma}^i & 0 \end{pmatrix} \tag{2.3.8}$$

In such representation, the Dirac Hamiltonian in the Dirac representation:

$$H_D^{(D)} = \begin{pmatrix} \mathbf{0} & c\,\boldsymbol{\sigma}\cdot\mathbf{p} \\ c\,\boldsymbol{\sigma}\cdot\mathbf{p} & \mathbf{0} \end{pmatrix} \tag{2.3.9}$$

The analogy is now clear: if c is replaced with v_{F}, the (3+1) Dirac Equation for a massless fermion is composed of two 2-dimensional equivalent blocks of the form:

$$H(\mathbf{k}) = \hbar v_{\mathrm{F}} \boldsymbol{\sigma} \cdot \mathbf{k} \tag{2.3.10}$$

This Hamiltonian measures the energy from the **K** point. For the purpose of this section, only one such valley will be considered given their symmetric role in the physics of ungapped graphene. In it, $\boldsymbol{\sigma}$ is known as the *pseudospin* and characterises many important properties of the quasiparticles [39].

The dot product is to be taken as $\boldsymbol{\sigma} \cdot \mathbf{k} = \sigma_x k_x + \sigma_y k_y$ over the in-plane wavevector, where σ_μ ($\mu = 1, 2$) are the Pauli matrices. In matrix form, the Hamiltonian of Eq. (2.3.10) reads:

$$H(\mathbf{k}) = \hbar v_{\mathrm{F}} \begin{pmatrix} 0 & k_x - ik_y \\ k_x + ik_y & 0 \end{pmatrix} = \hbar v_{\mathrm{F}} \left|\mathbf{k}\right| \begin{pmatrix} 0 & e^{-i\phi_{\mathbf{k}}} \\ e^{i\phi_{\mathbf{k}}} & 0 \end{pmatrix} \tag{2.3.11}$$

Where the phase is given by $\phi_{\mathbf{k}} = \arctan\left(\frac{k_y}{k_x}\right)$. As expected, this model accounts for the linearity of the dispersion calculated from first principles, that resulted in Eq. (2.2.24). The eigenvalues of $H(\mathbf{k})$ in Eq. (2.3.11) are:

$$\epsilon_{\mathbf{k}}^{\lambda} = \lambda \hbar v_{\mathrm{F}} |\mathbf{k}| \tag{2.3.12}$$

with two symmetric branches $\lambda = 1, -1$. Its associated normalised eigenstates may be obtained as:

$$|\lambda \mathbf{k}\rangle = \frac{1}{\sqrt{2}} \begin{pmatrix} e^{-\frac{i}{2}\phi_{\mathbf{k}}} \\ \lambda e^{\frac{i}{2}\phi_{\mathbf{k}}} \end{pmatrix} \tag{2.3.13}$$

The wavefunction of each band λ, represented by $\Psi^{\lambda}_{\mathbf{k}}(\mathbf{r})$, is a solution of the Time-Independent Schrödinger Equation:

$$H(\mathbf{k})\Psi^{\lambda}_{\mathbf{k}}(\mathbf{r}) = \epsilon_{\lambda,\mathbf{k}}\Psi^{\lambda}_{\mathbf{k}}(\mathbf{r}) \tag{2.3.14}$$

and simply is the $\mathbf{r}$-representation of the ket states:

$$\Psi^{\lambda}_{\mathbf{k}}(\mathbf{r}) = \langle \mathbf{r} \,|\, \lambda\mathbf{k} \rangle = \frac{1}{\sqrt{A}} e^{i\mathbf{k}\cdot\mathbf{r}} \begin{pmatrix} e^{-\frac{i}{2}\phi_{\mathbf{k}}} \\ \lambda e^{\frac{i}{2}\phi_{\mathbf{k}}} \end{pmatrix} \tag{2.3.15}$$

where A is the area of the sample. The splitting of the upper and lower components in this fashion is beneficial for future calculations. Consider the normalisation of such wavefunctions:

$$\begin{aligned} \int \left\langle \Psi^{\lambda'}_{\mathbf{k}'}(\mathbf{r}) \,\middle|\, \Psi^{\lambda}_{\mathbf{k}}(\mathbf{r}) \right\rangle d^2\mathbf{r} &= \frac{1}{A} \langle \lambda'\mathbf{k}' \,|\, \lambda\mathbf{k} \rangle \int e^{-i(\mathbf{k}'-\mathbf{k})\cdot\mathbf{r}} d^2\mathbf{r} \\ &= \frac{2\pi}{A} \langle \lambda'\mathbf{k}' \,|\, \lambda\mathbf{k} \rangle \, \delta(\mathbf{k}'-\mathbf{k}) \end{aligned} \tag{2.3.16}$$

As for the spinor normalisation, it reads:

$$\begin{aligned} \langle \lambda'\mathbf{k}' \,|\, \lambda\mathbf{k} \rangle &= \frac{1}{2} \left(e^{\frac{i}{2}(\phi_{\mathbf{k}'}-\phi_{\mathbf{k}})} + \lambda\lambda' e^{-\frac{i}{2}(\phi_{\mathbf{k}'}-\phi_{\mathbf{k}})} \right) \\ &= \begin{cases} \cos(\phi_{\mathbf{k}} - \phi_{\mathbf{k}'}) \text{ if } \lambda = \lambda' \\ i\sin(\phi_{\mathbf{k}} - \phi_{\mathbf{k}'}) \text{ if } \lambda \neq \lambda' \end{cases} \end{aligned} \tag{2.3.17}$$

Evidently, for $\mathbf{k}' = \mathbf{k}$, one obtains $\langle \lambda'\mathbf{k}' \,|\, \lambda\mathbf{k} \rangle = \delta_{\lambda'\lambda}$. With the knowledge of the wavefunction, many properties and features of the system may be unravelled.

2.3.1 Density of States

The density of states plays a particularly important role in the dynamics and interactions of electrons within a condensed matter system. It can be seen as a degree of

degeneracy, accounting for the number of available quantum states for a given fixed energy interval.

Unlike an electron in two dimensions modelled by the Schrödinger Equation, which admits a *constant* density of states (per unit volume per unit energy) [40], the linearity of the dispersion of low-momentum electrons just discussed leads, by extension, to another interesting result — the density of states of the carriers in graphene is also linearly proportional to their energy.

The calculation for a then-hypothetical graphene monolayer in 1952, a mere five years after the dispersion had been obtained by Wallace, was already well established [41], by a direct calculation of the specific heat using a Debye frequency distribution. In addition to that, the appearance of non-differentiable points in the density of states leads to fascinating phenomena, such as enhancemenet in the electric resistance and optical conductivity of the material [42]. For more physically-relevant graphene flakes, the effect of geometry, size and edge terminations have been reported to create various van Hove singularities which in turn affect the optical response of the flake [43].

Before engaging in this particular calculation, the general definition is given, where $g(\epsilon)$ denotes the density of states of the states in the interval $[\epsilon - \delta\epsilon, \epsilon + \delta\epsilon]$:

$$g(\epsilon) = g_v g_s \frac{1}{A} \sum_{\mathbf{k}} \delta(\epsilon - \epsilon(\mathbf{k})) \tag{2.3.18}$$

Here, A is the area of the monolayer sample. Since the dispersion of Eq. (2.2.24) is not dependent on which Dirac point the Hamiltonian is measured from nor on the spin contributions, since they do not appear in the quasirelativistic model so far developed, one must introduce the valley and spin degeneracy factors, respectively given by g_v and g_s. These are $g_v = g_s = 2$, respectively for the $\mathbf{K}$ and $\mathbf{K}'$ valleys and for the spin up and down contributions.

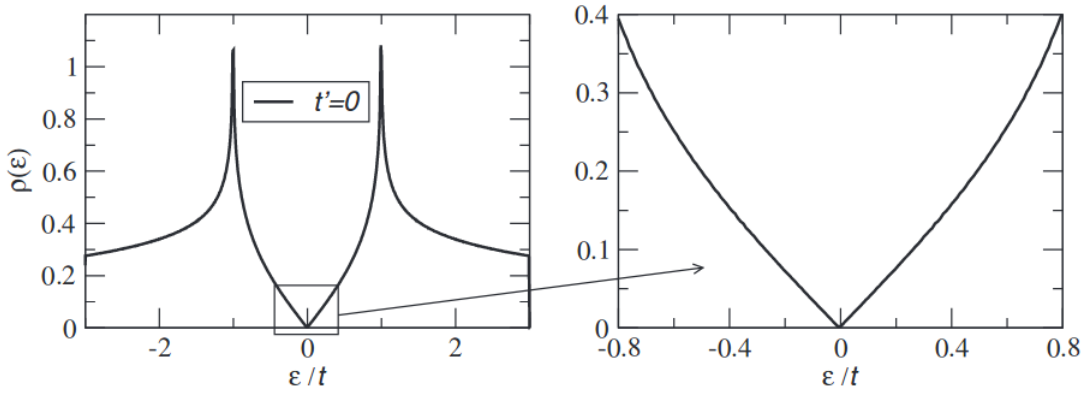

Figure 2.4: Plot of density of states of a honeycomb lattice using tight-binding methods in the nearest neighbour regime (the nnn-hopping amplitude is set to 0). This function hints at the existence of van Hove singularities, two non-differentiable critical points symmetrical about the point where the dispersion vanishes. Most importantly, a linear relation for low frequencies in such point may be seen in the right plot. Taken from [2]

The calculation of the density of states, as dictated by Eq. (2.3.18) is in general rarely obtained through analytical methods, given the intrinsic complexity of general dispersions. However, in the linear regime of the dispersion, the general definition of Eq. (2.3.18) can be simplified using the continuum approximation:

$$\sum_{\mathbf{k}} \mapsto \frac{A}{(2\pi)^2} \int d^2\mathbf{k} \tag{2.3.19}$$

where the sum is performed over momentum. Using the energy dispersion of Eq. (2.2.24) and integrating with polar coordinates $k \equiv \|\mathbf{k}\|$, $\phi \equiv \arctan(k_y/k_x)$, it becomes:

$$\begin{aligned} \frac{1}{(2\pi)^2} \int d^2\mathbf{k}\delta(\epsilon - \epsilon(\mathbf{k})) &= \frac{1}{(2\pi)^2} \int_0^\infty dkk \int_0^{2\pi} d\phi\delta(\epsilon - \epsilon(k)) \\ &= \frac{2\pi}{(2\pi)^2} \int_0^\infty dkk\delta(\epsilon - \epsilon(k)) \\ &= \frac{2\pi}{(2\pi)^2} \int_0^\infty dkk\delta(\epsilon - \hbar v_{\mathrm{F}} k) \end{aligned} \tag{2.3.20}$$

where the integration in both variables is independent given the dispersion is purely radial. The evaluation of the integrand is performed using the following identity of the Dirac-δ distribution:

$$\delta(f(k)) = \sum_{k_i} \frac{\delta(k - k_i)}{|f'(k_i)|} \tag{2.3.21}$$

where the sum is performed over the zeroes of $f(k)$, k_i. Letting $f(k) := \epsilon - \epsilon(k)$, and given that k is necessarily non-negative, a unique solution k_0 arises for a fixed ϵ, namely whenever $k_0 = \epsilon/(\hbar v_{\mathrm{F}})$, hence the density of states becomes:

$$g(\epsilon) = g_s g_v \frac{2\pi}{(2\pi)^2} \int_0^\infty dk k \left(\frac{1}{\hbar v_{\mathrm{F}}}\right) \delta\left(k - \frac{\epsilon}{\hbar v_{\mathrm{F}}}\right) \tag{2.3.22}$$

Finally, the sifting property of the δ distribution:

$$\int_{-\infty}^{\infty} f(k)\delta(k - k_0)dk = f(k_0) \tag{2.3.23}$$

implies that, for $f(k) \equiv k$, $g(\epsilon)$ takes the form:

$$g(\epsilon) = g_v g_s \frac{2\pi}{(2\pi)^2} \frac{|\epsilon|}{\hbar^2 v_{\mathrm{F}}^2} = \frac{2|\epsilon|}{\pi \hbar^2 v_{\mathrm{F}}^2} \tag{2.3.24}$$

where the modulus sign arises from the equivalence of k_0 for either a positive or negative energy.

It can then be seen that the density of states is piecewise linear. This result is surprising for a two-dimensional system and to be contrasted with a Fermi gas in two-dimensions, which admits a constant density of states. The neutrality point occurs at the Dirac point i.e. when $\epsilon = 0$, where $g(\epsilon)$ becomes non-differentiable. From a QFT point of view, the linearity of the spectrum is unique in that it implies the Coulomb interactions between the carriers are not screened [44]. As will be seen throughout this work, the Dirac points really are remarkable and dictate much of the physics observed in graphene.

2.4 The Optics of Graphene

2.4.1 Overview

In order to understand how matter behaves optically, an obvious ingredient is missing - *light*. Throughout this work, a semiclassical approach will be used to describe any light-matter interactions. This is to say that any electromagnetic field are taken as classical fields, while the carriers in the crystal are treated quantum mechanically. *Maxwell Equations* provide the fundamental relationship between electromagnetic fields and matter.

This relationship is not easy to quantify for most part: it is a feedback-based hierarchy of external and induced fields which act as a *response* to the external disturbance on their charge configuration. Finding macroscopic quantities that describe these two different types of contributions is at best challenging.

Light is classically understood, at the macroscopic level, by the specification of the electric field $\mathbf{E}(\mathbf{r}, t)$ and the magnetic field $\mathbf{B}(\mathbf{r}, t)$. Depending on the coupling profile, matter will respond to the perturbation. In the simplest picture, a charge distribution will take place, leading to the medium *polarisation*. Dynamical charge distributions create *electric currents* in the sample. The harmonic composition of such currents acts in many ways as a means to probe the light-matter interactions. However intuitive, this picture completely overlooks the difficulty of obtaining reliable estimates of such quantities.

To further complicate the task, these estimates depend hugely on which optical excitation regime is chosen. A rough separation of affairs concerns the electric field intensity. If the macroscopic polarisation responds linearly to the electric field, the system is said to be excited in the *linear optical regime*. Otherwise, it is known as *nonlinear*. It is known, and somewhat expected, that there is a remarkable qualitative departure from the linear regime when the field intensity becomes large,

leading to a modification of the optical properties of the material itself when probed. Therefore, these properties are field-dependent and thus frequency-dependent, in highly nontrivial ways.

The features are also strictly dependent on the features of the medium and a generalisation of the principles is not easy to achieve. The advancement of highly-coherent laser devices, with which intense monochromatic beams can be created relieably at the femtoscale, has revolutionised the field and proved to be a trustworthy platform to study intense excitation regimes. The field of Nonlinear Optics has been irrevocably linked to the methods and mechansisms that provide the framework for understanding *harmonic generation*, *sum* and *difference-frequency generation*, *saturable absorption*, *self-induced transparency* [45] and many other concepts not found in the more usual, linear branch of Optics [46, 47] and has inspired more general treatments such as Quantum Optics [48], where full quantum-mechanical properties of both matter and light fields are taken into account.

Not surprisingly, the linearity of the spectrum of massless Dirac fermions makes graphene an interesting platform to probe many optical phenomena. For instance, diffusive electron transport and temperature-dependent resistivity and conductivity vary from what is expected of a conventional semiconductor [49, 50].

As will be showed in Section 2.4.3, when excited with a weak electromagnetic field, a graphene monolayer absorbs all frequencies with the same efficiency of approximately 2.3%. Fascinatingly, this rate is not dependent on any excitation parameter, rendering it *universal*, given by the fundamental constants:

$$\pi \frac{e^2}{4\pi\varepsilon_0 \hbar c} = \pi \alpha_{\mathrm{QED}} \tag{2.4.1}$$

where α_{QED} is the fine-structure constant in Quantum Electrodynamics. Related to this behaviour is the conductivity of a graphene sheet, which is also a constant [51] and related to the quantum of conductance $2e^2/h$, as:

$$\sigma_0 = \frac{e^2}{4\hbar} \tag{2.4.2}$$

The frequency-dependent character of the conductivity as the excitation energy is increased may be appreciated in [52]. Despite the existence of defects and other environmental factors, the universal optical conductivity has been been experimentally verified in the spectral range of 0.2–1.2 eV [53].

In this section, a brief review of the necessary main optical and optoelectronic properties of graphene is given. The techniques needed to introduce light interactions within the formalism just exposed wil also be presented. With them, a calculation of the electric dipole moment induced by photon absorption is presented and used to compare the same quantity that is found for semiconductors. To make sense of what is meant by a weak field, a rather brief review of the concepts of linear optics will be given here and used in later sections to retrieve results pertaining to this regime.

2.4.2 Semiclassical Light-Matter Interactions

Nonlinear Susceptibility

For simplicity, a space-independent electric field $E(t)$ is considered for now. The (macroscopic) polarisation $P(t)$ is normally obtained through expansion in powers of the field [46]

$$\begin{aligned} P(t) &= \epsilon_0 \left(\chi^{(1)}E(t) + \chi^{(2)}E^2(t) + \chi^{(3)}E^3(t) + ...\right) \\ &\equiv P^{(1)}(t) + P^{(2)}(t) + P^{(3)}(t) + ... \end{aligned} \tag{2.4.3}$$

where ϵ_0 is the permittivity of free space. The quantity $\chi^{(i)}$ denotes the i$^{\text{th}}$ order of the *electric susceptibility*. The information about the optical properties of the material is encoded in it. Since the electric field is input as a scalar, the susceptibility is a constant, dependent on the material.

Given the nature of the expansion, each order of the polarisation $P^{(i)} \equiv \epsilon_0 \chi^{(i)} E^i$ only makes sense if subsequent terms become smaller i.e. $P^{(i)} > P^{(i+1)}$. Field intensities for which this expansion is broken are exceedingly high. For instance, an estimation of the susceptibility of a hydrogen atom leads to a second-order susceptibility $\chi^{(2)} \approx 1.94 \times 10^{-12}$ mV^{-1} and a third-order susceptibility $\chi^{(3)} \approx 3.78 \times 10^{-24}$ m^{2}V^{-2} [46]. A critical electric field intensity is then:

$$E_{\text{crit}} \approx \frac{\chi^{(2)}}{\chi^{(3)}} \tag{2.4.4}$$

leading to a critical intensity I_{crit} estimation of the order:

$$I_{\text{crit}} = \frac{1}{2}\epsilon_0 c E_{\text{crit}}^2 \approx 3.4 \times 10^{20} \text{ Wm}^{-2} \tag{2.4.5}$$

a rather large value! It is therefore generally safe to assume the expansion is meaningful. If the electric field is now a vector field $\mathbf{E} = (E_x, E_y, E_z)$, the susceptibility is much more complicated. Each expansion of it, $\chi^{(i+1)}$, becomes a rank-$(i+1)$ tensor. Anisotropic media need to be necessarily treated in this fashion.

The j^{th} component of the polarisation is now expressed as [54]:

$$P_j = \epsilon_0 \left(\sum_k \chi_{jk}^{(1)} E_k + \sum_{k,l} \chi_{jkl}^{(2)} E_k E_l + \sum_{k,l,m} \chi_{jklm}^{(3)} E_k E_l E_m + ... \right) \tag{2.4.6}$$

This formula assumes an instantaneous response: that the polarisation at a time t only depends on the susceptibility at that instant. In reality, the response depends

on past times $t' < t$ too, leading to a more general form for the polarisation:

$$\begin{aligned} P_j(t) = \epsilon_0 \Bigg[& \sum_{k=1}^{3} \int_0^\infty \chi^{(1)}_{jk}(\tau) E_k(t-\tau) d\tau \\ & + \sum_{k,l=1}^{3} \int_0^\infty \chi^{(2)}_{jkl}(\boldsymbol{\tau}) E_k(t-\tau_1) E_l(t-\tau_2) d\boldsymbol{\tau} \\ & + \sum_{k,l,m=1}^{3} \int_0^\infty \chi^{(3)}_{jklm}(\boldsymbol{\tau}) E_k(t-\tau_1) E_l(t-\tau_2) E_m(t-\tau_3) d\boldsymbol{\tau} + ... \Bigg] \end{aligned} \tag{2.4.7}$$

where $\boldsymbol{\tau}$ denotes a vector $\boldsymbol{\tau} = (\tau_1, \tau_2, \tau_3, ...)$, with its differential being $d\boldsymbol{\tau} = d\tau_1 d\tau_2 d\tau_3 ....$

In this fashion, the linear and nonlinear contributions can be retrieved easily. In particular, the first-order susceptibility tensor $\chi^{(1)}$ is a matrix that describes the *linear* part of the polarisation. If only the linear contribution is considered, Eq. (2.4.7) allows a simple decomposition to be made:

$$\mathbf{P}(t) = \epsilon_0 \int_0^\infty \chi^{(1)}(\tau) \mathbf{E}(t-\tau) d\tau \tag{2.4.8}$$

If Eq. (2.4.8) is Fourier-transformed, i.e. by obtaining the frequency-dependent polarisation and electric field:

$$\begin{aligned} \mathbf{P}(\omega) &\equiv \frac{1}{2\pi} \int_{-\infty}^{\infty} \mathbf{P}(t) e^{-i\omega t} dt \\ \mathbf{E}(\omega) &\equiv \frac{1}{2\pi} \int_{-\infty}^{\infty} \mathbf{E}(t) e^{-i\omega t} dt \end{aligned} \tag{2.4.9}$$

one can see that a non-instantaneous response leads to a frequency-dependent susceptibility $\chi^{(1)}(\omega)$, a phenomenon that leads to a particular *dispersion* profile of the medium. It can be simply obtained by the Convolution Theorem:

$$\mathbf{P}(\omega) = \epsilon_0 \chi^{(1)}(\omega) \mathbf{E}(\omega) \tag{2.4.10}$$

This equation defines the linear response of the system to the electric field. Interestingly, the first nonlinearity in most materials is found when considering the third-order term in the expansion i.e. the second-harmonic susceptibility contribution is null.
The condition for this phenomenon to occur is related to the *centrosymmetry* of the material: whether the lattice has the property for which the mapping $\mathbf{r} \mapsto -\mathbf{r}$ preserves its structure. To appreciate the role of centrosymmetry in second-order susceptibility, one must simply consider a simple homogeneous instantaneously-polarised medium [46]. Then, from Eq. (2.4.3), its corresponding second-order contribution to the polarisation is simply:

$$P^{(2)}(t) = \epsilon_0 \chi^{(2)} E^2(t) \tag{2.4.11}$$

It can now be seen that if $E \mapsto -E$, then $P^{(2)} \mapsto P^{(2)}$. However, if the system is centrosymmetric, $P^{(2)}$ must *also* change sign when the electric field does. This leads to the conclusion that $P^{(2)}$ must vanish. Since both ϵ_0 and $E(t)$ do not vanish, it follows that $\chi^{(2)}$ does i.e. $\chi^{(2)} = 0$.
This conclusion has deep consequences. In particular, graphene is a centrosymmetric medium and this result should hold. This can be seen, for instance, in its angular-symmetric conical dispersion, implying that $\epsilon_{\mathbf{k}} = \epsilon_{-\mathbf{k}}$. This argument will be seen to be somewhat incomplete, in the sense that if the dispersion becomes time-dependent and shifts considerably, $\epsilon_{\mathbf{k}}(t) \neq \epsilon_{-\mathbf{k}}(t)$ in general. The lattice is no longer static but also oscillates with the pulse. This phenomenon will ultimately allow second-harmonic waves to be generated in the sample, as will be discussed in Section 4.3.1.

Minimal Substitution

In order to couple light to electrons in a crystal structure, an accurate scheme to introduce the light contributions into the Schrödinger equation, the equation which models the dynamics of the carriers, must be found. Simple gauge arguments suffice and lead to the establishment of two additional fields: the electromagnetic vector

potential $\mathbf{A}$ and the electromagnetic (scalar) potential U .

Semiclassically, the interaction of radiation with matter may be appropriately obtaining by applying the *minimal substitution* – a change of the electronic momentum through the vector electromagnetic potential as given by:

$$\mathbf{p} \mapsto \mathbf{p} - \frac{q}{c}\mathbf{A} = \mathbf{p} + \frac{e}{c}\mathbf{A} \tag{2.4.12}$$

where $q = -e$ is the electron charge. The relevance of these fields can be understood by symmetry considerations: a free electron in the lattice is described by the time-dependent Schrödinger equation:

$$i\hbar\frac{\partial}{\partial t}\psi(\mathbf{r},t) + \left[\frac{\hbar^2}{2m}\nabla^2 + V(\mathbf{r})\right]\psi(\mathbf{r},t) = 0 \tag{2.4.13}$$

where $V(\mathbf{r})$ is the lattice potential introduced in Eq. (2.2.2). If a physically irrelevant phase $\chi(\mathbf{r},t)$ is applied to one of its solutions in the form of the *local* gauge transformation $\Psi(\mathbf{r},t) \mapsto \Psi(\mathbf{r},t)e^{i\chi(\mathbf{r},t)}$, the Schrödinger equation must be changed to:

$$i\hbar\frac{\partial}{\partial t}\Psi(\mathbf{r},t) + \left[\frac{\hbar^2}{2m}\left(\nabla + \frac{ie}{\hbar}\mathbf{A}\right)^2 - eU + V\right]\Psi(\mathbf{r},t) = 0 \tag{2.4.14}$$

in order to comply with the invariance of the probability density $|\Psi(\mathbf{r},t)|^2$. In this fashion, the equation was made gauge-invariant under such gauge transformation. Consequently, the potentials must transform as:

$$\begin{aligned} \mathbf{A}(\mathbf{r},t) &\mapsto \mathbf{A}(\mathbf{r},t) - \frac{\hbar}{e}\nabla\chi(\mathbf{r},t) \\ U(\mathbf{r},t) &\mapsto U(\mathbf{r},t) + \frac{\hbar}{e}\frac{\partial}{\partial t}\chi(\mathbf{r},t) \end{aligned} \tag{2.4.15}$$

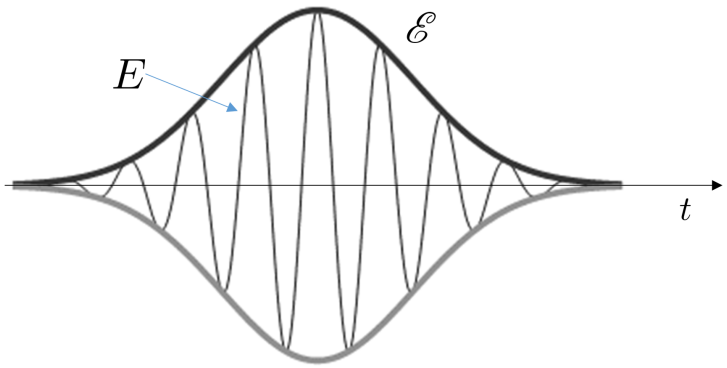

Figure 2.5: A typical electric field $\mathbf{E}(\mathbf{r}, t)$ pulse profile in the time domain, bounded by its upper (red) and lower (orange) envelopes. The pulse is well described by its envelope if it is fast-oscillating.

meaning both potentials are gauge-dependent and not physical. The physical electromagnetic fields can be unambiguously defined via:

$$\begin{aligned} \mathbf{E} &= -\nabla U - \frac{1}{c}\frac{\partial}{\partial t}\mathbf{A} \\ \mathbf{B} &= \nabla \times \mathbf{A} \end{aligned} \tag{2.4.16}$$

with the identification of the momentum operator as $\mathbf{p} \equiv -i\hbar\nabla$, the minimally-coupled Hamiltonian takes the form:

$$H = \frac{1}{2m}\left(\mathbf{p} + \frac{e}{c}\mathbf{A}(\mathbf{r}, t)\right)^2 - eU(\mathbf{r}, t) + V(\mathbf{r}) \tag{2.4.17}$$

The electromagnetic four-potential $a^\mu \equiv (U, \mathbf{A})$, where $\mathbf{A}$ denotes the three Cartesian components of the electromagnetic vector potential $\mathbf{A}$, is not uniquely defined given the constraints of Eq. (2.4.15). A useful complete gauge choice, and one that will be extensively used in all theory and simulations developed in this work, is known as the *radiation gauge*, achieved by the requirements that $\boldsymbol{\nabla} \cdot \mathbf{A} = 0$. The scalar electromagnetic potential can be set to $U(\mathbf{r}, t) = 0$. In this way, $\mathbf{E}(\mathbf{r}, t)$ is related to

$\mathbf{A}(\mathbf{r},t)$ simply as:

$$\mathbf{E}(\mathbf{r},t) = -\frac{1}{c}\frac{\partial \mathbf{A}(\mathbf{r},t)}{\partial t} \tag{2.4.18}$$

Dipole Approximation

Another assumption that simplifies subsequent calculations is given by the dipole approximation. The electric field $\mathbf{E}(\mathbf{r},t)$ associated with light, under some circumstances, may be assumed to be a function of time only. This results in no spatial dependence when considering the effects of light on the dynamics of an electron. The optical fields (both applied and induced) are supposed to have characteristic wavelengths much larger than the next-neighbour separation and the atom diameter. For instance, the applied electric field $\mathbf{E}(\mathbf{r},t)$, here taken in the form of a continuous wave, remains uniform throughout the whole carbon atom since, for an atom sitting at $\mathbf{r} = \mathbf{r_0}$:

$$\begin{aligned}
\mathbf{E}(\mathbf{r_0}+\mathbf{r},t) &= \mathbf{E}(t)e^{i\mathbf{k}\cdot(\mathbf{r_0}+\mathbf{r})} \\
&= \mathbf{E}(t)e^{i\mathbf{k}\cdot\mathbf{r_0}}\left(1 + i\mathbf{k}\cdot\mathbf{r} - \frac{(\mathbf{k}\cdot\mathbf{r})}{2!} + ...\right) \\
&\approx \mathbf{E}(t)e^{i\mathbf{k}\cdot\mathbf{r_0}}
\end{aligned} \tag{2.4.19}$$

where the approximation $\mathbf{k}\cdot\mathbf{r} \ll 1$ was explicitly used. The same reasoning can be applied to the electromagnetic vector potential $\mathbf{A}(\mathbf{r},t)$.

Slowly Varying Envelope Approximation

In general, and in the context of pulsed excitations, $\mathbf{E}(\mathbf{r},t)$ is a fast-oscillating wave over many optical cycles, bounded by an envelope $\mathcal{E}(\mathbf{r},t)$. This field configuration does not admit, in general, analytical solutions to dynamical equations which depend on it. Therefore, it becomes impractical - if not impossible - to retrieve $\mathbf{E}$ from its primitive, $\mathbf{A}$, as Eq. (2.4.18) suggests.

To find a method to relate $\mathbf{E}(\mathbf{r},t)$ to $\mathbf{A}(\mathbf{r},t)$, the Slowly Varying Envelope Approximation (SVEA) allows a huge deal of complexity to be removed from many models, while keeping the same physical information of the pulse. This of course is contingent on excitation conditions.

Generally, an electric field $\mathbf{E}(\mathbf{r},t)$, of optical frequency ω_0 may be decomposed through its envelope $\boldsymbol{\mathscr{E}}(\mathbf{r},t)$:

$$\mathbf{E}(\mathbf{r},t) = \frac{1}{2}\left(\boldsymbol{\mathscr{E}}(\mathbf{r},t)e^{-i\omega_0 t} + \boldsymbol{\mathscr{E}}^*(\mathbf{r},t)e^{i\omega_0 t}\right) \tag{2.4.20}$$

and likewise for $\mathbf{A}(\mathbf{r},t)$ with envelope $\boldsymbol{\mathscr{A}}(\mathbf{r},t)$:

$$\mathbf{A}(\mathbf{r},t) = \frac{1}{2}(\boldsymbol{\mathscr{A}}(\mathbf{r},t)e^{-i\omega_0 t} + \boldsymbol{\mathscr{A}}^*(\mathbf{r},t)e^{i\omega_0 t}) \tag{2.4.21}$$

Inserting Eqs. 2.4.20 and 2.4.21 into Eq. 2.4.18 yields

$$\frac{1}{2}\left(\boldsymbol{\mathscr{E}}(\mathbf{r},t)e^{-i\omega_0 t} + \boldsymbol{\mathscr{E}}^*(\mathbf{r},t)e^{i\omega_0 t}\right) = -\frac{1}{2c}\left(\dot{\boldsymbol{\mathscr{A}}}e^{-i\omega_0 t} - i\omega_0 e^{-i\omega_0 t}\boldsymbol{\mathscr{A}}\right) \tag{2.4.22}$$

which leads to the following relation between the field envelopes:

$$\boldsymbol{\mathscr{E}} = -\frac{1}{c}(\partial_t - i\omega_0)\boldsymbol{\mathscr{A}} \tag{2.4.23}$$

The *Slowly Varying Envelope Approximation* may now be used: one may assume that the temporal rate of change of the envelope is negligible, i.e. $|\partial_t \boldsymbol{\mathscr{A}}| \ll \omega_0 |\boldsymbol{\mathscr{A}}|$. Then:

$$\boldsymbol{\mathscr{E}} \approx \frac{i\omega_0}{c}\boldsymbol{\mathscr{A}} \Leftrightarrow \boldsymbol{\mathscr{A}} \approx -\frac{ic}{\omega_0}\boldsymbol{\mathscr{E}} \tag{2.4.24}$$

Optical Absorption

As the field penetrates the medium, the intensity of its corresponding electric field will decay. This decay can be associated with the sample's *absorption*. In order to

quantify this process, the refractive index $n(\omega)$ is defined as:

$$n(\omega) = \sqrt{\epsilon^{(1)}(\omega)} = \sqrt{1 + \chi^{(1)}(\omega)} \tag{2.4.25}$$

where the dielectric function $\varepsilon(\omega)$ quantifies the electric permittivity of the material when excited at a frequency ω.

For the case of two-dimensional materials without a substrate, the background contributions to these two quantities will not be considered. If they were, they would lead to a renormalisation of the field speed and the dieletric function [50].

As the pulse propagates throughout sample, the field wavevector, which is not to be confused with the electronic wavevector $\mathbf{k}$, will satisfy a *dispersion relation*, determined by the medium's frequent-dependent properties:

$$\mathbf{q}(\omega)^2 = \frac{\omega^2}{c^2} n^2(\omega) = \frac{\omega^2}{c^2} \varepsilon(\omega) \tag{2.4.26}$$

The field will have its intensity decreased as it penetrates the material. If this decay is exponential, then:

$$\mathbf{E}(\mathbf{r}, t) = \mathbf{E}(0, t) \exp(i\mathbf{q} \cdot \mathbf{r}) = \mathbf{E}(\mathbf{0}, t) \exp\left(i \frac{\omega}{c} (n^{'}(\omega) + i n^{''}(\omega)) \cdot \mathbf{r}\right) \tag{2.4.27}$$

where the refractive index has been split in its real and imaginary parts $n(\omega) \equiv n'(\omega) + in''(\omega)$. The damping is consequently related to the imaginary part of the refractive index.

Assuming the wave only propagates in the direction perpendicular to the plane occupied by the sample, its intensity may be computed as the average of the Poynting vector $\mathbf{S}(\mathbf{r}, t)$:

$$\mathbf{S}(z, t) = |\mathbf{E}(z, t) \times \mathbf{H}(z, t)| = \sqrt{\frac{\epsilon_0}{\mu_0}} |\mathbf{E}(z, t)|^2 \hat{\boldsymbol{z}} \tag{2.4.28}$$

and therefore proportional to $|\mathbf{E}|^2$. The auxiliary magnetic field $\mathbf{H}$ is simply proportional to the magnetic field density $\mathbf{B}$ since no magnetisation is present. If the time-dependent term is averaged, the spacial dependence on the intensity may be written as $I(z) = I_0 e^{-\alpha(\omega)z}$ given that:

$$\langle S(z)\rangle = \frac{\epsilon_0}{\mu_0}\langle E^2(0,t)\rangle \exp\left(-2\frac{\omega}{c}n''(\omega)z\right) \tag{2.4.29}$$

In this way, and attending to the definition in Eq. (2.4.25) and Taylor-expanding it up to first-order, the absorption coefficient $\alpha(\omega)$ is:

$$\alpha(\omega) = 2\frac{\omega}{c}\mathrm{Im}\left(\sqrt{1+\chi^{(1)}(\omega)}\right) \approx \frac{\omega}{c}\chi^{(1)''}(\omega) \tag{2.4.30}$$

where the susceptibility was also written as $\chi^{(1)}(\omega) \equiv \chi^{(1)'}(\omega) + i\chi^{(1)''}(\omega)$. This result will be used for Eq. (3.6.30), where the explicit evaluation of the linear susceptibility leads to the prediction of the law of universal absorption of graphene.

2.4.3 Optical Response

With all these ingredients presented, the light-matter coupling can be included in the Hamiltonian describing massless Dirac fermions. In order to do this, the minimal substitution that was given in Eq. (2.4.12) is applied to the Hamiltonian of Eq. (2.3.10):

$$\begin{aligned} H_{\mathbf{k}} \mapsto v_{\mathrm{F}}\boldsymbol{\sigma}\cdot\left(\mathbf{p}+\frac{e}{c}\mathbf{A}\right) &= v_{\mathrm{F}}\boldsymbol{\sigma}\cdot\mathbf{p} + \frac{ev_{\mathrm{F}}}{c}\boldsymbol{\sigma}\cdot\mathbf{A}(t) \\ &\equiv H_0 + H_{\mathrm{int}}(t) \end{aligned} \tag{2.4.31}$$

naturally yielding the explicit interaction term H_{int}. In SVEA conditions, Eq. 2.4.24 allows the interaction operator to be expressed in terms of the electric field envelope:

$$H_{\text{int}}(t) = -\frac{iev_{\text{F}}}{2\omega_0}\boldsymbol{\sigma}\cdot\boldsymbol{\mathscr{E}} \tag{2.4.32}$$

which, if compared to the standard electric dipole moment operator $\boldsymbol{\mu}$, satisfying $H_{\text{int}}(t) = -\boldsymbol{\mu}\cdot\boldsymbol{\mathscr{E}}(t)$, allows one to find the following representation of the electric dipole operator for massless Dirac fermions:

$$\hat{\boldsymbol{\mu}} = \frac{iev_{\text{F}}}{2\omega_0}\hat{\boldsymbol{\sigma}} \tag{2.4.33}$$

Electric Dipole Moment

With a representation of the interaction, the associated electric dipole moment, the observable of this operator, is simply its expectation value. Conveniently, the calculation of expectations of a position-independent operator $\hat{\mathcal{Q}}$ is easily achieved due to the orthogonality of the plane waves associated with different $|\lambda\mathbf{k}\rangle$ states, since:

$$\begin{aligned}\int_{\mathbb{R}^2}\Psi^{\dagger}_{\lambda',\boldsymbol{k}'}(\mathbf{r})\hat{\mathcal{Q}}\Psi_{\lambda,\mathbf{k}}(\mathbf{r})d^2\mathbf{r} &= \left\langle\lambda'\mathbf{k}'\right|\left.\hat{\mathcal{Q}}\right|\lambda\mathbf{k}\right\rangle\int_{\mathbb{R}^2}e^{i(\mathbf{k}-\mathbf{k}')\cdot\mathbf{r}}d^2\mathbf{r}\\ &= \frac{(2\pi)^2}{A}\delta(\mathbf{k}-\mathbf{k}')\left\langle\lambda'\mathbf{k}'\right|\left.\hat{\mathcal{Q}}\right|\lambda\mathbf{k}\right\rangle\end{aligned} \tag{2.4.34}$$

where the following identity for the p-dimensional Dirac δ function was used:

$$(2\pi)^p\delta^{(p)}(\mathbf{k}-\mathbf{k}') = \int_{\mathbb{R}^p}e^{i(\mathbf{k}-\mathbf{k}')\cdot\mathbf{r}}d^p\mathbf{r} \tag{2.4.35}$$

the expectation value of Eq. (2.4.34) vanishes for $\mathbf{k}'\neq\mathbf{k}$, implying that only transitions where the initial and final states have the same momentum are allowed (*vertical*

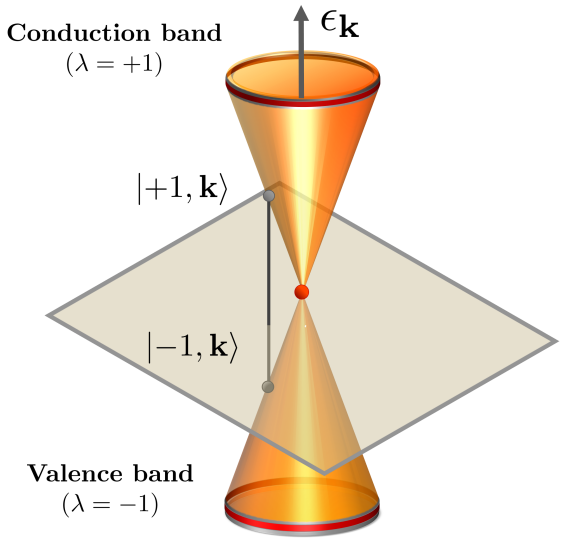

Figure 2.6: If carrier-carrier interactions are ignored, the only transitions are vertical and are between two energy eigenstates, effectively making it a two-level system. Due to the conical dispersion, any optical frequency will be in resonance with a suitable two-level system.

transitions i.e. $\mathbf{k} = \mathbf{k}'$:

$$\int_{\mathbb{R}^2} \Psi^{\dagger}_{\lambda',\mathbf{k}}(\mathbf{r}) \hat{\mathcal{Q}} \Psi_{\lambda,\mathbf{k}}(\mathbf{r}) d^2\mathbf{r} = \frac{4\pi^2}{A} \left\langle \lambda'\mathbf{k} \middle| \hat{\mathcal{Q}} \middle| \lambda\mathbf{k} \right\rangle \tag{2.4.36}$$

Furthermore, two kinds of transitions at $\mathbf{k}$ can be differentiated: *interband* transitions, satisfying $\lambda' = -\lambda$ and *intraband* transitions, satisfying $\lambda' = \lambda$. The matrix elements of the dipole moment operator $\hat{\boldsymbol{\mu}}$ for a Cartesian component j are thus simply:

$$\mu_i^{\lambda,\lambda'}(\mathbf{k}) = \langle \lambda'\mathbf{k} \,|\, \hat{\mu}_i \,|\, \lambda\mathbf{k} \rangle \tag{2.4.37}$$

with the knowledge of the SVEA representation of Eq. (2.4.33), the contribution to both in-plane coordinates x, y can be obtained.

For instance, the x component satisfies:

$$\begin{aligned}\langle\lambda\mathbf{k}|\mu_x|\lambda',\mathbf{k}\rangle &= \frac{iev_{\mathrm{F}}}{2\omega_0}\langle\lambda\mathbf{k}|\sigma_x|\lambda',\mathbf{k}\rangle = \frac{iev_{\mathrm{F}}}{4\omega_0}\begin{pmatrix}e^{i\phi_{\mathbf{k}}/2} & \lambda e^{-i\phi_{\mathbf{k}}/2}\end{pmatrix}\begin{pmatrix}0 & 1\\ 1 & 0\end{pmatrix}\begin{pmatrix}e^{-i\phi_{\mathbf{k}}/2}\\ \lambda' e^{i\phi_{\mathbf{k}}/2}\end{pmatrix}\\ &= \frac{iev_{\mathrm{F}}}{4\omega_0}\left(\lambda' e^{i\phi_{\mathbf{k}}} + \lambda e^{-i\phi_{\mathbf{k}}}\right)\\ &= \begin{cases}\frac{i\lambda ev_{\mathrm{F}}}{2\omega_0}\cos\phi_{\mathbf{k}} & \text{for} \quad \lambda' = \lambda \quad \text{(intraband)}\\ \frac{\lambda ev_{\mathrm{F}}}{2\omega_0}\sin\phi_{\mathbf{k}} & \text{for} \quad \lambda' = -\lambda \quad \text{(interband)}\end{cases}\end{aligned} \tag{2.4.38}$$

Similarly, the y component has:

$$\begin{aligned}\langle\lambda\mathbf{k}|\mu_y|\lambda',\mathbf{k}\rangle &= \frac{iev_{\mathrm{F}}}{2\omega_0}\langle\lambda\mathbf{k}|\sigma_y|\lambda',\mathbf{k}\rangle = -\frac{ev_{\mathrm{F}}}{4\omega_0}\begin{pmatrix}e^{i\phi_{\mathbf{k}}/2} & \lambda e^{-i\phi_{\mathbf{k}}/2}\end{pmatrix}\begin{pmatrix}0 & -1\\ 1 & 0\end{pmatrix}\begin{pmatrix}e^{-i\phi_{\mathbf{k}}/2}\\ \lambda' e^{i\phi_{\mathbf{k}}/2}\end{pmatrix}\\ &= -\frac{ev_{\mathrm{F}}}{4\omega_0}\left(-\lambda' e^{i\phi_{\mathbf{k}}} + \lambda e^{-i\phi_{\mathbf{k}}}\right)\\ &= \begin{cases}\frac{i\lambda ev_{\mathrm{F}}}{2\omega_0}\sin\phi_{\mathbf{k}} & \text{for} \quad \lambda' = \lambda \quad \text{(intraband)}\\ \frac{\lambda ev_{\mathrm{F}}}{2\omega_0}\cos\phi_{\mathbf{k}} & \text{for} \quad \lambda' = -\lambda \quad \text{(interband)}\end{cases}\end{aligned} \tag{2.4.39}$$

This quantity has dimensions $[\mu] = \frac{QL/T}{1/T} = [Q][L]$ as expected since classically, one has $\boldsymbol{\mu} = -e \cdot \mathbf{r}$.

How to interpret the effects of the interaction Hamiltonian on the eigenstates? In the picture that has been developed so far, electronic excitations can be collected according to their energy, giving rise to bands. In suitable resonant conditions, *photon absorption* leads to a change of the charge distribution throughout the sample, conceptualised as the creation of a polarisation field. To quantify this change at a fundamental level, the mechanism of photon absorption can be thought of as the

creation of a dipole between the newly-promoted valence electron to the conduction band and the vacant state in the valence band, since they carry opposite charges. This dipole thus create an attractive Coulomb interaction. In the quasiparticle picture, a photon of energy $\hbar\omega_0$ may, given a vertical energy separation between a valence and conduction bands $\Delta\epsilon < \hbar\omega_0$ induce an electronic excitation of that electron. This process is thus equivalent to the creation of a *hole* in the valence band and an electron in the conduction band.

Given the gapless nature of the spectrum, a spectrally-distributed pulse will have a frequency component resonant with some two-level system of a fixed momentum $\mathbf{k}$. In this setting, graphene is idealised as an infinite, non-interacting *two-level system*. This is a central concept throughout this work and will be dealt with in more detail in Section 3.2.

Fine-Structure Constant α_{G}

Without the machinery of linear optics which was just introduced, the law of universal absorption can be obtained by using Fermi's golden rule. If the light-matter interaction described by the dipole-field term in the Hamiltonian of Eq. 2.3.10 is treated as perturbation, Fermi's golden rule may be used to estimate the transition rate of valence to conduction electronic eigenstates.

The application of this approach is well justified as all calculations have been performed in the low field limit

The transition rate from $|-\lambda,\mathbf{k}\rangle$ to $|\lambda,\mathbf{k}'\rangle$ is:

$$T_{|-\lambda,\mathbf{k}\rangle\to|\lambda,\mathbf{k}\rangle} = \frac{2\pi}{\hbar}|\langle\lambda\mathbf{k}'\,|\,\boldsymbol{\mu}_{\mathbf{k},\mathbf{k}'}\cdot\boldsymbol{\mathscr{E}}\,|\,\lambda,\mathbf{k}'\rangle\,|^2 g(\epsilon_{\mathbf{k}'}). \tag{2.4.40}$$

Here, $g(\epsilon_{\mathbf{k}'})$ is the density of states at the energy of the final state $|\lambda,\mathbf{k}'\rangle$. The optical dipole matrix M for vertical transitions in $\mathbf{k}$ is diagonal. Using the symmetry of

the treatment in either the x or y components, one may, without loss of generality, consider $\mu_{x,\mathbf{k}}$, given in Eq. (2.4.38) . Again, considering the interband transitions $\lambda' = -\lambda$ and $\mathbf{k}' = \mathbf{k}$, M reads:

$$M_{\mathbf{k}\mathbf{k}'} = [\mu_{\mathbf{k}}\mathscr{E}]\delta_{\mathbf{k}\mathbf{k}'} = \frac{ev_{\mathrm{F}}}{2\omega_0}\sin(\phi_{\mathbf{k}})\mathscr{E} \tag{2.4.41}$$

This quantity is now angle-averaged i.e. $\langle f(\phi)\rangle \equiv 1/(2\pi)\int_0^{2\pi} f(\phi)d\phi$:

$$|\langle \mu_{\mathbf{k}}\mathscr{E}\rangle|^2 = \frac{e^2v_{\mathrm{F}}^2}{4\omega_0^2}|\mathscr{E}|^2\langle\cos^2(\phi_{\mathbf{k}})\rangle = \frac{e^2v_{\mathrm{F}}^2}{4\omega_0^2}|\mathscr{E}|^2\frac{\int_0^{2\pi}\sin^2(\phi_{\mathbf{k}})d\phi_{\mathbf{k}}}{2\pi} = \frac{e^2v_{\mathrm{F}}^2}{8\omega_0^2}|\mathscr{E}|^2 \tag{2.4.42}$$

In perfect resonance, at a transition energy ϵ_0 exactly equal to the difference energy between the initial and final states of $\delta\epsilon_{\mathbf{k}} = 2\epsilon_{\mathbf{k}}$, one has $\epsilon_0 = \epsilon_{\mathbf{k}}/2$ and the density of final states is therefore:

$$g(\epsilon_0) = \frac{2}{\pi\hbar^2v_{\mathrm{F}}^2}\frac{\hbar\omega_0}{2} = \frac{\omega_0}{\pi\hbar v_{\mathrm{F}}^2} \tag{2.4.43}$$

At this energy, the transition probability, the transition happens at $\mathbf{k} = \mathbf{k}_0$ (the wavevector of the external electromagnetic wave), T_{ω_0} takes the form:

$$\begin{aligned} T_{\omega_0} &= \frac{2\pi}{\hbar}|\langle -\lambda\mathbf{k}_0\,|\,\mu_{\mathbf{k}_0}\cdot\mathscr{E}\,|\,\lambda,\mathbf{k}_0\rangle|^2 g(\epsilon_0) \\ &= \frac{2\pi}{\hbar}\frac{e^2v_{\mathrm{F}}^2}{8\omega_0^2}|\mathscr{E}|^2\frac{\omega_0^2}{\pi\hbar v_{\mathrm{F}}^2} = \frac{e^2}{4\omega_0\hbar^2}|\mathscr{E}|^2 \end{aligned} \tag{2.4.44}$$

Therefore, the power of the absorbed radiation is $P_{\mathrm{ABS}} = T_{\omega_0}\epsilon_0 = T_{\omega_0}\hbar\omega_0$, whereas the total power input by the radiation field is $P_{\mathrm{IN}} = \frac{c}{4\pi}|\mathscr{E}|^2$. The optical absorption $\alpha(\omega_0)$ is given by their ratio:

$$\alpha(\omega_0) = \frac{P_{\mathrm{ABS}}}{P_{\mathrm{IN}}} = \frac{4\pi T_{\omega_0}\hbar\omega_0}{c|\mathscr{E}|^2} = \frac{\frac{e^2|\mathscr{E}|^2}{4\hbar}}{\frac{c|\mathscr{E}|^2}{4\pi}} = \frac{\pi e^2}{\hbar c} = \pi\alpha_{\mathrm{QED}} \tag{2.4.45}$$

where α_{QED} is the fine-structure constant from Quantum Electrodynamics (QED). Measurements of the universal absorption have been reported [3]. Fig. 2.7 shows

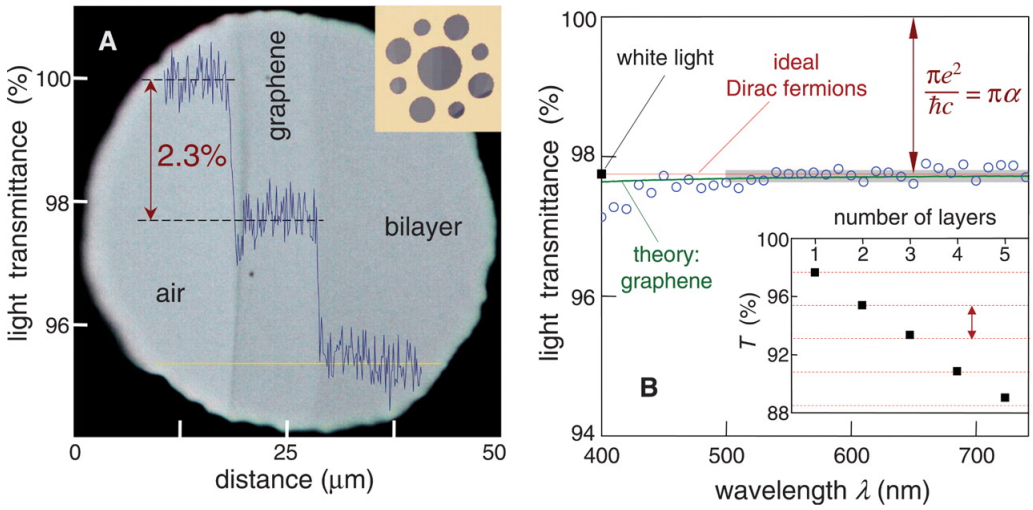

Figure 2.7: Experimental verification of the law of universal absorption of a graphene monolayer. As will be seen in Section 3.7.2, the transmittance allows for the absorbance of the medium to be retrieved. Taken from [3].

such measurements. Two features are prominent: (i) the decrease in the light transmittance is $\pi\alpha \approx 2.3\%$ and (ii) this value is a constant for all wavelengths. This result explains why graphene, unlike its related allotrope graphite, is optically transparent. The inset on the right shows how the number of graphene layers impacts the absorbance. Naturally, by around five layers the overall absorption is far greater and, for such a reduced number of layers, this decrease occurs in units of the monolayer absorbance α_{G}.

This constant also leads to other fundamental considerations regarding the nature of quantum field theories applied to graphene. This discussion will be made in Section 3.5.1.

In Section 3.7.2, this same result will be obtained via a rather different method, wherein the Semiconductor Bloch Equations will provide a numerical validation of this result.

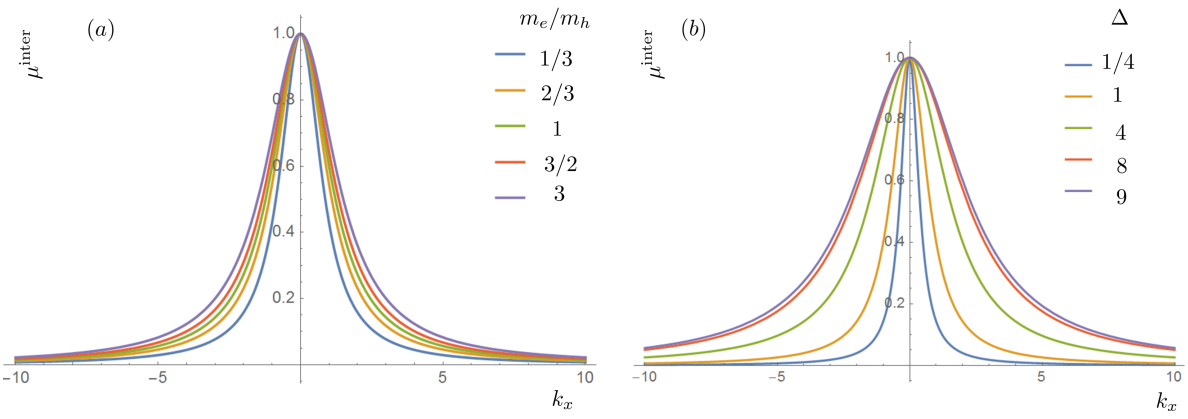

Figure 2.8: Plots of the normalised interband dipole moment element along k_x, in units of $\mu^{\text{inter}}(0)$. Its dependence on (a) electron-hole mass ratio m_e/m_h for a fixed energy gap and (b) the energy gap, in an intrinsic semiconductor

A Qualitative Comparison to Semiconductors

The dipole moment calculated in the last section is vastly different to what is normally expected of semiconductors. It is therefore instructive to see the qualitative difference between their optical transitions. For the case of a simple free-electron in a semiconductor the optical dipole matrix element changes depend on the modulus of $\mathbf{k}$. For a quadratic dispersion, with bands separated by Δ at $\mathbf{k} = 0$, it can be written as a Lorentzian curve [49]:

$$\mu_{\lambda\lambda'}(\mathbf{k}) = \mu_{\lambda\lambda'}(0)\frac{\Delta}{\Delta + \frac{\hbar^2|\mathbf{k}|^2}{2}\left(\frac{1}{m_e} + \frac{1}{m_h}\right)} \tag{2.4.46}$$

where m_e and m_h correspond respectively to the electron and hole masses of each band. Unlike the electrons in graphene, the electron and hole states in a semiconductor have a non-zero effective mass, determined by the curvature of their dispersion branch:

$$m_i = \hbar^2\left(\frac{\partial^2\epsilon_i(k)}{\partial k^2}\right)^{-1} \tag{2.4.47}$$

For graphene, the dipole moment can be seen to be inversely proportional to the optical frequency and hence the electron-hole separation $r = \mu/e$, for a fixed $\mathbf{k}$. Im-

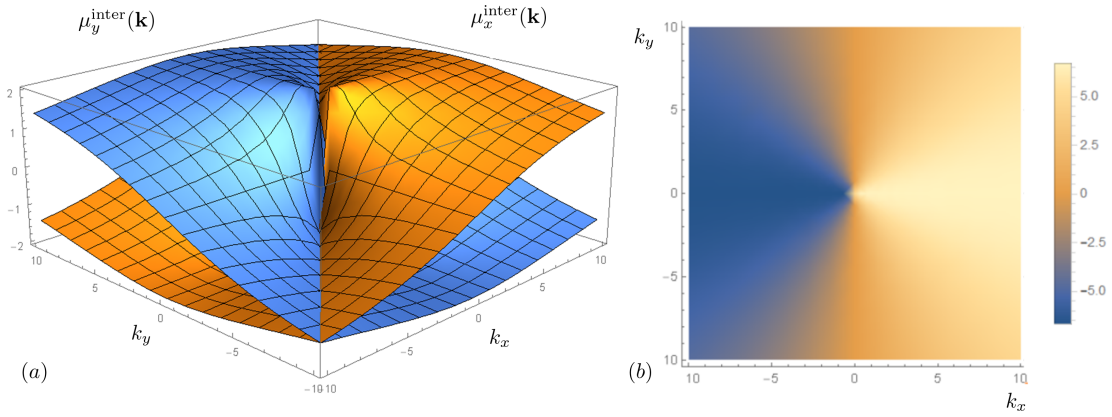

Figure 2.9: (a) Plot of the interband dipole matrix elements for graphene both Cartesian components. A singularity at $|\mathbf{k}|= 0$ is hinted. In (b), the density plot of the interband contribution, here plotted for an optical wavelength of $\omega_0 = 484$ THz shows it more explicitly.

portantly, this quantity is not-well defined for $\mathbf{k} = 0$, i.e. the Dirac points, as seen by the divergence of the elements calculated in Eq. (2.4.38)-(2.4.39), where, for instance, $\cos\phi_{\mathbf{k}} = k_x/|\mathbf{k}|$, undefined when $\mathbf{k} = 0$. This is easily understandable since the two-level system becomes degenerate there, given the band-touching.

Charge separation may be inferred from measurements of the dipole moment. For instance, for a pulse of frequency $\omega_0 = 484$ THz (visible, red radiation), the optical dipole moment is determined to be $|\mu|\approx 6.88 \times 10^{-8}$ e cm, corresponding to a separation of $r = 6.88$ Å$= 2.88a$.

Chapter 3

The Semiconductor Bloch Equations

3.1 Overview

The previous chapter was mainly concerned with the electronic properties of a general condensed matter system, in the presence of of an underlying lattice configuration. Subsequently, the two bands of the π electrons in graphene predicted in tight-binding conditions were obtained in Section 2.2. These lead to two valleys, located at two special points termed *Dirac* points, where the dispersion is linearly proportional to the crystal momentum.

Having exposed the treatment underlying electrons in a lattice and a classical electromagnetic field, this chapter focuses on how to couple both elements. This task will be implemented by using the framework of a two-level system, an ubiquitous concept permeating many areas of Physics. In particular, this chapter is devoted to one such implementation, which became known as the *Semiconductor Bloch Equations* (SBEs). The modus operandi behind the SBEs stems from well-established equations, known as the *Optical Bloch Equations* (OBEs) or sometimes the *Maxwell-Bloch Equations*

which describe the dynamics of a single two-level system when coupled to light, in particularly useful conditions. The first realisations of such systems came from Atomic Physics, where energy levels in particular atomic systems can be manipulated to achieve population inversion, leading to the first successful physical realisation of the laser [55].

The notion that a many-body quantum system like a semiconductor, encoding numerous complex scattering and responses when excited with light, may be described with two-level systems is perhaps unanticipated. It turns out that the versatility of a two-level treatment is excellently suited to treat light-matter interactions in many condensed matter systems. The SBEs offer a striking and revolutionary application of these principles in the realms of condensed matter physics.

Research within this formalism has been intensively applied to semiconductors [49, 56–58] and it has been extremely successful in explaining many phenomena such as dipole-dipole effects in dense media [59, 60], Rabi oscillations [61, 62] and optical bistability [63], self-induced transparency [45] and even single-mode inhomogenously broadened lasers [64]. The effect of ultrashort pulses on dense semiconducting media was studied not long after the SBEs were formulated [63]. The scope of the SBEs can be expanded to allow various incoherent and scattering contributions in the carrier dynamics to be considered [65].

Theoretical approaches to model the nonlinear dynamics of graphene typically rely on the Boltzmann transport equation, accounting only for intraband electron dynamics [32]. As a zero-gap semiconductor, the SBEs have been applied to graphene [66] by adapting the conical dispersion to the usual dispersion of a semiconductor in order to account for the interband dynamics only.

Not surprisingly, the main goal of this chapter is thus to present results concerning the application of the SBEs to monolayer graphene. In order to achieve that, the OBEs shall be derived and discussed as a means of introducing the necessary jargon and

concepts to obtain the SBEs, whose predictions are analysed in Section 3.7. The main success of the SBEs lies on the linear optical regime, wherein many well-established results in the literature may be retrieved, providing a validation of these models to model light-matter interactions accurately in such regime. In particular, the direct proportionality between the absorption and the fine structure constant in graphene, discussed in the previous chapter in Section 2.4.3, may be retrieved. Conveniently, this regime also allows for analytical solutions of the SBEs to be obtained in special probing conditions, which are derived in Section 3.6.

3.2 The Theory of Two-Level Systems

The building blocks of any of the models that will be presented throughout this thesis are what physicists like to term 'two-level systems'. Many realisations of this concept may be obtained in various branches of both Physics and Mathematics, varying from qbits, extensively exploited for Quantum Computing and Information, both theoretically [67] and experimentally [68], to the dynamics of a spin-1/2 particle interacting with a time-dependent magnetic field, for instance by Rabi as early as 1937 [69]. In the realm of Condensed Matter Physics, a myriad of systems display features that can be understood in such a framework [55].

It is surprising how many physical systems can be adequately described by two-level systems, given how simple it can be understood mathematically. A two-level system refers to a quantum system whose features can be fully captured by a superposition of two independent states, here denoted by the lower ket $|1\rangle$ and upper ket $|2\rangle$. The representation in which states from the underlying two-dimensional Hilbert space are presented is irrelevant at this level. For most applications to quantum systems, one would choose the space representation $|\psi_\mu(\mathbf{r})\rangle \equiv \langle \mathbf{r}|i\rangle$, with $i = 1, 2$.

In this framework, the system dynamics can always be described, in this basis, with the aid of a ket-state $|\psi(t)\rangle$

$$|\psi(t)\rangle = c_1(t)\,|1\rangle + c_2(t)\,|2\rangle = c_1(t)\begin{pmatrix}1\\0\end{pmatrix} + c_2(t)\begin{pmatrix}0\\1\end{pmatrix} = \begin{pmatrix}c_1(t)\\c_2(t)\end{pmatrix} \tag{3.2.1}$$

i.e. a linear combination of two states, described by a column vector, determined by suitable coefficients $c_i(t)$. The element $|c_i(t)|^2$ will evidently return the probability per unit time of observing the system in the state $|i\rangle$. The basis is now assumed to be comprised of the eigenstates of the Hamiltonian of the system, $\mathcal{H}_0$, with energies as given by $\mathcal{H}_0\,|i\rangle = \epsilon_i\,|i\rangle$. The general state of Eq. (3.2.1) must therefore solve the Time-Dependent Schrödinger Equation:

$$i\hbar\frac{d}{dt}\,|\psi(\mathbf{r},t)\rangle = \mathcal{H}_0\,|\psi(\mathbf{r},t)\rangle\,, \tag{3.2.2}$$

whose solution is straightforwardly given by:

$$|\psi(\mathbf{r},t)\rangle = \sum_i c_i \exp\left(-\frac{i\epsilon_i t}{\hbar}\right)|\psi_i(\mathbf{r})\rangle\,. \tag{3.2.3}$$

where $|\psi_i(\mathbf{r})\rangle$ are eigenstates of $\mathcal{H}_0$ and c_i the weight of such eigenstates in the linear superposition.

An important consequence of the existence of such a basis is that an Hermitian $\hat{Q}$ operator acting on the state space may always be written in the form:

$$\hat{Q} = \begin{pmatrix}\alpha & \gamma e^{-i\theta}\\ \gamma e^{i\theta} & \beta\end{pmatrix} \tag{3.2.4}$$

provided α, β, γ and $\theta \in \mathbb{R}$. Clearly, $\hat{Q} = \hat{Q}^\dagger$. Such operators are obviously of importance since their eigenvalues are real. In order to obtain a matrix representation

of such operator in this particular basis, one may exploit the fact that there must be 2×2 linearly independent operators, the projectors, acting on the ket-space and defined as the outer product $|i\rangle\langle j|$, $(i, j = 1, 2)$, with the aid of the completeness relation $\sum_i |i\rangle\langle i| = \mathbb{I}$, $\mathbb{I}$ being the identity operator.

The Hamiltonian $\mathcal{H}_0$ is thus easily found to be:

$$\begin{aligned}\mathcal{H}_0 = \mathbb{I}\cdot\mathcal{H}_0\cdot\mathbb{I} &= \left(\sum_i |i\rangle\langle i|\right)\mathcal{H}_0\left(\sum_j |j\rangle\langle j|\right) = \sum_{i,j} |i\rangle\langle i|\,\mathcal{H}_0\,|j\rangle\langle j| \\ &= \sum_{i,j} |i\rangle\,\epsilon_j\delta_{ij}\,\langle j| = \sum_i \epsilon_i\,|i\rangle\langle i| = \epsilon_1\,|1\rangle\langle 1| + \epsilon_2\,|2\rangle\langle 2| \\ &= \begin{pmatrix}\epsilon_1 & 0\\ 0 & \epsilon_2\end{pmatrix}\end{aligned} \tag{3.2.5}$$

The system thus far does not seem very interesting: each state of Eq. (3.2.3) will oscillate sinusoidally at its particular frequency $\omega_i = \epsilon_i/\hbar$. The Hamiltonian $\mathcal{H}_0$ is interpreted as being determined and known - after all this is why one may assume that the energies of such states are known. *What if the two-level system is now coupled to a perturbation that modifies such energies and perhaps even the basis?* In that instance, the dynamics could in principle become exceedingly complex, in turn leading to a much more challenging task of computing the time evolution of the coefficients $c_i(t)$.

A feasible way to incorporate interactions with the two-level system is to write the Hamiltonian of the system as a sum of a Hamiltonian known for a particular regime and a perturbation part as $\mathcal{H} = \mathcal{H}_0 + \mathcal{H}_\mathrm{I}$. The expected value of such a perturbation is then:

$$\begin{aligned}\langle\psi(t)\,|\,\mathcal{H}_\mathrm{I}\,|\,\psi(t)\rangle &= (c_1^*(t)\,\langle 1| + c_2^*(t)\,\langle 2|)\mathcal{H}_\mathrm{I}(c_1(t)\,|1\rangle + c_2(t)\,|2\rangle) \\ &= |c_1(t)|^2\langle 1\,|\,\mathcal{H}_\mathrm{I}\,|\,1\rangle + |c_2(t)|^2\langle 2\,|\,\mathcal{H}_\mathrm{I}\,|\,2\rangle \\ &+ c_1(t)c_2(t)^*\,\langle 2\,|\,\mathcal{H}_\mathrm{I}\,|\,1\rangle + c_2(t)c_1(t)^*\,\langle 1\,|\,\mathcal{H}_\mathrm{I}\,|\,2\rangle\end{aligned} \tag{3.2.6}$$

This interaction will be assumed to only induce a perturbation *between* the two states, meaning that $\langle i \,|\, \mathcal{H}_{\mathrm{I}} \,|\, i \rangle = 0$. This assumption is generally warranted, as will be seen in Section 3.4, when the interaction Hamiltonian will be explicitly given. In the same fashion, the matrix form of such a general interaction Hamiltonian may be obtained as:

$$\begin{aligned} \mathcal{H}_I = \mathbb{I} \cdot \mathcal{H}_I \cdot \mathbb{I} &= \left(\sum_i |i\rangle \langle i| \right) \mathcal{H}_I \left(\sum_j |j\rangle \langle j| \right) \\ &= \sum_{i,j} |i\rangle \underbrace{\langle i \,|\, \mathcal{H}_{\mathrm{I}} \,|\, j \rangle}_{\epsilon^{\mathrm{I}}_{ij}} \langle j| = \epsilon^{\mathrm{I}}_{12} |1\rangle \langle 2| + \epsilon^{\mathrm{I}}_{21} |2\rangle \langle 1| \\ &= \begin{pmatrix} 0 & \epsilon^{\mathrm{I}}_{12} \\ \epsilon^{\mathrm{I}}_{21} & 0 \end{pmatrix} \end{aligned} \tag{3.2.7}$$

Naturally, since $\mathcal{H}_{\mathrm{I}}$ must be hermitian, one has $\epsilon^{\mathrm{I}}_{12} = {\epsilon^{\mathrm{I}}_{21}}^*$ and a polar representation $\epsilon^{\mathrm{I}}_{ij} \equiv |\epsilon^{\mathrm{I}}_{ij}| e^{i\phi}$ is possible, leading to a full Hamiltonian in the general form of Eq. (3.2.4):

$$\mathcal{H} = \mathcal{H}_0 + \mathcal{H}_I = \begin{pmatrix} \epsilon_1 & |\epsilon^{\mathrm{I}}_{12}| e^{i\phi} \\ |\epsilon^{\mathrm{I}}_{12}| e^{-i\phi} & \epsilon_2 \end{pmatrix} \tag{3.2.8}$$

This step is exactly what allows *light-matter interactions* to be obtained between an external optical field and the two-level system. The two-level system is a mathematical realisation of *matter*, as was developed in Section 2.2, whereas the interaction Hamiltonian allows an external parameter to drive its dynamics. An appropriate form of $\mathcal{H}_{\mathrm{I}}$ is of course necessary to ultimately solve the Schrödinger equation encompassing the full dynamics and that is achieved in the next section.

3.3 The Optical Bloch Equations

A first step to solve the dynamics of the full Hamiltonian is now given, following the explanations provided in [48]. If the field is assumed constant in space and only varies in time, the interaction between the atom and the field is classically written as a dipole-like interaction:

$$\mathcal{H}_I(t) = -e\mathbf{r} \cdot \mathbf{E}(t) \tag{3.3.1}$$

where both vectors are given in their Cartesian coordinates. For the sake of simplicity, the field is now assumed to be linearly polarised in the $\hat{x}$ direction. In this dipole-type interaction, diagonal entries in the interaction Hamiltonian would imply a permanent dipole moment and so for this treatment one shall assume that these vanish.

From Eq. (3.2.6), it can thus be seen that the system will have zero dipole moment if the product $c_1 c_2^*(t) \neq 0$ i.e. whenever the atom is in a superposition of both states. In accordance with the expansion in the equation, the interaction Hamiltonian elements may be split as $\epsilon_{ij}^{\mathrm{I}} = -E(t)\mu_{ij}$, where $\mu_{ij} = e\,\langle i|\hat{x}|j\rangle$.

Finally, the Hamiltonian matrix of Eq. (3.2.8) is applied to the general state of Eq. (3.2.1) using the TDSE (Eq. (3.2.2)). At this stage, and for simplicity purposes, the electric field is taken to be a monochromatic plane wave of frequency ω_0, of the form $E(t) = \mathscr{E}\cos(\omega_0 t)$, where $\mathscr{E}$ is its amplitude. Splitting the magnitude and phase of the dipole moment $\mu_{12} = |\mu_{12}|e^{i\phi}$, the following system of differential equations is obtained:

$$\begin{aligned} \dot{c}_1(t) &= -i\omega_1 c_1(t) + i\Omega_R e^{-i\phi}\cos(\omega_0 t)c_2(t) \\ \dot{c}_2(t) &= -i\omega_2 c_2(t) + i\Omega_R e^{i\phi}\cos(\omega_0 t)c_1(t) \end{aligned} \tag{3.3.2}$$

The parameter $\Omega_{\mathrm{R}} = |\mu_{12}|\mathscr{E}/\hbar$ is the *Rabi frequency* and describes the driving frequency at which the populations will oscillate when coupled to the field.

However neatly expressed, this set of differential equations is in general not possible

to be solved analytically given the fast oscillation of the coefficients. One reasonable way out is to express the coefficients c_i in terms of their slowly-varying amplitudes $\tilde{c}_i = c_i e^{i\omega_i t}$. If the transition frequency is denoted by $\Delta\omega \equiv \omega_2 - \omega_1$, the equations become:

$$\begin{aligned} \dot{\tilde{c}}_1(t) &= \tfrac{i\Omega_R}{2} e^{-i\phi} \left(e^{i(\omega_0 - \Delta\omega)t} + e^{-i(\omega_0 + \Delta\omega)t} \right) \tilde{c}_2(t) \\ \dot{\tilde{c}}_2(t) &= \tfrac{i\Omega_R}{2} e^{i\phi} \left(e^{-i(\omega_0 - \Delta\omega)t} + e^{i(\omega_0 + \Delta\omega)t} \right) \tilde{c}_1(t) \end{aligned} \tag{3.3.3}$$

The Rotating Wave Approximation (RWA) is now applied, by only keeping the coherent terms i.e. terms close to resonance. Terms proportional to $\exp\left(\pm i(\Delta\omega + \omega_0)\right)$ are therefore ignored. This is in general a good assumption for many systems. However, as will be seen in the next chapter, these terms are important in dealing with ultrashort pulses, where the notion of a slow-varying oscillation is often ill-defined, if the frequency of the pulse is comparable with the inverse pulse duration.

Solving this set of equations leads to the *Optical Bloch Equations* (also known as the *Maxwell-Bloch Equations*). These were derived as far as 1965 [70] and provide a way to describe the dynamics of a single two-level system when coupled with a classical electromagnetic field of a single frequency mode:

$$\begin{aligned} c_1(t) &= \left(a_1 e^{i\frac{\Omega t}{2}} + a_2 e^{-i\frac{\Omega t}{2}} \right) e^{i\frac{\Delta t}{2}} \\ c_2(t) &= \left(b_1 e^{i\frac{\Omega t}{2}} + b_2 e^{-i\frac{\Omega t}{2}} \right) e^{-i\frac{\Delta t}{2}}. \end{aligned} \tag{3.3.4}$$

The coefficients $a_{1/2}$ and $b_{1/2}$ are determined by the system's initial conditions and provide no insight into the physics. What is remarkable is that the two-level system is described by two characteristic frequencies, namely the *detuning frequency* $\Delta = \Delta\omega - \omega_0$ and the *generalised Rabi frequency* $\Omega = \sqrt{\Omega_{\mathrm{R}}^2 + \Delta^2}$.

A sensible boundary condition is given as $c_2(0) = 0$ and $c_1(0) = 1$, meaning that the two-level system is initially in the ground state. It is customary to introduce more physically relevant dynamical variables than the coefficients themselves. Eq. (3.2.7)

already hinted at a definition: the polarisation [1] $p(t) = \tilde{c}_1^* \tilde{c}_2 \mu_{12} + \tilde{c}_1 \tilde{c}_2^* \mu_{12}^*$ and takes the form:

$$p(t) = 2\mathrm{Re}\left(\frac{i\Omega_\mathrm{R}}{\Omega}\mu_{12}\left(\cos\left(\frac{\Omega t}{2}\right) + \frac{i\Delta}{\Omega}\sin\left(\frac{\Omega t}{2}\right)\right)\sin\left(\frac{\Omega t}{2}\right)e^{i(\phi+\omega_0 t)}\right) \tag{3.3.5}$$

The inversion of a two-level system is defined as the difference of the occupation probabilities and may be expressed as:

$$w(t) = |c_2(t)|^2 - |c_1(t)|^2 = \left(\frac{\Delta^2 - \Omega_\mathrm{R}^2}{\Omega^2}\right)\sin^2\left(\frac{\Omega t}{2}\right) + \cos^2\left(\frac{\Omega t}{2}\right) \tag{3.3.6}$$

Interestingly, the polarisation oscillates with the same frequency as the field. As for the inversion, different detunings yield different Rabi cycles, reflecting different oscillations profiles between the ground and excited states. For a vanishing detuning, the system is said to be on resonance and the inversion is total - $w(t) = \cos(\Omega_\mathrm{R} t)$, meaning that the populations will shift sinusoidally between the lower and upper states. For extremely detuned systems, the interaction is minimal and the inversion does not change much from its initial conditions, leading to an inversion $w(t) \approx -1$.

3.4 Derivation

To understand the philosophy of the SBEs, their derivation is now shown, following the outline presented in [49]. The main elements in it are conceptually very close to what was presented in the previous section. The notation will nonetheless be more suited for a condensed matter system. In particular, the variables needed to describe the system's evolution will be chosen to be physically more transparent. Despite such similarities, the density matrix of the two-level system will be used instead.

[1] The polarisation may take several names in the literature: dipole moment, coherence or transition probability. In this work, these will not be referring to the exact same quantity but will be related by different phase factors.

The convenience of it relies on the fact that at no point of the derivation neither the knowledge of the eigenstates nor the Time-Dependent Schrödinger equation are needed.

Electronic transitions in semiconductors are adequately understood with the aid of the electronic bands that originate as an aggregate of reactive orbitals. Since the bands are functions of the crystal momentum, it is convenient to take the two levels as the eigenstates of the free Hamiltonian for fixed momentum $\mathbf{k}$ - here denoted by $|v,\mathbf{k}\rangle$ and $|c,\mathbf{k}\rangle$. The energy of each state $|c/v,\mathbf{k}\rangle$ will be denoted as $\epsilon_{c/v,\mathbf{k}}$. The wavefunction in direct space of such states can be simply obtained by taking the scalar product $\psi_{\mathbf{k}}(\mathbf{r}) = \langle \mathbf{r}|\lambda,\mathbf{k}\rangle$.
As usual, the two-level system may be generally represented as:

$$|\psi_{\mathbf{k}}(t)\rangle = \eta_v(t)\,|v,\mathbf{k}\rangle + \eta_c(t)\,|c,\mathbf{k}\rangle \tag{3.4.1}$$

It is natural to associate the coefficients η_v and η_c to the valence and conduction bands, respectively, given the considerations that led to Eq. (3.2.1). The density matrix of the two-level system is simply given by the general definition:

$$\begin{aligned}\rho_{\mathbf{k}}(t) = |\psi_{\mathbf{k}}(t)\rangle\langle\psi_{\mathbf{k}}(t)| &= \begin{pmatrix}\eta_{v,\mathbf{k}}(t)\\ \eta_{c,\mathbf{k}}(t)\end{pmatrix}\begin{pmatrix}\eta^*_{v,\mathbf{k}}(t) & \eta^*_{c,\mathbf{k}}(t)\end{pmatrix}\\ &= \begin{pmatrix}\eta^2_{v,\mathbf{k}}(t) & \eta_{v,\mathbf{k}}(t)\eta^*_{c,\mathbf{k}}(t)\\ \eta_{c,\mathbf{k}}(t)\eta^*_{v,\mathbf{k}}(t) & \eta^2_{c,\mathbf{k}}(t)\end{pmatrix}\\ &\equiv \begin{pmatrix}n_{v,\mathbf{k}}(t) & p^*_{\mathbf{k}}(t)\\ p_{\mathbf{k}}(t) & n_{c,\mathbf{k}}(t)\end{pmatrix}\end{aligned} \tag{3.4.2}$$

Similarly to the OBEs, new dynamical variables were chosen. In this new picture, the excitation is a combination of valence and conduction states, situated in their

respective branches of the dispersion. Subsequently, the occupation number for each band is simply the square $n_{c/v,\mathbf{k}} \equiv \eta^2_{c/v,\mathbf{k}}$, naturally a real quantity. The system is conservative, as seen by the normalisation of the density matrix - $\mathrm{Tr}(\rho_{\mathbf{k}}) = 1$:

$$n_{c,\mathbf{k}} + n_{v,\mathbf{k}} = 1, \tag{3.4.3}$$

which in turn implies quasiparticle number conservation and rendering the electron and hole occupations dependent.

The microscopic polarisation was introduced as the product in the off-diagonal entries and is a measure of the mixing of two states in the basis: only when the excitation is in a combination of valence and conduction states will the product $\eta_{v,\mathbf{k}}\eta^*_{c,\mathbf{k}}$ be nonzero. Employing the dipole approximation, the coupling to light is introduced as usual, leading to purely off-diagonal electric dipole momentum operator, as shown in Eq. (3.2.7):

$$H^{\mathrm{I}}_{\mathbf{k}} = \begin{pmatrix} 0 & -\boldsymbol{\mu}^*_{\mathbf{k}} \cdot \mathbf{E} \\ -\boldsymbol{\mu}_{\mathbf{k}} \cdot \mathbf{E} & 0 \end{pmatrix} \tag{3.4.4}$$

where the dot product is performed over the Cartesian components of the field and the dipole moment. The full Hamiltonian of the two-level system at wavevector $\mathbf{k}$ under consideration is then:

$$\mathcal{H}_{\mathbf{k}} = \mathcal{H}^0_{\mathbf{k}} + \mathcal{H}^{\mathrm{I}}_{\mathbf{k}} = \begin{pmatrix} \epsilon_{v,\mathbf{k}} & -\boldsymbol{\mu}^*_{\mathbf{k}} \cdot \mathbf{E} \\ -\boldsymbol{\mu}_{\mathbf{k}} \cdot \mathbf{E} & \epsilon_{c,\mathbf{k}} \end{pmatrix}. \tag{3.4.5}$$

Given the properties of the density matrix, it follows that for a general operator $\hat{Q}$, its expectation value may be calculated as $\langle \hat{Q} \rangle = \mathrm{Tr}\left(\rho_{\mathbf{k}} \hat{Q}\right)$. This fact allows the

energy of the Hamiltonian of Eq. (3.4.5) to be calculated as:

$$\begin{aligned}\left\langle \hat{\mathcal{H}}_{\mathbf{k}} \right\rangle &= \mathrm{Tr}\left(\begin{pmatrix} \epsilon_{v,\mathbf{k}} & -\boldsymbol{\mu}^*_{\mathbf{k}} \cdot \mathbf{E} \\ -\boldsymbol{\mu}_{\mathbf{k}} \cdot \mathbf{E} & \epsilon_{c,\mathbf{k}} \end{pmatrix} \begin{pmatrix} n_{v,\mathbf{k}} & p^*_{\mathbf{k}} \\ p_{\mathbf{k}} & n_{c,\mathbf{k}} \end{pmatrix} \right) \\ &= \epsilon_{v,\mathbf{k}} n_{v,\mathbf{k}} + \epsilon_{c,\mathbf{k}} n_{c,\mathbf{k}} - p_{\mathbf{k}} \boldsymbol{\mu}^*_{\mathbf{k}} \cdot \mathbf{E} - p^*_{\mathbf{k}} \boldsymbol{\mu}_{\mathbf{k}} \cdot \mathbf{E}\end{aligned} \tag{3.4.6}$$

With all necessary elements in place, the evolution of this mixed state, is determined by the Liouville-von Neumann Equation:

$$\dot{\rho}_{\mathbf{k}} = -\frac{i}{\hbar}[\mathcal{H}_{\mathbf{k}}, \rho_{\mathbf{k}}] - \dot{\rho}_{\mathbf{k}}|_{\mathrm{decoh}}$$

The last term was added to account for decoherence mechanisms, naturally present in any open system. There are many ways to achieve such a term that preserves the properties of the density matrix, the most notable being given by the Lindblad master equation [71]. Alternatively, phenomenological decay rates γ_1 and γ_2, respectively for the inversion and microscopic polarisation and whose physical relevance will be examined in Section 3.5.2, may adequately be added, given that incoherent effects are not central in this work.

In this way, the free-carrier Semiconductor Bloch equations are obtained:

$$\dot{p}_{\mathbf{k}} + i(\omega_{\mathbf{k}} - i\gamma_2)p_{\mathbf{k}} + \tfrac{i}{\hbar} w_{\mathbf{k}} \mathbf{E} \cdot \boldsymbol{\mu}_{\mathbf{k}} = 0 \tag{3.4.7}$$

$$\dot{w}_{\mathbf{k}} + \gamma_1(w_{\mathbf{k}} - w^0_{\mathbf{k}}) - \tfrac{2i}{\hbar} \mathbf{E} \cdot (\boldsymbol{\mu}_{\mathbf{k}} p^*_{\mathbf{k}} - \boldsymbol{\mu}^*_{\mathbf{k}} p_{\mathbf{k}}) = 0 \tag{3.4.8}$$

Here, the detuning is different for each state i.e. $\omega_{\mathbf{k}} = (\epsilon_{c,\mathbf{k}} - \epsilon_{v,\mathbf{k}})/\hbar$ and therefore dependent on the shape of the dispersion. $w^0_{\mathbf{k}}$ is the equilibrium value of the populations for each momentum and a broader discussion of it may be found in Section 3.5.2 whereas $\mu_{\mathbf{k}}$ is the interband dipole moment matrix element that was introduced in Section 2.4.3.

In the absence of dephasing i.e. for $\gamma_1 = \gamma_2 = 0$, the conservation of probability, given by the normalisation of Eq. (3.4.3) is re-expressed in the new dynamical variables as:

$$w_{\mathbf{k}}^2 + 4|q_{\mathbf{k}}|^2 = 1 \tag{3.4.9}$$

As performed previously, these equations can be adapted to model the slowly-varying part of the oscillations. In this case, the microscopic polarisation is split as $p_{\mathbf{k}} = q_{\mathbf{k}} e^{-i\omega_0 t}$ and, using the decomposition of Eq. (2.4.20) for a space-independent electric field $E(t)$, the SVEA-approximated becomes:

$$\begin{aligned} \dot{q}_{\mathbf{k}} + i(\omega_{\mathbf{k}} - \omega_0 - i\gamma_2) q_{\mathbf{k}} + \frac{i}{2\hbar} w_{\mathbf{k}} \boldsymbol{\mathscr{E}} \mu_{\mathbf{k}} = 0 \\ \dot{w}_{\mathbf{k}} + \gamma_1 (w_{\mathbf{k}} - w_{\mathbf{k}}^0) - \frac{i}{\hbar} \left(\boldsymbol{\mathscr{E}} \mu_{\mathbf{k}} q_{\mathbf{k}}^* - \boldsymbol{\mathscr{E}}^* \mu_{\mathbf{k}}^* q_{\mathbf{k}} \right) = 0 \end{aligned} \tag{3.4.10}$$

The polarisation oscillates now with the detuning $\delta_{\mathbf{k}} \equiv \omega_{\mathbf{k}} - \omega_0$. Importantly, only terms oscillating with $e^{-i\omega_0 t}$ were kept. It will be seen in the next section that this assumption is equivalent to applying the Rotating Wave Approximation.

3.4.1 Macroscopic Polarisation

Following the discussion in Section 2.4.2, the polarisation of the medium, through its susceptibility, which acts as a response to the interaction with an electromagnetic field, encompasses a breadth of information about the light-matter interactions present.
The SBEs allow for the identification between the microscopic dynamics of the two-level systems to the polarisation described by Eq. (2.4.7) to be obtained.
To obtain the time dynamics of the polarisation, the carrier-field contribution $\hat{\mathcal{H}}_{F-C}$ from the Hamiltonian in Eq. (2.3.10) allows for a sensible definition of it, namely from the condition:

$$E(t) \sum_{\mathbf{k}} \left(\mu_{\mathbf{k}} \alpha_{\mathbf{k}}^\dagger \beta_{-\mathbf{k}}^\dagger + \mu_{\mathbf{k}}^* \hat{\beta}_{-\mathbf{k}} \hat{\alpha}_{\mathbf{k}} \right) = \varepsilon_0 V \ \hat{P}(t) E(t) \tag{3.4.11}$$

where the volume of the sample $V = Ad$ is comprised of its area and the atomic thickness $d \approx 0.33$ nm and ϵ_0 the electric permittivity of free space. The polarisation operator is thus:

$$\hat{P}(t) = \frac{1}{\varepsilon_0 V} \sum_{\mathbf{k}} \left(\mu_{\mathbf{k}} \alpha^{\dagger}_{\mathbf{k}} \beta^{\dagger}_{-\mathbf{k}} + \mu^{*}_{\mathbf{k}} \hat{\beta}_{-\mathbf{k}} \hat{\alpha}_{\mathbf{k}} \right) \tag{3.4.12}$$

with the aid of the density matrix of Eq. (3.4.2), its expectation value, describing the time dynamics of the polarisation is:

$$\begin{aligned} P(t) = \left\langle \hat{P} \right\rangle = Tr(\hat{P}\rho_{\mathbf{k}}) &= \frac{1}{\varepsilon_0 V} \sum_{\mathbf{k}} \mathrm{Tr} \left(\begin{pmatrix} 0 & \mu^{*}_{\mathbf{k}} \\ \mu_{\mathbf{k}} & 0 \end{pmatrix} \begin{pmatrix} n_{v,\mathbf{k}} & p^{*}_{\mathbf{k}} \\ p_{\mathbf{k}} & n_{c,\mathbf{k}} \end{pmatrix} \right) \\ &= \frac{1}{\varepsilon_0 V} \sum_{\mathbf{k}} p_{\mathbf{k}} \mu^{*}_{\mathbf{k}} + p^{*}_{\mathbf{k}} \mu_{\mathbf{k}} \end{aligned} \tag{3.4.13}$$

Furthermore, since the polarisation is real-valued, and all dipole moments rotate with the frequency of the incident field, the following decomposition is possible:

$$\mathbf{P}(t) = \frac{1}{2} \left(\mathbf{Q}(t) e^{-i\omega_0 t} + \mathbf{Q}^{*}(t) e^{i\omega_0 t} \right) \tag{3.4.14}$$

Equating (3.4.14) to (3.4.13) and again decomposing the microscopic polarisation via $p_{\mathbf{k}} = q_{\mathbf{k}} e^{-i\omega_0 t}$, give:

$$\frac{1}{2} \left(Q(t) e^{-i\omega_0 t} + Q^{*}(t) e^{i\omega_0 t} \right) = \frac{1}{\varepsilon_0 V} \sum_{\mathbf{k}} \mu^{*}_{\mathbf{k}} q_{\mathbf{k}} e^{-i\omega_0 t} + \mu_{\mathbf{k}} q^{*}_{\mathbf{k}} e^{i\omega_0 t} \tag{3.4.15}$$

The polarisation can thus be obtained by adequately calculating the **k**-dependent polarisation, weighting it by the dipole moment and average this quantity over momentum space:

$$Q(t) = \frac{2}{\varepsilon_0 V} \sum_{\mathbf{k}} \mu^{*}_{\mathbf{k}} q_{\mathbf{k}}(t) \tag{3.4.16}$$

This scheme is rather useful! If the SBEs can be numerically solved, it is, in principle, possible to produce the macroscopic polarisation of the sample due to the optical excitation. This is exactly what shall be done in the Section 3.7.

3.5 Additional Effects & Mechanisms

3.5.1 Coulomb Interactions

A major question not discussed up to this stage concerns the addition of Coulomb interactions. After all, electron-electron interactions are the fundamental mechanism driving an overwhelming number of phenomena in compounds and structures. In order to introduce such effects, and in view of what has been developed so far, two-level systems at different momenta must be able to exchange energy.

Rather surprisingly, their effect can be beautifully understood in terms of the picture so far developed. Eqs.(3.4.7)-(3.4.8) are coupled in two variables at the same $\mathbf{k}$. Once a Coulomb potential is introduced in the dynamics of the carriers, the corresponding optical variables depend on any other across momentum space, meaning all two-level systems are now *coupled*.

The effective consequence is that the two-level systems suffer a *renormalisation* of all the parameters so far discussed. To see this, a second quantisation of the Hamiltonian is more suitable. In this setting, and for this particular problem, the operators of interest will be the usual creation and annihilation operators for each band. Using the band index $c(v)$ for conduction (valence), the creation (annihilation) of an electron of momentum $\mathbf{k}$ is denoted by $\hat{a}^{\dagger}_{c/v,\mathbf{k}}(\hat{a}_{c/v,\mathbf{k}})$.

In the electron-hole picture, one speaks strictly of creation and annihilation of these quasiparticles, rendering the band index unnecessary. For this purpose, one defines the electron creation and annihilation operators respectively by $\hat{\alpha}^{\dagger}_{\mathbf{k}} \equiv \hat{a}^{\dagger}_{c,\mathbf{k}}$. Likewise, the hole creation and annihilation operators are respectively defined as $\hat{\beta}^{\dagger}_{-\mathbf{k}} \equiv \hat{a}_{v,\mathbf{k}}$,

leading to a Hamiltonian:

$$\begin{aligned}\hat{\mathcal{H}} = &\underbrace{\sum_{\mathbf{k}} \left(\epsilon_{e,\mathbf{k}} \hat{\alpha}^{\dagger}_{\mathbf{k}} \hat{\alpha}_{\mathbf{k}} + \epsilon_{h,\mathbf{k}} \hat{\beta}^{\dagger}_{-\mathbf{k}} \hat{\beta}_{-\mathbf{k}} \right)}_{\hat{\mathcal{H}}_K} - \underbrace{\sum_{\mathbf{k}} E(t) \left(\mu_{\mathbf{k}} \alpha^{\dagger}_{\mathbf{k}} \beta^{\dagger}_{-\mathbf{k}} + \mu^{*}_{\mathbf{k}} \hat{\beta}_{-\mathbf{k}} \hat{\alpha}_{\mathbf{k}} \right)}_{\hat{\mathcal{H}}_{F-C}} \\ &\underbrace{+ \frac{1}{2} \sum_{\substack{\mathbf{k},\mathbf{k}',\mathbf{q} \\ \mathbf{q} \neq \mathbf{0}}} V_{\mathbf{q}} \left(\hat{\alpha}^{\dagger}_{\mathbf{k}+\mathbf{q}} \hat{\alpha}^{\dagger}_{\mathbf{k}'-\mathbf{q}} \hat{\alpha}_{\mathbf{k}'} \hat{\alpha}_{\mathbf{k}} + \hat{\beta}^{\dagger}_{\mathbf{k}+\mathbf{q}} \hat{\beta}^{\dagger}_{\mathbf{k}'-\mathbf{q}} \hat{\beta}_{\mathbf{k}'} \hat{\beta}_{\mathbf{k}} - 2 \hat{\alpha}^{\dagger}_{\mathbf{k}+\mathbf{q}} \hat{\beta}^{\dagger}_{\mathbf{k}'-\mathbf{q}} \hat{\beta}_{\mathbf{k}'} \hat{\alpha}_{\mathbf{k}} \right)}_{\mathcal{H}_{C-C}},\end{aligned} \tag{3.5.1}$$

where the free Hamiltonian $\hat{\mathcal{H}}_K$ denotes the kinetic contributions of the carriers, $\hat{\mathcal{H}}_{C-C}$ denotes the carrier-carrier Coulomb interactions (electron-electron, hole-hole and electron-hole) and $\hat{\mathcal{H}}_{F-C}$ contains the dipole coupling to the optical field $E(t)$. $V_{\mathbf{q}}$ is the Fourier-transformed Coulomb potential.

Through this formalism, the occupation probability $n_{e/h,\mathbf{k}}(t)$ and the transition probability $p_{\mathbf{k}}$ are expressed as the expectation value of suitable creation and annihilation operators:

$$\begin{aligned} n_{e,\mathbf{k}}(t) &= \left\langle \hat{\alpha}^{\dagger}_{\mathbf{k}} \hat{\alpha}_{\mathbf{k}} \right\rangle \\ n_{h,\mathbf{k}}(t) &= \left\langle \hat{\beta}^{\dagger}_{-\mathbf{k}} \hat{\beta}_{-\mathbf{k}} \right\rangle \\ p_{\mathbf{k}}(t) &= \left\langle \hat{\beta}_{-\mathbf{k}} \hat{\alpha}_{\mathbf{k}} \right\rangle \end{aligned} \tag{3.5.2}$$

Unfortunately, this procedure is recursive, demonstrating the richness of many-body correlations among the carriers. A closed-form of a dynamical equation describing the evolution of some interaction operator is in general not possible to be found. This can be seen through the Heisenberg equation of motion . For an operator $\hat{Q}$:

$$\frac{d}{dt}\hat{Q} = \frac{i}{\hbar}\left[\hat{\mathcal{H}}, \hat{Q}\right] \tag{3.5.3}$$

If the Hamiltonian of Eq. (3.5.1) is introduced in it, the evaluation of the commutator will indefinitely create new higher-order expectations: in the first step, four-operator expectation values coming from $\mathcal{H}_{C-C}$ would have to be determined. In principle, they can be evaluated again using Eq. (3.5.3), yielding new, longer products of operators.

Even though this procedure clearly does not terminate, an exact decomposition of its left-hand side is possible [2]. In particular, the expectation value of the operator in question may be split in a *Hartree-Fock* term and a scattering term:

$$\frac{d}{dt}\left\langle \hat{Q} \right\rangle \equiv \frac{d}{dt}\left\langle \hat{Q} \right\rangle \Big|_{\text{HF}} + \frac{d}{dt}\left\langle \hat{Q} \right\rangle \Big|_{\text{scatter}} \tag{3.5.4}$$

The Hartree-Fock term contains the exactly-solvable contributions whereas the second term contains scattering events which are responsible for the higher-order correlations. Any model therefore requires a truncation so an approximation to the solution may be obtained.

If one truncates the expansion at the level of four-operators, the Hartree-Fock (or mean-field approximation) decomposes its expectation value in terms of the two-operator expectation values in Eq. (3.5.2). For instance:

$$\langle \alpha^{\dagger}_{\mathbf{k}'+\mathbf{q}} \beta_{-\mathbf{k}+\mathbf{q}} \alpha_{\mathbf{k}'} \alpha_{\mathbf{k}} \rangle \approx p_{\mathbf{k}'} n_{e,\mathbf{k}} \delta_{\mathbf{k}-\mathbf{q},\mathbf{k}'} \tag{3.5.5}$$

This decomposition allows the equations of motion of the variables to be obtained as:

$$\begin{aligned} \dot{p}_{\mathbf{k}} + i(\tilde{\omega}_{e,\mathbf{k}} + \tilde{\omega}_{h,\mathbf{k}}) p_{\mathbf{k}} + i(n_{e,\mathbf{k}} + n_{h,\mathbf{k}} - 1)\tilde{\omega}_{\mathrm{R},\mathbf{k}} - \dot{p}_{\mathbf{k}}|_{\text{scatter}} &= 0 \\ \dot{n}_{e,\mathbf{k}} + 2\mathrm{Im}\left(\tilde{\omega}_{\mathrm{R},\mathbf{k}} p^{*}_{\mathbf{k}}\right) - \dot{n}_{e,\mathbf{k}}|_{\text{scatter}} &= 0 \\ \dot{n}_{h,\mathbf{k}} + 2\mathrm{Im}\left(\tilde{\omega}_{\mathrm{R},\mathbf{k}} p^{*}_{\mathbf{k}}\right) - \dot{n}_{h,\mathbf{k}}|_{\text{scatter}} &= 0 \end{aligned} \tag{3.5.6}$$

Equations in (3.5.6) resemble the carrier-free Semiconductor Bloch Equations in Eqs. (3.4.7)-(3.4.8). Apart from the scattering contributions, the Hartree-Fock part is formally the same. The difference is, of course, that the quasiparticles' energy and

[2] A derivation of this decomposition may be found in the Appendix of [49]

the Rabi frequency have been *renormalised*, respectively as:

$$\begin{aligned}\tilde{\omega}_i &= \omega_i - \frac{1}{\hbar}\sum_{\mathbf{q}} V_{|\mathbf{k}-\mathbf{q}|} n_{i,\mathbf{q}} \\ \tilde{\omega}_{\mathrm{R},\mathbf{k}} &= \omega_{\mathrm{R},\mathbf{k}} + \frac{1}{\hbar}\sum_{\mathbf{q}\neq\mathbf{k}} V_{|\mathbf{k}-\mathbf{q}|} p_{\mathbf{k}}\end{aligned} \tag{3.5.7}$$

In practice, due to the the conservation expressed in Eq. (3.4.3) and the fact that the Coulomb scattering terms in $\mathcal{H}_{C-C}$ conserve quasiparticle number, the quasiparticles' occupations are not independent of each other and can thus be lumped into a single variable $w_{\mathbf{k}} \equiv 2n_{e,\mathbf{k}} - 1$ - the inversion at $\mathbf{k}$.

This renormalisation is manifested in optical and electronic properties of semiconductors. Graphene again defies the expectable: it seems that the Rabi frequency renormalisation may be ignored in some energy scales. Firstly, Quantum Field Theories of graphene are not easy to obtain due to its non-perturbative nature. This is to be contrasted with perturbative renormalisation group methods, which are known to converge reliably. The fine-structure constant of (suspended) graphene is:

$$\alpha_{\mathrm{G}} = \frac{e^2}{\hbar v_{\mathrm{F}}} \approx 2.2. \tag{3.5.8}$$

This expression is obtained through the replacement $c \mapsto v_{\mathrm{F}}$ in the QED fine structure $\alpha_{\mathrm{QED}} \approx 1/137$, a number well below unity. Consequently, since $v_{\mathrm{F}} \approx c/300$, this means that $\alpha_{\mathrm{G}} \approx 300\alpha_{\mathrm{QED}}$, a figure above unity and thus troublesome to apply perturbative methods.

Most metals are described as Landau fermi liquids and their Coulomb interactions appropriately accounted for in such framework. A QED analysis of graphene reveals some differences, due to its quasirelativistic nature [44]. The vanishing of the density of states at the Fermi level leads to short-range interactions being irrelevant [72].

Similar conclusions were obtained by Hofmann et al [73] by applying non-perturbative Random Phase Approximation methods to conclude that long-ranged interactions are screened in the layer and the many-body system shows features of a weekly-interacting Landau Fermi Liquid. The screening effect no longer applies at very low electronic densities, at which stage a renormalisation of the Fermi velocity is both predicted [74] and measured [75]. For these reasons, the conceptualisation of graphene as a non-interacting ensemble of two-level systems should not lead to any major disagreement about its physics. This is what is assumed from now and no Coulomb interactions shall be considered in the graphene SBEs and, later in Section 4, in the DBEs.

3.5.2 Temperature and Doping

Up until this point, the decay rates which render the two-level system decoherent have not been explained or introduced conceptually. This section is devoted to shed some light on the physics behind it and how to incorporate these mechanisms in the SBEs [3].

Since the band occupations $n_{\lambda,\mathbf{k}}$ arise from electron and hole distributions in momentum space and changes thereof, it is not surprising that the inversion is given by them. In particular:

$$\begin{aligned} w_{\mathbf{k}} &= n_{\mathbf{k},e} + n_{\mathbf{k},h} - 1 = n_{\mathbf{k}} + (1 - n_{-\mathbf{k}}) - 1 \\ &= n_{\mathbf{k}} - n_{-\mathbf{k}} \end{aligned} \tag{3.5.9}$$

If the sample is in a quasi-equilibrium regime described by a temperature T, and the system is doped by μ so that the Fermi level no longer sits at the Dirac points, an approximation of the carrier distribution in momentum space may be obtained with the aid of the Fermi-Dirac distribution of the each type of carrier.

[3] The Dirac-Bloch Equations, the subject-matter of Chapter 4, models the two-level system decoherence in the exact same fashion.

For $\mu_e = \mu_h \equiv \mu$, the quasi-equilibrium populations follow:

$$\begin{aligned} n^0_{\mathbf{k}} = f_{\mathbf{k}} - f_{-\mathbf{k}} &= \frac{1}{1+\exp\left(\frac{\hbar v_F|\mathbf{k}|-\mu}{k_BT}\right)} - \frac{1}{1+\exp\left(-\frac{\hbar v_F|\mathbf{k}|+\mu}{k_BT}\right)} \\ &= -\frac{\sinh\left(\frac{\hbar v_F|\mathbf{k}|}{k_BT}\right)}{\cosh\left(\frac{\mu}{k_BT}\right)+\cosh\left(\frac{\hbar v_F|\mathbf{k}|}{k_BT}\right)} \end{aligned} \tag{3.5.10}$$

Scattering mechanisms, such as carrier-carrier or carrier-phonon, radiative recombination, or defects in the sample drive the occupation distribution to change towards a quasi-equilibrium distribution, as alluded in the previous section.

In general, this re-equilibration takes time in a certain scale and is not easy to quantify. Moreover, many different processes take place. For a sample initially in thermal equilibrium, the carriers show a very narrow, isotropic occupation distribution in momentum space. After the application of an optical field, over a time in the order of approximately $5-15$ fs, the system is no longer thermally distributed and a highly anisotropic, broad distribution is found to promote high-momentum states. Within a certain thermalisation time, this distribution is again equilibrated. This process is achieved mainly due to electron-electron scattering, especially of high momentum and, in graphene, takes roughly 50 fs. This results in a narrow, quasi-equilibrium distribution at a different temperature than the initial one. Subsequently, phonon-electron scattering, optical-to-phonon decay fully thermalise the distribution within a much slower time interval, of approximately 1 ps.

Modelling this situation presents many theoretical and experimental challenges. In particular, an estimate of such decay rates for suspended graphene seems unlikely to be accurately taken. To further complicate the matter, experimental measurements of samples on a subtrates vary significantly given their composition and chemical preparation. Time and Angle-Resolved Photoemission Spectroscopy (ARPES) techniques estimate these relaxation times as $T_1 \approx 150$ fs and $T_2 \approx 0.8$ ps [76]. These figures

are heavily affected by a combination of initial temperature, doping, pump fluence, excitation energy and substrate type. On the theoretical side, the SBEs themselves have been used in order to model such mechanisms [77].

With these figures, an estimate of the decay rates can be taken simply as the inverse of these lifetimes i.e. $\gamma_i \equiv T_i^{-1}$. In the context of this work, the optical excitation considered is an ultrafast regime, allowing to safely disregard the decoherence rates altogether. This is approximately true for ultrashort pulses in the coherent regime, i.e. for pulse durations much shorter than the dephasing times, $t_0 \ll T_{1,2}$, where t_0 is the input pulse duration.

3.6 Low-Field Regime

As a starting point to understand nonlinear interactions, it is instructive to analyse the predictions of the SBEs when the external electric field intensity is small. The results that are obtained should be in conformity with the principles of Linear Optics, outlined in Section 2.4.1. The SBEs are explicitly dependent on the field and thus exceedingly complicated to solve analytically.

However, the $\mathbf{k}$-dependent microscopic polarisation $p_{\mathbf{k}}$ in the regime of low field intensity can be obtained analytically by solving the SBEs with suitable conditions. If one further assumes that the system is initially found in its ground state i.e. $w_{\mathbf{k}}[t = 0] \approx -1$, this situation reflects a picture where all carriers are in a suitable $\mathbf{k}$-state in the valence band and only a negligible subset of carriers undergoes optical excitation or de-excitation. If the field dynamics is assumed to maintain this situation, the inversion becomes a simple constant dictated by this initial condition. Mathematically, this instance presents an advantage since the SBEs may be solved analytically. Although the SBEs are composed of two coupled equations, this prescription allows the dynamical equation governing the population inversion in the

regime of low field intensity to be dismissed, leading to

$$w_{\mathbf{k}}(t) = n_{e,\mathbf{k}}(t) + n_{h,\mathbf{k}}(t) - 1 \approx -1 \tag{3.6.1}$$

for all momenta.

The solutions vary given the electric field profile and will be explored shortly. Before engaging in the derivation, the SVEA-approximated SBEs of Eq. (3.4.10) may be computed numerically.

The dimensionless scaling of all the quantities are given in Appendix A.1. The pulse central frequency is now described by the dimensionless parameter Ω_0, quantifying the number of optical cycles per pulse. The dimensionless field intensity parameter ψ_0 runs between 0 and roughly 10 in order to capture linear to extreme nonlinear intensities, as will be shortly seen. In order not to confuse other usages of the symbol τ, the dimensionless time parameter will still be denoted by t.

In order to have a taste of what the SBEs predict, the complex-valued microscopic polarisation $q_{\mathbf{k}}$ and the real-valued inversion $w_{\mathbf{k}}$ are now shown for a field of dimensionless amplitude $\psi_0 = 10^{-2}$ and frequency $\Omega_0 = 30$, ensuring the field envelope describes the field fairly well. A momentum state will be denoted by $|\tilde{\mathbf{k}}, \phi_{\tilde{\mathbf{k}}}\rangle$ - the dimensionless momentum magnitude and angle, respectively. $\tilde{\mathbf{k}}$ is scaled so that electronic states for which the band separation exactly matches the photon energy have dimensionless momentum $\tilde{\mathbf{k}} = 1$. The dimensionless detuning is then simply $\delta_{\tilde{\mathbf{k}}} = \tilde{\mathbf{k}} - 1$.

Fig. 3.1 shows the dynamics of the real and imaginary part of the microscopic polarisation $q_{\tilde{\mathbf{k}}}$ when probed with a sech plotted for various values of the detuning, for a fixed angle $\phi_{\tilde{\mathbf{k}}} = \pi/3$. The dimensionless electromagnetic field and respective vector potential may be found in Eq. (4.5.1) in the same appendix. Fig. 3.2(a) shows the same situation as before, but now showing how the detuning affects the inversion. In

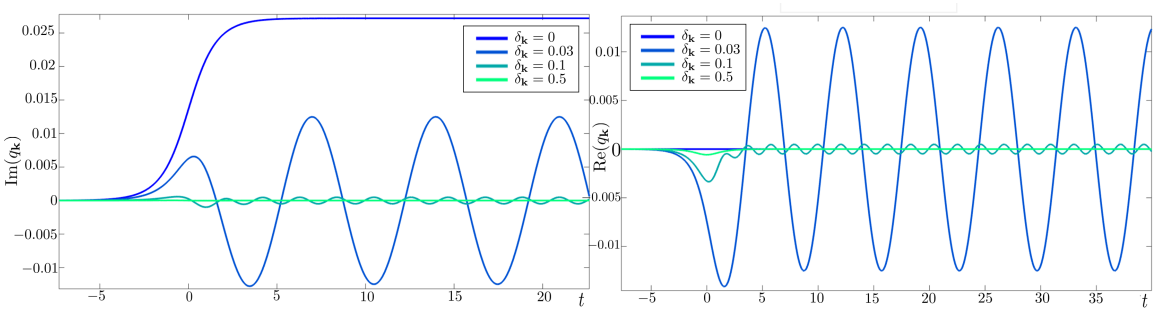

Figure 3.1: The role of the detuning on the slowly-varying microscopic polarisation – (left) $\mathrm{Im}(q_{\tilde{\mathbf{k}}})$ and (right) $\mathrm{Re}(q_{\tilde{\mathbf{k}}})$ – for sech pulse of field intensity $\psi_0 = 10^{-2}$ and frequency $\Omega_0 = 30$. An angle $\phi_{\tilde{\mathbf{k}}} = \pi/3$ is fixed.

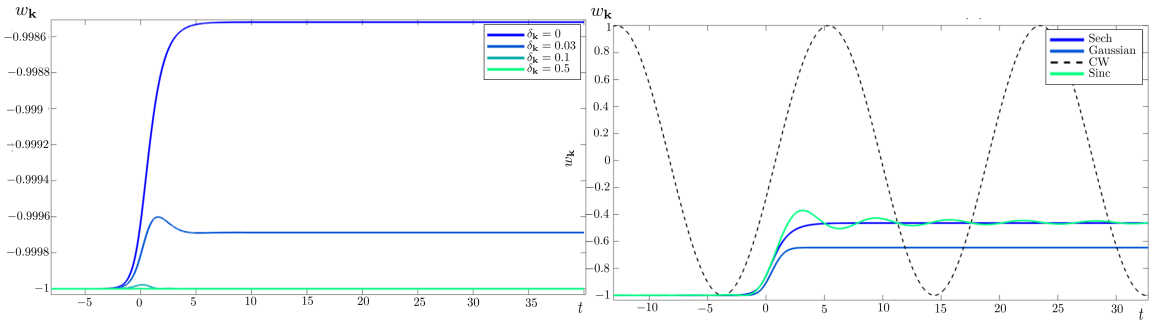

Figure 3.2: The role of (left) the detuning on the inversion for a sech pulse of field intensity $\psi_0 = 10^{-2}$ and frequency $\Omega_0 = 30$, for a fixed angle $\phi_{\tilde{\mathbf{k}}} = \pi/3$ (right) the field envelope on the inversion for a resonant state $|1, \pi/3\rangle$.

both figures, it is clear that the dynamics of the two-level system is heavily affected by the detuning $\delta_{\tilde{\mathbf{k}}}$: resonant or near-resonant states attain higher values of the inversion and have greater coherence amplitudes. Conversely, very detuned states are barely affected by the field.

3.6.1 Analytical Solutions of the SBEs

Setting $w_{\mathbf{k}} = -1$, and making use of the field decomposition in Eq. (2.4.20), the SVEA-approximated equation governing the microscopic polarisation (the first equa-

tion in Eq. (3.4.10)) reads:

$$\dot{q}_{\mathbf{k}} + i(\omega_{\mathbf{k}} - \omega_0 - i\gamma_2)q_{\mathbf{k}} = \frac{i\mu_{\mathbf{k}}}{2\hbar}\mathscr{E}(t) \tag{3.6.2}$$

The solution is obtained using the integrating factor $e^{\int i(\omega_{\mathbf{k}}-\omega_0-i\gamma_2)dt} = e^{i(\omega_{\mathbf{k}}-\omega_0-i\gamma_2)t}$, leading to:

$$q_{\mathbf{k}}(t) = \frac{i}{2\hbar}e^{-i(\omega_{\mathbf{k}}-\omega_0-i\gamma_2)t}\int_{-\infty}^{t} e^{i(\omega_{\mathbf{k}}-\omega_0-i\gamma_2)t'}\mu_{\mathbf{k}}\mathscr{E}(t')dt \tag{3.6.3}$$

Noting that the dipole moment is not time-dependent and introducing a new variable $\tau = t - t'$, it becomes:

$$q_{\mathbf{k}}(t) = \frac{i}{2\hbar}\mu_{\mathbf{k}}\int_{0}^{\infty} \mathscr{E}(t-\tau)e^{-i(\omega_{\mathbf{k}}-\omega_0-i\gamma_2)\tau}d\tau \tag{3.6.4}$$

This form is useful as long as such integral may be expressed analytically. Its formal simplicity stems from something more fundamental. The SVEA that was applied to the electric field implies the Rotating Wave Approximation (RWA). To see this, the full field is now kept in Eq. (3.4.10), leading to:

$$q_{\mathbf{k}}(t) = \frac{i}{2\hbar}\mu_{\mathbf{k}}e^{-i(\omega_{\mathbf{k}}-\omega_0-i\gamma_2)t}\int_{-\infty}^{t} e^{i(\omega_{\mathbf{k}}-\omega_0-i\gamma_2)t'}\left(\mathscr{E}(t') + \mathscr{E}^*(t')e^{2i\omega_0 t'}\right)dt' \tag{3.6.5}$$

For the sake of simplicity, a continuous wave of amplitude $\mathscr{E}_0$ is assumed so the field may be taken out of the integral, which can be evaluated as:

$$q_{\mathbf{k}}(t) = \frac{\mu_{\mathbf{k}}\mathscr{E}_0}{2\hbar}\left(\frac{1}{\omega_{\mathbf{k}} - \omega_0 - i\gamma_2} + \frac{e^{2i\omega_0 t}}{\omega_{\mathbf{k}} + \omega_0 - i\gamma_2}\right). \tag{3.6.6}$$

It is clear that the resonant term, for which $\omega_{\mathbf{k}} - \omega_0 \approx 0$, dominates over the non-resonant term for which $\omega_{\mathbf{k}} + \omega_0 \approx 2\omega_0$, meaning:

$$\frac{1}{\omega_{\mathbf{k}} - \omega_0} \gg \frac{1}{\omega_{\mathbf{k}} + \omega_0} \tag{3.6.7}$$

and therefore neglecting the terms rotating with $e^{i\omega_0 t}$ in the SBEs is congruent with the RWA.

The condition $w_{\mathbf{k}} = -1$ can be somewhat relaxed in an approximation known as the *quasi-equilibrium approximation* [78], in which the inversion is simply assumed to vary little in the dephasing time $1/\gamma_2$ i.e. $w_{\mathbf{k}}(t') \approx w_{\mathbf{k}}(t)$ for $t' < 1/\gamma_2$, conveniently allowing this term to be taken out of the integral.

The form just found in Eq. (3.6.4) is very suggesting. If causality is imposed through the inclusion of the Heaviside Θ-step function, the integration range may be extended to the reals:

$$q_{\mathbf{k}}(t) = \frac{i}{2\hbar}\mu_{\mathbf{k}} \int_{-\infty}^{\infty} \mathscr{E}(t-\tau) e^{-i(\delta_{\mathbf{k}} - \omega_0 - i\gamma_2)\tau} \Theta(\tau) d\tau \tag{3.6.8}$$

thus allowing a response function $R(\tau) = e^{-i(\omega_{\mathbf{k}} - \omega_0 - i\gamma_2)\tau}\Theta(\tau)$ to be identified. This looks remarkably similar to the linear response expressed in Eq. (2.4.8)! The time-dependent polarisation is then expressed as a convolution of the field and the response function. A frequency-dependent polarisation may be obtained as:

$$q_{\mathbf{k}}(t) = \frac{i\mu_{\mathbf{k}}}{2\hbar}\left(R(t) \circledast \mathscr{E}(t)\right) \Leftrightarrow \tilde{q}_{\mathbf{k}}(\delta_\omega) = \frac{i\mu_{\mathbf{k}}}{2\hbar}\tilde{R}(\delta_\omega)\tilde{\mathscr{E}}(\delta_\omega) \tag{3.6.9}$$

where the tilded variables represent the Fourier transform of their time-dependent counterparts and $\circledast$ denotes the convolution operation. This is nothing more than re-expressing Eq. (2.4.10) in its *microscopic* version. Given the SVEA treatment taken, the frequency argument refers to the detuning frequency i.e. $\delta_\omega = \omega - \omega_0$. The response function can be easily Fourier-transformed to:

$$\begin{aligned} \tilde{\mathcal{R}}(\delta_\omega) &= \mathcal{F}[e^{-i(\delta_{\mathbf{k}} - i\gamma_2)\tau}\Theta(\tau)] = \tilde{\Theta}(\delta_\omega + \delta_{\mathbf{k}} - i\gamma_2) \\ &= \frac{1}{i\left(\delta_\omega + \delta_{\mathbf{k}} - i\gamma_2\right)} + \pi\delta(\delta_\omega + \delta_{\mathbf{k}} - i\gamma_2) \end{aligned} \tag{3.6.10}$$

yielding a Fourier-transformed microscopic polarisation:

$$\tilde{q}_{\mathbf{k}}(\delta_\omega) = \frac{\mu_{\mathbf{k}}}{2\hbar}\tilde{\mathscr{E}}(\delta_\omega)\left(\frac{1}{\delta_\omega + \delta_{\mathbf{k}} - i\gamma_2} + i\pi\delta(\delta_\omega + \delta_{\mathbf{k}} - i\gamma_2)\right) \tag{3.6.11}$$

Even after applying a generous number of assumptions to simplify the problem, time-dependent solutions to Eq. (3.6.8) are challenging to obtain given the generality of the field profile. A continuous wave presented no difficulty, resulting in the solution in Eq. (3.6.6).

Analytical solutions for two pulse-like excitations are now shown - a Gaussian and sech profiles. The effect of dephasing is also ignored by setting $\gamma_2 = 0$. The dipole moment, approximated by SVEA and calculated in Eq. (2.4.38), rescales simply to $\mu_{\tilde{\mathbf{k}}} = \sin\phi_{\tilde{\mathbf{k}}}$.

Gaussian Pulse

If the electric field is taken as a Gaussian pulse, whose electric field is $\psi(t)$ of the form:

$$\psi(t) = \psi_0 e^{-\frac{1}{2}(t-t_\mathrm{f})^2}, \tag{3.6.12}$$

where ψ_0 is the field amplitude, attained when $t = t_f$, the polarisation is found to be:

$$q_{\tilde{\mathbf{k}}}(t) = \frac{\sqrt{\pi}}{2}\psi_0 \sin\phi_{\tilde{\mathbf{k}}} e^{\frac{1}{4}\left(2i(t_\mathrm{f}-2t)-\delta_{\tilde{\mathbf{k}}}\right)\delta_{\tilde{\mathbf{k}}}}\ \mathrm{Erfc}\left(\frac{1}{2}\left(t_\mathrm{f} - 2t + i\delta_{\tilde{\mathbf{k}}}\right)\right) \tag{3.6.13}$$

Here, $\delta_{\tilde{\mathbf{k}}}$ is the dimensionless detuning and Erfc the complex complementary error function. The analytical form of the microscopic polarisation just derived may be compared with the its numerical output, computed from Eq. (3.4.10). For this comparison to be meaningful, a field intensity must be chosen so that the approximation in Eq. (3.6.1) holds. Note that, on resonance, the polarisation is purely imaginary. As for a general off-resonant state, real and imaginary part of the microscopic polar-

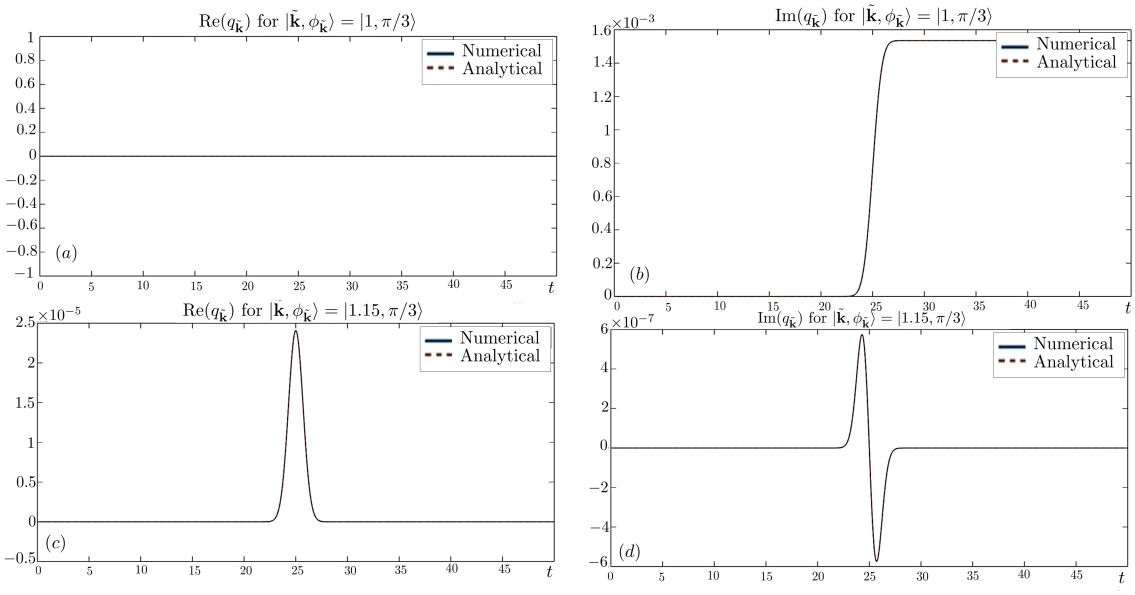

Figure 3.3: Comparison of the microscopic polarisation of a state $|\tilde{\mathbf{k}}, \phi_{\tilde{\mathbf{k}}}\rangle$ between its numerical and analytical form, when probed with a Gaussian pulse in the low field regime, with $\psi_0 = 10^{-3}$. (a) and (b) show respectively its real and imaginary part for a resonant momentum state $|1, \pi/3\rangle$. (c) and (d) show the same, for an off-resonant state $|1.15, \pi/3\rangle$.

isation show general features: its real part is roughly similar in shape as the electric field, whereas its imaginary part is roughly similar to the derivative of the field.

Secant Pulse

If the excitation is now chosen to be a sech pulse given by $\psi(t) = \psi_0 \text{sech}\,(t)$ and with the aid of new variables $s = \frac{1}{2}(1 + i\delta_{\tilde{\mathbf{k}}})$ and $y = e^t$, the polarisation of Eq. (3.6.4) takes the form:

$$q_s(y) = i\psi_0 \sin\phi_{\tilde{\mathbf{k}}} \left(\frac{y}{s}\right) {}_2F_1(1; s; s+1; -y^2) \tag{3.6.14}$$

where the Gaussian hypergeometric function is defined as:

$${}_2F_1(\alpha, \beta; \gamma; t) = \sum_{k=0}^{\infty} \frac{(\alpha)_k (\beta)_k}{(\gamma)_k} \frac{t^k}{k!} \tag{3.6.15}$$

and $(\alpha)_k$ is the Pochhammer symbol:

$$(\alpha)_k = \prod_{j=0}^{k-1}(\alpha + j) \tag{3.6.16}$$

Hypergeometric functions are known to be incredibly general. In fact, most elementary functions may be expressed as a limiting case of them, for particular functional relations in its four defining parameters. One such instance is provided by the resonant two-level systems with dimensionless wavevector $\tilde{\mathbf{k}} = 1$, i.e. $\delta_{\tilde{\mathbf{k}}} = 0$ and consequently $s = \frac{1}{2}$, leading to:

$$\begin{aligned} q_{\frac{1}{2}}(y) &= 2i\psi_0 \sin\phi_{\tilde{\mathbf{k}}} y \, {}_2F_1(1, \frac{1}{2}; \frac{3}{2}; -y^2) \\ &= 2i\psi_0 \sin\phi_{\tilde{\mathbf{k}}} \sum_{k=0}^{\infty} \left(\frac{\left(\frac{1}{2}\right)_k (1)_k}{\left(\frac{3}{2}\right)_k} \right) \frac{(-1)^k y^{2k+1}}{k!}. \end{aligned} \tag{3.6.17}$$

With the identification of $(1)_k = k!$, the computation of the remaining Pochhammer symbols yields:

$$\frac{\left(\frac{1}{2}\right)_k}{\left(\frac{3}{2}\right)_k} = \frac{\frac{1}{2} \cdot \frac{3}{2} \cdot \frac{5}{2} \cdot \ldots \cdot \frac{2k-1}{2}}{\frac{3}{2} \cdot \frac{5}{2} \cdot \frac{7}{2} \cdot \ldots \cdot \frac{2k+1}{2}} = \frac{1}{2k+1} \tag{3.6.18}$$

in the original variables, the resonant polarisation becomes:

$$q_{1/2}(t) = 2i\psi_0 \sin\phi_{\tilde{\mathbf{k}}} \sum_{k=0}^{\infty} \frac{(-1)^k}{2k+1} (e^t)^{2k+1} = 2i\psi_0 \sin\phi_{\tilde{\mathbf{k}}} \arctan(e^t) \tag{3.6.19}$$

a purely imaginary function. The induced polarisation of off-resonant states may also be obtained by considering a general detuning. The Pochhammer symbols of the underlying hypergeometric function of Eq. (3.6.14) can be computed exactly as:

$$\begin{aligned} \frac{(1)_k (s)_k}{(s+1)_k k!} = \frac{(s)_k}{(s+1)_k} &= \frac{s \cdot (s+1) \cdot (s+2) \cdot \ldots \cdot (s+k-1)}{(s+1) \cdot (s+2) \cdot (s+3) \cdot \ldots \cdot (s+k)} \\ &= \frac{s}{s+k}. \end{aligned} \tag{3.6.20}$$

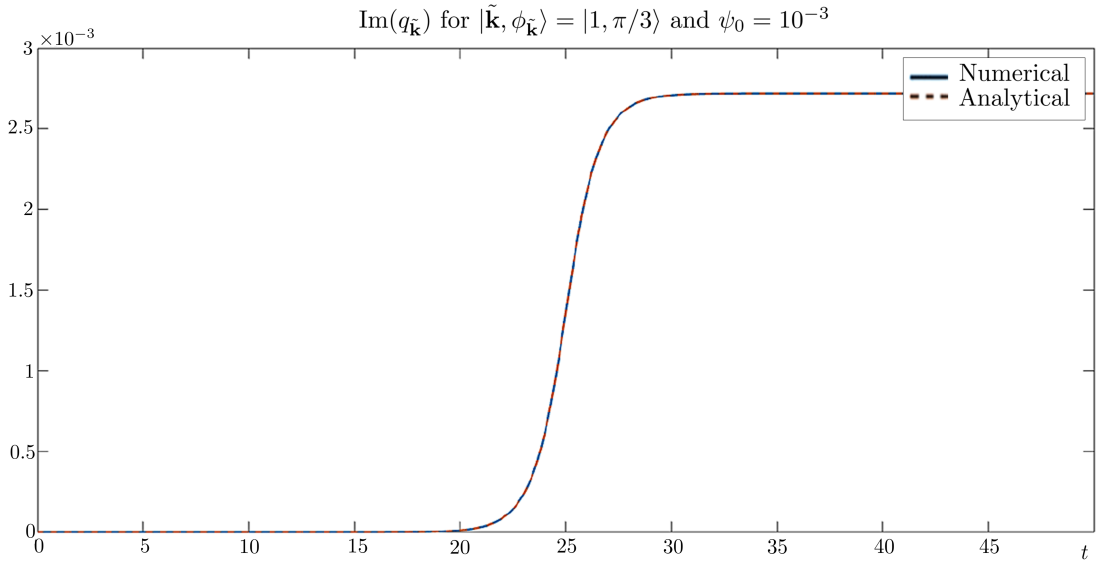

Figure 3.4: Comparison of $\mathrm{Im}(q_{\mathbf{k}})$ between its simulation output and analytical form, for the momentum state $|\tilde{\mathbf{k}}, \phi_{\tilde{\mathbf{k}}}\rangle = |1, \pi/3\rangle$ in the low field regime.

meaning:

$$\begin{aligned} q_s(t) &= i\psi_0 y \sin\phi_{\tilde{\mathbf{k}}} \sum_{k=0}^{\infty} \left(\frac{1}{k+s}\right) (-1)^k y^{2k} \\ &= i\psi_0 y \sin\phi_{\tilde{\mathbf{k}}} \Phi(-y^2, 1, s) \end{aligned} \tag{3.6.21}$$

where the Hurwitz-Lerch Φ Transcendental is defined as:

$$\Phi(z, \alpha, \beta) = \sum_{k=0}^{\infty} \frac{z^k}{(k+\beta)^{\alpha}}. \tag{3.6.22}$$

It h may be expressed as a less esoteric function: using the integral identity:

$$\Phi(z, s, a) = \frac{1}{\Gamma(s)} \int_0^{\infty} \frac{u^{s-1} e^{-au}}{1 - ze^{-u}} du \tag{3.6.23}$$

valid as long for $t < 0$, as $\mathrm{Re}(s) > 0$, $\mathrm{Re}(a) > 0$ and $z \in \mathbb{C}\backslash[1, \infty)$, the Hurwitz-Lerch Φ Transcendental further reduces to an incomplete Beta function:

$$\begin{aligned}\Phi(-e^{2t}, 1, s) &= \frac{1}{\Gamma(1)} \int_0^\infty \frac{e^{-su}}{1 + e^{2t-u}} du \\ &= \frac{1}{s} + (-e^{2t})^{-s} B(-e^{2t}, s+1, 0)\end{aligned} \tag{3.6.24}$$

where the incomplete Beta function is:

$$B(z, a, b) = \int_0^z u^{a-1}(1-u)^{b-1} du \tag{3.6.25}$$

As expected, all the machinery developed so far must break down when the condition $w_{\mathbf{k}}(t) \approx -1$ is violated. From this expectation, a reasonable critical field intensity ψ_0 may be inferred, separating the linear from the nonlinear regime.

In order to verify this condition, the inversion $w_{\mathbf{k}}$ is plotted alongside the comparison of the polarisation obtained from analytical and numerical methods. Fig. 3.5 shows, as before, the comparison between the low-field-approximated microscopic polarisation, alongside its corresponding inversion obtained numerically from Eq. (3.4.10), for varying electric field amplitudes ψ_0 for a state on resonance i.e. for $\delta_{\tilde{\mathbf{k}}} = 0$. The imaginary part of the coherence in increasing field intensity are shown in $(a), (b), (e)$ and (g). Their respective inversions are shown in $(b), (d), (f)$ and (h).

These allow to capture three different situations after the low-field assumption is broken. The first regime is described by a slight dephasing from the numerical microscopic polarisation, retaining the main shape. This happens for instances that change the inversion in time, but never enough to reach a positive value. For fields with intensity $\psi_0 \approx 0.5$ it can be seen that the difference in the saturation value of the polarisation is very considerable. Its inversion is still always negative.

The assumption is then severely broken for field intensities that allow the inversion to attain positive values, happening for around $\psi_0 = 1$ and seen in (f). In that instance,

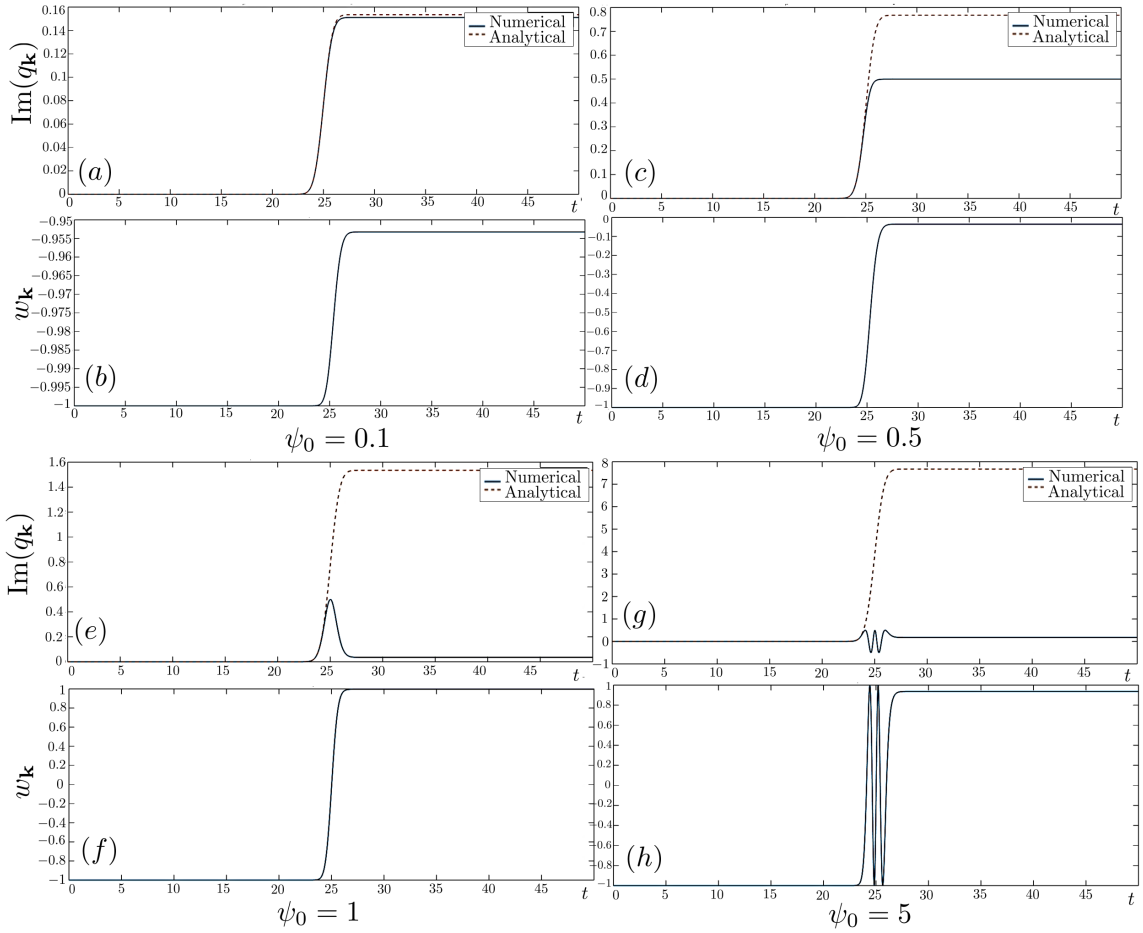

Figure 3.5: Comparison of $\mathrm{Im}(q_{\mathbf{k}})$ between its simulation (blue, full) and analytical form (red, dashed) alongside a plot of its respective inversion for the resonant momentum state $|\tilde{\mathbf{k}}, \phi_{\tilde{\mathbf{k}}}\rangle = |1, \pi/3\rangle$. Four cases are shown, for a varying field amplitude. (a) and (b) were obtained with $\psi_0 = 0.1$, (c) and (d) with $\psi_0 = 0.5$, (e) and (f) with $\psi_0 = 1$ and (g) and (h) with $\psi_0 = 5$.

the theoretical prediction fails to account for the inflection point occurring when the inversion switches sign. Subsequently, higher fields further modulate the inversion, as seen for a field intensity of $\psi_0 = 5$ in (g) and (h). In general the number of lobes which modulate the main shape of the polarisation seems to match the value of ψ_0. The low-field breaking can be made more transparent mathematically if the conservation law of Eq. (3.4.9) is analysed: if the inversion is solved from it, it follows:

$$w_{\mathbf{k}} = \pm\sqrt{1 - 4|q_{\mathbf{k}}|^2} \tag{3.6.26}$$

In the low excitation regime, the negative root is used, since the initial condition $w_{\mathbf{k}}^0 = -1$. However, if the field is strong enough to excite the system so $|q_{\mathbf{k}}| \approx 1/2$, the inversion will take either branches throughout the time dynamics.

With this analysis, one may take an educated guess that a departure from the linear optical regime is attained for field intensity parameters of around $\psi_0 = 0.2$. By $\psi_0 = 1$ the complete divergence between the predictions from linear response is notable and linear theory no longer applies at all.

In the next section, these notions will become clearer as the macroscopic polarisation will be obtained. Most importantly, it will be seen that, particularly for high field intensities, and most importantly ultrashort pulses, the slowly-varying amplitude of the field and its effect on the slowly-varying polarisation fails to capture the exact light-matter dynamics.

3.6.2 Law of Universal Absorption

The framework of the SBEs allow for a rather important result of linear optics to be obtained. It was derived in Section 2.4.3 that, for low field amplitudes, the absorbance of a graphene monolayer, a quantity which measures the efficiency of light absorbed

from a source, is a constant across the frequency spectrum i.e. independent of the input pulse frequency. This constant is related to the fine structure constant of QED, and takes the value $\pi\alpha_{\mathrm{QED}} \approx 2.3\%$.

For this result to be retrieved from the SBEs, a low-field regime must naturally be assumed, by neglecting the inversion dynamics. In this regime, the microscopic polarisation, which in frequency domain takes the form given in Eq. (3.6.11) may be inserted into the definition of the macroscopic polarisation envelope Q, given in Eq. (3.4.15):

$$\tilde{Q}(\delta_\omega) = \frac{g_s g_v}{\hbar\varepsilon_0 A d_{\mathrm{G}}} \sum_{\mathbf{k}} \left(|\mu_{\mathbf{k}}|^2 \left(\frac{1}{\delta_\omega + \delta_{\mathbf{k}} - i\gamma_2} + i\pi\delta(\delta_\omega + \delta_{\mathbf{k}} - i\gamma_2) \right) \right) \tilde{\mathscr{E}}(\delta_\omega) d^2\mathbf{k} \tag{3.6.27}$$

In this fashion, the linear optical susceptibility $\chi^{(1)}(\delta_\omega)$, as introduced in Eq. (2.4.10) can easily be read off as the function multiplying the Fourier-transformed field envelope. The absorption is related to its imaginary part $\chi^{''}(\delta_\omega)$, as was derived in Eq. (2.4.30). In the limit of vanishing dephasing i.e. $\gamma_2 \to 0$, and applying the continuum approximation, it is:

$$\chi^{''}(\delta_\omega) = \frac{1}{\hbar\epsilon_0 d_{\mathrm{G}} \pi} \int_0^{2\pi} |\mu_{\mathbf{k}}|^2 d\phi_{\mathbf{k}} \int_0^{\infty} \delta(\delta_\omega + \delta_{\mathbf{k}}) k dk \tag{3.6.28}$$

where the the integral was split in its angular and radial variables. With the interband-driven SVEA-approximated dipole moment $\mu_{\mathbf{k}} = (ev_{\mathrm{F}}/\omega_0)\sin(\phi_{\mathbf{k}})$ from Eq. (2.4.38).

As for the radial integration, the integrand is expressed in terms of the linear variable k with the aid of Eq. (2.3.21) which, with the sifting property of the(Eq. (2.3.23)) gives:

$$\int_0^{\infty} \delta(\delta_{\mathbf{k}} + \delta_\omega) k dk = \frac{1}{2v_{\mathrm{F}}} \int_0^{\infty} \delta\left(k - \frac{\omega_0 - \delta_\omega}{2v_{\mathrm{F}}} \right) k dk = \frac{\omega_0 - \delta_\omega}{4v_{\mathrm{F}}^2} \tag{3.6.29}$$

where the momentum detuning is $\delta_{\mathbf{k}} = \omega_{\mathbf{k}} - \omega_0 = 2v_{\mathrm{F}}k - \omega_0$. Therefore, at the optical frequency i.e. $\delta_\omega = 0$, the linear optical absorption coefficient is, as dictated by the calculation obtained in Eq. (2.4.30):

$$\alpha(\omega_0) = \frac{\omega_0}{c}\chi''(0) = \frac{e^2}{4\epsilon_0\hbar c d_{\mathrm{G}}} = \pi\alpha_{\mathrm{QED}}d_{\mathrm{G}} \tag{3.6.30}$$

i.e. a *constant* and, more importantly, *independent of optical frequencies*, as expected. Note that the α_{G} is the *absorption* i.e. the absorption per unit length times (*absorbance*) multiplied by the distance d_{G}.

The response function that dictated the introduction of the δ distribution is, strictly speaking, an abuse of notation as it is meaningless without being integrated. The same result could be obtained by starting from the microscopic polarisation of Eq. (3.6.6) and integrating it to obtain Q, leading to:

$$\chi(\delta_\omega) = \frac{1}{\hbar\varepsilon_0 d_{\mathrm{G}}\pi^2}\int_0^{2\pi}|\mu_{\mathbf{k}}|^2 d\phi_{\mathbf{k}}\int_0^{\infty}\frac{1}{\omega_{\mathbf{k}} - \omega_0 - i\gamma_2}kdk \tag{3.6.31}$$

The radial complex integral can be evaluated with the aid of the Sokhotski–Plemelj theorem stating that for a function $f : \mathbb{C} \to \mathbb{C}$ continuous on $\mathbb{R}$:

$$\lim_{\gamma_2\to 0^+}\int_\alpha^\beta \frac{f(\zeta)}{\zeta \pm i\gamma_2}d\zeta = \mathcal{P}\left[\int_\alpha^\beta \frac{f(\zeta)}{\zeta}d\zeta\right] \mp i\pi f(0) \tag{3.6.32}$$

$\mathcal{P}[f]$ denotes the Cauchy principal value of f, which expresses the improper integral without its singularity at $\zeta = \zeta_0$:

$$P\left[\int_\alpha^\beta f(\zeta)d\zeta\right] \equiv \lim_{\gamma_2\to 0^+}\left[\int_\alpha^{\zeta_0-\gamma_2} f(\zeta)d\zeta + \int_{\zeta_0+\gamma_2}^\beta f(\zeta)d\zeta\right] \tag{3.6.33}$$

The real part is irrelevant for this purpose. By inspection, if the variable ζ is chosen as $\zeta = \omega_{\mathbf{k}} - \omega_0 = 2v_{\mathrm{F}}k - \omega_0$, one has $f(\zeta) = (\zeta + \omega_0)/(2v_{\mathrm{F}})$ and hence Eq. (3.6.32) can be used, yielding the same imaginary part as obtained in Eq. (3.6.30).

This result will be verified in the next section, where a method will be devised to verify this law numerically. In order to do this, the reflected and transmitted fields have to be constructed from the macroscopic polarisation. For these objects to constructed, the SBEs have to be obtained numerically.

3.7 Simulations of Optical Properties

So far, the variables under consideration refer to microscopic quantities, bearing no significance to observables of the sample. In the framework so far developed, the system is comprised of all allowed momentum states, each one a two-level system. In this section, the connection between the microscopic quantities pertaining to all two-levels and described by the SBEs to macroscopic responses of the system will be made.

The regime that was used in obtaining the dynamics of the two-level system determines which momentum states are necessary to account for the macroscopic dynamics. If the full electric field and the polarisation are considered, any macroscopic quantity will be defined once all contributions are considered i.e. all momentum states considered. Naturally, the numerical realisation of this integral must contain a finite, momentum cutoff k_{c}.

Conversely, if SVEA is applied to the SBEs, the resonant momentum states i.e. $\tilde{\mathbf{k}} \approx 1$ will contribute the most. It is thus natural to introduce a cutoff in the magnitude of $\mathbf{k}$ to ensure only states within a width x from resonance are considered i.e. the region $(k_0 - x, k_0 + x)$, where k_0 is the photon momentum.

Hence for a general $\mathbf{k}$ dependent function $f_{\mathbf{k}}$, its macroscopic counterpart is:

$$\sum_{\mathbf{k}} f_{\mathbf{k}} = \begin{cases} \frac{A}{(2\pi)^2} \int_0^{2\pi} \int_{-x}^{x} f_{\boldsymbol{\sigma}} d\sigma d\phi & \text{(SVEA)} \\ \frac{A}{(2\pi)^2} \int_0^{2\pi} \int_0^{k_c} f_{\mathbf{k}} k dk d\phi & \text{(Full Field)} \end{cases} \tag{3.7.1}$$

where $\sigma = k - k_0$ is the detuning from the photon momentum k_0.

3.7.1 Macroscopic Polarisation

In the previous section, a straightforward comparison against the predictions from low-field theory allowed a quick estimate for when nonlinear effects should be relevant in the dynamics of a two-level system coupled to light. This resulted in a critical value $\psi_0 \approx 0.2$.

The same methodology can now be applied to the averaged, *macroscopic* polarisation $Q(t)$. Fig. 3.6 shows the simulated envelope polarisation field when excited with a sech pulse. It has been normalised by $Q_0 = e\omega_0/(2v_{\mathrm{F}}\pi^2\epsilon_0 d_{\mathrm{G}})$. The linear regime can

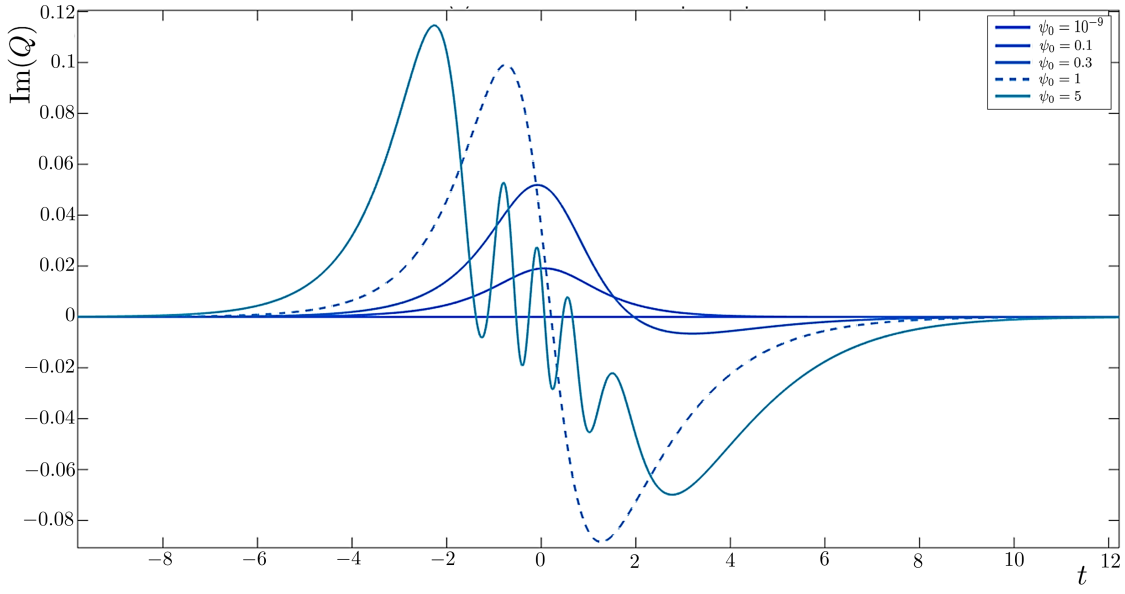

Figure 3.6: Evolution of $\mathrm{Im}(Q)$ for various electric field intensities of a sech pulse. The integration was carried out with a width $x = 0.15$.

be roughly estimated when the sample is probed with a field intensity approximately within the range $\psi_0 \in [0, 0.3]$.

Deviations from the linear regime occur when the polarisation profile shows a lobe, which becomes perfectly symmetrical when $\psi_0 = 1$. Extreme nonlinear conditions are provided for much higher values, when the lobe becomes modulated.

As one would expect, the dynamics of the polarisation in the nonlinear regime is nontrivial and depends hugely on the incident field profile, leading to very different time dynamics of the polarisation for the same field amplitude. To see this, the evolution of the polarisation when probed with four different pulse profiles – a Gaussian (a), a sinc (b), a sechtanh (c) and a supergaussian (d) – is shown in Fig. 3.9. The blue plots show the linear response, with $\psi_0 = 10^{-9}$.

In comparison with the red line ($\psi_0 = 0.2$), a critical value when the nonlinear regime is accessed, and the yellow line ($\psi_0 = 5$) probed in clearly nonlinear conditions, the linear polarisation does not show signs of modulation by the field. In contrast to that situation, its extreme nonlinear counterparts show very nontrivial behaviour.

3.7.2 Dynamics of the Reflected and Transmitted Fields

With the knowledge of the macroscopic polarisation, which accounts for the field generated by the time variation of the electric dipoles in the sample as a result of the optical excitation, it is possible to construct the reflected and transmitted fields that are set up as a consequence of the optical interaction.

If an incident wave of electric field ψ_{I} propagates in a medium of refractive index n_1, the Maxwell equations can be used to model the light propagation in the graphene sample and construct the reflected field ψ_{R}, which propagates in the outgoing direction, and transmitted field ψ_{T}, which propagates in the incoming direction in a medium of refractive index n_2. These naturally depend on the incoming field but also

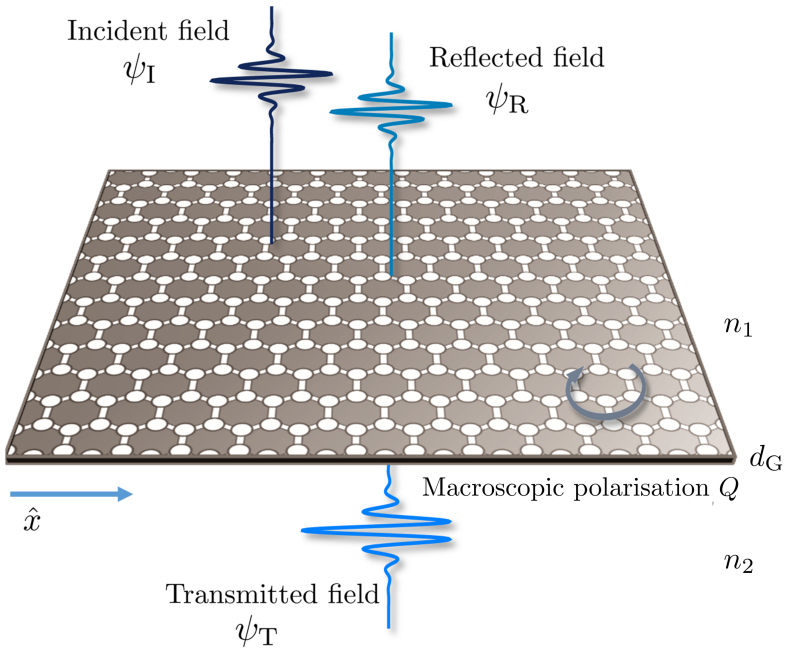

Figure 3.7: Sketch representing the reflected and transmitted fields that are set up when a graphene monolayer is illuminated by an incident pulse. The light-matter interactions can be captured in the generated polarisation of the sample.

on the generated polarisation of the medium:

$$\psi_{\mathrm{R}}(t) = \left(\frac{n_1 - n_2}{n_1 + n_2}\right)\psi_{\mathrm{I}}(t) + \left(\frac{Q_0}{A_0}\right)\frac{d_G}{(n_1+n_2)c}\left(i\omega_0 Q - \partial_t Q\right) \tag{3.7.2}$$

$$\psi_{\mathrm{T}}(t) = \left(\frac{2n_1}{n_1 + n_2}\right)\psi_{I}(t) + \left(\frac{Q_0}{A_0}\right)\frac{d_G}{(n_1+n_2)c}\left(i\omega_0 Q - \partial_t Q\right) \tag{3.7.3}$$

These fields are dimensionless, with $Q_0 = \frac{e\omega_0}{2v_{\mathrm{F}}\epsilon_0 d_G \pi^2}$ and $A_0 = \frac{2\hbar\omega_0}{ev_{\mathrm{F}}t_0}$.

If the incident field intensity is low, the polarisation is also low and the first terms in Eqs. (3.7.3)-(3.7.2) dominate. This can be seen in Fig. 3.8 where an incident field amplitude $\psi_0 = 10^{-6}$, well within the linear regime, is used to excite the sample. The behaviour may be appreciated for different pulse profiles and seen as general, in the sense that the incident (blue) and (transmitted) fields retain their shape, regardless of field profile. The energy carried in the transmitted field is reduced, giving rise to a reflected field (red) of small amplitude, in the opposite direction.

In Fig. (3.10), the dynamics of the reflected field when set up by an incident sech

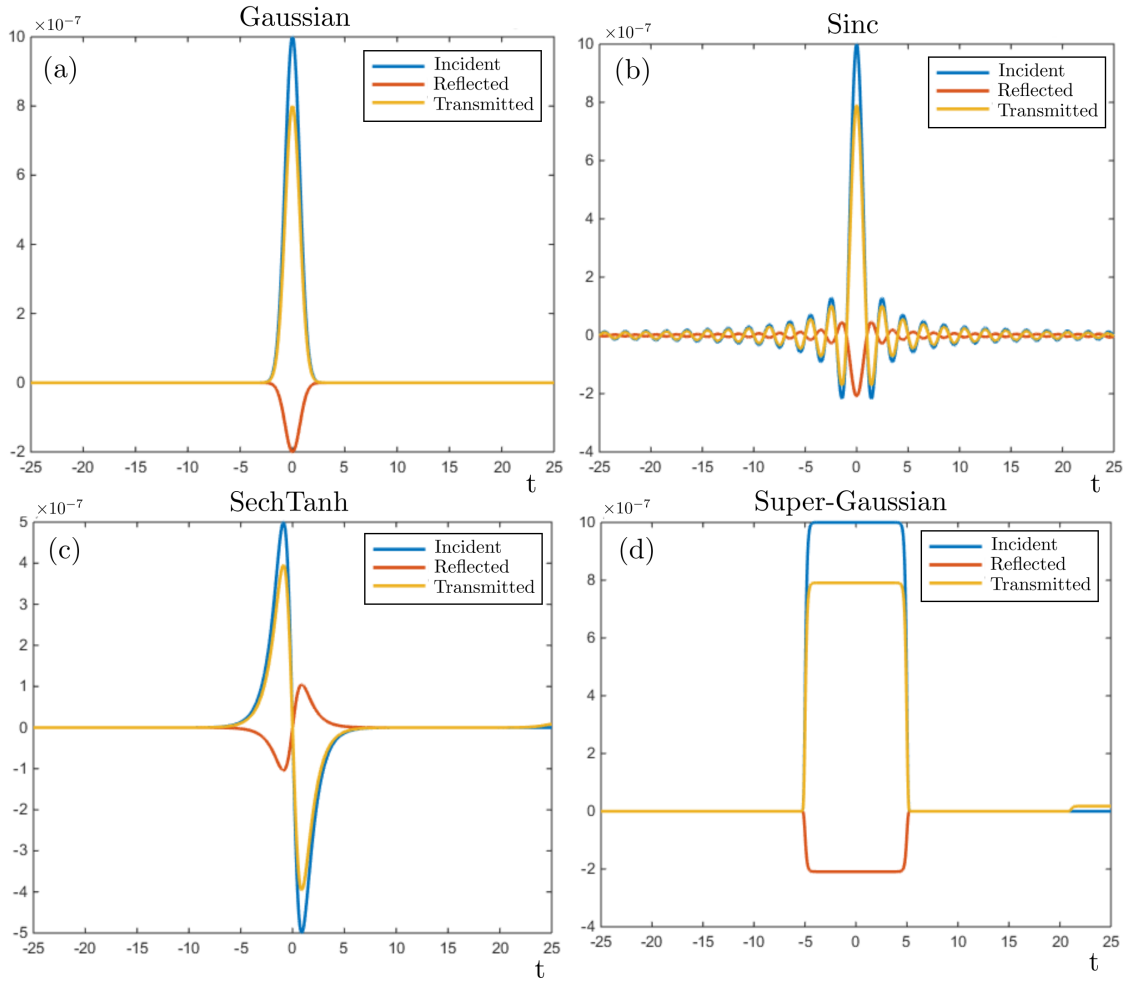

Figure 3.8: Plot of the incident, reflected and transmitted fields in the sample for various pulse profiles in the linear regime. The incident amplitude is $\psi_0 = 10^{-6}$.

pulse of central frequency $\Omega_0 = 50$ is shown by varying the incident field amplitude ψ_0. In the linear regime of excitation shown in (a), one expects the reflected and transmitted fields to keep roughly the shape of the incoming field, albeit with a decreased amplitudes and with different signs given their propagation direction, as just discussed.

However, once the field is strong enough to create a nontrivial polarisation, the reflected field too becomes nontrivial and it depends exclusively on it when both media have the same refractive index i.e. $n_1 = n_2$.

These features just discussed also depend on the frequency of the pulse. In the di-

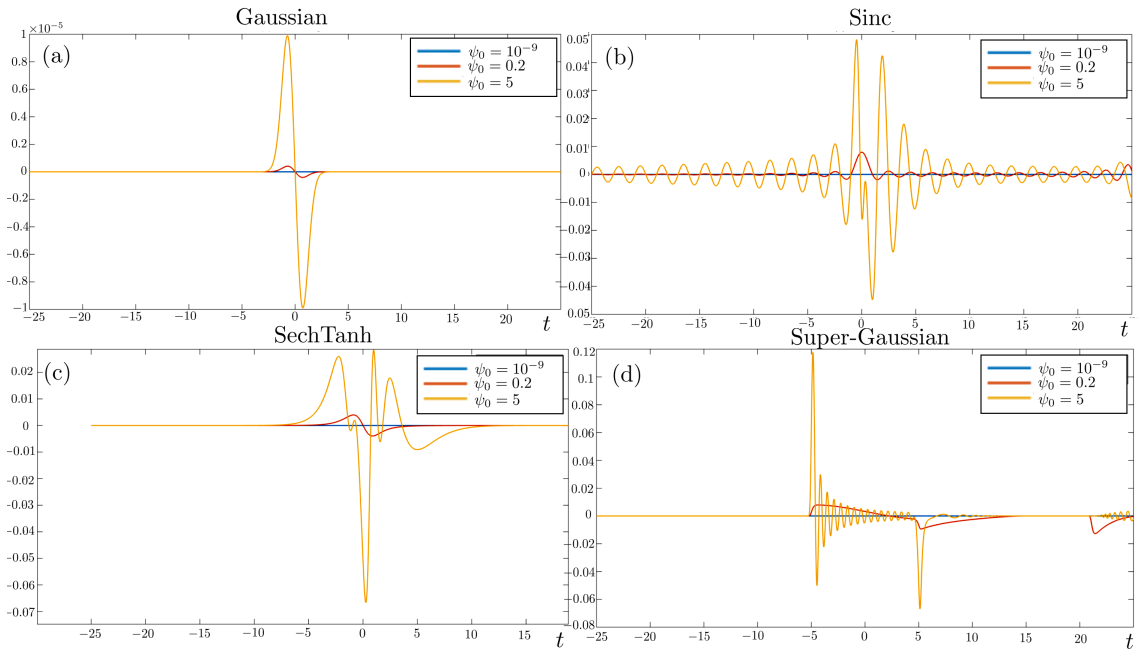

Figure 3.9: Effect of the incident field amplitude on the macroscopic polarisation, seen through Im(Q). The sample is excited with different pulse profiles and the result shown in each window $(a) - (d)$. Three regimes are shown: linear (blue), with $\psi_0 = 10^{-9}$, extreme nonlinear (yellow), with $\psi_0 = 5$, as well as a transiting linear-to-nonlinear regime (red), with $\psi_0 = 0.2$ are shown.

mensionless units used, $\Omega_0 = \omega_0 t_0$ conveys the number of optical cycles. It can be seen in Fig. 3.11 that the reflected field converges rather quickly when increasing the pulse frequency. It is however clear that few-cycle pulses excite the sample very differently as seen in (a), where a one-cycle pulse, the ultimate limit imposed by the Heisenberg Uncertainty Principle, is shown. By roughly 10 optical cycles, has greatly converged to the field set up by a long pulse, as seen in (b). One can see in (c) that by roughly 25 optical cycles, the pulse starts to show features of a *long* one, given its similarity to a pulse with 50 optical cycles, shown in (d). These aspects will become crucial in understanding the full-field dynamics in the DBEs.

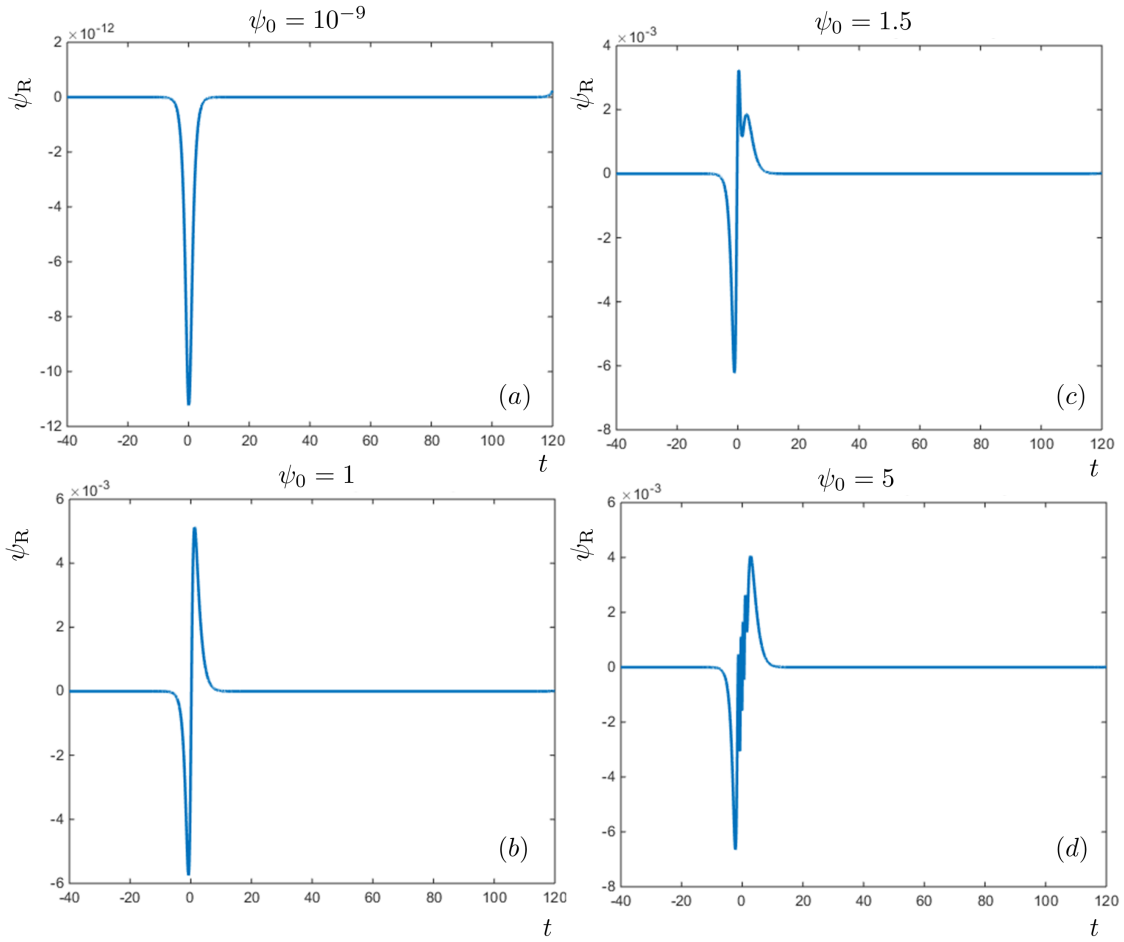

Figure 3.10: Role of the incident field intensity on the reflected field for a sech pulse, of central frequency $\Omega_0 = 50$

3.7.3 Law of Universal Absorption

With the time dynamics of the reflected and transmitted fields set up, the reflectance R, transmittance T and absorbance A are the coefficients satisfying:

$$R = \frac{\int_{-\infty}^{\infty} |\psi_R|^2 dt}{\int_{-\infty}^{\infty} |\psi_I|^2 dt} \qquad T = \frac{\int_{-\infty}^{\infty} |\psi_T|^2 dt}{\int_{-\infty}^{\infty} |\psi_I|^2 dt} \qquad A = 1 - R - T \tag{3.7.4}$$

After the SBEs are solved numerically and averaged, the reflected and transmitted fields are constructed respectively through Eq. (3.7.2) and Eq. (3.7.3) and consequently the optical coefficients of Eq. (3.7.4) are retrieved through their numerical

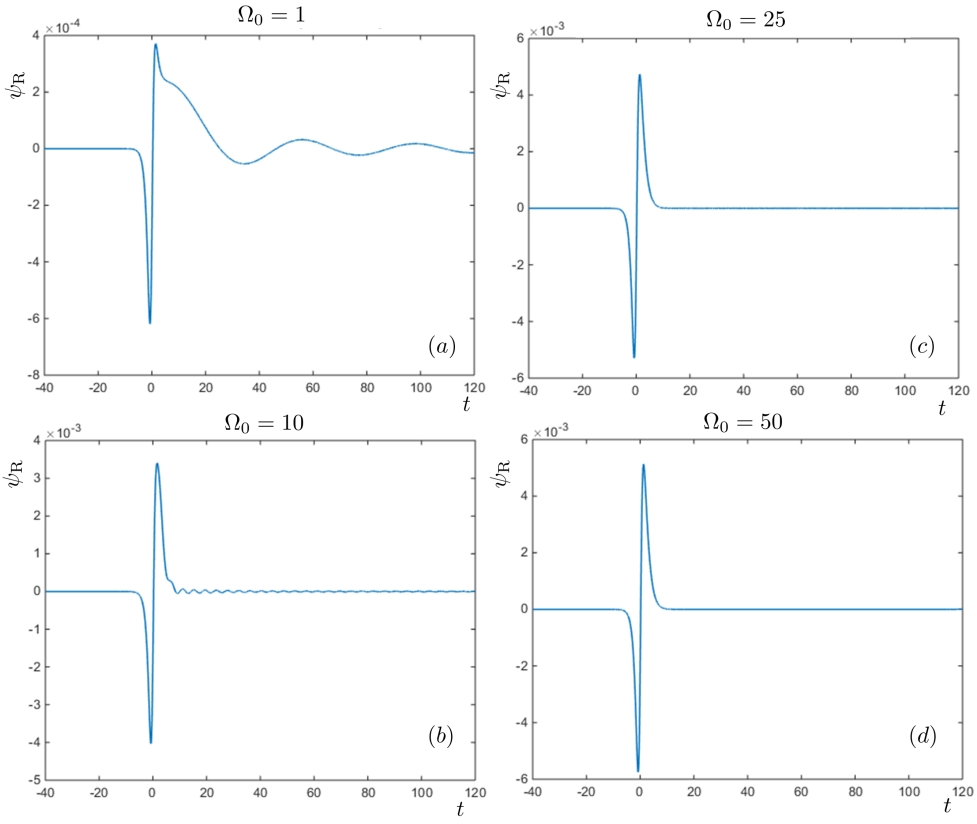

Figure 3.11: Role of the incident field central frequency Ω_0 on the reflected field for a sech pulse, of amplitude $\psi_0 = 1$

integration in time. If the variation of two independent coefficients, in this case the absorbance A and transmittance T, in terms of the field amplitude is shown, the same analysis regarding the linear-to-nonlinear regime transition holds.

Fig. (3.12) displays this exact setup, where the x axis shows the logarithm of the incident field intensity for easier visualisation. Firstly, the low-field intensity regime shows a plateau in the absorbance, shown in window (a), at exactly the value of the absorption $\pi\alpha_{\text{QED}} \approx 2.3\%$, confirming the law of universal absorption.

This is understandably also seen in (b), where the transmittance plots shows a plateau $T \approx 97.75\%$. Subsequent higher values of the field lead to a decrease of the absorbance and an increase of the transmittance. Field intensities for which this behaviour is no longer constant again set a critical transition value. This is seen for

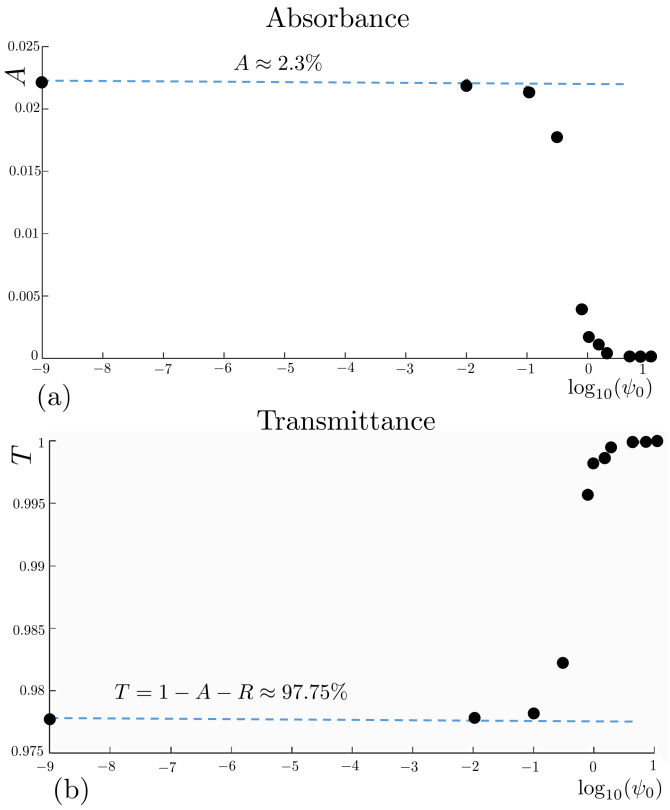

Figure 3.12: (a) Absorbance of the sample as a function of the log of the incident field intensity, as defined in Eq. (3.7.4). In the linear regime, a plateau at $A = 2.3\%$ confirms the law of universal absorption. (b) The same functional behaviour is found for the transmittance, where the plateau is now placed at $T \approx 97.75\%$.

$\log_{10} \psi_0 \approx -1$, agreeing with the previous estimate.

3.7.4 Third-harmonic Generation

The construction of the reflected and transmitted fields is also useful since their harmonic composition allows to infer the existence of *harmonic generation* in the sample, through the nonlinear polarisation. A validation of the claim of strong $\chi^{(3)}$ nonlinearities in graphene can also be found by using the SBEs.

For a clearly nonlinear incident field intensity $\psi_0 = 1$, the full-field SBEs (Eqs.-(3.4.7)-(3.4.8)) may be employed and appropriately averaged according to the prescription given in Eq. (3.7.1). The time-dependent of all fields in the sample may consequently be reconstructed. The Fourier-transform of the reflected and transmitted fields are plotted in terms of the harmonic order $(\omega/\omega_0) - 1$ in Fig. 3.13. The pump frequency is thus found at zero.

As it is expected from centrosymmetric media, no even harmonics are generated, meaning sample-produced optical fields should not have intensity peaks centred at odd positions on the harmonic order axis. This is indeed observed. Interestingly, the the third-harmonic components of the transmitted field is *higher* than its counterpart in the reflected field. This behaviour is characteristic of materials with a high $\chi^{(3)}$. In this setting, one may see that graphene indeed shows nonlinear features, starting at the first allowed nonlinear contribution, the third.

The reason why the full-field polarisation was considered is related to the fact that the third-harmonic enhancement of the transmitted field cannot be captured by SVEA conditions i.e. the peaks would overlap with the peak of the reflected field. It is therefore reasonable to assume that the full-field dynamics, containing the full oscillations of the optical fields, is necessary to capture signatures of ultrashort, intense pulses. In the next chapter, this treatment will be employed to graphene but using a different, yet related, set of equations to model the carrier dynamics – *the Dirac-Bloch Equations*.

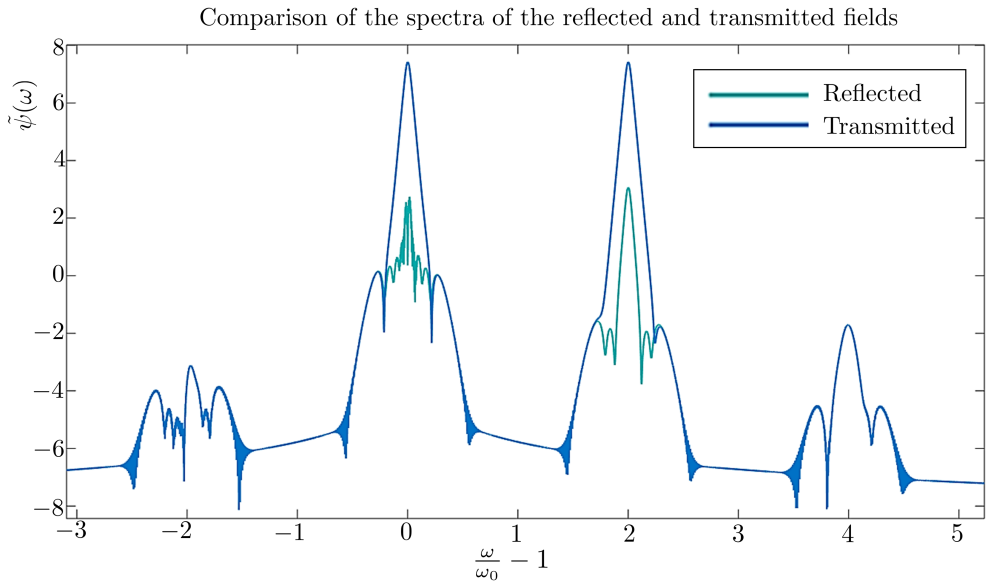

Figure 3.13: Fourier-transform of the reflected and transmitted fields generated from a graphene sample, plotted against the harmonic order. The pump frequency is found at 0.

Chapter 4

The Dirac-Bloch Equations

4.1 Overview

In the previous chapter, the SBEs were used to model the optical behaviour of graphene. Although the linear regime was well described by them, it was seen that the slowly-varying polarisation used in the derivation of the SBEs fails to predict third harmonic generation in graphene, a well-established result in the literature [46]. That in itself does not prove the unsuitability of the SBEs - it merely shows that full field should be considered. This is particularly true for ultrashort pulses, whose envelope does not resemble the full field, leading to a wrong estimation of the dynamics of the two-level system and hence of any optical quantity which depends on it.

In Chapter 2, the reduction of the Schrödinger Equation to the Dirac Equation was established. If next-nearest-neighbour effects are neglected and the dispersion is expanded around two special, *Dirac points*, located at the corners of the first Brillouin zone, the bands become degenerate there, changing linearly with the momentum of the electron - leading to the famous Dirac cones. For that reason, graphene is rather peculiar, what is known as a *zero-gap semiconductor*.

Given this realisation, an appropriate question to ask is *"why should graphene be*

modelled by the Semiconductor Bloch Equations?" One can wonder if the two-level systems modelling the carriers in graphene, obeying a completely different equation, given their pseudo-relativistic nature, are suitably described by the SBEs. This chapter tries to answer that question, by applying the machinery so far developed to a two-level system described by the Dirac Equation, leading to the *Dirac-Bloch Equations* (DBEs).

As will be seen in Section 4.5, both the SBEs and DBEs share a great deal of similarity. However, crucial differences lead to the prediction of an unusual phenomenon – the *dynamical centrosymmetry breaking*. This occurs when a graphene monolayer is illuminated by a short and intense pulse at normal incidence and can only be predicted by the DBEs [79, 80]. Due to the pulse-induced oscillations of the Dirac cones, a dynamical breaking of the layer's centrosymmetry takes place, leading to the generation of second harmonic waves.

This is a deeply unintuitive result, given the previous discussion of centrosymmetric media! In order to obtain it, a slightly different route will be taken: the photo-generated current will be analysed, as opposed to the macroscopic polarisation. With this procedure, more information can be accessed and, with that, a more rigorous understanding can be obtained when the predicted current output by both the SBEs and DBEs is compared and analysed.

4.2 Derivation

The Dirac-Bloch Equations are now derived. The starting point must obviously be the Dirac equation for a massless electron in graphene. To couple light, the minimal substitution of Eq. (2.4.12), explained in Section 2.4.2, is applied to the corresponding

Hamiltonian of the Dirac Equation, given in Eq. (2.3.10), leading to:

$$i\hbar\frac{d}{dt}\left|\Psi_{\mathbf{k}}^{\xi}(t)\right\rangle = \underbrace{v_{\mathrm{F}}\ \boldsymbol{\sigma}(\xi)\cdot\left(\mathbf{p}+\frac{e}{c}\mathbf{A}(t)\right)}_{H_{\mathbf{k}}^{\xi}(t)}\left|\Psi_{\mathbf{k}}^{\xi}(t)\right\rangle, \tag{4.2.1}$$

The operator on the right-hand side may be identified with the time-dependent Hamiltonian $H_{\mathbf{k}}^{\xi}(t)$. In this formalism, both valleys – $\mathbf{K}$ ($\xi=+1$) and $\mathbf{K}'$ ($\xi=-1$) – are simultaneously considered through the inclusion of the valley degree of freedom ξ. As usual, $v_{\mathrm{F}}\approx c/300$ is the Fermi velocity in a graphene monolayer, c the speed of light in vacuum, $-e$ is electron charge, $\boldsymbol{\sigma}(\xi)\equiv(\xi\sigma_x,\sigma_y)$ a valley-dependent 2D Pauli-matrix vector. In this way, and ignoring the field dependence for now i.e. by setting $\mathbf{A}(t)=0$, one can see that the Hamiltonian of a valley is related to the other simply by making the transformation $p_x\mapsto -p_x$. The time-dependent 2-spinor $\left|\Psi_{\mathbf{k}}^{\xi}(t)\right\rangle$ is the solution to the equation and represents electrons in the conduction and valence bands for a specific electronic momentum $\mathbf{p}\equiv\hbar\mathbf{k}$.

This Hamiltonian has been minimally-coupled to light. The composition on the momentum that originates from it leads to the promotion of the time-dependent momentum to the field-dependent canonical momentum, with the following polar representation:

$$\mathbf{p}\mapsto\mathbf{p}+\frac{e}{c}\mathbf{A}(t)\equiv\boldsymbol{\pi}_{\mathbf{k}}(t)\Leftrightarrow\begin{cases}\phi_{\mathbf{k}}\mapsto\arctan\left[\frac{p_y}{p_x+\frac{e}{c}A(t)}\right]\equiv\theta_{\mathbf{k}}(t)\\ |\mathbf{p}|\mapsto\sqrt{\left[p_x+\frac{e}{c}A(t)\right]^2+p_y^2}\equiv|\boldsymbol{\pi}_{\mathbf{k}}(t)|\end{cases} \tag{4.2.2}$$

The phase $\theta_{\mathbf{k}}(t)$ is termed the *dynamical angle*. The electric field $\mathbf{E}\equiv-(1/c)\dot{\mathbf{A}}$ is assumed linearly polarised. Without loss of generality, since the dispersion is radial, such polarisation may be assumed to be along the arbitrary $\hat{x}$ axis i.e. $\mathbf{A}(t)=(A(t),0,0)$. As before, normal incidence conditions are assumed, as well as the Coulomb gauge given by the condition $\nabla\cdot\mathbf{A}=0$ and explained in Section 2.4.2.

A very subtle difference, which will only be lightly touched for now and expanded in Section 4.5, is that, unlike the treatment applied to the OBEs, and consequently the SBEs, the treatment in the DBEs is non-perturbative. Mathematically, this means that the solution to Eq. (4.2.1) must be obtained with the *presence of the field*. The concept of eigenstates in a time-dependent setting is a tricky one, as by definition these are stationary states. This fact presents a challenge!

To see this, the field-free Hamiltonian is considered, i.e. with $\mathbf{A} = 0$. Then, since the Hamiltonian is time-independent, the solution to Eq. (4.2.1) is simply given by the evolution operator $U_{\mathbf{k}}(t) = e^{-\frac{it}{\hbar}H^{\xi}_{\mathbf{k}}}$, meaning $|\Psi^{\xi}_{\mathbf{k}}(t)\rangle = U_{\mathbf{k}}(t)\,|\psi^{\xi}_{\mathbf{k}}\rangle$, for an initial spinor $|\psi^{\xi}_{\mathbf{k}}\rangle$.

The reason is rather simple: if the evolution operator is Taylor-expanded:

$$U_{\mathbf{k}}(t) = \sum_{j=0}^{\infty} \frac{1}{j!}\left(\frac{-it}{\hbar}\right)^{j}\left(H^{\xi}_{\mathbf{k}}\right)^{j} \tag{4.2.3}$$

it can be conveniently expressed as a matrix by using an orthonormal basis comprised of the Hamiltonian eigenstates $|u^{\xi}_{\lambda,\mathbf{k}}\rangle$, i.e. two states ($\lambda = -1, 1$) for which $H^{\xi}_{\mathbf{k}}\,|u^{\xi}_{\lambda,\mathbf{k}}\rangle = \epsilon^{\xi}_{\lambda,\mathbf{k}}\,|u^{\xi}_{\lambda,\mathbf{k}}\rangle$ and $\langle u^{\xi}_{\lambda',\mathbf{k}}|u^{\xi}_{\lambda,\mathbf{k}}\rangle = \delta_{\lambda,\lambda'}$.

Given the Hamiltonian representation derived in Eq. (3.2.5), naturally diagonal, the computation of $U_{\mathbf{k}}(t)$ follows directly:

$$\begin{aligned} U_{\mathbf{k}}(t) &= \sum_{j=0}^{\infty} \frac{1}{j!}\left(-\frac{it}{\hbar}\right)^{j}\left(\sum_{\lambda}\left(\epsilon^{\xi}_{\lambda,\mathbf{k}}\right)^{j}|u^{\xi}_{\lambda,\mathbf{k}}\rangle\,\langle u^{\xi}_{\lambda,\mathbf{k}}|\right) \\ &= \sum_{\lambda} e^{-\frac{it}{\hbar}H^{\xi}_{\mathbf{k}}}\,|u^{\xi}_{\lambda,\mathbf{k}}\rangle\,\langle u^{\xi}_{\lambda,\mathbf{k}}|\,. \end{aligned} \tag{4.2.4}$$

This representation clearly satisfies the required time evolution dictated by the solution: for a general, time-independent $|\psi^{\xi}_{\mathbf{k}}\rangle = \sum_{\lambda'} c^{\xi}_{\lambda'} |u^{\xi}_{\lambda',\mathbf{k}}\rangle$:

$$\begin{aligned} U_{\mathbf{k}}(t) |\psi^{\xi}_{\mathbf{k}}\rangle &= e^{-\frac{it}{\hbar} H^{\xi}_{\mathbf{k}}} \sum_{\lambda,\lambda'} c^{\xi}_{\lambda'} |u^{\xi}_{\lambda,\mathbf{k}}\rangle \langle u^{\xi}_{\lambda,\mathbf{k}} | u^{\xi}_{\lambda',\mathbf{k}}\rangle \\ &= U_{\mathbf{k}}(t) |\psi^{\xi}_{\mathbf{k}}\rangle = |\Psi^{\xi}_{\mathbf{k}}(t)\rangle \end{aligned} \tag{4.2.5}$$

The reason why this solution may be obtained is of course due to the time-independence of the eigenstates. The addition of the electromagnetic potential $\mathbf{A}(t)$ makes the Hamiltonian time-dependent and the reasoning just exposed breaks down. Naively, one could guess that the solution would be given by the integrating factor $I(t) = e^{\int_{-\infty}^{t'} H^{\xi}_{\mathbf{k}}(t')dt'}$. However, the Hamiltonian is now a matrix, which does not commute at different times and such quantity seems hard, if not impossible, to retrieve.

Unlike what one could suppose, this issue is not solved by considering another *dynamical picture* (or representation) of the system. It is often the case that such a representation change does not allow the problem to be solved. For these reasons, general analytical solutions of Eq. (4.2.1) are not known.

However, a procedure, originally outlined in two seminal papers by Ishikawa [81, 82], may be applied to yield an ansatz i.e. a formal guess which solves Eq. (4.2.1). Conceptually, it is not terribly different to what was developed so far: the eigenstates will be generalised to their instantaneous counterparts and the evolution phase factor will now depend on time in such a way that the Dirac Equation is satisfied.

The instantaneous eigenstates are spinors which satisfy

$$H^{\xi}_{\mathbf{k}}(t) |u^{\xi}_{\lambda,\mathbf{k}}(t)\rangle = \epsilon^{\xi}_{\lambda,\mathbf{k}}(t) |u^{\xi}_{\lambda,\mathbf{k}}(t)\rangle \tag{4.2.6}$$

where the instantaneous energy $\epsilon^{\xi}_{\lambda,\mathbf{k}}(t)$ is now time-dependent too. In order to obtain both, the Hamiltonian is first written in matrix form :

$$\begin{aligned} H^{\xi}_{\mathbf{k}}(t) &= \begin{pmatrix} 0 & v_{\mathrm{F}}(\xi\pi_x(t) - i\pi_y(t)) \\ v_{\mathrm{F}}(\xi\pi_x(t) + i\pi_y(t)) & 0 \end{pmatrix} \\ &= \xi v_{\mathrm{F}}|\boldsymbol{\pi}_{\mathbf{k}}(t)| \begin{pmatrix} 0 & e^{-i\xi\theta_{\mathbf{k}}(t)} \\ e^{i\xi\theta_{\mathbf{k}}(t)} & 0 \end{pmatrix} \end{aligned} \tag{4.2.7}$$

where the canonical momentum polar coordinates were introduced through the identity $\xi\pi_x(t) - i\pi_y(t) = \xi|\boldsymbol{\pi}_{\mathbf{k}}(t)|e^{-i\xi\theta_{\mathbf{k}}(t)}$.

Two symmetric dispersion branches arising from it take the form:

$$\epsilon^{\xi}_{\lambda,\mathbf{k}}(t) = \lambda v_{\mathrm{F}}|\boldsymbol{\pi}_{\mathbf{k}}(t)| = \lambda v_{\mathrm{F}}\sqrt{\left(p_x + \frac{e}{c}A(t)\right)^2 + p_y^2} \tag{4.2.8}$$

This time-dependent dispersion is globally equivalent across both valleys and is plotted in Fig 4.2. For this reason, the positive branch of the dispersion, equal for both valleys, will be denoted as $\epsilon_{\mathbf{k}}$ i.e. $\epsilon^{\xi}_{\lambda,\mathbf{k}} = \lambda\epsilon_{\mathbf{k}}$. Unsurprisingly, the instantaneous eigenstates are not formally different to the eigenstates found for the free Dirac fermions in Eq. (2.3.13), albeit generalised to any valley ξ. The instantaneous eigenstate is now decomposed into its upper and lower components:

$$|u^{\xi}_{\lambda}(t)\rangle \equiv \begin{pmatrix} \varphi^{\xi}_{\lambda,\mathbf{k}}(t) \\ \phi^{\xi}_{\lambda,\mathbf{k}}(t) \end{pmatrix} \tag{4.2.9}$$

in turn yielding the following system of equations to solve:

$$\begin{cases} \xi e^{-i\xi\theta_{\mathbf{k}}}\phi^{\xi}_{\lambda,\mathbf{k}} = \lambda\varphi^{\xi}_{\lambda,\mathbf{k}} \\ \xi e^{i\xi\theta_{\mathbf{k}}}\varphi^{\xi}_{\lambda,\mathbf{k}} = \lambda\phi^{\xi}_{\lambda,\mathbf{k}} \end{cases} \tag{4.2.10}$$

Both amplitudes must therefore satisfy $\varphi_\lambda^\xi = \xi e^{-i\xi\theta_\mathbf{k}}\phi_\lambda^\xi$. It is convenient to explicitly include the dynamical angle in the spinor. To do that, the lower component may be fixed to $\phi_\lambda^\xi \equiv \lambda e^{-i\xi\theta_\mathbf{k}/2}$. Noting that $\lambda^2 = \xi^2 = 1$, this choice leads to normalised states satisfying $\langle u_{\lambda,\mathbf{k}}^\xi(t)|u_{\lambda',\mathbf{k}}^\xi(t)\rangle = \delta_{\lambda\lambda'}$:

$$|u_{\lambda,\mathbf{k}}^\xi(t)\rangle = \frac{1}{\sqrt{2}}\begin{pmatrix}\xi e^{-i\xi\theta_\mathbf{k}(t)/2}\\ \lambda e^{i\xi\theta_\mathbf{k}(t)/2}\end{pmatrix} \tag{4.2.11}$$

Considering the discussion that lead to the construction of the spinor when applying the tight-binding model for graphene in Section 2.2.2, it can be seen that the amplitude of the upper and lower components, which correspond to each sublattice A and B, are the same. This is a statement of sublattice equivalence and leads to the invariance of physics under each sublattice. The next chapter will address a way to break such symmetry.

Having obtained, in a sense, a time-dependent basis, the natural question to ask is: *how can a solution* $|\Psi_\mathbf{k}^\xi(t)\rangle$ *be obtained?* A sensible *ansatz* is provided upon constructing the superposition:

$$|\Psi_\mathbf{k}^\xi(t)\rangle = \sum_\lambda c_{\lambda,\mathbf{k}}^\xi(t)\,|u_{\lambda,\mathbf{k}}^\xi(t)\rangle\, e^{-i\lambda\Omega_\mathbf{k}(t)} \tag{4.2.12}$$

where an additional yet-to-be-determined phase $\Omega_\mathbf{k}(t)$ was added. In this fashion, the field interaction is accounted for by generalising the field-free eigenstates to a time-dependent ansatz. After inserting this ansatz in Eq. (4.2.1), its left-hand side becomes:

$$i\hbar\frac{d}{dt}|\Psi_\mathbf{k}^\xi\rangle = i\hbar\sum_\lambda\left(\dot{c}_{\lambda,\mathbf{k}}^\xi\,|u_{\lambda,\mathbf{k}}^\xi\rangle + c_{\lambda,\mathbf{k}}^\xi\,|\dot{u}_{\lambda,\mathbf{k}}^\xi\rangle - i\lambda\dot{\Omega}_\mathbf{k}c_{\lambda,\mathbf{k}}^\xi\,|u_{\lambda,\mathbf{k}}^\xi\rangle\right)e^{-i\lambda\Omega_\mathbf{k}} \tag{4.2.13}$$

As for the right-hand side:

$$H^{\xi}_{\mathbf{k}} \left|\Psi^{\xi}_{\mathbf{k}}\right\rangle = H^{\xi}_{\mathbf{k}} \sum_{\lambda} c^{\xi}_{\lambda,\mathbf{k}} \left|u^{\xi}_{\lambda,\mathbf{k}}\right\rangle e^{-i\lambda\Omega_{\mathbf{k}}} = \sum_{\lambda} \epsilon^{\xi}_{\lambda,\mathbf{k}} c^{\xi}_{\lambda,\mathbf{k}} \left|u^{\xi}_{\lambda,\mathbf{k}}\right\rangle e^{-i\lambda\Omega_{\mathbf{k}}} \tag{4.2.14}$$

it is clear that the third term in Eq. (4.2.13) cancels with the term from Eq. (4.2.14) if $\hbar\dot{\Omega}_{\mathbf{k}} = \epsilon_{\mathbf{k}}$. This phase, termed *dynamical phase*, is then:

$$\begin{aligned} \Omega_{\mathbf{k}}(t) &= \frac{1}{\hbar}\int_{-\infty}^{t} \epsilon_{\mathbf{k}}(t')dt' \\ &= \frac{v_{\mathrm{F}}}{\hbar}\int_{-\infty}^{t} \sqrt{\left(p_x + \frac{e}{c}A(t')\right)^2 + p_y^2}\; dt' \end{aligned} \tag{4.2.15}$$

Now, noting that $\left|\dot{u}^{\xi}_{\bar{\lambda}\mathbf{k}}\right\rangle = (-i\xi\dot{\theta}_{\mathbf{k}}/2)\left|u^{\xi}_{-\bar{\lambda},\mathbf{k}}\right\rangle$, the first two terms in Eq. (4.2.13) can be pre-multiplied by $\langle u^{\xi}_{\bar{\lambda},\mathbf{k}}|$. Then, using the state orthonormality, the sum over $\lambda \in \{\bar{\lambda}, -\bar{\lambda}\}$ leads to the condition:

$$\dot{c}^{\xi}_{\bar{\lambda}} = \left(\frac{i\xi\dot{\theta}_{\mathbf{k}}}{2}\right) c^{\xi}_{-\bar{\lambda}} e^{2i\bar{\lambda}\Omega_{\mathbf{k}}} \tag{4.2.16}$$

As per usual, the coefficients dynamical variables are converted the optically-relevant variables:

$$w^{\xi}_{\mathbf{k}} \equiv \left|c^{\xi}_{+,\mathbf{k}}\right|^2 - \left|c^{\xi}_{-,\mathbf{k}}\right|^2 \qquad (\textit{inversion}) \tag{4.2.17}$$

$$q^{\xi}_{\mathbf{k}} \equiv c^{\xi}_{+,\mathbf{k}} \left(c^{\xi}_{-,\mathbf{k}}\right)^* e^{-2i\Omega_{\mathbf{k}} + i\omega_0 t} \qquad (\textit{microscopic polarisation}) \tag{4.2.18}$$

In the framework of the DBEs, the variable $\rho^{\xi}_{\mathbf{k}} \equiv c^{\xi}_{+,\mathbf{k}} \left(c^{\xi}_{-,\mathbf{k}}\right)^*$, previously used in the OBEs and SBEs, is termed *coherence*. The additional phase just introduced allows the DBEs to be conveniently written in same form as the OBEs. As usual, ω_0 denotes the central frequency of the input pulse. The derivatives of Eqs. (4.2.17)-(4.2.18) are

straightforwardly obtained as:

$$\begin{aligned} \dot{w}_{\mathbf{k}}^{\xi} &= \dot{c}_{+,\mathbf{k}}^{\xi}\left(c_{+,\mathbf{k}}^{\xi}\right)^{*} + c_{+,\mathbf{k}}^{\xi}\left(\dot{c}_{+,\mathbf{k}}^{\xi}\right)^{*} - \dot{c}_{-,\mathbf{k}}^{\xi}\left(c_{-,\mathbf{k}}^{\xi}\right)^{*} - c_{-,\mathbf{k}}^{\xi}\left(\dot{c}_{-,\mathbf{k}}^{\xi}\right)^{*} \\ \dot{q}_{\mathbf{k}}^{\xi} &= i(\omega_0 - 2\dot{\Omega}_{\mathbf{k}})q_{\mathbf{k}}^{\xi} + \left(\dot{c}_{+,\mathbf{k}}^{\xi}(c_{-,\mathbf{k}}^{\xi})^{*} + c_{+,\mathbf{k}}^{\xi}(\dot{c}_{-,\mathbf{k}}^{\xi})^{*}\right) e^{i(\omega_0 t - 2\Omega_{\mathbf{k}})} \end{aligned} \tag{4.2.19}$$

Using the condition in Eq. (4.2.16), the *Dirac-Bloch Equations* for monolayer graphene are finally obtained as:

$$\dot{q}_{\mathbf{k}}^{\xi} + i(2\dot{\Omega}_{\mathbf{k}} - \omega_0 - i\gamma_2)q_{\mathbf{k}}^{\xi} + \frac{i\xi}{2}w_{\mathbf{k}}^{\xi}\dot{\theta}_{\mathbf{k}}e^{i\omega_0 t} = 0, \tag{4.2.20}$$

$$\dot{w}_{\mathbf{k}}^{\xi} + \gamma_1(w_{\mathbf{k}}^{\xi} - w_{\mathbf{k}}^{0}) + i\xi\dot{\theta}_{\mathbf{k}}\left(q_{\mathbf{k}}^{\xi}e^{-i\omega_0 t} - q_{\mathbf{k}}^{\xi^{*}}e^{i\omega_0 t}\right) = 0, \tag{4.2.21}$$

The dephasing effects are, as usual, included phenomenologically through the coefficients $\gamma_{1,2} \equiv 1/T_{1,2}$ whereas the effect of intrinsic, field-independent parameters such as temperature and chemical potential can be incorporated in a momentum-dependent equilibrium value of the populations $w_{\mathbf{k}}^{0}$, following a methodology outlined in Section 3.5.2.

Following the discussion in the same section, these equations do not take into account any kind of effective Coulomb interactions amongst the carriers. Despite that, no approximations were applied in obtaining the dynamics of the coefficients. This fact presents a remarkable possibility: to express the electric current generated in the sample as a consequence of the optical excitation in an exact way. It is expected that the dynamics of two-level system, described by the evolution of $w_{\mathbf{k}}^{\xi}$ and $q_{\mathbf{k}}^{\xi}$, determines such a current. This is indeed verified in the next section, where the link between the evolution of the dynamical variables and the photo-generated current is established. The price to pay for this exact form is, of course, that no analytical solutions of the DBEs may be found as was the case for the SBEs in the linear regime. One must therefore apply reliable numerical routines to solve the DBEs.

4.3 The Relationship between the SBEs and DBEs

At this stage, the difference between the Semiconductor Bloch equations derived in Section 3.4, a mere cosmetic conceptual adjustment to the Optical Bloch equations given in Section 3.3 has not been justified beyond the introduction of the instantaneous eigenstates that resulted from the minimal substitution in the Hamiltonian of Eq. (4.2.1). It may even feel like such a distinction is based on theoretical pedantry alone. However, this feature is crucial in understanding the discrepancies in the current that is predicted by both models.

What exactly makes the SBEs and DBEs different? The answer boils down to the way the wavefunction is obtained and how it, in turn, relates to observables. The philosophy underlying the DBEs must be contrasted with the one employed in the SBEs. The Hamiltonian used in Eq. (4.2.1), unlike the OBEs and SBEs, is not understood as a "free" plus "perturbed" one, of the form $H_{\mathbf{k}}(t) = H^0_{\mathbf{k}} + H^{\text{int}}_{\mathbf{k}}(t)$ but rather as a non-separable time-dependent system, where the dependence comes from the *composition* $\mathbf{k} \mapsto \mathbf{k} + e/(\hbar c)\mathbf{A}(t)$. Mathematically, this situation is reflected in the structure of the wavefunction itself, which is accounted for by *all* contributions in the Hamiltonian, as opposed to using the field-free wavefunction.

An observable $\mathcal{O}(t)$ is thus obtained as $\langle \Psi^{\xi}_{\mathbf{k}}(t)|\hat{\mathcal{O}}(t)|\Psi^{\xi}_{\mathbf{k}}(t)\rangle$, where the spinor solves the full Hamiltonian, as opposed to the perturbative form $\langle \Psi^{\xi}_{\mathbf{k}}|\hat{\mathcal{O}}(t)|\Psi^{\xi}_{\mathbf{k}}\rangle$, where the latter spinor is a solution to the field-free Hamiltonian.

The SBEs are *exactly* a limiting case of the DBEs. In order to reduce the DBEs in Eqs. (4.2.20-4.2.21) to the SBEs in Eqs.(3.4.7)-(3.4.8), one must *neglect* the contribution of the photon momentum $(e/c)A(t)$ in the quantities $\dot{\Omega}_{\mathbf{k}}$ and $\dot{\theta}_{\mathbf{k}}$, obtaining exactly the SBEs used, for instance, in Ref. [83]. This reduction is *never* acceptable in gapless media as will be shown shortly.

This difference leads, of course, to some differentiating features of the DBEs. These

may be appreciated by comparing the full-field SBEs in to the DBEs. After an explicit computation from the definition of the dynamical angle given in Eq. (4.2.2) is performed:

$$\dot{\theta}_{\mathbf{k}} = \frac{ep_y E(t)}{|\boldsymbol{\pi}_{\mathbf{k}}(t)|^2} = \frac{e\sin\theta_{\mathbf{k}} E(t)}{|\boldsymbol{\pi}_{\mathbf{k}}(t)|}, \tag{4.3.1}$$

the function that multiplies the electric field may be interpreted as the dipole moment:

$$\mu^{\xi}_{\mathbf{k}}(t) = \xi\frac{\dot{\theta}_{\mathbf{k}}(t)}{2E(t)}. \tag{4.3.2}$$

Consequently, if $A(t) = 0$ is set, the time-independent dipole moment of the SBEs is obtained. Additionally, it is clear that the SVEA-approximated dipole moment calculated in Eq. (2.4.38) is obtained by evaluating the SBE dipole moment when the electronic momentum is resonant with the photon's i.e. whenever $|\mathbf{k}| = \omega_0/(2v_{\mathrm{F}}) \equiv |\mathbf{k}^0|$:

$$\mu^{\xi}_{\mathbf{k}}(t) = \underbrace{\frac{\xi}{2}\frac{ep_y}{\left((p_x + \frac{e}{c}A(t))^2 + p_y^2\right)}}_{\text{DBEs}} \xrightarrow[A(t)=0]{} \underbrace{\frac{\xi e}{2}\frac{\sin\phi_{\mathbf{k}}}{|\mathbf{k}|}}_{\text{SBEs}} \xrightarrow[\substack{\mathbf{k}=\mathbf{k}^0\\ \mathbf{K}\text{valley}}]{} \underbrace{\frac{ev_{\mathrm{F}}}{\omega_0}\sin\phi_{\mathbf{k}}}_{\text{SVEA}-\text{SBEs}} \tag{4.3.3}$$

The dipole moment in the DBEs is a time-dependent quantity – meaning that the dipole moment is temporally oscillating with the pulse. Given the lack of applications in any other realistic physical situations in the literature, this is very unusual in the theory of two-level systems. Furthermore, the light-matter coupling is not attained simply by incorporating the electric field in the equations, as was done in the OBEs and SBEs; the driving term now exhibits a complex coupling that includes both the electric field $\mathbf{E}$ and the vector potential $\mathbf{A}$.

As an illustration of the point, the macroscopic polarisation is shown in Fig. 4.1 for the case of an extremely ultrashort ($\Omega_0 = 1$) and intense ($\psi_0 = 1$) pulse. (a) shows its real part, while (b) its imaginary part. The red line shows the prediction of the DBEs when using the SVEA dipole moment. The internal oscillations, dictated by

the time dependence of the full-field dipole moment and shown by the blue plots, are absent from the SVEA approximation. Consequently, the harmonic composition of the polarisation must therefore show qualitative differences.

Additionally, the frequency detuning between a specific two-level system with

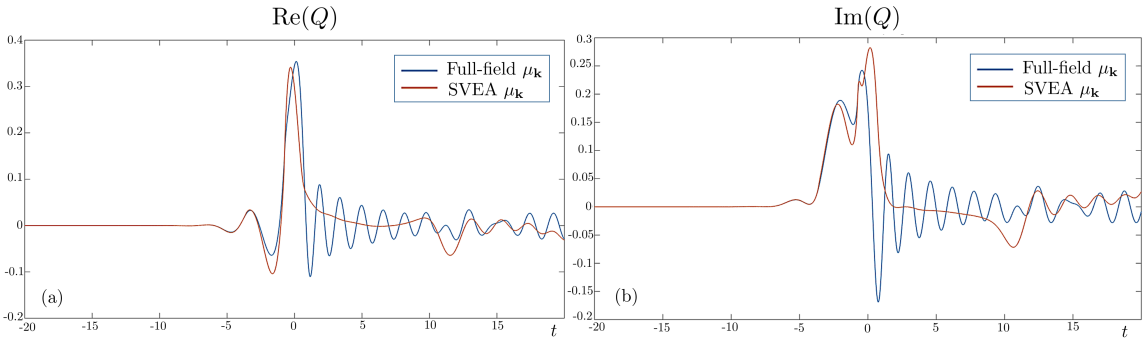

Figure 4.1: Comparison of the macroscopic polarisation predicted by the DBEs, when considering a full-field (blue) or SVEA (red) electric dipole moment. The sample is probed with an electric field with parameters $\Omega_0 = 1$ and $\psi_0 = 1$.

wavevector $\mathbf{k}$ and the pulse frequency ω_0 is also oscillating in time as:

$$2\dot{\Omega}_{\mathbf{k}}(t) - \omega_0 = \frac{2v_{\mathrm{F}}}{\hbar}\sqrt{\left(p_x + \frac{e}{c}A(t)\right)^2 + p_y^2} - \omega_0 \tag{4.3.4}$$

as seen in the second term in Eq. (4.2.20). In other words, the pulse itself modulates the band structure continuously, leading to *global dynamical oscillations* of the Dirac cone. This feature stems from the use of the dynamical phase of Eq. (4.2.15). It is expected that this rather non-trivial phase affects the generation of currents. The confirmation will be given when the significance of such a modulation in the generation of new harmonics will be given in Section 4.5, where both models are compared.

4.3.1 Dynamical Centrosymmetry Breaking

A fundamental feature found in the DBEs that must be discussed before proceeding to any comparison between the models is what will be termed a *dynamical centrosym-*

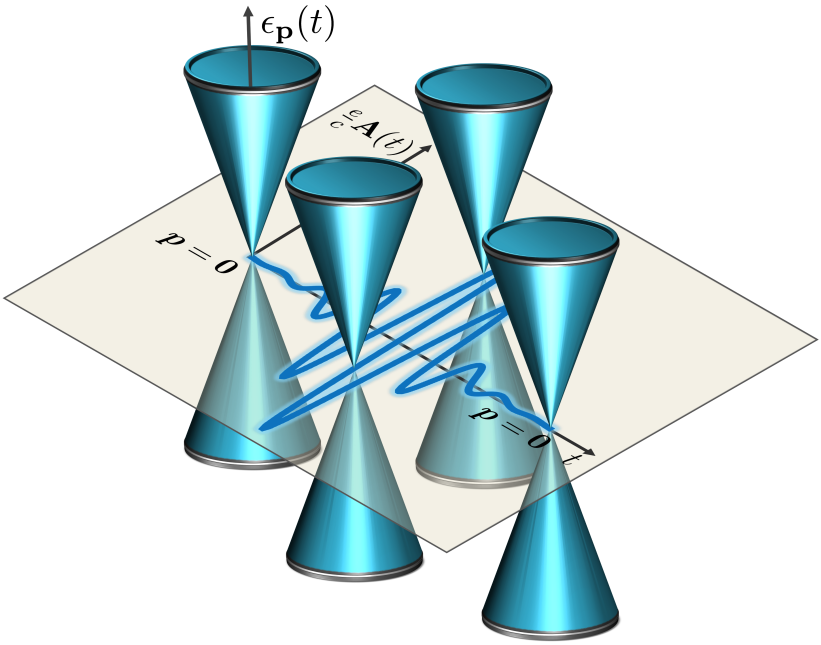

Figure 4.2: Sketch showing the dynamical centrosymmetry breaking mechanism in graphene, when illuminated by short, intense pulses at normal incidence. The Dirac cone is shaken from the $p_x = p_y = 0$ position by the time-dependent pulse momentum $\frac{e}{c}A(t)$

metry breaking mechanism. As was seen in the previous section, the fundamental difference between the SBEs and DBEs is due to the role of the photon momentum. The instantaneous energy eigenvalues derived in Eq. (4.2.8) show the global time dependence for all $\mathbf{k}$ states.

This view is to be contrasted with the time-independent dispersion – found in Eq. (2.3.12) – used in the SBEs. When $A(t) = 0$, one recovers the unperturbed Dirac cone band structure $\epsilon_{\lambda,\mathbf{k}} = \lambda\hbar v_{\mathrm{F}}|\mathbf{k}|$. However, for $A(t) \neq 0$, the whole Dirac cone oscillates around the $\mathbf{k} = 0$ point together with the pulse along the p_x direction due to the pulse polarisation along $\hat{x}$.

A graphical depiction of this oscillation is shown in the sketch of Fig. 4.2. When the Dirac cone is displaced the inversion symmetry in momentum space, namely $\mathbf{k} \to -\mathbf{k}$, is temporarily broken, and so is the inversion symmetry in real space $\mathbf{r} \to -\mathbf{r}$, leading to a *dynamical breaking of the centrosymmetry, induced by the pulse*

itself. The extent of the shift depends, of course, on the field intensity. Thefore, one expects substantial dynamical predictions for intense pulses. The linear regime is thus still well-described by the SBEs, where this effect is manifestly absent.

Most light-matter interactions may be treated perturbatively. In contrast, it will be seen that, if the pulse is intense enough, this situation leads to the possibility of radiating second-harmonic-generated radiation at normal incidence, a situation which is normally forbidden due to the supposed centrosymmetry of the graphene lattice.

It must be categorically emphasized that this mechanism, which will in turn lead to the prediction of second-harmonic waves, is not the only one through which such harmonics may be generated. Many other mechanisms are well established in the literature and proposed through a myriad of techniques, encapsulated, for instance, in the well-known *photon-drag effect*. It is a relativistic phenomenon in which the pulse is illuminated obliquely on the graphene layer. In this setting, the photon-drag effect uses perturbative methods and also leading to the prediction of THz and SHG radiation effects [84, 85]. Furthermore, electric field in-plane biasing [86] and quadrupole interactions [87] have also shown the possibility of creating such harmonics.

The novelty of these results relies on the existence of a theoretical mechanism supported by the Dirac-Bloch formalism which, in the extreme nonlinear optical regime, predicts previously-forbidden even harmonics to be generated at *normal incidence* in centrosymmetric relativistic-like media.

4.3.2 Shortcomings of SBEs

More relevantly, the SBEs are often inadequate when studying gapless Dirac media like graphene and, for pulses that are short or intense enough, they will also fail even in the case of gapped Dirac media such as MoS_2, WSe_2 and phosphorene [88].

The study of gapped relativistic dispersions, which will eventually lead to the generalisation of the DBEs to accommodate for a gap, is the subject-matter of Chapter 5.

In order to show precise conditions for the failure of SBEs, the model of Eqs. (4.2.20)-(4.2.21) is extended to a gapped layer solely for the purpose of obtaining its dispersion. For simplicity, only the **K** valley is considered. In order to do this, a mass term in Eq. (4.2.1), proportional to the energy gap Δ is inserted and only the **K** valley is considered i.e. $\xi = 1$:

$$i\hbar\frac{d}{dt}\left|\Psi_{\mathbf{k}}(t)\right\rangle = \left[v_{\mathrm{F}}\ \boldsymbol{\sigma}\cdot\left(\mathbf{p}+\frac{e}{c}\mathbf{A}\right)+\frac{\Delta}{2}\sigma_z\right]\left|\Psi_{\mathbf{k}}(t)\right\rangle, \tag{4.3.5}$$

where σ_z is the diagonal Pauli matrix.

From Eq. (4.3.5), one can write straightforwardly the instantaneous energy eigenstates as

$$\epsilon_{\lambda,\mathbf{k}}(t) = \lambda v_{\mathrm{F}}\sqrt{(p_x+\frac{e}{c}A(t))^2+p_y^2+\left(\frac{\Delta}{2v_{\mathrm{F}}}\right)^2} \tag{4.3.6}$$

In the vicinity of the band gap centre ($p_x = p_y = 0$), the contribution of the photon momentum can be neglected only for those pulse amplitudes satisfying $|eA/c| \ll \Delta/2v_{\mathrm{F}}$. In this case, the DBEs are identical to the SBEs, since in this way the time dependence of the frequency detuning and the dipole moment $\mu_{\mathbf{k}}$ are eliminated. Therefore, the SBEs are a valid description of light-matter interaction in gapped 2D Dirac media only when the pulse spectrum does not overlap substantially with the Dirac point, or when the intensity of the pulse is not too large with respect to the gap energy.

The above condition for the SBEs to be approximately valid can be translated into a condition for the input pulse intensity: $I \ll I_{\mathrm{cr}}$, where

$$I_{\mathrm{cr}} \equiv \frac{1}{8}c\epsilon_0\left(\frac{\omega_0\Delta}{ev_{\mathrm{F}}}\right)^2. \tag{4.3.7}$$

If the intensity of the pulse is such that $I \geq I_{\text{cr}}$, the SBE description loses its validity. To make things worse, even for low-intensity light, short pulses satisfying the condition $\omega_0 t_0 < \Delta/(4\hbar\omega_0)$ will overlap too much with the Dirac point, also leading to the breaking of the validity of the SBEs.

Therefore the SBEs description of gapped Dirac layers is approximately valid only if pulses are neither too short nor too intense. It is crucial to observe that for gapless media such as graphene, for which $\Delta = 0$, *it is in principle never possible to accurately describe light-matter interactions via the SBE*, since the condition $I \ll I_{\text{cr}}$ can never be satisfied.

4.4 Currents

Given the considerations that established that the treatment employed in the DBEs is nonperturbative in nature, since the full field is accounted for (as opposed to the usual field expansion and order truncation methods shown in Section 2.4.2), as well as the full pulse properties (as opposed to slowly-varying envelope / rotating wave approximation conditions), a desirable quantity to study is the two-dimensional current generated across the sample. Although the macroscopic polarisation produced in the sample provides many crucial insights, the photo-generated current allows for far more detailed information.

In the same spirit as the one used for obtaining the macroscopic polarisation in terms of the microscopic polarisation, the physical, *macroscopic* current generated in the sample may be obtained by adequately averaging over all *microscopic* current contributions generated by each momentum state.

This method ultimately allows an analysis of the system response to be obtained when probed in extreme nonlinear optical conditions, without any field expansion.

The procedure to attain this goal is shown in this section.

In order to obtain the time dynamics of the photo-generated current, one proceeds by first determining the μ-component ($\mu = x, y$) of the current contribution of a particular momentum state $\mathbf{p}$ in a valley ξ, in time domain. For consistency purposes, such contribution to the current is termed a *microscopic current* $j^{\xi}_{\mu,\mathbf{k}}$ and can be obtained by applying a suitable current density operator $\hat{j}^{\xi}_{\mu}$ to the ansatz $|\Psi^{\xi}_{\mathbf{k}}\rangle$ given in Eq. (4.2.12), which reads:

$$\begin{aligned}\langle\Psi^{\xi}_{\mathbf{k}}|\hat{j}^{\xi}_{\mu}|\Psi^{\xi}_{\mathbf{k}}\rangle &= \sum_{\lambda,\lambda'}(c^{\xi}_{\lambda})^{*}c^{\xi}_{\lambda'}e^{-i(\lambda'-\lambda)\Omega_{\mathbf{k}}}\,\langle u^{\xi}_{\lambda\mathbf{k}}|\hat{j}^{\xi}_{\mu}|u^{\xi}_{\lambda'\mathbf{k}}\rangle \\ &= \sum_{\lambda}\Big[|c^{\xi}_{\lambda}|^{2}\langle u^{\xi}_{\lambda\mathbf{k}}|\hat{j}^{\xi}_{\mu}|u^{\xi}_{\lambda\mathbf{k}}\rangle + (c^{\xi}_{\lambda})^{*}c^{\xi}_{-\lambda}e^{2i\lambda\Omega_{\mathbf{k}}}\,\langle u^{\xi}_{\lambda\mathbf{k}}|\hat{j}^{\xi}_{\mu}|u^{\xi}_{-\lambda\mathbf{k}}\rangle\Big]\end{aligned} \tag{4.4.1}$$

Naively, one may expect this element to give the current observable as it is the expectation value of the current density operator for the wavefunction employed in this framework. However, since the system admits time reversibility, it is known that energy bands approximated within a tight-binding formalism must satisfy a sum rule that prevents dissipative currents in the valence bands to be produced [89].

The dispersion of the infinitely-extended bands given in Eq. (4.2.8) and instantaneous eigenstates of Eq. (4.2.11) are a result of an approximation in momentum space, namely for electronic states in the vicinity of the Dirac points, where they possess relativistic properties.

Therefore, the physical current cannot be simply accounted for by Eq. (5.5.1), as it contains unphysical divergences. The current can nonetheless be regularised through the introduction of a term which acts as an ad-hoc subtraction of the current generated

in the valence band thus:

$$j^{\xi}_{\mu,\mathbf{k}}(t) = \underbrace{|c^{\xi}_{+}|^2\langle u^{\xi}_{+,\mathbf{k}}|\hat{j}^{\xi}_{\mu}|u^{\xi}_{+,\mathbf{k}}\rangle + |c^{\xi}_{-}|^2\langle u^{\xi}_{-,\mathbf{k}}|\hat{j}^{\xi}_{\mu}|u^{\xi}_{-,\mathbf{k}}\rangle}_{\text{intraband}} - \underbrace{\langle u^{\xi}_{-,\mathbf{k}}|\hat{j}^{\xi}_{\mu}|u^{\xi}_{-,\mathbf{k}}\rangle}_{\text{valence band current}} + \underbrace{q^{\xi}_{\mathbf{k}}e^{-i\omega_0 t}\langle u^{\xi}_{-,\mathbf{k}}|\hat{j}^{\xi}_{\mu}|u^{\xi}_{+,\mathbf{k}}\rangle + (q^{\xi}_{\mathbf{k}})^{*}e^{i\omega_0 t}\langle u^{\xi}_{+,\mathbf{k}}|\hat{j}^{\xi}_{\mu}|u^{\xi}_{-,\mathbf{k}}\rangle}_{\text{interband}}. \tag{4.4.2}$$

The Hamiltonian of Eq. (5.3.2) is a low-momentum representation of the carriers, since it was obtained as a first-order $\mathbf{k}\cdot\mathbf{p}$ approximation. A local form of the current density operator may be found which renders the current density operator valley-dependent. The full current, which takes in both valley contributions is of course independent of ξ. For a Cartesian coordinate μ, it is given as:

$$\hat{j}^{\xi}_{\mu,\mathbf{k}} = -\frac{e}{\hbar}\frac{\partial}{\partial k_{\mu}}H^{\xi}_{\mathbf{k}} \tag{4.4.3}$$

resulting in momentum-independent resulting in

$$\begin{aligned}\hat{j}^{\xi}_{x} &= -(\xi e v_{\mathrm{F}}/\hbar)\sigma_x \\ \hat{j}^{\xi}_{y} &= -(e v_{\mathrm{F}}/\hbar)\sigma_y.\end{aligned} \tag{4.4.4}$$

In this fashion, the construction of the current in Eq. (4.4.2) allows for the separation of current terms which originate within the same band (intraband) and across different

bands (interband).

$$\begin{aligned}
\langle u^{\xi}_{\lambda,\mathbf{k}}|\hat{j}^{\xi}_{x}|u^{\xi}_{\lambda',\mathbf{k}}\rangle &= -\xi e v_{\mathrm{F}} \langle u^{\xi}_{\lambda,\mathbf{k}}|\sigma_x|u^{\xi}_{\lambda,\mathbf{k}}\rangle \\
&= -\frac{\xi e v_{\mathrm{F}}}{2}\begin{pmatrix} \xi e^{i\xi\theta_{\mathbf{k}}/2} & \lambda e^{-i\xi\theta_{\mathbf{k}}/2}\end{pmatrix}\begin{pmatrix} 0 & 1 \\ 1 & 0\end{pmatrix}\begin{pmatrix} \xi e^{-i\xi\theta_{\mathbf{k}}/2} \\ \lambda' e^{i\xi\theta_{\mathbf{k}}/2}\end{pmatrix} \\
&= -\frac{e v_{\mathrm{F}}}{2}\left(\lambda' e^{i\xi\theta_{\mathbf{k}}} + \lambda e^{-i\xi\theta_{\mathbf{k}}}\right) \\
&= \begin{cases} -\lambda e v_{\mathrm{F}} \cos\theta_{\mathbf{k}} & \text{for} \quad \lambda' = \lambda \quad \text{(intraband)} \\ \lambda\xi i e v_{\mathrm{F}} \sin\theta_{\mathbf{k}} & \text{for} \quad \lambda' = -\lambda \quad \text{(interband)}\end{cases}
\end{aligned} \tag{4.4.5}$$

where, by parity, $\cos(\xi\theta_{\mathbf{k}}) = \cos(\theta_{\mathbf{k}})$ and $\sin(\xi\theta_{\mathbf{k}}) = \xi\sin(\theta_{\mathbf{k}})$.

As for the y component:

$$\begin{aligned}
\langle u^{\xi}_{\lambda,\mathbf{k}}|\hat{j}^{\xi}_{y}|u^{\xi}_{\lambda',\mathbf{k}}\rangle &= -e v_{\mathrm{F}} \langle u^{\xi}_{\lambda,\mathbf{k}}|\sigma_y|u^{\xi}_{\lambda',\mathbf{k}}\rangle \\
&= -\frac{i e v_{\mathrm{F}}}{2}\begin{pmatrix} \xi e^{i\xi\theta_{\mathbf{k}}/2} & \lambda e^{-i\xi\theta_{\mathbf{k}}/2}\end{pmatrix}\begin{pmatrix} 0 & -1 \\ 1 & 0\end{pmatrix}\begin{pmatrix} \xi e^{-i\xi\theta_{\mathbf{k}}/2} \\ \lambda' e^{i\xi\theta_{\mathbf{k}}/2}\end{pmatrix} \\
&= -\frac{\xi i e v_{\mathrm{F}}}{2}\left(-\lambda' e^{i\xi\theta_{\mathbf{k}}} + \lambda e^{-i\xi\theta_{\mathbf{k}}}\right) \\
&= \begin{cases} -\lambda e v_{\mathrm{F}} \sin\theta_{\mathbf{k}} & \text{for} \quad \lambda' = \lambda \quad \text{(intraband)} \\ -\lambda\xi i e v_{\mathrm{F}} \cos\theta_{\mathbf{k}} & \text{for} \quad \lambda' = -\lambda \quad \text{(interband)}\end{cases}
\end{aligned} \tag{4.4.6}$$

Importantly, the current elements satisfy the conditions:

$$\langle u^{\xi}_{\lambda,\mathbf{k}}|\hat{j}^{\xi}_{\mu}|u^{\xi}_{\lambda,\mathbf{k}}\rangle = -\langle u^{\xi}_{-\lambda,\mathbf{k}}|\hat{j}^{\xi}_{\mu}|u^{\xi}_{-\lambda,\mathbf{k}}\rangle \qquad (\textit{intraband}) \tag{4.4.7}$$

$$\langle u^{\xi}_{\lambda,\mathbf{k}}|\hat{j}^{\xi}_{\mu}|u^{\xi}_{-\lambda,\mathbf{k}}\rangle = \langle u^{\xi}_{-\lambda,\mathbf{k}}|\hat{j}^{\xi}_{\mu}|u^{\xi}_{\lambda,\mathbf{k}}\rangle^{*} \qquad (\textit{interband}) \tag{4.4.8}$$

Inserting the current elements calculated in Eqs.(4.4.5)-(4.4.6) in Eq. (4.4.2) leads to the microscopic current:

$$\begin{aligned} j^{\xi}_{x,\mathbf{k}} &= -ev_{\mathrm{F}}\left(|c^{\xi}_{+,\mathbf{k}}|^2\cos\theta_{\mathbf{k}} - \left(|c^{\xi}_{-,\mathbf{k}}|^2{+}1\right)\cos\theta_{\mathbf{k}} + i\xi\sin\theta_{\mathbf{k}}\left(q^{\xi}_{\mathbf{k}}e^{-i\omega_0 t} - (q^{\xi}_{\mathbf{k}})^* e^{i\omega_0 t}\right)\right) \\ &= -ev_{\mathrm{F}}\left(\cos\theta_{\mathbf{k}}(w^{\xi}_{\mathbf{k}}+1) - 2\xi\sin\theta_{\mathbf{k}}\mathrm{Im}\left(q^{\xi}_{\mathbf{k}}e^{-i\omega_0 t}\right)\right) \end{aligned} \tag{4.4.9}$$

Similarly for the y component:

$$\begin{aligned} j^{\xi}_{y,\mathbf{k}} &= -ev_{\mathrm{F}}\left(|c^{\xi}_{+,\mathbf{k}}|^2\sin\theta_{\mathbf{k}} - \left(|c^{\xi}_{-,\mathbf{k}}|^2{+}1\right)\sin\theta_{\mathbf{k}} - i\xi\cos\theta_{\mathbf{k}}\left(q^{\xi}_{\mathbf{k}}e^{-i\omega_0 t} - (q^{\xi}_{\mathbf{k}})^* e^{i\omega_0 t}\right)\right) \\ &= -ev_{\mathrm{F}}\left(\sin\theta_{\mathbf{k}}(w^{\xi}_{\mathbf{k}}+1) + 2\xi\cos\theta_{\mathbf{k}}\mathrm{Im}\left(q^{\xi}_{\mathbf{k}}e^{-i\omega_0 t}\right)\right) \end{aligned} \tag{4.4.10}$$

The valence band current term that has been subtracted is incorporated as a regularisation for the intraband current leading, in a sense, to a reassignment $w_{\mathbf{k}} \mapsto w_{\mathbf{k}} + 1$ in Eqs. (4.4.9)-(4.4.10), which has been used in [81]. With the knowledge of the contribution from a particular momentum state and valley to the μ component of the current, the physical photo-generated current is obtained through:

$$\begin{aligned} \mathbf{J}_{\mu}(t) &\equiv \mathbf{J}^{\mathrm{intra}}_{\mu}(t) + \mathbf{J}^{\mathrm{inter}}_{\mu}(t) \\ &= \sum_{\mathbf{k},\xi} j^{\xi}_{\mathbf{k}}(t) \approx \frac{g_s}{d_{\mathrm{G}}4\pi^2}\sum_{\xi}\left(\int j^{\xi}_{\mathbf{k}}(t)d^2\mathbf{k}\right) \end{aligned} \tag{4.4.11}$$

where $g_{\mathrm{s}} = 2$ denotes the spin degeneracy (given that the quasirelativistic equations do not account for spin), $d^2\mathbf{k} \equiv |\mathbf{k}|\, d|\mathbf{k}|d\phi_{\mathbf{k}}$ is the 2D differential in momentum space and $d_{\mathrm{G}} = 0.33$ nm is the thickness of the monolayer. The macroscopic contributions from intraband and interband currents may of course be accessed given the explicit separation in $j^{\xi}_{\mu,\mathbf{k}}$.

Rather importantly, it must be emphasized that the integration over momentum must

cover the whole space, as opposed to the usual first Brillouin zone, since the dispersion is not periodic, given the low-momentum approximation.

4.5 A Comparison of the DBEs and SBEs

In the same spirit of Section 3.7, and in order to establish the fundamentally different predictions from both the DBEs – Eqs. (4.2.20)-(4.2.21) – and the full-field SBEs –Eqs.(3.4.7)-(3.4.8) – in the nonlinear regime, both sets of equations were numerically simulated with the same parameters. As before, a highly accurate Runge-Kutta algorithm was used and, to this end, the equations were rescaled so all variables are dimensionless. The scaling of both the DBEs and SBEs is given in Appendix A.1.

With a numerical output of the inversion and microscopic polarisation, the microscopic currents may be composed as given by Eqs. (4.4.9)-(4.4.10). The final, *macroscopic* current, whose definition is found in Eq. (4.4.11), is obtained by discretising momentum space in a reasonably fine mesh. The integration in momentum space is performed using the trapezoidal rule and, given the formalism that was developed, the space is parametrised by the polars of each dimensionless momentum state, as before denoted as $\tilde{\mathbf{k}} = ||\tilde{\mathbf{k}}|, \phi_{\tilde{\mathbf{k}}}\rangle$.

In order to ensure that all appropriate contributions are taken, the radial integration is performed up to a cutoff value, predetermined to ensure that the amplitude of the microscopic polarisation is at that scale is below a strict threshold. A sensible value for such cutoff was found to be $|\tilde{\mathbf{k}}| = 10$.

Finally, the current in time domain is Fourier-transformed so a harmonic analysis may be performed. The same methodologies apply to the SBEs, where the current contributions are obtained by setting $A(t) = 0$ in their DBEs counterparts.

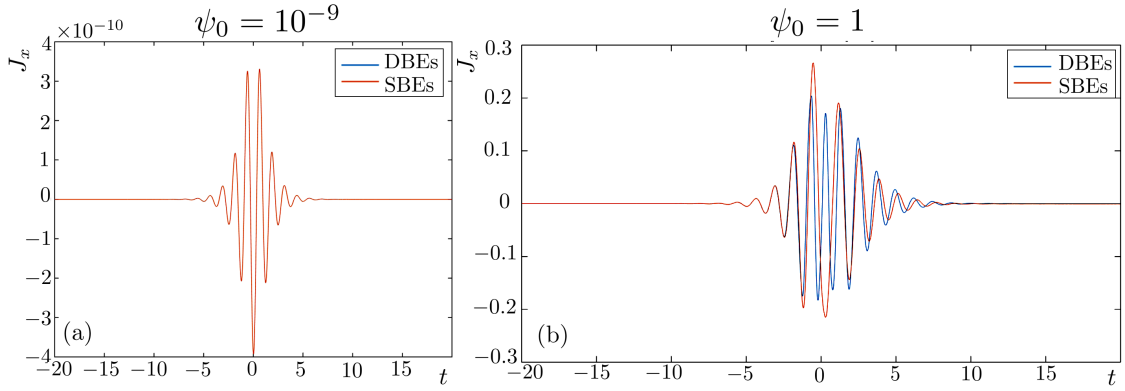

Figure 4.3: Comparison of the macroscopic current J_x between the DBEs and the SBEs, in the full-field treatment, for a sech pulse of central frequency $\Omega_0 = 5$. (a) shows an extreme similarity between the models since it is obtained in the linear regime. For intense fields, (b) shows slightly different outputs. These are crucial in understanding harmonic generation in the sample.

In order to solidify the claim that the nonlinear regime induces different time dynamics in the photo-generated current, the SBEs and DBEs were solved in the linear regime, for a field amplitude $\psi_0 = 10^{-9}$ and nonlinear regime, for a field amplitude $\psi_0 = 1$. The current predicted by both methods is shown in Fig. 4.3. Firstly, the current only shows a nonzero component J_y , namely the one in the light polarisation direction, which was taken to be in $\hat{x}$. Consequently, the integrated current component J_y vanishes identically.

4.3(a) shows a perfect match between both models in the linear regime. However, a an intense field leads to additional time dependences in the DBEs, which ultimately make the current output slightly different to the SBEs.

The current formulae dictating its dynamics are dependent on which valley the excitations take place. It is thus in principle possible to obtain different outputs for each valley, leading to an asymmetrical contribution of the valleys to the overall current. However, the valley-dependent currents are the same. Consequently, a degeneracy factor of 2 may be introduced in the first line of Eq. (4.4.11). This degeneracy factor has also been found in works by Ishikawa [81, 82].

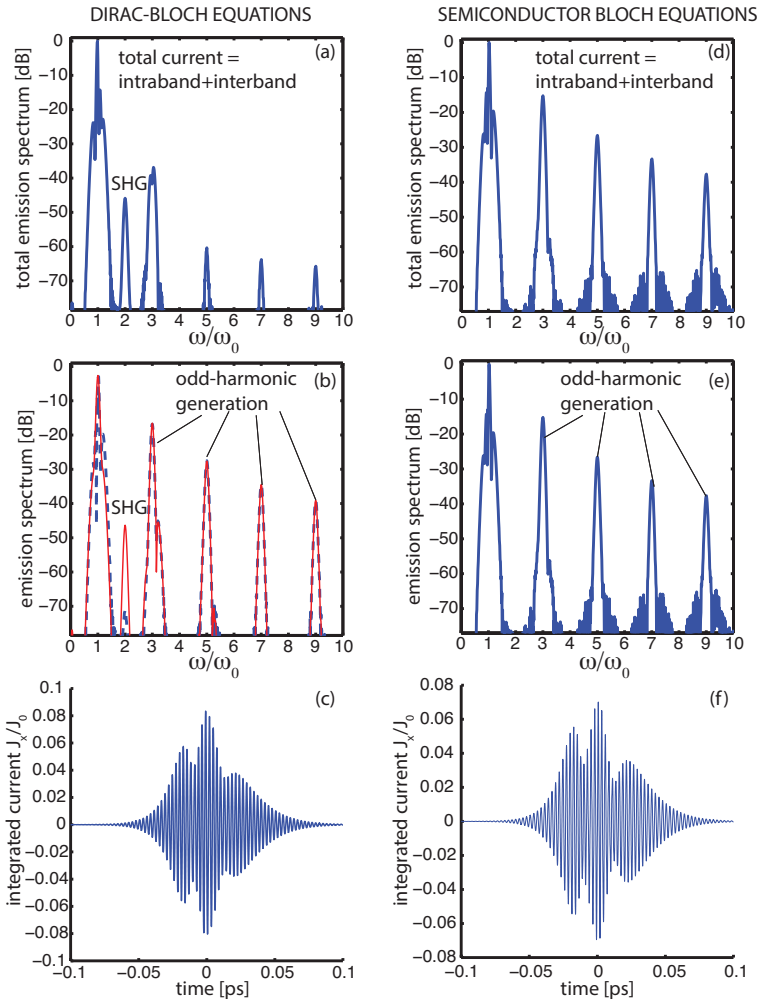

Figure 4.4: Total and partial emission spectra and currents excited by a $t_0 = 10$ fs pulse, normally incident and linearly polarized, with an input energy $I = 114$ GW/cm^2, at zero temperature. (a, b, c) shows results obtained by solving numerically the DBEs (4.2.20-4.2.21), (a) the total (intraband + interband) spectrum, (b) the separated interband (blue line) and intraband (red line) spectra, and (c) the current $J_x(t)$ circulating on the graphene layer [$J_0 \equiv -e\omega_0^2/(4dv_{\rm F})$ is a reference scale]. Similar figures are calculated in (d, e, f) using the SBEs, i.e. neglecting the photon momentum in the DBEs.

For the simulations that produced Fig. 4.4, the graphene sheet is pumped with a normally incident pulse, of duration $t_0 = 10$ fs, central wavelength $\lambda_0 = 800$ nm, intensity $I = 114$ GW/cm^2, and at temperature $T = 0$ °K.

Realistic, zero-averaged localised electric and vector potential fields, in order not to introduce unphysical static electric fields. Their respective dimensionless definitions

are given as:

$$\begin{aligned} \psi(\tau) &= \psi_0 \mathrm{sech}(\tau)\cos(\Omega_0\tau) - \left(\tfrac{\psi_0}{\Omega_0}\right)\mathrm{sech}(\tau)\tanh(\tau)\sin(\Omega_0\tau) \\ a(\tau) &= -\tfrac{\psi_0}{\Omega_0}\mathrm{sech}(\tau)\sin(\Omega_0\tau) \end{aligned} \tag{4.5.1}$$

The output spectra $S(\omega) = |\omega \mathbf{J}(\omega)|^2$ in dB and the integrated circulating current $J_x(t)$ are shown in Fig. 4.4(a,b,c) (first column). The factor ω, proportional to the density of states in Eq. (2.3.24) is added so that the spectrum does not show decaying harmonic peaks.

The output spectrum in dB of the total current, comprised of the intraband and interband currents, when using the DBEs, is shown in Fig. 4.4(a). The dynamical centrosymmetry breaking described above leads to a relatively strong SHG signal, indicated in the figure, at $\omega/\omega_0 = 2$. This SHG signal is an absolute novelty in the theory of graphene, since it was previously thought to be impossible to obtain such signal in normal incidence conditions. Figure 4.4(a) also shows the more conventional high-harmonic generation typical of a $\chi^{(3)}$ material, with peaks emitted at odd integer values of ω/ω_0.

Figure 4.4(b) is the same as Fig. 4.4(a), but the contributions of the intraband (red solid line) and the interband (dashed blue line) currents are separated. For the odd-order high-harmonic generation peaks, the intraband and interband currents basically contribute equally to the emission (the two lines are almost superimposed), while the SHG peak mainly comes from the contribution of the intraband current.

Figure 4.4(c) shows the temporal evolution of the total current $J_x(t)$. In particular, it is found that $J_y(t) = 0$ after integration over the momenta, as it should be since the pulse is linearly polarised along the $\hat{x}$-axis. However, nothing prevents the study of arbitrary polarisation configurations of the system, yielding in general $J_y \neq 0$.

Figs. 4.4(d,e,f) show the same quantities as (a,b,c), this time calculated by using the SBEs. No SHG is predicted by the SBEs and therefore these equations ultimately

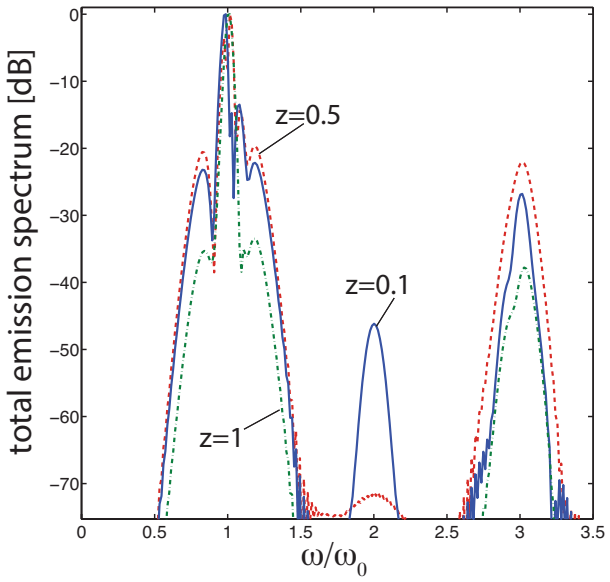

Figure 4.5: Total emission spectra for non-vanishing chemical potential μ, parametrised by $z \equiv 2\mu/(\hbar\omega_0)$, for $z = 0.1$ (solid blue line), 0.5 (dashed red line) and 1 (dashed-dotted green line). Temperature is $T = 300$ °K. One can observe a drastic reduction of the SHG peak when progressively increasing the doping.

fail to show evidence of important physics contained in the Dirac equation (4.2.1). One can also notice that Fig. 4.4(d) and (e) are identical, since the intraband contributions are totally absent in the SBE formulation. Furthermore, the intensities of the odd-harmonic peaks in the SBEs in Fig. 4.4(d, e) are overestimated with respect to their counterparts obtained by using the DBEs in Fig. 4.4 (a, b).

It must be noted in (b) that the SHG mainly originates from the intraband current, while intraband and interband currents contribute equally to the generation of the odd harmonics. Also, (d) and (e) are identical since in the SBEs the intraband current integrates out to zero, and therefore the SHG cannot be predicted by the SBEs.

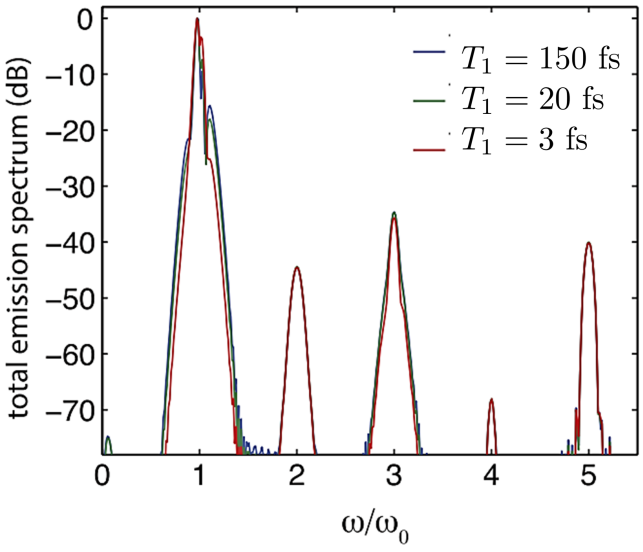

Figure 4.6: Effect of dephasing on the second harmonic signal. The sample is at a temperature $T = 300$ °K and the polarisation decay rate is fixed for a dephasing time $T_2 = 0.8$ ps. The SHG peak does not change when changing the population decay times T_1.

4.5.1 The Effects of Temperature and Chemical Potential

The influence of a non-vanishing chemical potential μ on the harmonic composition of the current may also be accessed with the aid of the DBEs and may be appreciated in Fig. 4.5. For a dimensionless doping parameter $z \equiv 2\mu/(\hbar\omega_0)$. When increasing z from relatively small values ($z = 0.1$) to large values ($z = 1$), one can see that the SHG peak rapidly disappears. This is due to the fact that the interband transitions become progressively suppressed when increasing z.

The role of the dephasing can also be appreciated in Fig. 4.6. In it, the spectra predicted by the DBEs is shown for a sample at room temperature i.e. $T = 300$ °K. The polarisation decay rate is fixed for a dephasing time $T_2 = 0.8$ ps. The population decay time is changed from a rather long figure (150 ps) to a time comparable to ultrashort excitation (3 fs). It is clear that the SHG peak remains affected by the dephasing of the two-level systems.

The dynamical centrosymmetry breaking mechanism has just been proved to predict the generation of second harmonic waves. The step that follows any theoretical prediction must revolve about the question: *Has this effect been observed experimentally?*.

Given the considerations which lead to the conclusion that doping suppresses the signal intensity of such radiation, the use of suspended graphene is adequate for probing the dynamical centrosymmetry mechanism. The experimental realisation of this effect is thus technically challenging. Recently, Kung-Hsuan Lin et al. reported the observation of SHG in exactly the same conditions considered in this chapter [90]. Despite the presence of impurities in the sample, the authors ruled out this factor as the cause responsible for SHG. Instead, they attribute it to long-range curvature effects caused by transverse mechanical fluctuations of the layer which would break the centrosymmetry. However, the predictions from the previous section show that such imperfections would provide exceedingly small SHG signals, and would be strongly temperature-dependent and mostly independent on the input pulse duration. A strong case can be made that this observation is explained in the framework of the DBEs and its underlying dynamical centrosymmetry breaking mechanism.

4.6 Summary & Outlook

In summary, a novel nonlinear optical effect in graphene where a short and intense pulse can modulate the Dirac cone in time, leading to the temporary breaking of the centrosymmetry is discovered. This effect produces an emission of SHG waves even at normal incidence. The SBEs are not able to predict the onset of the dynamical centrosymmetry breaking.

It must be categorically emphasized that the observation of SHG in graphene samples is well established in the literature and proposed through a myriad of techniques, for

instance by shining light obliquely at the surface [85], electric field in-plane biasing [86] and quadrupole interactions [87]. The novelty of these results relies on the existence of a theoretical mechanism supported by the Dirac-Bloch formalism which, in the extreme nonlinear optical regime, predicts previously-forbidden even harmonics to be generated at normal incidence in centrosymmetric relativistic-like media.

Chapter 5

Opening the Gap

5.1 Overview

The main novelty of graphene as a solid state system is that its quasiparticles may be adequately modelled as relativistic massless Dirac fermions, which admit a linear energy dispersion. Since this electronic dispersion is ungapped, with the conduction and valence bands extrema touching each other at the Dirac points $\mathbf{K}$ and $\mathbf{K}'$, the system behaves like a zero-gap semiconductor. Furthermore, both bands are symmetrical, implying electron-hole symmetry.

However, this property is only expected for free-standing, pristine graphene samples. A gap in the spectrum can be opened at the Dirac points, which are located on the edge of the Brillouin zone and shown in Fig. 5.1(a). As explained in the previous chapter, low-momentum states around such points are collectively known as a valley and unsurprisingly indexed by the Dirac point where extrema are found. The gap opening allows carriers to be endowed with an effective mass.

In this chapter, an important modification to the theory is presented: *What is the effect of opening a gap in the generation of harmonics?* This question turns out to be encompassing in the sense that a myriad of seemingly unrelated conditions may

be conceptualised in the same mathematical fashion - namely by adequately opening a gap in the two-band spectrum.

A different yet conceptually equivalent way to frame the problem at hand is to imagine the appearance of a gap as a consequence of the existence of a staggered sublattice potential, in which each triangular sublattice of the honeycomb lattice (**A** and **B** in Fig. 2.1) admits opposite non-zero on-site energies, contrasting with the previous assumption that, in a gapless sample, each site is described by the same orbitals and Hamiltonian. A prototypical example of this is normally given when graphene is deposited on hexagonal boron nitride. A brief review of mechanisms conducive to gapping the spectrum, respective experimental realisations and the connection between the existence of a staggered mathematical model and the appearance of a gap are given in Section 5.2.

Opening the gap leads to other appreciable effects. Rather unsurprisingly, the inclusion of a gap in the spectrum leads to a transition to a semiconducting regime, in turn harnessing substantially different optoelectronic feature for which devices such as graphene-based transistors and photodetectors rely on [91].

As was seen in the previous chapter, the Dirac equation of the quasiparticles in graphene may be linked to the original $(3+1)$ dimensional Dirac equation modelling an electron when the sublattice index takes the role of the electron spin — this is why such index is termed *pseudospin*. This mathematical analogy is well-justified but it does not, consequently, consider the effect of spin. These can, of course, be included explicitly in the Hamiltonian to yield the required effects on the dispersion. The inclusion of such processes is not part of the purpose of this chapter and hence only a gap is included in the treatment for now. This will eventually lead to the *Massive Dirac-Bloch Equations*. In Chapter 6, these and further effects are included in an encompassing, general Hamiltonian.

Of crucial important is the observation that the appeareance of a gap leads to

further modifications to the optical behaviour of the plane-confined carriers by excitonic effects, in turn caused by screening mechanisms. These may be appreciated through theoretical models of the optical conductivity spectra and phenomenological dependence on disorder and imperfections in Ref. [92]. The existence of excitons are known to lead to a Fermi velocity and energy band renormalisation [49], as previously discussed. The Coulomb interactions in the system are now expected to be relevant in the dynamics of the carriers. In a recent work by Di Mauro et al [93], the massive DBEs were generalised, from the carrier-free treatment that is presented in this Chapter, to accommodate for the inclusion of Coulomb interactions. However, this analysis is performed in the low excitation regime, where excitonic effects may be adequately understood. In the spirit of Section 3.6, the DBEs become decoupled by fixing the inversion , which in these conditions may be approximated by $w_{\mathbf{k}} \approx -1$, allows analytical expressions to be found for the microscopic polarisation and with that, the dependence of the optical absorption on the band gap.

Inconveniently, the numerical implementation of this mechanism in the nonlinear regime, the subject-matter of this chapter and indeed throughout the whole thesis, is rather challenging since it must consider the dynamics of all two-level systems at once. As opposed to the free-carrier model that has been used so far, each two-level system at $\mathbf{k}$ only depends on its own parameters and can thus be calculated separately and then averaged at the final step. Additionally, even though such interactions do refine the understanding of the system, a carrier-free treatment must be solved first to gain insight not only into the qualitative predictions of the model but also into the numerical machinery that allows such models to output reliable data. For these reasons, Coulomb interactions are not considered in this and subsequent chapters.

In this chapter, the role of the energy gap in the ultrafast generation of high harmonic radiation is studied along with related nonlinear processes, within a semiclas-

sical quasirelativistic formalism, by extending the Dirac-Bloch equations and their framework, previously applied to massless Dirac fermions [79, 81, 82] and thoroughly discussed and explained in Chapter 4, to incorporate a gapped Dirac spectrum.

The DBEs in Eqs. (4.2.20-(4.2.21) which were proposed to model graphene already predict startling results. Graphene, as a centrosymmetric material, should not allow the generation of even harmonics for normal incidence. However, it will be shown that intense and ultrashort pulses provide a regime where an extreme nonlinear optical effect termed "*Second Harmonic Generation in disguise of Third Harmonic Generation*" allows for odd harmonics to interfere amongst themselves, generating even harmonics, once the sample is gapped.

The formalism employed also allows for the identification of a time and momentum-dependent Berry phase not found in the massless DBEs. The combination of the appearance of such a gap and Berry phase leads to interesting qualitatively different optical behaviour in the nonlinear ultrashort regime and these are studied in Section 5.6. The versatility of the present treatment allows the role of few-cycle intense pulses in the medium polarisation to be accessed [94].

5.2 Origin and Measurement of the Gap

The inclusion of a gap in any discussion about light-matter interaction is natural in the sense that massless Dirac fermions in graphene are only a faithful mathematical representation of the sample when it is pristine, impurity-free and free-standing. More physically realisable samples are normally deposited on particular dielectric substrates; this intrinsic property is known to modify the electronic and optical properties of the sample [95] and consequently gap the spectrum.

Alternatively, using various synthesis and preparation techniques, impurities, local lattice defects and vacancies [96], and strain effects [97] may be physically realised and

have also been shown to gap the spectrum. More challenging procedures to achieve this rely on electric biasing of graphene bilayers [98] and monolayer nanostructuring into nanoribbons [99].

The characteristic gap opening scale is obviously dependent on the process in question. Substrate-induced effects seem to be the most efficient to open a gap which, with the aid of ARPES measurement techniques, has been estimated to be 0.26 eV for epitaxially-grown graphene on silicon carbide (SiC) [95]. Density Functional Theory calculations estimate monolayer graphene can acquire a gap of 0.35 eV when deposited on a SiO_2 substrate [100].

Furthermore, it is worth mentioning that the extent of such a gap opening is linked to the relative geometrical configurations of the substrate and the sample alongside the dominant chemical bonds in their interaction. For instance, graphene deposited on Si-terminated silica surfaces with inactive dangling bonds has been proposed as a configuration to retrieve the linear, gapless dispersion typical of free-stranding graphene [101].

The inclusion of a gap in the single-particle spectrum does not suggest any kind of intervalley interactions. Unless an imbalance is physically realised, for instance through an electric field bias or sample inhomogeneities, intervalley scattering is highly unlikely[102], as it requires exceedingly large phonon momenta, roughly of the order of the separation $|\mathbf{K} - \mathbf{K}'|$.

It can thus be reasonably assumed that the dynamics of both valleys is decoupled of each other and the carriers can be endowed with an additional degree of freedom, the *valley isospin* ξ, where $\xi = +1$ (-1) refers to states in the $\mathbf{K}$ $(\mathbf{K}')$ valley. As usual, a further degree of freedom, the *pseudospin* λ, with $\lambda = +1$ (-1) denoting conduction (valence) band states, distinguishes between electron and hole states.

The fundamental reason why a gap can appear in a periodic solid state system can

be appreciated from an ab-initio calculation based on a tight-binding approximation. As shown in Section 2.2, the N branches of the dispersion of carriers contained in a lattice may be calculated from the secular equation (Eq. (2.2.12)). By solving it, a gap can arise if the on-site energies of each sublattice are different from each other. Setting the on-site energies as:

$$\begin{aligned} \epsilon^{(A)} &= \epsilon^0 + \frac{\Delta}{2} \\ \epsilon^{(B)} &= \epsilon^0 - \frac{\Delta}{2} \end{aligned} \tag{5.2.1}$$

where the latter term can be seen as a staggered potential, alternating between each sublattice. If next-nearest neighbour effects and overlap contributions are ignored by setting $t' = s = 0$, the system is in quasi-orthogonality conditions i.e. $s_{ij} \approx N\delta_{ij}$ and leads the secular equation to simply to:

$$\epsilon^{\lambda}_{\mathbf{k}} = \epsilon^0 + \lambda\sqrt{\left(\frac{\Delta}{2}\right)^2 + t^2|\gamma_{\mathbf{k}}|^2} \tag{5.2.2}$$

The onsite-energy ϵ^0 stemming from the $|p_z\rangle$ orbital, being a common figure for both sublattices, again induces a physically irrelevant shift in the dispersion. What is relevant to this discussion is that the existence of the alternating potential across the lattice opens a gap in the dispersion. Applying the usual Taylor-expansion around $\mathbf{k} = 0$ for the nn hopping amplitude $\gamma_{\mathbf{k}}$ thus leads to the dispersion:

$$\epsilon^{\lambda}_{\mathbf{k}} = \lambda\sqrt{\left(\frac{\Delta}{2}\right)^2 + \left(\hbar v_{\mathrm{F}}|\mathbf{k}|\right)^2} \tag{5.2.3}$$

This is a hyperbolic dispersion in $\mathbf{k}$ and, most importantly, it can be seen that the bands are now separated by a gap Δ. This is however categorically not the same dispersion as found for a single band in the Schrödinger equation – it is a relativistic Dirac-like spectrum! In the next section, a procedure to implement these considera-

tions is incorporated in the Dirac Equation and shown to reproduce the tight-binding predictions just shown.

5.3 Massive Dirac Fermions

In order to understand light-matter interactions in this gapped system, one may proceed by obtaining the wavefunction $|\Psi^{\xi}_{\mathbf{k}}(t)\rangle$ of an electron of effective mass $m \equiv \Delta/(2v_{\mathrm{F}}^2)$ and momentum $\mathbf{p} = \hbar\mathbf{k}$ in the vicinity of a particular Dirac point in valley ξ, which must obey the two-dimensional Dirac equation:

$$i\hbar\frac{d}{dt}\left|\Psi^{\xi}_{\mathbf{k}}(t)\right\rangle = H^{\xi}_{\mathbf{k}}(t)\left|\Psi^{\xi}_{\mathbf{k}}(t)\right\rangle \tag{5.3.1}$$

with a Hamiltonian of the form:

$$H^{\xi}_{\mathbf{k}}(t) = v_{\mathrm{F}}\ \left(\boldsymbol{\sigma}(\xi)\cdot\left(\mathbf{p}+\frac{e}{c}\mathbf{A}(t)\right)\right) + \frac{\Delta}{2}\sigma_z, \tag{5.3.2}$$

where $\boldsymbol{\sigma}(\xi) \equiv (\xi\sigma_x, \sigma_y)$ is a vector comprised of the 2D Pauli matrices, $e > 0$ is the absolute value of the electron charge and c is the speed of light in vacuum. Attending to the discussion of the previous section, the gap opening is achieved by simply adding a σ_z term. This way, each on-site energy is the negative of each other, as required.

To obtain the appropriate Hamiltonian for such interactions, the canonical momentum was introduced through the minimal substitution $\mathbf{p} \mapsto \mathbf{p} + (e/c)\mathbf{A}(t) \equiv \boldsymbol{\pi}_{\mathbf{k}}(t)$ in the field-free Hamiltonian i.e. when $\mathbf{A}(t) = 0$.

The same optical polarisation configuration is considered: the pulse is further assumed to be normally-incident and linearly polarised along an arbitrary direction, here taken along the $\hat{x}$ direction. Its electromagnetic vector potential $\mathbf{A}$, is again chosen to satisfy the Coulomb gauge $\nabla\cdot\mathbf{A} = 0$ and can thus be written as $\mathbf{A}(t) = (A(t), 0, 0)$. Consequently, the canonical momentum becomes $\boldsymbol{\pi}_{\mathbf{k}}(t) = (p_x + (e/c)A(t), p_y, 0)$.

This vector is more easily incorporated in the model when converted to polars, with magnitude $|\boldsymbol{\pi}_{\mathbf{k}}(t)|$ and angle $\theta_{\mathbf{k}}(t)$. Their definitions are exactly the same as given when deriving the graphene DBEs, which are shown in Eq. (4.2.2).

Using these considerations and the simplification $\xi\pi_x - i\pi_y = \xi|\boldsymbol{\pi}_{\mathbf{k}}|e^{-i\xi\theta_{\mathbf{k}}}$, the Hamiltonian of Eq. (5.3.2) can be written in matrix form as:

$$H^{\xi}_{\mathbf{k}}(t) = \begin{pmatrix} \frac{\Delta}{2} & \xi v_{\mathrm{F}}|\boldsymbol{\pi}_{\mathbf{k}}|e^{-i\xi\theta_{\mathbf{k}}} \\ \xi v_{\mathrm{F}}|\boldsymbol{\pi}_{\mathbf{k}}|e^{i\xi\theta_{\mathbf{k}}} & -\frac{\Delta}{2} \end{pmatrix} \tag{5.3.3}$$

It is not surprising, given the discussion in the previous section concerning the opening of a gap in the tight-binding approximation, that having two nonzero on-site energies, here represented as the diagonal entries of Eq. (5.3.3), leads to the desired gapped dispersion $\epsilon^{\xi}_{\lambda\mathbf{k}}$, now time-dependent:

$$\epsilon^{\xi}_{\lambda\mathbf{k}}(t) = \lambda\sqrt{\left(\frac{\Delta}{2}\right)^2 + \left(v_{\mathrm{F}}|\boldsymbol{\pi}_{\mathbf{k}}(t)|\right)^2} \equiv \lambda\epsilon_{\mathbf{k}}(t) \tag{5.3.4}$$

where $\epsilon_{\mathbf{k}}$ denotes the band-independent positive branch. Ignoring the optical field, the two bands are separated exactly by Δ at the Dirac points, found when $|\mathbf{k}|= 0$, as expected.

The spectrum Eq. (5.3.4) may be seen in Fig. 5.1(a). Since it does not depend on the valley isospin ξ, the valley spectra are globally equivalent. Even though a gap is now present, note that the spectrum was obtained from the Dirac Equation and hence takes a hyperbolic relation with $|\boldsymbol{\pi}_{\mathbf{k}}|$, unlike the typical parabolic Schrödinger-like dispersion found for semiconductors.

The instantaneous eigenstates of $H^{\xi}_{\mathbf{k}}(t)$, two two-component spinors which satisfy $H^{\xi}_{\mathbf{k}}\,|u^{\xi}_{\lambda}(t)\rangle = \epsilon^{\xi}_{\lambda,\mathbf{k}}\,|u^{\xi}_{\lambda}(t)\rangle$, with amplitudes denoted by the upper and lower components

as was done in Eq. (4.2.9), must simultaneously satisfy the relations:

$$\begin{cases} \frac{\Delta}{2}\varphi^{\xi}_{\lambda,\mathbf{k}} + \hbar v_{\mathrm{F}}|\boldsymbol{\pi}_{\mathbf{k}}|e^{-i\xi\theta_{\mathbf{k}}}\phi^{\xi}_{\lambda,\mathbf{k}} = \lambda\epsilon_{\mathbf{k}}\varphi^{\xi}_{\lambda,\mathbf{k}} \\ \hbar v_{\mathrm{F}}|\boldsymbol{\pi}_{\mathbf{k}}|e^{i\xi\theta_{\mathbf{k}}}\varphi^{\xi}_{\lambda,\mathbf{k}} - \frac{\Delta}{2}\phi^{\xi}_{\lambda,\mathbf{k}} = \lambda\epsilon_{\mathbf{k}}\phi^{\xi}_{\lambda,\mathbf{k}} \end{cases} \Rightarrow \begin{cases} \phi^{\xi}_{\lambda,\mathbf{k}} = \lambda e^{i\xi\theta_{\mathbf{k}}/2} \\ \varphi^{\xi}_{\lambda} = \left(\frac{2\epsilon_{\mathbf{k}}+\lambda\Delta}{2\hbar v_{\mathrm{F}}|\boldsymbol{\pi}_{\mathbf{k}}|}\right) e^{-i\xi\theta_{\mathbf{k}}}\phi^{\xi}_{\lambda} \end{cases} \tag{5.3.5}$$

The freedom to chose one such component allows one to fix the lower component. Finally, using $\lambda^2 = 1$ and normalising the spinors such that $\langle u^{\xi}_{\lambda\mathbf{k}}(t)|u^{\xi}_{\lambda'\mathbf{k}}(t)\rangle = \delta_{\lambda\lambda'}$, they take the form:

$$|u^{\xi}_{\lambda}(t)\rangle = \frac{v_{\mathrm{F}}|\boldsymbol{\pi}_{\mathbf{k}}|}{\sqrt{\epsilon_{\mathbf{k}}(\lambda\Delta + 2\epsilon_{\mathbf{k}})}} \begin{pmatrix} \left(\frac{\lambda\Delta+2\epsilon_{\mathbf{k}}}{2v_{\mathrm{F}}|\boldsymbol{\pi}_{\mathbf{k}}|}\right) e^{-i\xi\theta_{\mathbf{k}}/2} \\ \lambda e^{i\xi\theta_{\mathbf{k}}/2} \end{pmatrix} \tag{5.3.6}$$

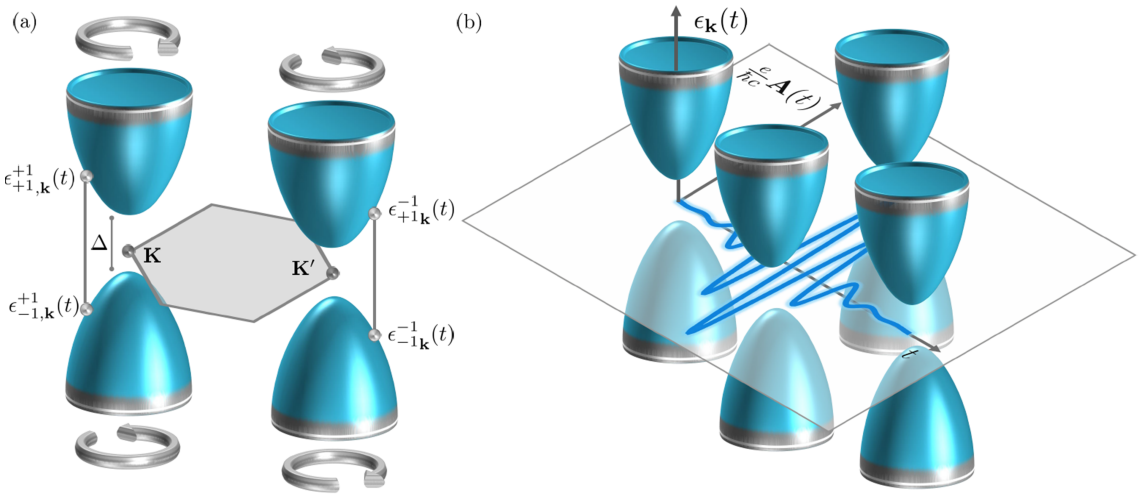

Figure 5.1: (*a*) Sketch of the Hamiltonian spectra for both valleys in the low-momentum regime. Each valley admits two bands, gapped by Δ. The relative sign of the field-induced Berry phase is represented by the silver arrows. (*b*) Depiction of the time-dependent electronic dispersion in momentum space, as given in Eq. (5.3.4), for a particular valley. Note that the pulse shifts the dispersion globally by the time-dependent photon momentum $\mathbf{A}(t)$. The deviation of this field-driven effect from the field-free dispersion is only appreciable for ultrashort and intense pulses.

These solutions have a straightforward interpretation: for a particular valley ξ, electron and hole states exist respectively in the conduction ($\lambda = +1$) and valence ($\lambda = -1$) bands, which are themselves gapped by Δ.

It can be seen straightforwardly that the eigenstates of Eq. (5.3.6) converge to their massless counterparts of Eq. (4.2.11) when the gap vanishes. The upper and lower components of the spinor can be construed as amplitudes in each of the triangular sublattices that decompose the honeycomb lattice. The instantaneous eigenstates of ungapped graphene shown in Eq. (4.2.11) show an equivalence of the amplitude of both components.

The addition of the gap changes that picture, leading to two plane wave contributions of each sublattice having different amplitudes, modulated by Δ. For this reason, one says that the sublattice inversion symmetry is broken. This symmetry is not to be confused with the inversion symmetry $\mathbf{p} \mapsto -\mathbf{p}$. Clearly, the addition of a gap to the field-free Hamiltonian *still* renders the dispersion of Eq. (5.3.4) centrosymmetric in the sense that $\epsilon^{\xi}_{\lambda\mathbf{k}}(-\infty) = \epsilon^{\xi}_{\lambda-\mathbf{k}}(-\infty)$, since it is purely radial and hyperbolic.

5.3.1 Berry Phase & Connection

The massive Dirac fermions calculated in Eq. (5.3.6) encapsulate an additional phase not present in the massless regime. The definition of such a phase is fairly general yet many designations for it - *Berry, adiabatic or geometric* - may be found in the literature. The nomenclature '*geometric phase*' will be applied and, before engaging in a discussion of its meaning in the context of the theory presented, a calculation of it is presented.

The geometric phase associated with the instantaneous eigenstate $|u^{\xi}_{\lambda}(t)\rangle$ of Eq. (5.3.6) will be denoted by $\gamma^{\xi}_{\lambda\mathbf{k}}$ and its derivative in time is defined as:

$$\dot{\gamma}^{\xi}_{\lambda\mathbf{k}}(t) \equiv i \left\langle u^{\xi}_{\lambda}(t) | \dot{u}^{\xi}_{\lambda\mathbf{k}}(t) \right\rangle = \xi\lambda \left(\frac{\Delta \dot{\theta}_{\mathbf{k}}(t)}{4\epsilon_{\mathbf{k}}(t)} \right) \equiv \xi\lambda\dot{\gamma}_{\mathbf{k}}(t). \tag{5.3.7}$$

where $\dot{\gamma}_{\mathbf{k}}(t)$ is band and valley-independent. The instantaneous geometric phase is of course given by:

$$\gamma^{\xi}_{\lambda,\mathbf{k}}(t) = \int_{-\infty}^{t} \dot{\gamma}^{\xi}_{\lambda\mathbf{k}}(t')dt' = \xi\lambda \int_{-\infty}^{t} \frac{\Delta\dot{\theta}_{\mathbf{k}}(t')}{4\epsilon_{\mathbf{k}}(t')}dt' \equiv \xi\lambda\gamma_{\mathbf{k}}(t) \tag{5.3.8}$$

This integral seems functionally too general to be obtained. However, it may be found that it takes the analytical form

$$\gamma_{\mathbf{k}}(t) = \frac{\Lambda_{\mathbf{k}}(t) - \Lambda_{\mathbf{k}}(-\infty)}{4}, \tag{5.3.9}$$

with

$$\Lambda_{\mathbf{k}}(t) \equiv \arctan\left[\frac{4\Delta\epsilon_{\mathbf{k}}(t)\tan\theta_{\mathbf{k}}(t)}{\Delta^2 - 4\epsilon^2_{\mathbf{k}}(t)\tan^2\theta_{\mathbf{k}}(t)}\right]. \tag{5.3.10}$$

A proof of this result may be examined in Eq. (5.4.15). The Berry phase is now introduced as the time-independent quantity:

$$\gamma^{0}_{\mathbf{k}} \equiv \Lambda_{\mathbf{k}}(-\infty) = \Lambda_{\mathbf{k}}(+\infty). \tag{5.3.11}$$

Such phase may be visualised in momentum space in Fig. 5.2. In (b), iso-contours show that the function is even in $\mathbf{k}$. Most importantly, the Berry phase at the Dirac point is ill-defined given the indeterminate form $0/0$. The temporal dynamics of the instantaneous Berry phase for various momentum states is shown in Fig. (5.4), by splitting the radial and angular component of their momentum vector $\mathbf{k}$ respectively as k as $\phi_{\mathbf{k}}$, as well as rescaling k to a dimensionless magnitude $\tilde{k} \equiv (2v_{\mathrm{F}}/\omega_0)k$. In this fashion, resonance conditions are met when $\tilde{k} = 1$.

Considering a continuous wave for simplicity, the geometric phase is plotted in Fig. 5.3. Interestingly, close to the Dirac points i.e. for $\tilde{k} \approx 0$, the Berry phase dynamics is independent of the field in the sense that only an oscillatory disturbance is necessary to set it up. This can be seen in (c) where this phase becomes square-like and hence

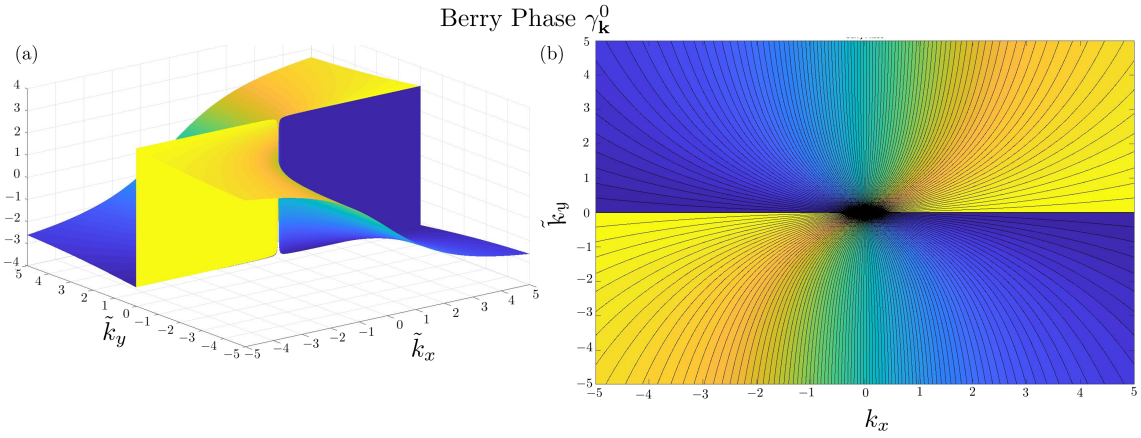

Figure 5.2: (Time-independent) Berry Phase $\gamma^0_{\mathbf{k}}$ plotted in momentum space. Note that this field has the property $\gamma^0_{\mathbf{k}} = \gamma^0_{-\mathbf{k}}$. It is badly-behaved at the Dirac point and is discontinuous in the y direction.

discontinuous whenever $A(t) = 0$. The same dynamics is found if a pulse is considered, and this can be appreciated in Fig. 5.4, where the same behaviour is shown at $\tilde{\mathbf{k}} = 0$, for a sech pulse.

Most importantly, this phase is only appreciable in the nonlinear regime. This can be seen in (d), where a resonant state $|1, \pi/3\rangle$ is considered. It can be seen that, due to the existence of a gap, a Berry phase naturally arises. Its amplitude is exceedingly small, given the field amplitude $\psi_0 = 10^{-9}$. Nonlinear features of the system must therefore consider this additional phase in order to understand its dynamics.

The Berry phase is expected to be modulated by the optical field. By juxtaposing the envelope of the electric field, it can be seen that this field-dependent phase evolves rather non-trivially and oscillates asymmetrically in time. It is instructive to see how it changes for increasing magnitudes for a fixed angle, here arbitrarily taken as $\phi_{\mathbf{k}} = \pi/3$. Phase oscillations only attain appreciable amplitudes for quasiresonant, low-energy states i.e. when $\epsilon_{\mathbf{k}} \approx \Delta/2$, found in the vicinity of the Dirac points at $\tilde{k} = 0$. For those states, the geometric phase undergoes continuous step-like transitions between 0 and $-\pi/2$.

Conversely, high-momentum states satisfying $\tilde{k} \geqslant 1$ are extremely detuned from the

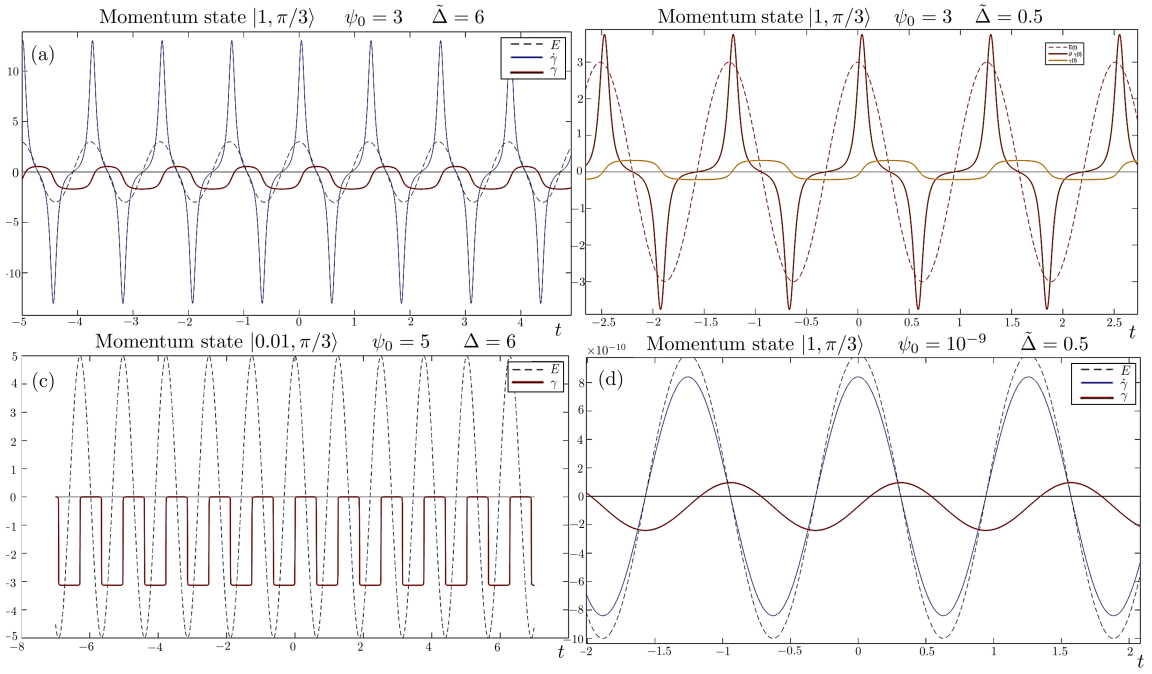

Figure 5.3: Time dynamics of the Berry phase acquired by (a), (b), (c) a resonant state $|1, \pi/3\rangle$ and (d) a state $|0.01, \pi/3\rangle$ near the Dirac point. Heavy fermions are considered in (a) and (c), whereas light fermions are assumed in (b) and (d). The sample is excited with a continuous wave of various intensities.

gap and acquire a small phase amplitude, which vanishes monotonically very rapidly, as the magnitude is increased. Thefore, the Berry phase cannot be neglected in the dynamics of low-momentum states.

Note that Fig. (5.4) shows the phases acquired by electrons in the conduction band in the **K** valley. The relative signs acquired for each band and valley, as derived in Sec. 5.3.1, are depicted in Fig. (5.1)(a). For instance, valence band carriers acquire a relative negative sign.

The notion that the Berry phase is most relevant for low-momentum states can also be visualised by plotting it as a scalar field in momentum space. Its variation in time, accounted for by the additional contributions of $A(t)$ in the quantity $\Lambda_{\mathbf{k}}(t)$ in Eq. (5.3.10) may be captured by picking two particular time instants - one where the field is absent and the canonical momentum $\boldsymbol{\pi}_{\mathbf{k}}(t)$ is minimally shifted, for instance

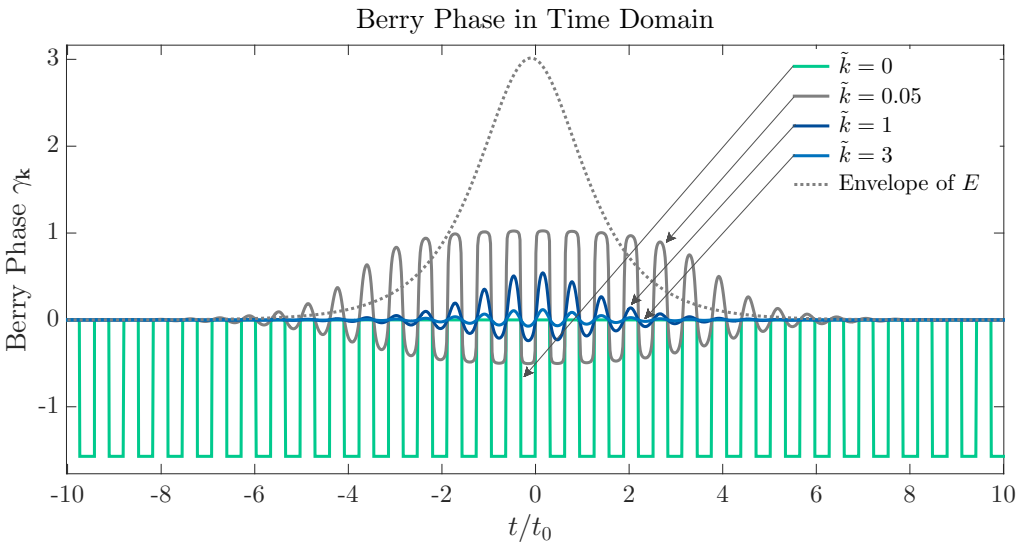

Figure 5.4: Berry phase in time domain acquired by carriers in the conduction band in the $\mathbf{k}$ valley. With a fixed angle $\phi_{\mathbf{k}} = \pi/3$, the dependence of the phase on the rescaled momentum magnitude $\tilde{k}$ reveals highly nontrivial dynamics for momentum states close to the Dirac points, where transitions are resonant and hence strongest, showing a step-like behaviour. For off-resonant states, this phase becomes negligible as its amplitude vanishes. A juxtaposition of the electric field envelope reveals that such phase oscillations are highly asymmetrical.

at $t = -15$ and another one for which the canonical momentum maximally shifted, for instance $t = -0.15$. These can be visualised by considering the vector potential in 5.5(a). It is not surprising that the origins of the geometric phase lie deep in the geometry of the configuration space of the system. For the Hamiltonian of Eq. (5.3.3), it is natural to associate the canonical momentum $\boldsymbol{\pi}_{\mathbf{k}}(t)$ to the basis of such a space - in this case momentum. This is not strictly necessary however: any set of parameters which define the dynamical state are acceptable.

In this setting, a geometric phase $\gamma^{\xi}_{\lambda\mathbf{k}}(t)$ can be assigned to a trajectory $\mathcal{C}$, parametrised by t, traced in the parameter space $\mathcal{M}$. This phase was believed to be physically irrelevant [103] given that one can gauge-transform the instantaneous eigenstates in Eq. (5.3.6) as:

$$|\tilde{u}^{\xi}_{\lambda\mathbf{k}}(t)\rangle \equiv e^{i\gamma^{\xi}_{\lambda\mathbf{k}}(t)}\,|u^{\xi}_{\lambda\mathbf{k}}(t)\rangle\,, \tag{5.3.12}$$

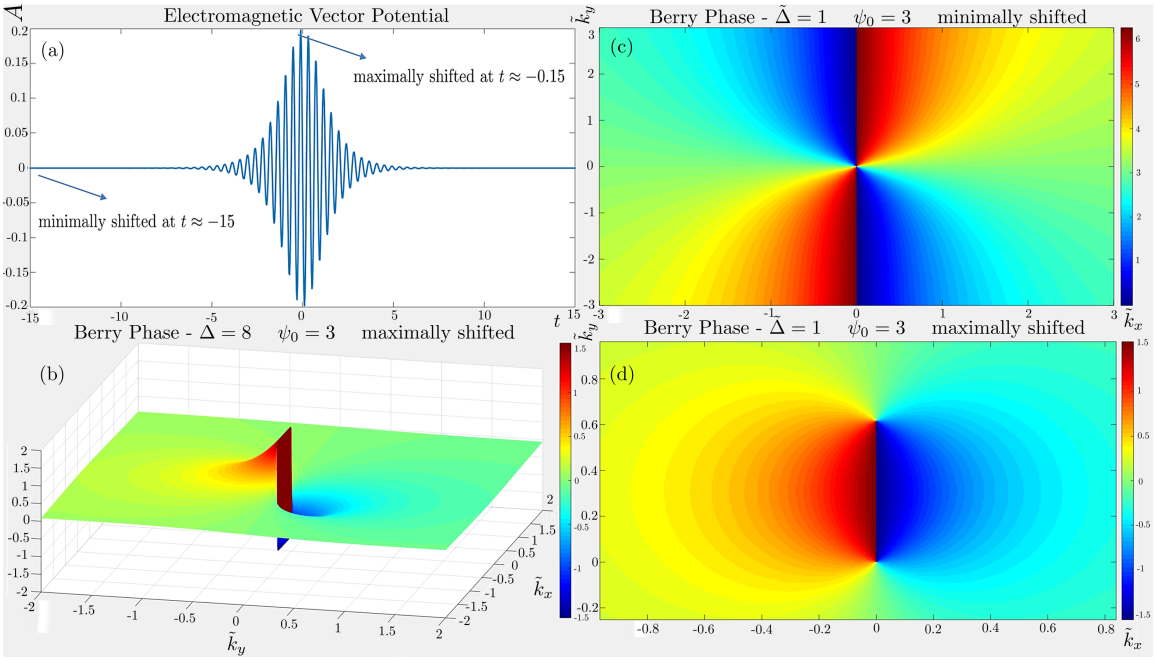

Figure 5.5: (*a*) Temporal evolution of a sech pulse with the identification of two particular instants where the vector potential A is minimally and maximally shifted. (*b*) Plot of the Berry phase in momentum space when the canonical momentum is maximally shifted. It is mostly flat across the space, apart from low-momentum states. (*c*) Density plot of the Berry phase when minimally shifted. A unique singularity is found at the Dirac point

leading to a vanishing element $i\,\langle \tilde{u}^{\xi}_{\lambda\mathbf{k}}(t)|\dot{\tilde{u}}^{\xi}_{\lambda\mathbf{k}}(t)\rangle = 0$. However, this reasoning fails when the system evolves cyclically, where this phase becomes gauge-invariant. In this instance, the phase is termed *Berry* phase and such phase becomes measurable and physical. Chapter 2 of Ref. [104] presents the terminology rather adequately.

The geometric phase presented in Eq. (5.3.10) can also be reproduced by constructing the so-called Berry connection, a gauge-invariant one-form defined on the parameter space $\mathcal{M}$. For a coordinate μ of such space, it is defined as $\mathcal{A}_\mu \equiv i\,\langle u^{\xi}_{\lambda\mathbf{k}}|\partial_\mu u^{\xi}_{\lambda\mathbf{k}}\rangle$. Then, the Berry phase is the integral of the Berry connection over a closed loop $\mathcal{C}$:

$$\gamma^0_{\mathbf{k}} = \oint_{\mathcal{C}} \mathcal{A}(\boldsymbol{\pi}_{\mathbf{k}})\, d\boldsymbol{\pi}_{\mathbf{k}}. \tag{5.3.13}$$

For simplicity, the indices $\xi, \lambda, \mathbf{k}$ are now dropped since they remain fixed throughout the calculation. If the dynamical variables of the system are chosen to be the vector of polars $\boldsymbol{\pi}_{\mathbf{k}} = (|\boldsymbol{\pi}_{\mathbf{k}}|, \theta_{\mathbf{k}})$, from now on denoted by $\boldsymbol{\pi} = (\pi, \theta)$, the eigenstates of Eq. (5.3.6) may be written as $|u(\pi,\theta)\rangle$, since the energy is a function of π only:

$$|u(\pi,\theta)\rangle = \frac{v_{\mathrm{F}}\pi}{\sqrt{\epsilon(\pi)(\lambda\Delta + 2\epsilon(\pi))}} \begin{pmatrix} \left(\frac{\lambda\Delta + 2\epsilon(\pi)}{2\xi v_{\mathrm{F}}\pi}\right) e^{-i\xi\theta/2} \\ \lambda e^{i\xi\theta/2} \end{pmatrix}, \tag{5.3.14}$$

The associated Berry connection components to these variables are:

$$\begin{aligned} \mathcal{A}_\pi &= i\,\langle u(\pi,\theta)|\partial_\pi u(\pi,\theta)\rangle = i\frac{v_{\mathrm{F}}^2\pi - \epsilon(\pi)\frac{d}{d\pi}\epsilon(\pi)}{\Delta\lambda\epsilon(\pi) + 2\epsilon^2(\pi)} = 0 \\ \mathcal{A}_\theta &= i\,\langle u(\pi,\theta)|\partial_\theta u(\pi,\theta)\rangle = \frac{\Delta^2 + 2\Delta\lambda\epsilon(\pi)}{4\Delta\lambda\xi\epsilon(\pi) + 8\xi\epsilon^2(\pi)} \end{aligned} \tag{5.3.15}$$

where the radial component vanishing follows from the dispersion relation in Eq. (5.3.4) $\frac{d}{d\pi}\epsilon(\pi) = \frac{v_{\mathrm{F}}^2\pi}{\epsilon(\pi)}$.

A general curve $\mathcal{C}$ in $\boldsymbol{\pi}$ space, parametrised by $t \mapsto \boldsymbol{\pi}(t)$ and with endpoints $\boldsymbol{\pi}(t_0)$ and $\boldsymbol{\pi}(t_{\mathrm{f}})$, acquires a Berry phase along that curve as:

$$\gamma_{t_0\to t_{\mathrm{f}}} = \int_{\mathcal{C}} \mathcal{A}(\boldsymbol{\pi})\cdot d\boldsymbol{\pi} = \int_{t_0}^{t_{\mathrm{f}}} \mathcal{A}(\boldsymbol{\pi}(t))\cdot\frac{d}{dt}\boldsymbol{\pi}dt \tag{5.3.16}$$

The gauge-independent Berry phase is obtained through integration along a closed path $\mathcal{C}$:

$$\gamma = \oint_{\mathcal{C}} \mathcal{A}(\boldsymbol{\pi})\cdot d\boldsymbol{\pi} \tag{5.3.17}$$

For a parametrisation that gives a closed loop, the definition of $\pi(t) = \mathbf{k} + \frac{e}{c}A(t)$ works adequately: indeed, for a pulse for which $A(-\infty) = A(+\infty) = 0$, the canonical momentum satisfies cyclicity since $\boldsymbol{\pi}_{\mathbf{k}}(-\infty) = \boldsymbol{\pi}_{\mathbf{k}}(+\infty) = \mathbf{k}$.

The association between the geometric phase found in Eq. (5.3.10) and the Berry

phase may now be made. If one takes $t_0 = -\infty$ and an arbitrary $t_\mathrm{f} \equiv t$, one obtains:

$$\gamma_{-\infty\to t} = \int_{-\infty}^{t} \mathcal{A}(\boldsymbol{\pi}(t')) \cdot \dot{\boldsymbol{\pi}}(t') dt' \tag{5.3.18}$$

The integrand of which reads:

$$\begin{aligned} \mathcal{A}(\boldsymbol{\pi}(t)) \cdot \frac{d}{dt}\boldsymbol{\pi}(t) &= \mathcal{A}_\theta(\pi(t), \theta(t)) \frac{d}{dt}\theta(t) \\ &= \left(\frac{\Delta^2 + 2\Delta\lambda\epsilon(\pi(t))}{4\Delta\lambda\xi\epsilon(\pi(t)) + 8\xi\epsilon^2(\pi(t))} \right) \dot{\theta}(t) \\ &= \xi\lambda \frac{\Delta\dot{\theta}(t)}{4\epsilon(\pi(t))}. \end{aligned} \tag{5.3.19}$$

i.e. the derivative in time of the geometric phase calculated in Eq. (5.3.7).

In this fashion, the geometric phase may be identified as an instantaneous Berry phase and conceptualised as a variation of the Berry phase due to the field perturbation. Letting $t = +\infty$, one retrieves the time-independent Berry phase as the loop becomes close.

It can be seen that, in the gapless limit, the Berry phase converges as:

$$\lim_{\Delta\to 0} \gamma^0_{\mathbf{k}} = \arctan\left(\frac{0}{-(v_\mathrm{F}|\mathbf{k}|)^2} \right) = \pi \tag{5.3.20}$$

for all states since the numerator vanishes while the denominator is strictly negative, except at the Dirac point, found at $|\mathbf{k}| = 0$, where a divergence arises. This result has been extensively reported both theoretically [105] and experimentally [9]. In this regime, this phase is strongly localised around $|\mathbf{k}| = 0$ where it diverges. Otherwise, it is smooth for nonzero gaps.

To understand where the divergence at the Dirac points arises, one may look at the Berry connection in momentum space. Neglecting the optical field and Taylor-

expanding the connection component in $|\mathbf{k}|$ gives:

$$\mathcal{A}_\theta = \frac{1}{2} - \frac{(\hbar v_\mathrm{F}|\mathbf{k}|)^2}{\Delta^2} + \frac{3(\hbar v_\mathrm{F}|\mathbf{k}|)^4}{\Delta^4} + O\left(|\mathbf{k}|^6\right). \tag{5.3.21}$$

For any nonzero gap, this quantity presents no difficulties at $\mathbf{k} = 0$, attaining a maximum at $1/2$. However, it diverges precisely when the gap is closed.

Unlike what one could naively suppose, Berry connection does not behave like a Dirac-δ distribution in $\mathbf{k}$ space. Firstly, the maximum peak at $\mathbf{k} = 0$ does not grow indefinitely as just seen. Secondly, if $\mathcal{A}_\theta$ were to converge to a Dirac$-\delta$, its area would have to be finite for any Δ. This isn't the case since the dispersion is composed of infinitely-extending bands:

$$2\pi \int_0^\infty \mathcal{A}_\pi(|\mathbf{k}|)|\mathbf{k}|d|\mathbf{k}| = \left[\frac{\pi\Delta\epsilon(|\mathbf{k}|)}{2v_\mathrm{F}^2}\right]_0^\infty \tag{5.3.22}$$

making this quantity *not* bounded.

5.3.2 Density of States

The density of states in gapless graphene, linear with energy, was seen to be unconventional, given that two-dimensional semiconductors show a *constant* profile.

What is the role of the mass in the density of states?

The starting point is the general definition of the density of states at an energy ϵ:

$$g(\epsilon) = g_v g_s \frac{1}{A} \sum_{\mathbf{k}} \delta(\epsilon - \epsilon(\mathbf{k})) \tag{5.3.23}$$

where g_v and g_s are the valley and spin degeneracies in the system and, as usual, A is the monolayer area. Since this model is spin-independent, one takes $g_s = 2$. As for the valley degeneracy, this too has to be $g_v = 2$ since the dispersion is not

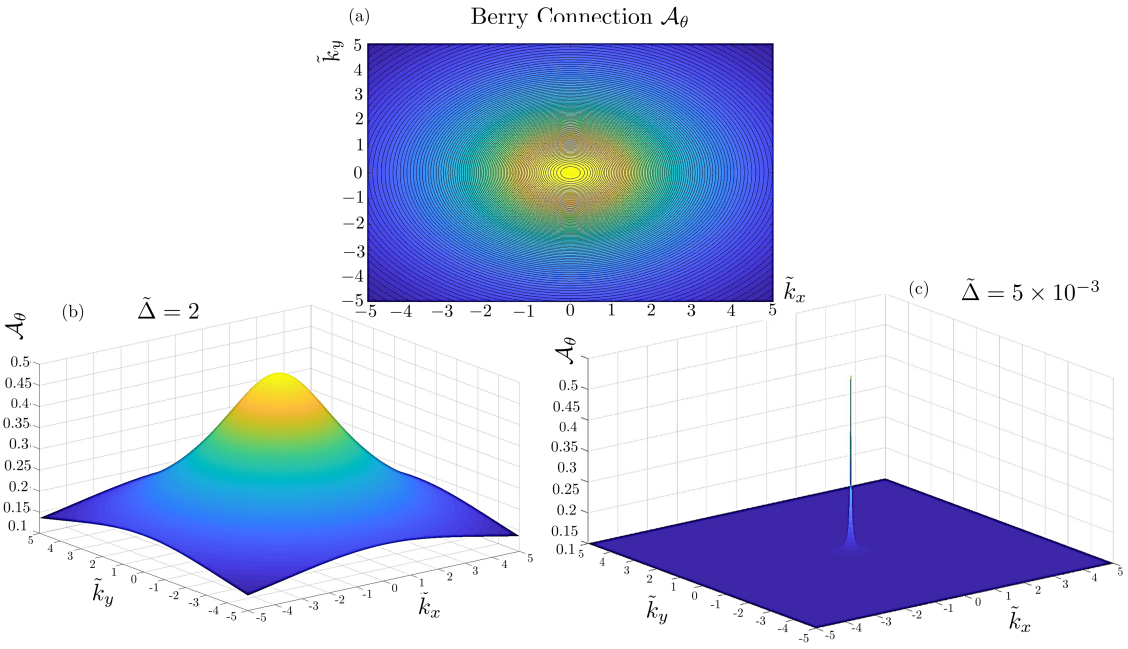

Figure 5.6: Angular component of the Berry connection in $\mathbf{k}$ space using Cartesian coordinates. (a)-(b) The connection, obtained for a gap $\tilde{\Delta} = 2$, is stronger for smaller momentum values, decreasing monotonically. Its contours show an angular asymmetry. (c) shows the same for a gap $\tilde{\Delta} = 5 \times 10^{-3}$. Note that the peak does not quite attain the value of $1/2$ due to the mesh density at the critical region $|\mathbf{k}| \approx 0$

valley-dependent. By approximating this sum to the continuum limit:

$$\sum_{\mathbf{k}} \mapsto \frac{A}{(2\pi)^2} \int d^2\mathbf{k} \tag{5.3.24}$$

and using the energy dispersion of Eq. (5.3.4) and integrating with polar coordinates $k \equiv \|\mathbf{k}\|$, $\phi_{\mathbf{k}} \equiv \arctan(k_y/k_x)$, the density of states of Eq. (5.3.23).

$$\begin{aligned} g(\epsilon) &= \frac{1}{\pi^2} \int d^2\mathbf{k} \delta(\epsilon - \epsilon(\mathbf{k})) \\ &= \frac{1}{\pi^2} \int_0^\infty dk k \int_0^{2\pi} d\phi_{\mathbf{k}} \delta(\epsilon - \epsilon(\mathbf{k})) \\ &= \frac{2}{\pi} \int_0^\infty dk k \delta(\epsilon - \epsilon(\mathbf{k})) \end{aligned} \tag{5.3.25}$$

The evaluation of the integrand is performed using the identity

$$\delta(f(k)) = \sum_i \frac{\delta(k-k_i)}{|\partial_k(k_i)|} \tag{5.3.26}$$

where the sum is performed over the zeroes of a general function $f(k)$, k_i. To calculate them, $\epsilon(\mathbf{k}) = \epsilon$ must be solved, yielding only one solution $\bar{k}$, which depends stepwise on ϵ:

$$\bar{k} = \frac{1}{\hbar v_{\mathrm{F}}}\sqrt{\left(\epsilon - \frac{\Delta}{2}\right)\left(\epsilon + \frac{\Delta}{2}\right)} \leftrightarrow \begin{cases} \bar{k}^{(1)} > 0 \text{ whenever } \epsilon > \frac{\Delta}{2} \\ \bar{k}^{(2)} = \bar{k}^{(1)} > 0 \text{ whenever } \epsilon < \frac{\Delta}{2} \\ \bar{k}^{(3)} \in \mathbb{C} \text{ whenever } -\frac{\Delta}{2} < \epsilon < \frac{\Delta}{2} \\ \bar{k}^{(4)} = 0 \text{ whenever } \epsilon = \pm\frac{\Delta}{2} \end{cases} \tag{5.3.27}$$

For the case (1) and (2), the integrand reads:

$$\delta(\epsilon - \epsilon(\mathbf{k})) = \frac{\delta\left(k-\bar{k}\right)}{\left|\frac{k v_{\mathrm{F}}^2 \hbar^2}{\epsilon(k)}\right|_{k=\bar{k}}} = \frac{\delta\left(k - \frac{1}{\hbar v_{\mathrm{F}}}\sqrt{\left(\epsilon-\frac{\Delta}{2}\right)\left(\epsilon+\frac{\Delta}{2}\right)}\right)}{\hbar v_{\mathrm{F}}\sqrt{\frac{(\epsilon+\frac{\Delta}{2})(\epsilon-\frac{\Delta}{2})}{\epsilon^2}}} \tag{5.3.28}$$

Finally, using the sifting property of the Dirac δ-function,

$$\int_{-\infty}^{\infty} f(k)\delta(k-\bar{k})dk = f(\bar{k}) \tag{5.3.29}$$

$f(k)$ is still linear in k. Hence $g(\epsilon) = 0$ whenever $-\frac{\Delta}{2} \leq \epsilon \leq \frac{\Delta}{2}$.

For nontrivial $\bar{k}$:

$$\begin{aligned} g(\epsilon) &= \left(\frac{2}{\pi\hbar^2 v_{\mathrm{F}}^2}\right)\frac{\sqrt{\left(\epsilon+\frac{\Delta}{2}\right)\left(\epsilon-\frac{\Delta}{2}\right)}}{\sqrt{\frac{(\epsilon+\frac{\Delta}{2})(\epsilon-\frac{\Delta}{2})}{\epsilon^2}}} \\ &= \frac{2|\epsilon|}{\pi\hbar^2 v_{\mathrm{F}}^2} \end{aligned} \tag{5.3.30}$$

With the aid of the Heaviside Θ step function, the dispersion is given for all energy ranges as:

$$g(\epsilon) = \frac{2|\epsilon|}{\pi\hbar^2 v_{\mathrm{F}}^2}\Theta(|\epsilon| - \frac{\Delta}{2}) \tag{5.3.31}$$

Comparing the density of states obtained for ungapped graphene, found in Eq. (2.3.24), it may then be concluded that the addition of a gap does not fundamentally change the density of states, apart from a suppression of energy states below the energy gap.

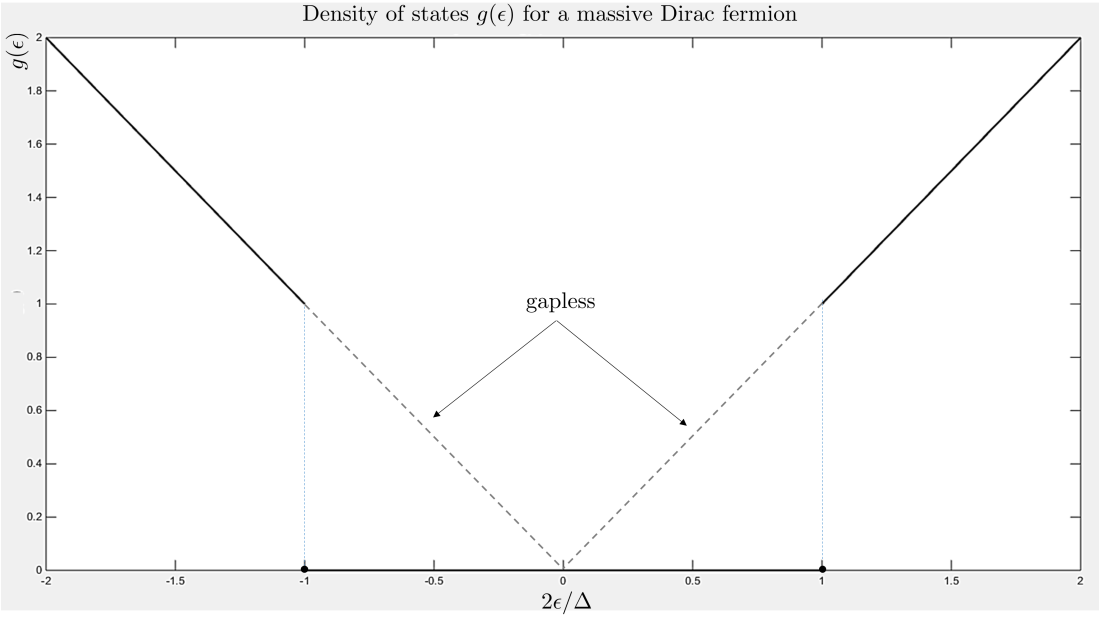

Figure 5.7: Density of states $g(\epsilon)$ as a function of the rescaled energy variable $2\epsilon/\Delta$. The same linear dependence on the energy, characteristic of gapless graphene, is seen for energies satisfying $|\epsilon| > \Delta/2$. At those critical values, the density of states vanishes given the appearance of the gap. Consequently, all energies in between the gap separation also vanish, unlike the gapless density of states, shown by the dashed, gray line.

5.4 The Massive Dirac-Bloch Equations

So far no form of the wavefunction solution to the Dirac Equation has been given. In general, as previously discussed in Section 4.2, no analytical solutions of Eq. (5.3.1) may be given due to the time dependence of the Hamiltonian through the external

parameter $\mathbf{A}(t)$. To tackle this, a general *ansatz* is constructed through expansion over a basis comprised of the instantaneous eigenstates calculated in Eq. (5.3.6):

$$|\psi^{\xi}_{\mathbf{k}}(t)\rangle = \sum_{\lambda} c^{\xi}_{\lambda\mathbf{k}}(t) \underbrace{e^{-i\lambda\Omega_{\mathbf{k}}(t)}}_{\text{dynamical}} \underbrace{e^{i\xi\lambda\gamma_{\mathbf{k}}(t)}}_{\text{Berry}} |u^{\xi}_{\lambda\mathbf{k}}(t)\rangle \tag{5.4.1}$$

Each band wavefunction is comprised of its instantaneous eigenstate and is appropriately shifted by the dynamical phase $\Omega_{\mathbf{k}}(t) = (1/\hbar)\int_{-\infty}^{t} \epsilon_{\mathbf{k}}(t')dt'$ and the instantaneous Berry phase $\gamma_{\mathbf{k}}(t)$.

Once the ansatz in Eq. (5.4.1) is inserted into Eq. (5.3.1), an equivalent differential equation is obtained for the time dynamics of the coefficients $c^{\xi}_{\lambda\mathbf{k}}(t)$: if both coefficients are lumped into a vector $C^{\xi}_{\mathbf{k}} \equiv \left(c^{\xi}_{+,\mathbf{k}}, c^{\xi}_{-,\mathbf{k}}\right)^{T}$, an equivalent condition to solve is:

$$\dot{C}^{\xi}_{\mathbf{k}} = M^{\xi}_{\mathbf{k}} C^{\xi}_{\mathbf{k}}, \tag{5.4.2}$$

where the coefficient matrix takes the form:

$$M^{\xi}_{\mathbf{k}} = \left(\frac{v_{\mathrm{F}}|\boldsymbol{\pi}_{\mathbf{k}}|}{\epsilon_{\mathbf{k}}}\right) \begin{pmatrix} 0 & e^{2i(\Omega_{\mathbf{k}} - \xi\gamma_{\mathbf{k}})}\left(i\frac{\xi\dot{\theta_{\mathbf{k}}}}{2} + \cot\theta_{\mathbf{k}}\dot{\gamma}_{\mathbf{k}}\right) \\ e^{-2i(\Omega_{\mathbf{k}} - \xi\gamma_{\mathbf{k}})}\left(i\frac{\xi\dot{\theta_{\mathbf{k}}}}{2} - \cot\theta_{\mathbf{k}}\dot{\gamma}_{\mathbf{k}}\right) & 0 \end{pmatrix} \tag{5.4.3}$$

where the following simplifications were used:

$$\begin{gathered} \dot{\theta}_{\mathbf{k}} = -\frac{\pi_y \dot{\pi}_x}{|\boldsymbol{\pi}_{\mathbf{k}}|^2} \qquad \dot{\pi}_x = \frac{|\boldsymbol{\pi}_{\mathbf{k}}||\dot{\boldsymbol{\pi}_{\mathbf{k}}}|}{\pi_x} \\ \dot{\epsilon}_{\mathbf{k}}\epsilon_{\mathbf{k}} = v_{\mathrm{F}}^2|\dot{\boldsymbol{\pi}_{\mathbf{k}}}||\boldsymbol{\pi}_{\mathbf{k}}| = -v_{\mathrm{F}}^2|\boldsymbol{\pi}_{\mathbf{k}}|^2\cot\theta_{\mathbf{k}}\dot{\theta}_{\mathbf{k}} \quad \dot{\pi}_x = \frac{e}{c}\dot{A}(t) = -eE(t) \end{gathered} \tag{5.4.4}$$

Note that $M^{\xi}_{\mathbf{k}}$ is anti-Hermitian:

$$(M^{\xi}_{\mathbf{k}})_{ij} = -(M^{\xi}_{\mathbf{k}})^{*}_{ji} \tag{5.4.5}$$

which implies that $e^{M^{\xi}_{\mathbf{k}}}$ is unitary.

To comply with the spirit of the Bloch equations, a change of variables is now performed so the electron dynamics can be more easily understood. The microscopic inversion $w^{\xi}_{\mathbf{k}} \equiv |c^{\xi}_{+,\mathbf{k}}|^2 - |c^{\xi}_{-,\mathbf{k}}|^2$ and the microscopic polarisation $q^{\xi}_{\mathbf{k}} \equiv (c^{\xi}_{+,\mathbf{k}})(c^{\xi}_{-,\mathbf{k}})^* e^{-2i\Omega_{\mathbf{k}}+i\omega_0 t}$ are now introduced as the dynamical variables of the system. The phase factor introduced for $q^{\xi}_{\mathbf{k}}$, including the pulse central frequency ω_0, ensures that the final dynamical equations retain the same form as the standard Bloch equations of a two-level system.

In this fashion, the dynamics of the two-level system when coupled to the optical field is *exactly* described by the following set of coupled equations, hereby termed the *Massive Dirac-Bloch Equations*:

$$\begin{aligned} \dot{w}^{\xi}_{\mathbf{k}} + \gamma_1 \left(w^{\xi}_{\mathbf{k}} - w^{0}_{\mathbf{k}} \right) - \left(\frac{v_{\mathrm{F}} |\boldsymbol{\pi}_{\mathbf{k}}|}{\epsilon_{\mathbf{k}}} \right) \Bigg(& 2\xi \dot{\theta}_{\mathbf{k}} \mathrm{Im}(q^{\xi}_{\mathbf{k}} e^{i(2\xi\gamma_{\mathbf{k}} - \omega_0 t)}) \\ & + 4 \cot\theta_{\mathbf{k}} \dot{\gamma}_{\mathbf{k}} \mathrm{Re}(q^{\xi}_{\mathbf{k}} e^{i(2\xi\gamma_{\mathbf{k}} - \omega_0 t)}) \Bigg) = 0 \end{aligned} \tag{5.4.6}$$

$$\dot{q}^{\xi}_{\mathbf{k}} + i \left(2\dot{\Omega}_{\mathbf{k}} - \omega_0 - i\gamma_2 \right) q^{\xi}_{\mathbf{k}} + \left(\frac{v_{\mathrm{F}} |\boldsymbol{\pi}_{\mathbf{k}}|}{\epsilon_{\mathbf{k}}} \right) \left(\cot\theta_{\mathbf{k}} \dot{\gamma}_{\mathbf{k}} + \frac{i\xi\dot{\theta}_{\mathbf{k}}}{2} \right) e^{-i(2\xi\gamma_{\mathbf{k}} - \omega_0 t)} w^{\xi}_{\mathbf{k}} = 0 \tag{5.4.7}$$

The constants $\gamma_{1(2)} \equiv 1/T_{1(2)}$ were added in a ad-hoc fashion and are phenomenological decay rates of the population inversion (microscopic polarisation), in no way different to what was done in previous sections. The quantity $w^{0}_{\mathbf{k}}$ is the equilibrium value of inversion and may be seen as the starting value of the inversion, not accounting for the optical interactions. This is assumed to be the same for both valleys.

If the system is undoped, with a Fermi level $\mu = 0$, and at temperature $T = 0$, the carriers will be all found in the valence band (and hence in an eigenstate of the system). Mathematically, this means that $c^{\xi}_{-,\mathbf{k}} = 1$ and $c^{\xi}_{+,\mathbf{k}} = 0$, implying a starting inversion of $w^{0}_{\mathbf{k}} = -1$ for all states. Otherwise, if the system is doped or is at a nonzero finite temperature, a distribution in momentum will be produced: one has

$w^0_{\mathbf{k}} = -\sinh(y)/[\cosh(x)+\cosh(y)]$, where $y = \epsilon_{\mathbf{k}}/(k_{\mathrm{B}}T)$, $x = -\mu/(k_{\mathrm{B}}T)$ and k_{B} is the Boltzmann constant.

Furthermore, if the decay rates vanish i.e. if $\gamma_1 = \gamma_2 = 0$, the two-level system is conservative and a conservation law must exist. The carrier state is a linear superposition of valence and conduction states. For a normalised quantum system, the condition $|c^{\xi}_{+,\mathbf{k}}|^2+|c^{\xi}_{-,\mathbf{k}}|^2= 1$ is thus satisfied and, in this formalism, leads to the equivalent condition:

$$\frac{d}{dt}\left(4|q^{\xi}_{\mathbf{k}}|^2+{w^{\xi}_{\mathbf{k}}}^2\right) = 0 \tag{5.4.8}$$

5.4.1 Electric Dipole Moment

The dipole moment, as was discussed previously in the derivation of the gapless DBEs, becomes far more complex than the one predicted in the SBEs. To obtain the electric dipole moment,one may impose that the driving term in the massive DBE for $\dot{q}^{\xi}_{\mathbf{k}}$ (the term which contains $w^{\xi}_{\mathbf{k}}$ in Eq. (5.4.7)) is written in the standard Bloch form:

$$i\mu^{\xi}_{\mathbf{k}}E(t) = \left(\frac{v_{\mathrm{F}}|\boldsymbol{\pi}_{\mathbf{k}}|}{2\epsilon_{\mathbf{k}}}\right)\left(\frac{\Delta\cot\theta_{\mathbf{k}}}{2\epsilon_{\mathbf{k}}}+\xi i\right)\dot{\theta}_{\mathbf{k}} \tag{5.4.9}$$

Using the functional form of $\dot{\theta}_{\mathbf{k}}$ found in Eq. (5.4.4), the electric dipole moment may be simplified to:

$$\mu^{\xi}_{\mathbf{k}} = ev_{\mathrm{F}}\left(\xi\frac{\sin\theta_{\mathbf{k}}}{2\epsilon_{\mathbf{k}}}-i\frac{\Delta\cos\theta_{\mathbf{k}}}{4\epsilon^2_{\mathbf{k}}}\right) \tag{5.4.10}$$

and one may see that the addition of a gap leads to the existence of an imaginary part of dipole moment! Furthermore, the dipole moment is anti-hermitian in the valley isospin index, meaning:

$$\mu^{\xi}_{\mathbf{k}} = -(\mu^{-\xi}_{\mathbf{k}})^*. \tag{5.4.11}$$

This property was already hinted by the anti-hermicity of the coefficient matrix calculated in Eq. (5.4.3).

5.4.2 Relation Between Valley-Dependent Dynamics

The massive Dirac-Bloch equations describe the evolution of a particular electronic state around a particular valley. One may wonder what the relationship between the coherences and inversions of each valley are.

The physical (macroscopic) polarisation of the medium is related to the coherences by the relation found in Eq. (3.4.15). The individual contribution of each valley to the polarisation is the same, implying that

$$(\mu_{\mathbf{k}}^{\xi})^* q_{\mathbf{k}}^{\xi} = (\mu_{\mathbf{k}}^{-\xi})^* q_{\mathbf{k}}^{-\xi}. \tag{5.4.12}$$

With the knowledge of the form of the dipole moment of Eq. (5.4.10), this condition implies that the microscopic polarisation of a valley must be related to its counterpart in the other valley as:

$$q_{\mathbf{k}}^{\xi} = -\frac{\mu_{\mathbf{k}}^{\xi}}{(\mu_{\mathbf{k}}^{\xi})^*} q_{\mathbf{k}}^{-\xi} = \left(\frac{\Delta^2 - 4\epsilon_{\mathbf{k}}^2 \tan^2\theta_{\mathbf{k}}}{\Delta^2 + 4\epsilon_{\mathbf{k}}^2 \tan^2\theta_{\mathbf{k}}} - i\xi \frac{4\Delta\epsilon_{\mathbf{k}} \tan\theta_{\mathbf{k}}}{\Delta^2 + 4\epsilon_{\mathbf{k}}^2 \tan^2\theta_{\mathbf{k}}} \right) q_{\mathbf{k}}^{-\xi} \tag{5.4.13}$$

If this equation is converted to polars as $q_{\mathbf{k}}^{\xi} \equiv |q_{\mathbf{k}}^{\xi}| e^{i\varphi_{\mathbf{k}}^{\xi}}$, $z_{\mathbf{k}}^{\xi} := -\frac{\mu_{\mathbf{k}}^{\xi}}{(\mu_{\mathbf{k}}^{\xi})^*} \equiv |z_{\mathbf{k}}^{\xi}| e^{i\eta_{\mathbf{k}}^{\xi}}$, one immediately notices that:

$$|z_{\mathbf{k}}^{\xi}| = 1 \qquad \text{and} \qquad \eta_{\mathbf{k}}^{\xi} = \xi \arctan\left(\frac{4\Delta\epsilon_{\mathbf{k}} \tan\theta_{\mathbf{k}}}{\Delta^2 - 4\epsilon_{\mathbf{k}}^2 \tan^2\theta_{\mathbf{k}}} \right) := \xi\Lambda_{\mathbf{k}}, \tag{5.4.14}$$

leading to the conclusion that the coherences of either valley must be only shifted by a phase. Additionally, this valley-dependent phase has the property $\eta_{\mathbf{k}}^{\xi} = -\eta_{\mathbf{k}}^{-\xi}$.

The fact that, if $\Delta = 0$ is set, they obey $q_{\mathbf{k}}^{\xi} = e^{i\pi} q_{\mathbf{k}}^{-\xi}$ hints at the possibility that this phase may be related to the Berry phase acquired by the carriers, as discussed in Section (5.3.1).

These phases are indeed equivalent! To see this, $\Lambda_{\mathbf{k}}$ as given in Eq. (5.3.10) needs to

be differentiated, allowing the following condition to be verified:

$$\begin{aligned}\dot{\Lambda}_{\mathbf{k}}(t) = 4\dot{\gamma}_{\mathbf{k}}(t) \Leftrightarrow \int_{-\infty}^{t} \dot{\Lambda}_{\mathbf{k}}(t')dt' &= \int_{-\infty}^{t} 4\dot{\gamma}_{\mathbf{k}}(t')dt' \\ \Leftrightarrow \Lambda_{\mathbf{k}}(t) - \Lambda_{\mathbf{k}}(-\infty) &= 4(\gamma_{\mathbf{k}}(t) - \gamma_{\mathbf{k}}(-\infty)) \\ \Leftrightarrow \gamma_{\mathbf{k}}(t) &= \frac{\Lambda_{\mathbf{k}}(t) - \Lambda_{\mathbf{k}}(-\infty)}{4}\end{aligned} \tag{5.4.15}$$

where $\gamma_{\mathbf{k}}(-\infty)$ was arbitrarily set to 0 i.e. $\gamma^0_{\mathbf{k}} \equiv 0$. In this fashion, a global phase is applied to the band wavefunctions used in the ansatz of Eq. (5.4.1) and the instantaneous Berry phase starts at 0, being changed as the field fluctuates. Consequently, all states acquire a vanishing geometric phase before any optical interaction, the evolution of which is exemplified in Fig. (5.4).

As for the real-valued inversion, one may simply use the conservation law of Eq. (5.4.8) to show they are the same for both valleys i.e. $w^{\xi}_{\mathbf{k}} = w^{-\xi}_{\mathbf{k}}$

5.5 Currents

The main ambition of this investigation concerns the prediction of the current generated in graphene samples when they have been subjected to conditions that gap the spectrum. To this end, a concise procedure must be applied so that signatures of nonlinear light-matter interactions can be found and analysed.

Such a current has, in general, two components and, in time domain, may be represented as $\mathbf{J}(t) = (\mathbf{J}_x(t), \mathbf{J}_y(t))^T$. The same conceptual treatment employed for ungapped graphene in Section 4.4 is employed here in order to investigate the role of the gap and the Berry phase in the current produced by each valley.

To attain this, one proceeds by first determining the μ-component ($\mu = x, y$) of the current contribution of a particular momentum state $\mathbf{p}$ in a valley ξ in time domain, here termed a *microscopic current* $j^{\xi}_{\mu,\mathbf{k}}$, by applying a suitable current density operator

$\hat{j}^{\xi}_{\mu}$ to the ansatz $|\Psi^{\xi}_{\mathbf{k}}\rangle$ given in Eq. (5.4.1), which reads:

$$\begin{aligned}\langle\Psi^{\xi}_{\mathbf{k}}|\hat{j}^{\xi}_{\mu}|\Psi^{\xi}_{\mathbf{k}}\rangle &= \sum_{\lambda,\lambda'}(c^{\xi}_{\lambda,\mathbf{k}})^{*}c^{\xi}_{\lambda',\mathbf{k}}e^{-i(\lambda'-\lambda)(\Omega_{\mathbf{k}}-\xi\gamma_{\mathbf{k}})}\,\langle u^{\xi}_{\lambda\mathbf{k}}|\hat{j}^{\xi}_{\mu}|u^{\xi}_{\lambda'\mathbf{k}}\rangle \\ &= \sum_{\lambda}\left[|c^{\xi}_{\lambda,\mathbf{k}}|^{2}\langle u^{\xi}_{\lambda\mathbf{k}}|\hat{j}^{\xi}_{\mu}|u^{\xi}_{\lambda\mathbf{k}}\rangle + (c^{\xi}_{\lambda,\mathbf{k}})^{*}c^{\xi}_{-\lambda,\mathbf{k}}e^{2i\lambda(\Omega_{\mathbf{k}}-\xi\gamma_{\mathbf{k}})}\,\langle u^{\xi}_{\lambda\mathbf{k}}|\hat{j}^{\xi}_{\mu}|u^{\xi}_{-\lambda\mathbf{k}}\rangle\right]\end{aligned} \tag{5.5.1}$$

Following the same reasoning as outlined in the previous section, a valence band must be subtracted ad-hoc to ensure no divergences are present, meaning the full microscopic current takes the form:

$$j^{\xi}_{\mu,\mathbf{k}}(t) = \langle\Psi^{\xi}_{\mathbf{k}}|\hat{j}^{\xi}_{\mu}|\Psi^{\xi}_{\mathbf{k}}\rangle - \langle u^{\xi}_{-,\mathbf{k}}|\hat{j}^{\xi}_{\mu}|u^{\xi}_{-,\mathbf{k}}\rangle \tag{5.5.2}$$

The current elements are now calculated. Two current contributions are present, depending on whether the current is originated from electronic transitions within the same band (*intraband*), or across different bands (*interband*).

When $\mu = x$, the elements take the form:

$$\begin{aligned}&\langle u^{\xi}_{\lambda\mathbf{k}}|\hat{j}^{\xi}_{x}|u^{\xi}_{\lambda'\mathbf{k}}\rangle = -ev_{\mathrm{F}}\xi\,\langle u^{\xi}_{\lambda\mathbf{k}}|\sigma_{x}|u^{\xi}_{\lambda'\mathbf{k}}\rangle = \left(\frac{-i\xi ev_{\mathrm{F}}^{3}|\boldsymbol{\pi}_{\mathbf{k}}|^{2}}{\epsilon_{\mathbf{k}}\sqrt{(\lambda\Delta+2\epsilon_{\mathbf{k}})(\lambda'\Delta+2\epsilon_{\mathbf{k}})}}\right)\times \\ &\left(\left(\xi\tfrac{\lambda\Delta+2\epsilon_{\mathbf{k}}}{2v_{\mathrm{F}}|\boldsymbol{\pi}_{\mathbf{k}}|}\right)e^{i\xi\theta_{\mathbf{k}}/2} \quad \lambda e^{-i\xi\theta_{\mathbf{k}}/2}\right)\begin{pmatrix}0 & -1\\ 1 & 0\end{pmatrix}\begin{pmatrix}\left(\xi\tfrac{\lambda'\Delta+2\epsilon_{\mathbf{k}}}{2v_{\mathrm{F}}|\boldsymbol{\pi}_{\mathbf{k}}|}\right)e^{-i\xi\theta_{\mathbf{k}}/2}\\ \lambda' e^{i\xi\theta_{\mathbf{k}}/2}\end{pmatrix} \\ &= \left(\frac{-i\xi ev_{\mathrm{F}}^{2}|\pi|}{\sqrt{(\lambda\Delta+2\epsilon_{\mathbf{k}})(\lambda'\Delta+2\epsilon_{\mathbf{k}})}}\right)\left(\frac{\lambda\lambda'\Delta}{\epsilon_{\mathbf{k}}}\cos(\xi\xi\theta_{\mathbf{k}}) + (\lambda e^{-i\xi\theta_{\mathbf{k}}} - \lambda' e^{i\xi\theta_{\mathbf{k}}})\right) \\ &= \begin{cases} -\frac{\lambda ev_{\mathrm{F}}^{2}|\boldsymbol{\pi}_{\mathbf{k}}|}{\epsilon_{\mathbf{k}}}\cos\theta_{\mathbf{k}} & \text{for } \lambda'=\lambda \ \text{ (intraband)} \\ \frac{ev_{\mathrm{F}}\Delta}{2\epsilon_{\mathbf{k}}}\cos\theta_{\mathbf{k}} + i\xi\lambda ev_{\mathrm{F}}\sin\theta_{\mathbf{k}} & \text{for } \lambda'=-\lambda \ \text{ (interband)}\end{cases}\end{aligned} \tag{5.5.3}$$

As for the $\mu = y$ component, they are:

$$\begin{aligned}
&\langle u^{\xi}_{\lambda\mathbf{k}}|\hat{j}^{\xi}_{y}|u^{\xi}_{\lambda'\mathbf{k}}\rangle = -ev_{\mathrm{F}}\,\langle u^{\xi}_{\lambda\mathbf{k}}|\sigma_y|u^{\xi}_{\lambda'\mathbf{k}}\rangle = \left(\frac{-iev_{\mathrm{F}}^3|\boldsymbol{\pi}_{\mathbf{k}}|^2}{\epsilon_{\mathbf{k}}\sqrt{(\lambda\Delta+2\epsilon_{\mathbf{k}})(\lambda'\Delta+2\epsilon_{\mathbf{k}})}}\right)\times \\
&\left(\left(\xi\tfrac{\lambda\Delta+2\epsilon_{\mathbf{k}}}{2v_{\mathrm{F}}|\boldsymbol{\pi}_{\mathbf{k}}|}\right)e^{i\xi\theta_{\mathbf{k}}/2}\quad \lambda e^{-i\xi\theta_{\mathbf{k}}/2}\right)\begin{pmatrix}0 & -1\\ 1 & 0\end{pmatrix}\begin{pmatrix}\left(\xi\tfrac{\lambda'\Delta+2\epsilon_{\mathbf{k}}}{2v_{\mathrm{F}}|\pi|}\right)e^{-i\xi\theta_{\mathbf{k}}/2}\\ \lambda' e^{i\xi\theta_{\mathbf{k}}/2}\end{pmatrix} \\
&= \left(\frac{-i\xi ev_{\mathrm{F}}^2|\boldsymbol{\pi}_{\mathbf{k}}|}{\sqrt{(\lambda\Delta+2\epsilon_{\mathbf{k}})(\lambda'\Delta+2\epsilon_{\mathbf{k}})}}\right)\left(-i\frac{\lambda\lambda'\Delta}{\epsilon_{\mathbf{k}}}\sin(\xi\theta_{\mathbf{k}})+(\lambda e^{-i\xi\theta_{\mathbf{k}}}-\lambda' e^{i\xi\theta_{\mathbf{k}}})\right) \\
&= \begin{cases} -\frac{\lambda ev_{\mathrm{F}}^2|\boldsymbol{\pi}_{\mathbf{k}}|}{\epsilon_{\mathbf{k}}}\sin\theta_{\mathbf{k}} & \text{for}\quad \lambda'=\lambda\quad\text{(intraband)}\\ \frac{ev_{\mathrm{F}}\Delta}{2\epsilon_{\mathbf{k}}}\sin\theta_{\mathbf{k}} - i\xi\lambda ev_{\mathrm{F}}\cos\theta_{\mathbf{k}} & \text{for}\quad \lambda'=-\lambda\quad\text{(interband)}\end{cases}
\end{aligned} \tag{5.5.4}$$

These ingredients finally allow an expression for the regularised current of Eq. (5.5.2) to be written as:

$$\begin{aligned}
j^{\xi}_{x,\mathbf{k}}(t) = |c^{\xi}_{+,\mathbf{k}}|^2\left(-\frac{ev_F^2|\boldsymbol{\pi}_{\mathbf{k}}|}{\epsilon_{\mathbf{k}}}\cos\theta_{\mathbf{k}}\right)+\left(|c^{\xi}_{-,\mathbf{k}}|^2-1\right)\left(\frac{ev_F^2|\boldsymbol{\pi}_{\mathbf{k}}|}{\epsilon_{\mathbf{k}}}\cos\theta_{\mathbf{k}}\right) \\
+q^{\xi}_{\mathbf{k}}e^{i(2\xi\gamma_{\mathbf{k}}-\omega_0 t)}\left(\frac{ev_{\mathrm{F}}\Delta}{2\epsilon_{\mathbf{k}}}\cos\theta_{\mathbf{k}}-\xi iev_{\mathrm{F}}\sin\theta_{\mathbf{k}}\right) \\
+(q^{\xi}_{\mathbf{k}})^* e^{-i(2\xi\gamma_{\mathbf{k}}-\omega_0 t)}\left(\frac{ev_{\mathrm{F}}\Delta}{2\epsilon_{\mathbf{k}}}\cos\theta_{\mathbf{k}}+\xi iev_{\mathrm{F}}\sin\theta_{\mathbf{k}}\right) \\
= -ev_F\left(\frac{v_{\mathrm{F}}|\boldsymbol{\pi}_{\mathbf{k}}|}{\epsilon_{\mathbf{k}}}\cos\theta_{\mathbf{k}}(w^{\xi}_{\mathbf{k}}+1)-\frac{\Delta}{\epsilon_{\mathbf{k}}}\cos\theta_{\mathbf{k}}\mathrm{Re}\left(q^{\xi}_{\mathbf{k}}e^{i(2\xi\gamma_{\mathbf{k}}-\omega_0 t)}\right)\right. \\
\left.-2\xi\sin\theta_{\mathbf{k}}\mathrm{Im}\left(q^{\xi}_{\mathbf{k}}e^{i(2\xi\gamma_{\mathbf{k}}-\omega_0 t)}\right)\right)
\end{aligned} \tag{5.5.5}$$

$$\begin{aligned}
j^{\xi}_{y,\mathbf{k}} = |c^{\xi}_{+,\mathbf{k}}|^2\left(-\frac{ev_F^2|\pi|}{\epsilon_{\mathbf{k}}}\cos\theta_{\mathbf{k}}\right)+\left(|c^{\xi}_{-,\mathbf{k}}|^2-1\right)\left(\frac{ev_F^2|\boldsymbol{\pi}_{\mathbf{k}}|}{\epsilon_{\mathbf{k}}}\cos\theta_{\mathbf{k}}\right) \\
+q^{\xi}_{\mathbf{k}}e^{i(2\xi\gamma_{\mathbf{k}}-\omega_0 t)}\left(\frac{ev_{\mathrm{F}}\Delta}{2\epsilon_{\mathbf{k}}}\sin\theta_{\mathbf{k}}+\xi iev_{\mathrm{F}}\cos\theta_{\mathbf{k}}\right) \\
+(q^{\xi}_{\mathbf{k}})^* e^{-i(2\xi\gamma_{\mathbf{k}}-\omega_0 t)}\left(\frac{ev_{\mathrm{F}}\Delta}{2\epsilon_{\mathbf{k}}}\sin\theta_{\mathbf{k}}-\xi iev_{\mathrm{F}}\cos\theta_{\mathbf{k}}\right) \\
= -ev_F\left(\frac{v_{\mathrm{F}}|\pi|}{\epsilon_{\mathbf{k}}}\sin\theta_{\mathbf{k}}w^{\xi}_{\mathbf{k}}-\frac{\Delta}{\epsilon_{\mathbf{k}}}\sin\theta_{\mathbf{k}}\mathrm{Re}\left(q^{\xi}_{\mathbf{k}}e^{i(2\xi\gamma_{\mathbf{k}}-\omega_0 t)}\right)\right. \\
\left.+2\xi\cos\theta_{\mathbf{k}}\mathrm{Im}\left(q^{\xi}_{\mathbf{k}}e^{i(2\xi\gamma_{\mathbf{k}}-\omega_0 t)}\right)\right)
\end{aligned} \tag{5.5.6}$$

It can thus be seen that once an appropriate evaluation of the inversions and coherences is obtained, the current contribution of a single two-level system is uniquely determined.

Given the decomposition of the currents performed in Eqs. (5.5.3)-(5.5.4), the intraband current terms may be identified as the ones containing $(w_{\mathbf{k}}^{\xi}+1)$ (where the term +1 comes from the regularisation), whereas the interband current terms depend on the microscopic polarisation $q_{\mathbf{k}}^{\xi}$. Two such terms may be found; in particular, the one containing $(\Delta/\epsilon_{\mathbf{k}})$ is a mass-induced contribution and naturally vanishes for ungapped dispersions.

It can be seen that, when taking $\Delta = 0$, both valleys contribute exactly the same to the current, i.e. $\mathbf{j}_{\mathbf{k}}^{\xi}(t) = \mathbf{j}_{\mathbf{k}}^{-\xi}(t)$, leading to a valley degeneracy factor $g_{\mathrm{v}} = 2$ in the current of Eq. (6.4.41) as previously reported in Refs. [79, 82].

The physical current is finally obtained by appropriately taking all momentum contributions of both valleys into account. In the continuum limit, it is:

$$\mathbf{J}(t) = \frac{g_s}{d(2\pi)^2} \sum_{\xi} \int \mathbf{j}_{\mathbf{k}}^{\xi}(t) d\mathbf{k}, \tag{5.5.7}$$

where d is the thickness of the monolayer and $g_s = 2$ is a spin degeneracy factor, $d\mathbf{k} = kdkd\phi$ is the 2-dimensional differential in momentum space and the sum is performed over both valleys.

The analytical expressions calculated in Eqs. (5.5.5) -(5.5.6) encapsulate the *exact* light-matter interactions predicted by the Dirac equation , since no approximations were applied, and displays remarkable physics richness. The next section will be focused on analysing and interpreting such current output.

5.6 Simulations

The massive Dirac-Bloch equations encapsulate a breadth of optical phenomena which become highly nontrivial in the nonlinear optical regime, once the electrons are coupled to ultrashort and intense light fields. No analytical solution to these equations can be obtained, especially in this regime. Therefore, a numerical evaluation of them is necessary.

To that end, Eqs (5.4.7)-(5.4.6) have been rescaled so that they are dimensionless. Such dimensionless equations, alongside the respective scaling for all variables, may be found in Appendix A.1. In particular, the role of the gap is now introduced via the dimensionless parameter $\tilde{\Delta} \equiv \Delta/(\hbar\omega_0)$, conveniently rescaled such that a gap satisfying $\tilde{\Delta} = 1$ is exactly resonant with the pump photon.

As for the numerical algorithm used to obtain a solution to the massive DBEs, an explicit, adaptive, parallelised fourth-order Runge-Kutta algorithm was used. Once the microscopic polarisations and inversions are known, the microscopic currents may be obtained and consequently integrated appropriately in momentum space. A fine mesh of the space must be used, in general requiring approximately 1000 radial points and and 500 angular points.

Furthermore, since the present model deals with infinitely-extending bands, a radial cut-off must be imposed in such a way that microscopic current amplitudes are within a strict tolerance ε_{c} from zero.

In order to estimate where to apply such cutoff boundary, one may look for a wavevector $\mathbf{k}_{\mathrm{c}}$ such that $\max|q_{\mathbf{k}_{\mathrm{c}}}| < \varepsilon_{\mathrm{c}}$. In Fig 5.8, such a quantity is shown over momentum space for a gap $\tilde{\Delta} = 1$. In (a), it is clear that at $\tilde{\mathbf{k}} = 0$, where the gap is exactly the same as the photon energy, the polarisation hits its maximum of $1/2$.

Subsequently, this value decreases as the momentum increases, and hence the detuning, increases. Such a polarisation decrease seems to be further enhanced by higher

values of the gap, as seen in (*b*) for a gap of $\tilde{\Delta} = 1$ and $\tilde{\Delta} = 4$. In any case, one may confidently say that by $|\tilde{\mathbf{k}}| \approx 10$, the contributions to the current are negligible and the integral over momentum space is properly accounted for by considering states *up to* this critical value.

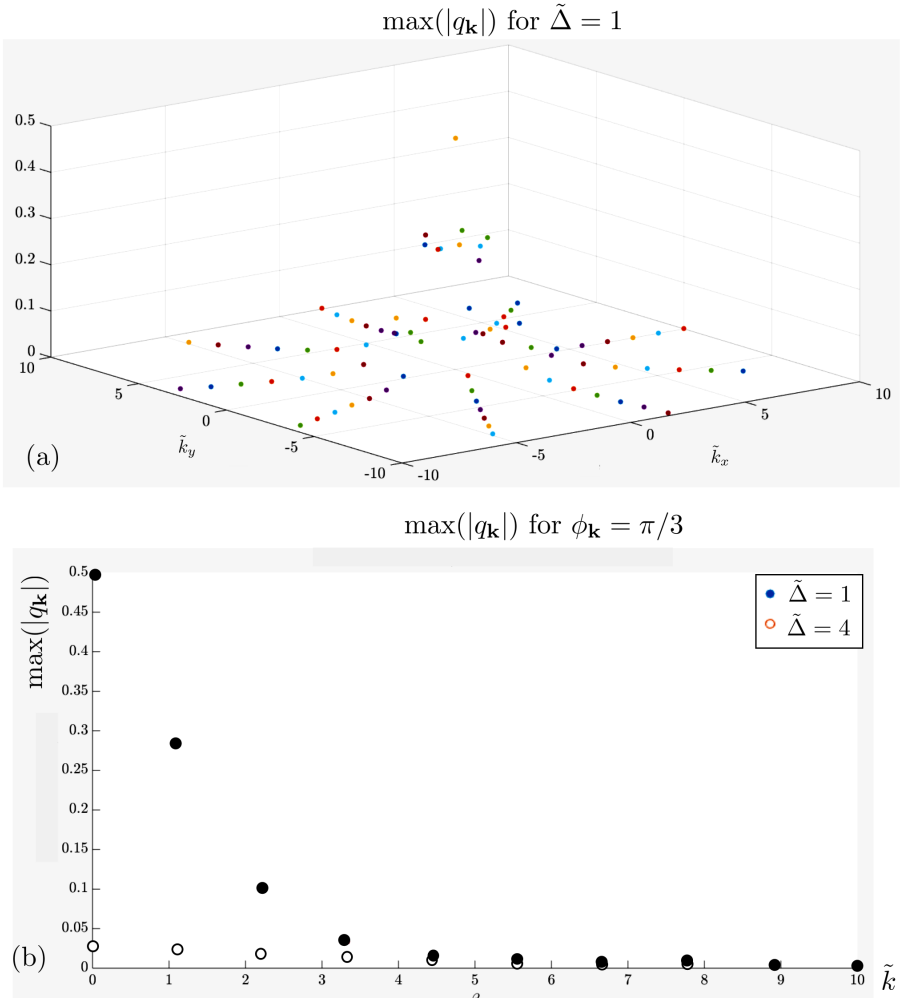

Figure 5.8: Visualisation of max$|q_{\mathbf{k}}|$ (a) in momentum space for a gap $\tilde{\Delta} = 1$. (b) for a fixed angle $\phi_{\tilde{\mathbf{k}}} = \pi/3$, varying the magnitude $\tilde{k}$, for $\tilde{\Delta} = 1$ and $\tilde{\Delta} = 4$.

To probe the system response in the adequate regime, one may take the following excitation conditions: the graphene monolayer is pumped with a normally-incident pulse of duration $t_0 = 31.9$ fs, central wavelength $\lambda_0 = 4\mu$m and frequency $\omega_0 = 4.71 \times 10^{14}$ s^{-1}, photon energy $\hbar\omega_0 = 0.31$ eV, intensity $I = 0.45$ GW/cm^2

and at temperature $T = 0$°K. Additionally, realistic localised zero-averaged fields are assumed: $A(t) = A_0 \text{sech}(t/t_0)\sin(\omega_0 t)$ and $E(t) = -\partial_t A/c$. In order not to introduce unphysical static fields, these fields were chosen so that they satisfy $\int_{-\infty}^{\infty} A(t)dt = \int_{-\infty}^{\infty} E(t)dt = 0$.

Attending to the considerations outlined in Section 3.5.2, the timescales of any dephasing time is much larger than the pulse duration t_0 and hence neglected. Mathematically, this leads to setting $\gamma_1 = \gamma_2 = 0$. In this instance, all two-level systems are coherent and the probability conservation law expressed in Eq. (5.4.8) applies.

This condition is used in the code to ensure that the numerical outputs are confidently given within a strict tolerance threshold. The opening of a gap leads to such a constraint to be much more easily achieved: for instance, if the massive DBEs are solved with a discretised time array with $2^{15} = 32768$ datapoints, tolerances of approximately 10^{-15} may be achieved for all simulated states.

5.6.1 The Role of the Energy Gap

The role of energy gap in the generated current is now studied with the aid of a dimensionless gap parameter $\tilde{\Delta}$. As previously mentioned, massless Dirac electrons in either valley contribute equally to the generation of current. The linearly-polarised pulse, along the $\hat{x}$ direction, does not create $\mathbf{J}_y$ currents which must therefore vanish identically, once their corresponding microscopic currents are integrated over all momenta and valley contributions; this is indeed observed in these simulations, and is a crucial indicator of the validity of the underlying numerics [79].

In the massive regime, both components are addressed differently by the valleys, even in this simple polarisation configuration. As will be seen, in this regime, each valley contribution to the current, once a gap is present, does not necessarily equate to a

valley degeneracy factor $g_v = 2$.

In particular, given the optical field linear polarisation, which was assumed to be along the $\hat{x}$ direction, the model should only produce currents in the same direction. This expectation is of course not warranted if some anisotropy mechanism takes place in the sample. For instance, optical activity in chiral media is known to rotate the incoming electric field, thus possibly allowing for current generation in a new direction.

Graphene is not known to admit such mechanisms. However, the calculation of the y component of the current produced in one valley becomes nonzero. For this exact reason, it is necessary to account for both valleys - as it will be seen, only the sum of both contributions yields a vanishing J_y. As for the J_x, it is seen to be composed of two identical contributions from both valleys.

The effect of the mass and Berry phase on the current may be seen in Fig. 5.9(a), where the full current in time domain $J_x(t)$ is shown. Its amplitude increases as the energy gap is increased, until a maximum is reached when the photon is resonant with the energy gap i.e. when $\tilde{\Delta} = 1$. Subsequently, the current amplitude vanishes for increasingly larger gaps.

This behaviour is best understood if the intraband and interband currents are plotted separately. Fig. 5.9(b) shows the intraband current contribution, where it can be seen that its amplitude is maximal when $\tilde{\Delta} = 0$ and monotonically decreasing with increasing energy gap. Fig. 5.9(c) shows the interband current, itself composed of the two polarisation-dependent terms in Eq. (5.5.5), once integrated over momentum and valley isospin. The full current dependence on the mass stems primarily from the interband contributions, as Fig. 5.9(c) follows the pattern just described.

It must be remarked that both interband current terms are in phase. Figs 5.9 (b, c) further reveal that the full current emerges from a very complex interplay of the competing, out-of-phase contributions of intraband and interband currents.

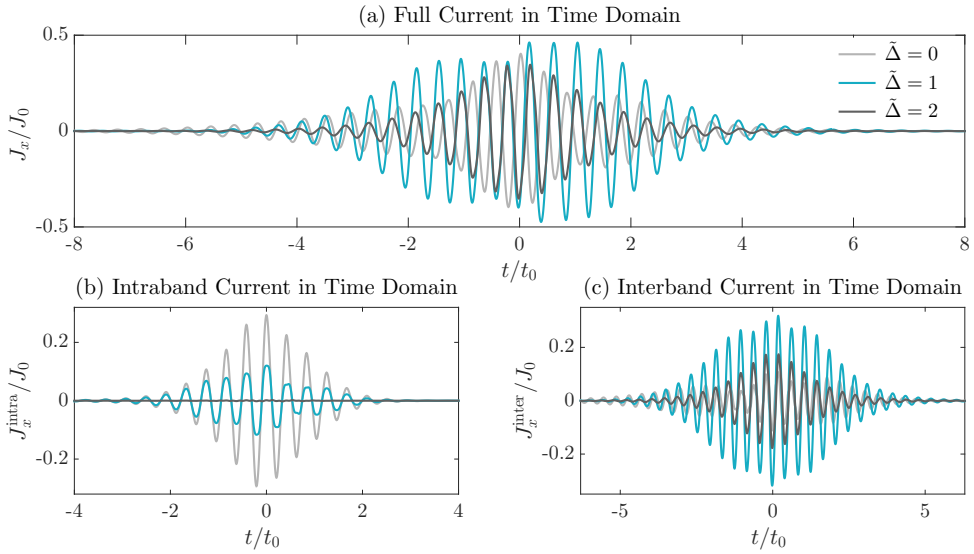

Figure 5.9: The full photo-generated current and its separate contributions in time domain, rescaled in units of $J_0 = -e\omega_0^2/(4dv_{\mathrm{F}})$. (a) The total current, composed of both intraband and interband contributions. Its overall dependence on the mass stems primarily from the interband contribution. (b) The intraband current, generated from electronic transitions within the same band. Its amplitude is monotonically decreasing as the gap increases and maximal when the dispersion is ungapped. (c) The interband contribution, generated from electronic transitions across the bands. It is comprised of two terms, one being exclusively present only for gapped dispersions. The interband current amplitude is maximal when the photon energy is resonant with the gap, rapidly decreasing for larger gaps.

More optically pertinent information can be obtained by analysing the full current spectrum $S(\omega) = |\omega \mathbf{J}(\omega)|^2$, in dB units, versus the harmonics order ω/ω_0, a dimensionless parameter so that the pump pulse is centred spectrally at $\omega/\omega_0 = 1$, which is displayed in in Fig. 5.10(a).

The spectra show strong odd harmonics being generated, commonly expected of a $\chi^{(3)}$ material. The exceedingly small peaks found for $\omega/\omega_0 = 2, 4, ...$ on this logarithmic scale can be seen as numerical artefacts and suggest that even harmonic generation is generally absent. However, particular gap values can be seen to yield rather enhanced even-harmonic peaks.

The intraband and full current, itself composed of both the intraband and interband contributions, allows for the identification of the interband current as the one re-

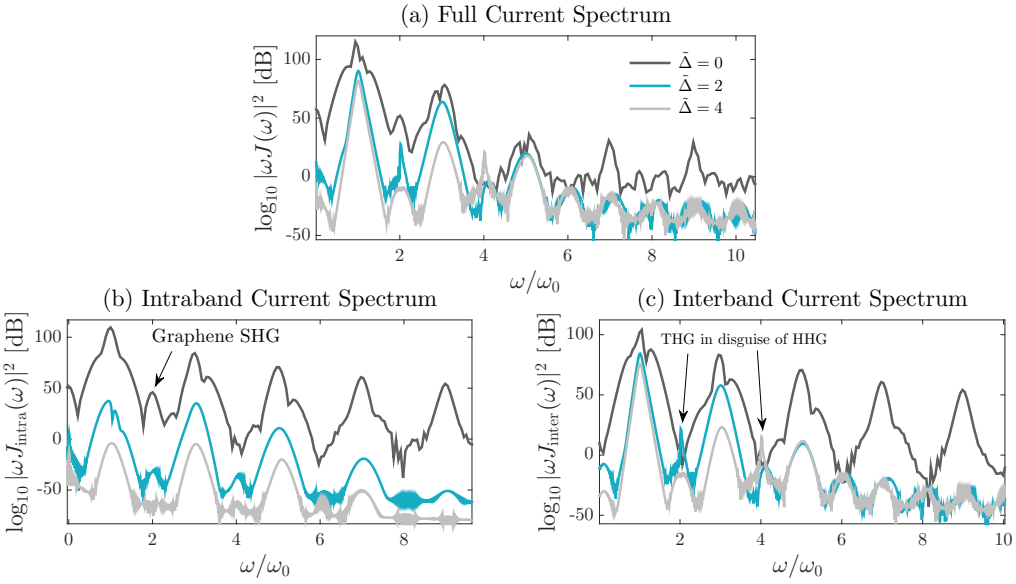

Figure 5.10: Current spectra predicted by the massive DBEs. (a) The total spectrum shows stronger odd harmonic generation than even harmonic generation. For gapped systems, even-harmonic peaks, which are plotted in (c), are generated through third harmonic generation (THG) in disguise of higher harmonic generation (HHG). Such peaks are shown with the second and fourth-harmonic enhancements, respectively for gaps satisfying $\tilde{\Delta} = 2, 4$. For vanishing gaps, even harmonic generation originates from the centrosymmetry breaking mechanism, which breaks the static centrosymmetry of the lattice and is seen in the intraband spectrum of (b). Generally, the intraband harmonic peaks decrease monotonically as the gap is increased.

sponsible for the resonant peaks found in the spectrum.

This can be seen in Fig. 5.11, where a large set of dimensionless gap parameters is displayed. Importantly, the intraband does not show second harmonic waves apart from the gapless case, as seen in (a). Strikingly, any real value of the $\tilde{\Delta}$ leads to an harmonic enhancement at that particular harmonic order. These can be appreciated in (b): for instance, a $\tilde{\Delta} = 2.75$ shows a peak in the harmonic order $\omega/\omega_0 = 2.75$. One may then wonder: *"Do integer values of $\tilde{\Delta}$ increase the harmonic intensity at those particular orders considerably?"*

In order to understand the origin of this behaviour, now with only two nonzero integer dimensionless gap parameters to simplicity the analysis, both the intraband and interband current spectra are respectively shown in Fig. 5.10(b, c).

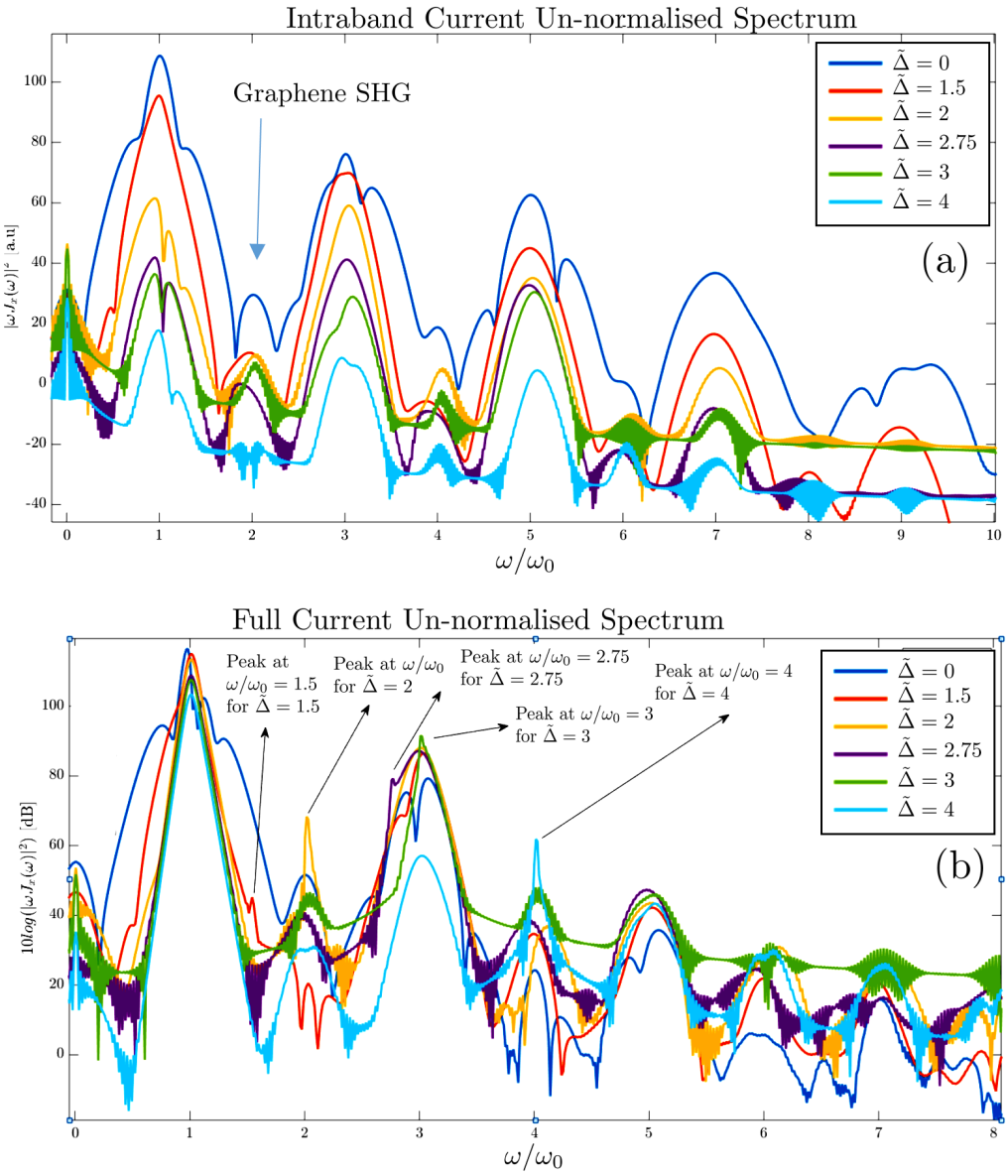

Figure 5.11: Output spectra for $\psi_0 = 2$. (a) Intraband current spectrum and (b) Full current spectrum. The role of the dimensionless gap parameter $\tilde{\Delta}$ can be analysed. The interband-driven resonant peaks are generally found at the same harmonic order as $\tilde{\Delta}$.

For both contributions, odd-order harmonic peaks are predominant over even-order harmonic peaks. As for the interband current, clear n^{th}-order harmonic peaks appear when the gap is tuned so that $\tilde{\Delta} = n$, for a positive integer $n \geq 2$. It must be remarked that such peaks are always generated for *any* gap value but will not be contribute to particular harmonic orders unless this tunability condition is met i.e. for integer $\tilde{\Delta}$. In particular, when tuned to even integers, peaks at even harmonic orders are generated in the emission spectrum, as shown in Fig. 5.10.

Physically, the observed even harmonic peaks do not arise from $\chi^{(2)}$-like processes (occurring only in non-centrosymmetric media) but are rather understood through the coherent interference among odd harmonics, a well-established strong-field effect termed "*THG in disguise of SHG*" occurring exclusively at the femtosecond scale. In the ultrashort (few-cycle), and intense optical regime, the electromagnetic field is able to excite abruptly a tremendous amount of carriers which would otherwise remain in the valence band due to their off-resonant condition.

The signature of such transitions can be inferred from the inversion $w_{\mathbf{k}}$. For instance, very few transitions to the conduction band are attained in the linear optical regime - leading to the condition $w_{\mathbf{k}} \approx -1$ for all momenta. In contrast, high field intensities allow Rabi flopping of a coherent two-level system - thus rendering such assumption unrealistic - and may consequently generate highly nontrivial inversion behaviour on which the generated current depends on. Most notably, ungapped graphene admits instantaneous band transitions, leading to a step-like behaviour of $w_{\mathbf{k}}$ around the Dirac points (as can be seen in Fig. (3) of Ref. [82]).

Fig (3.6) of Ref. [106] is illustrative of the emergence of the mechanism of *"THG in disguise of SHG"*: if one fixes the transition frequency $\omega_T \equiv (\epsilon^{\xi}_{+1,\mathbf{k}} - \epsilon^{\xi}_{-1,\mathbf{k}})/\hbar = 2\epsilon_{\mathbf{k}}/\hbar$, the generated spectrum can be obtained for a fixed field excitation parameter, here taken as the Rabi frequency peak $\omega_R = \max(\mu_{\mathbf{k}} E/\hbar)$.

For instance, if one fixes $\omega_T = 2\omega_0$ and considers quasiresonant states (for which

$\epsilon_{\mathbf{k}} \approx \Delta/2$), it can be seen that this condition is approximate to $\Omega_T/\omega_0 = 2\epsilon_{\mathbf{k}}/(\hbar\omega_0) \approx \Delta/(\hbar\omega_0)$. Now, if ω_R is progressively increased, it seems clear that a THG peak appears. However, and most interestingly, when it hits the critical value $\Omega_R = 2\omega_0$, the THG peak is heavily suppressed and interfere with the fundamental mode to create a visible spike at $\omega/\omega_0 = 2$.

This phenomenon is also predicted to be only present for few-cycle pulses, where a suppression of this peak at $\omega/\omega_0 = 2$ is observed when increasing the pulse duration (Fig. (3.7) of Ref. [106]). These simulations were performed with a 15-cycle pulse and these peaks are also observed in them [Fig. 5.13(a)], even if a slightly different formalism is employed.

As given by Eq. (6.4.41), the spectrum of Fig. (5.10) is comprised of a sum of two-level systems, each one with a different ω_T. However, the condition $\Delta/(\hbar\omega_0) = 2$ is sufficient to capture the collective contributions of these quasiresonant states on the SHG peak. Pages 38-40 and 157-158 of Ref. [106], as well as Ref. [107] include plenty of information on the physics underlying this process.

As a final check, one may wonder if these results, mainly the interband-driven harmonic enhancement that was consistently found in the simulations, is not dependent on the parity of the electromagnetic fields. For this comparison, the spectrum is obtained when exciting with an even or odd electromagnetic vector potential $\mathbf{A}$, giving the following set of dimensionless fields:

$$\Psi(t)_{\text{odd}} = \psi_0 \text{sech}(t)\cos(\Omega_0 t) - \frac{\psi_0}{\Omega_0}\text{sech}(t)\tanh(t)\sin(\Omega_0 t) \tag{5.6.1}$$

$$A(t)_{\text{odd}} = \frac{\psi_0}{\Omega_0}\text{sech}(t)\sin(\Omega_0 t) \tag{Odd A}$$

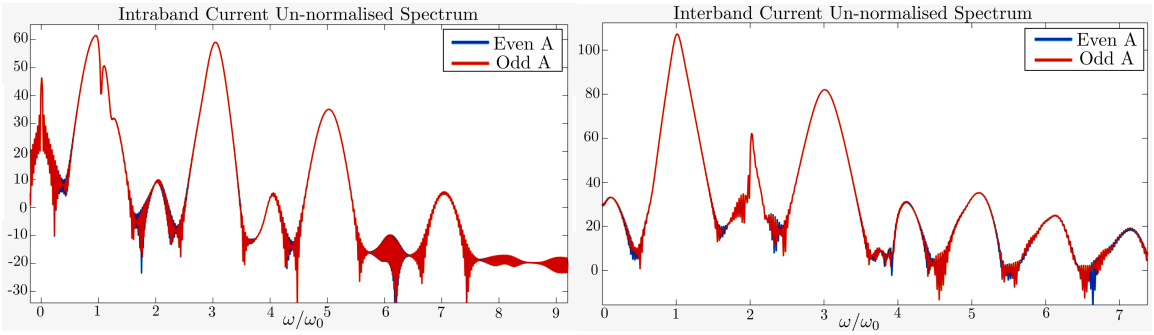

Figure 5.12: Comparison of the spectrum of (a) the intraband current and (b) the interband current obtained when exciting the sample with an even vector potential (blue) or odd (red), for a gap $\tilde{\Delta} = 2$. The interband-driven harmonic enhancement prediction is not affected by the field parity.

$$\Psi(t)_{\text{even}} = -\psi_0 \text{sech}(t)\sin(\Omega_0 t) - \frac{\psi_0}{\Omega_0}\text{sech}(t)\tanh(t)\cos(\Omega_0 t) \tag{5.6.2}$$

$$A(t)_{\text{even}} = -\frac{\psi_0}{\Omega_0}\text{sech}(t)\cos(\Omega_0 t) \qquad \text{(Even A)}$$

5.6.2 The Role of the Berry Phase

The Berry phase in Eq. (5.3.10) induces non-trivial contributions to the current spectra just discussed and its role on the generation of new harmonics is now discussed. In order to achieve this, the Berry phase and its derivative are neglected by setting $\gamma_{\mathbf{k}}(t) = \dot{\gamma}_{\mathbf{k}}(t) = 0$ in the massive DBEs [Eqs. (4.2.20)-(4.2.21)] and in the microscopic current of Eq. (5.5.2). This procedure is physically consistent since $\mathbf{J}_y(t)$ still vanishes after such terms are disregarded. The spectra of the full current and its intraband/interband contributions, obtained by including or excluding such terms, may now be compared.

General features can be captured and are exemplified for a particular gap with $\tilde{\Delta} = 2$ (resulting in a realistic energy gap value of $\Delta = 0.62$ eV), whose spectra are shown in Fig. 5.13. One can observe that the Berry phase acts on the full current, shown in Fig. 5.13(a), and considerably suppresses odd harmonics and enhances the relevant even harmonics. The extent of the odd harmonics suppression seems to grow for

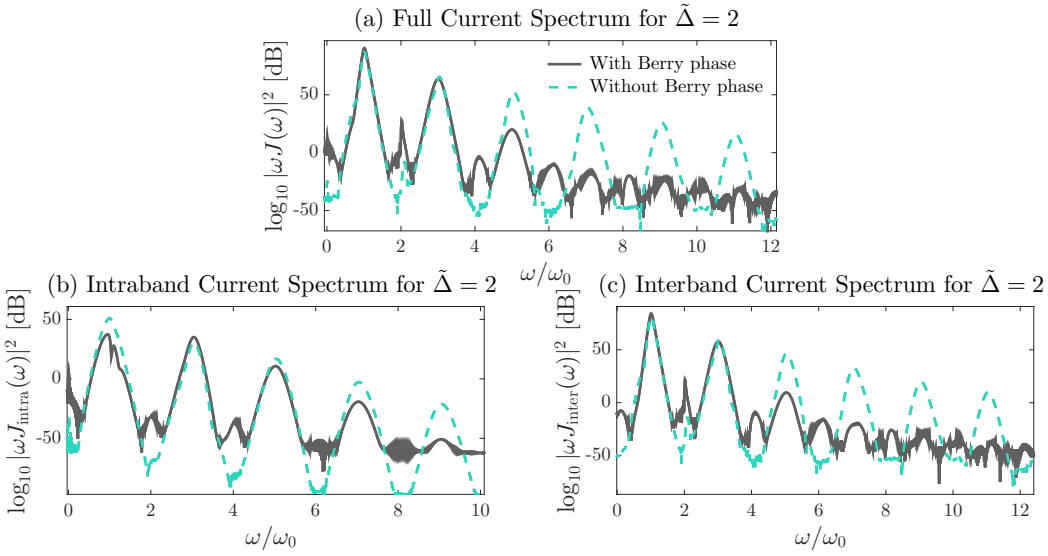

Figure 5.13: Comparison of current spectra in the presence or absence of the Berry phase for a gap $\Delta = 2\hbar\omega_0 = 0.62$ eV. The full current spectrum is shown in (a), displaying a general peak suppression of the dominant, odd harmonics. Rather negligible even harmonic peaks only exist once this phase is considered. These features are caused by the dominant, interband current, plotted in (c). The effect of the harmonic interference on the Berry phase contribution to the interband current for such a gap, here seen through the peak suppression at $\omega/\omega_0 = 2$. The intraband spectrum, shown in (b), displays a general suppression of odd harmonics, whose extent increases as the harmonic order increases.

higher harmonics but is much more prominent in the interband currents, where the peak differences are biggest.

The full behaviour can again be seen to originate from the dominant, interband contributions, plotted in Fig. 5.13(c). The Berry phase can be identified as the agent that mostly drives odd harmonics interference (and consequently possible even harmonic generation when appropriately tuned) by considering the substantial peak enhancement at $\omega/\omega_0 = 2$ when the phase is switched on, as previously discussed. These results can again be understood in light of the discussed THG in disguise of SHG. The intraband current spectrum comparison is shown in Fig. 5.13(b), where it can be seen that any possibly small even harmonic peak vanishes once the Berry phase is neglected.

5.7 Summary & Outlook

In conclusion, relativistic two-dimensional massive fermions are shown to acquire a momentum-dependent Berry phase when interacting with normally-incident electromagnetic pulses. The spectrum generated by the electronic nonlinear current shows prominent odd-harmonic generation, which is generally suppressed as the energy gap is increased. Although even harmonics are generally absent for gapped dispersions, their generation is shown to be attainable at the femtosecond scale through THG in disguise of SHG when the photon energy is appropriately tuned to the energy gap, generating radiation with the desired harmonic order. These processes may be conceptualised as coherent interactions of odd harmonics. Signatures of these interband-driven phenomena can be seen in the enhancement of harmonic peaks. The Berry phase plays a major role in the interband current dynamics and hence in the generation of even harmonics.

It must be emphasized that excitonic effects are absent in the present formalism and the carrier-free treatment is therefore meant to be seen as a foundational step in understanding the intricacies of the optical behaviour of the sample. The numerical implementation of those effects is challenging since it must consider the dynamics of all two-level systems at once. As opposed to the free-carrier model that has been used so far, each two-level system at $\mathbf{k}$ only depends on its own parameters since it is decoupled from other carriers of different momenta. Dynamical quantities of each two-level system may be calculated separately and then averaged at the final step. Additionally, even though such interactions do refine the understanding of the system, a carrier-free treatment must be solved first to gain insight not only into the qualitative predictions of the model but also into the numerical machinery that allows such models to output reliable data.

These results and methods help establish new techniques to understand and predict the nonlinear optical behaviour of a range of two-dimensional hexagonal relativistic-

like semiconductors, and help pave the way to predict quantitatively, in a generalised fashion, the effect of wide range of phenomena, namely monolayer-substrate interactions, sample imperfections, local defects and strain effects, expected to be found in more realistic samples.

Chapter 6

Transition Metal Dichalcogenides

6.1 Overview

So far, only graphene and modifications thereof have been considered. For all the interesting and unique properties of this material, a major challenge still remains: the absence of a gap (or very small gaps given common substrate types) severely hinders the development of hypothetically advantageous applications for electronics. To overcome this barrier, an ample range of semiconductor crystals known as *transition metal dichalcogenides* (TMDs) has recently sparked the attention of the research community for reliably exhibiting robust optical and electronic properties when grown in the form of two-dimensional monolayers.

These structures admit direct bandgaps around the near-infrared/visible range and, rather interestingly, their quasiparticles can be modelled as massive two-dimensional Dirac fermions in the low momentum regime. Presently, most prominent and widely researched TMDs include disulphides (MoS_2), diselenides (WSe_2, $MoSe_2$, WSe_2) as well as ditellurides (WTe_2, $MoTe_2$).

Although advancing, the theoretical understanding of their nonlinear optical properties remains broadly uncharted. Recent studies highlight strong nonlinear features grounded on both theoretical [108] and experimental work [109].

One of the most nontrivial optical features of these crystals is tied to the role of the valley isospin of the carriers. *Valleytronics*, in analogy to spintronics, has been gaining ground as to provide a platform to study many novel features due to the existence of this degree of freedom. Due to strong spin-orbit coupling, the inversion symmetry breaking leads to spin-valley-locked dynamics and valley-dependent electromagnetic response [110, 111] through optical selection rules for specific light field polarisations [108].

Nanophotonic devices and applications to enhance light-matter interactions in these materials have also been proposed [112]. Combinations of exotic materials has also been studied, for instance by depositing graphene on TMD monolayers [113]. Various ab-initio calculations support the notion that electron-hole symmetry is also generally broken [114] and trigonal warping effects, responsible for distortions in the otherwise isotropic energy dispersion, have also been observed and studied [115]. Excitonic effects are also relevant in these crystals, leading, generally speaking, to enchancement of many optical properties [116, 117].

In this chapter, the machinery of the Dirac-Bloch Equations will be applied to a general transition metal dichalcogenide layer. This task will eventually lead to *generalised* Dirac-Bloch Equations in Section 6.3, suitable to model any effective relativistic two-band model of arbitrary lattice spacing. The advantage of this formalism is, as previously stressed, reflected on a method to obtain the nonlinear current without using any perturbative methods. Such scheme is shown in Section 6.4.

The calculations will invariably focus on TMD monolayers. As will be seen in Section 6.1.1, these crystals present more intricate features in their lattice structure and,

most importantly, lack a centre of inversion. The optics and related features of these materials are thus fundamentally different to what was seen for graphene. In particular, the second-order nonlinearity should be rather strong. This has already been observed in MoS_2 monolayers [115].

The spectrum of these materials is expectedly much more intricate. In particular, given the importance of the 3d orbitals, tight-binding methods are more challenging to apply. Recently, a three-band model was proposed to model the dispersion of group-VI TMD monolayer across the entire Brillouin zone [1]. In it, a reduction to an effective two-band model is obtained.

Using that setting, this chapter will, after generalising the Dirac-Bloch Equations to any relativistic two-band dispersion, study such an effective model, in order to gain insights about the generated currents in the sample. To do this, a total of nine energy parameters are necessary to describe the Hamiltonian of the carriers within the desired accuracy and range across the Brillouin zone - γ_i $(i = 0, ..., 6)$, γ_{SOC} and Δ. These equations can, in effect, model many other systems. Of particular relevance, bilayer graphene has shown to be modelled by an effective two-band model [118, 119]. A myriad of new and intriguing dynamics arise from these equations. Most notably, effects of trigonal warping, responsible for anisotropic features in the dispersion can be accounted for. These consequently break the angular symmetry of the dispersion and play an important role in harmonic generation. A broader discussion of these features will follow in Section 6.5.

6.1.1 Characterisation

TMDs are structures of the form MX_2, composed of a layer of a transition metal M interposed between two layers of a chalcogen X and with a typical thickness of around $6 - 7$Å. Depending on the metal's group, their stacking arrangement can either be trigonal prismatic or octahedral. For group-VI metals, such as Mo and W, these three

layers tend to stack in the former arrangement.

This can be seen in Fig 6.1(a), where the two species, which bond covalently, occupy either one of the two possible triangular sublattices, labelled **A** and **B**, in a honeycomb lattice. The trigonal prismatic arrangement can be seen by the relative arrangement of the three planes: in the chalcogen-occupied planes, three atoms form the basis (a regular triangle formed by these atoms) of a prism whose vertex lies on the metal-occupied plane, perpendicular to the vertical ($\hat{z}$) axis. This geometrical arrangement naturally defines the disposition of the orbitals, consequently playing a role in the optoelectronics of TMDs. Multilayer or bulk structures can be realised due to weak van der Waals interlayer interactions. Extensive and detailed analysis of the chemical bonding mechanisms behind TMDs can be found in [120]

A TMD monolayer admits twelve symmetry operations, which are illustrated in Fig. 6.1 $(a) - (b)$. These consist of three 3-fold rotations around the $\hat{z}$ axis, three 2-fold rotations around the axes laying on the horizontal plane, better seen in (b), two 3-fold improper rotations (composed of a 3-fold rotation followed by a reflection on the metal-occupied plane) and three reflections on their respective vertical planes.

Rather importantly, this structure lacks an inversion centre. To see why, the only hypothetical inversion centres, the centre of an arbitrary hexagon (labelled **P**) and a lattice point **Q** are shown in (b). Inversion through **P** is not possible due to the alternate nature of each sublattices; as for **Q**, only the lattice points of the same species are invertible (in this instance the metal species). This arrangement cannot therefore preserve inversion symmetry.

The precise configuration of the TDM structure plays a role in the observation of this symmetry. Unlike monolayers, TDMs grown in bulk or multilayers of an even number of layers admit an inversion centre [120].

Several works, e.g. in Refs. [108, 111], apply the Hamiltonian of gapped graphene in Eq. (5.3.2) to TMD monolayers monolayers. As will be seen in Section 6.1.1, the

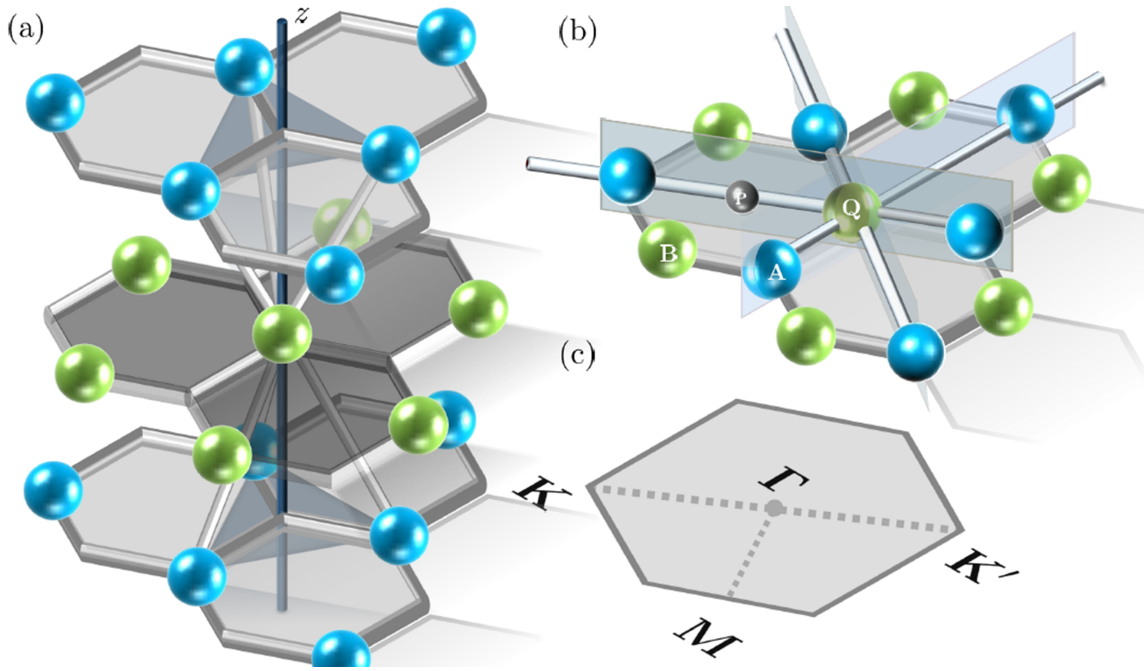

Figure 6.1: Lattice structures of a TMD monolayer in the trigonal prismatic arrangement. (*a*) The transition metal layer (green atoms on dark gray plane) is interposed between two identical layers of a chalcogen (blue atoms on light gray planes) and spatially stacked so that the metal atoms are coordinated with the three nearest chalcogen atoms on either respective layer, here represented by the white bonds. The vertical axis and the horizontal metal-occupied plane generate three 3-fold rotations, one reflection and two improper rotations as symmetry operations. (b) Top-view of the lattice, with both chalcogen-occupied layers superimposed. Both species have their respective atoms arranged alternately in triangular sublattices **A** and **B**. The point group symmetry of the monolayer is completely determined by including three further reflections about the three gray axes and three reflections about the vertical planes. The only hypothetical monolayer centres of inversion, here arbitrary taken at the points **P** and **Q** are shown on the plane. (*c*) Brillouin zone, showing the high-symmetry points; the unit cell, containing two atoms.

underlying lattice of the monolayer does not admit a centre of inversion. For that reason, an adequate Hamiltonian modelling the carriers in this system cannot be centrosymmetric. For that reason, a $\mathbf{k} \cdot \mathbf{p}$ expansion cannot be truncated below the third order. However, if one is only concerned with the electronic properties of TMDs, which are accounted mostly by low momentum states, a first-order approximation is accurate to that end and hence the Hamiltonian modelling gapped graphene, clearly centrosymmetric, is sufficient.

With regard to the optical response of these materials, such an approximation is also adequate if the system is probed with weak optical excitations, consequently leading to a fairly good model for their linear optical properties.

The main focus of this work is of course in the extreme nonlinear regime where, not surprisingly, such an approximation is clearly insufficient to accurately capture nonlinear light-matter phenomena of non-centrosymmetric two-dimensional media, for which higher-order terms in the $\mathbf{k}\cdot\mathbf{p}$ expansion explicitly break the centrosymmetry $\mathbf{k} \leftrightarrow -\mathbf{k}$, rendering the conduction and valence bands asymmetric.

6.2 Quasiparticle Properties

Within the framework of the $\mathbf{k} \cdot \mathbf{p}$ expansion that approximates the Hamiltonian of the carriers, the explicit breaking of the centrosymmetry is obtained by including higher-order contributions to the Hamiltonian. More importantly, such an expansion renders the dispersion anisotropic. Unlike centrosymmetric dispersions, where both valleys contributed equally to the current generated and did not create transverse components to the polarisation direction, this expectation is not warranted for such complicated dispersions.

If the incoming optical field is linearly polarised and still perpendicular to the monolayer, a natural question to ask is: *"Is there any dependence of the sample's*

optical properties on the relative polarisation angle of the electromagnetic field with respect to an arbitrary direction along the layer?

In order to probe this situation, the vector potential is expressed as $\mathbf{A}(t) = (A_x(t), A_y(t), 0)$, which can be split in polars as $\mathbf{A}(t) = A(t)(\cos\Theta, \sin\Theta, 0)$.

In order to avoid powers of $\hbar$ in already lengthy expressions, the minimal substitution will subsequently be performed on the wavevector $\mathbf{k}$ and not the momentum $\mathbf{p} = \hbar\mathbf{k}$ as was done in the previous sections.

Hence, a momentum vector $\mathbf{k} = (k_x, k_y) = |\mathbf{k}|(\cos\phi_{\mathbf{k}}, \sin\phi_{\mathbf{k}})$ is mapped to a time-dependent wavevector $\boldsymbol{\pi}_{\mathbf{k}}(t)$ through the reassignment $\mathbf{k} \mapsto \mathbf{k} + e/(\hbar c)\mathbf{A}(t)$ i.e. $\boldsymbol{\pi}_{\mathbf{k}}(t) = (\pi_x(t), \pi_y(t)) = |\boldsymbol{\pi}_{\mathbf{k}}(t)|(\cos\theta_{\mathbf{k}}(t), \sin\theta_{\mathbf{k}}(t))$, with:

$$\begin{aligned} |\boldsymbol{\pi}_{\mathbf{k}}(t)| &= \sqrt{\left[k_x + \frac{e}{\hbar c}A(t)\cos\Theta\right]^2 + [k_y + \frac{e}{c\hbar}A(t)\sin\Theta]^2} \\ &= \sqrt{|\mathbf{k}|^2 + \left(\frac{e}{c\hbar}A(t)\right)^2 + \frac{2e}{c\hbar}A(t)\cos(\phi_{\mathbf{k}} - \Theta)} \end{aligned} \tag{6.2.1}$$

$$\theta_{\mathbf{k}}(t) = \arctan\left[\frac{|\mathbf{k}|\sin\phi_{\mathbf{k}} + \frac{e}{c\hbar}A(t)\sin\Theta}{|\mathbf{k}|\cos\phi_{\mathbf{k}} + \frac{e}{\hbar c}A(t)\cos\Theta}\right] \tag{6.2.2}$$

It is no surprise that, just like in Chapters 4 and 5, its derivative will play a role in the light coupling:

$$\dot{\theta}_{\mathbf{k}}(t) = \frac{e\sin(\phi_{\mathbf{k}} - \Theta)E(t)}{\hbar|\boldsymbol{\pi}_{\mathbf{k}}|(t)} \tag{6.2.3}$$

Hamiltonian & Dispersion

In order to model the carriers in these monolayers, the Hamiltonian will be considered up to third-order when performing a $\mathbf{k}\cdot\mathbf{p}$ expansion. This consideration leads to the construction:

$$H_{\mathbf{k}}(\xi, s, t) = H^{(1)}_{\mathbf{k}}(\xi, t) + H^{(2)}_{\mathbf{k}}(\xi, t) + H^{(3)}_{\mathbf{k}}(\xi, t) + H^{\mathrm{SOC}}_{\mathbf{k}}(\xi, s) \tag{6.2.4}$$

where $H_{\mathbf{k}}^{(i)}$ are the i$^{\text{th}}$ contributions in the $\mathbf{k}\cdot\mathbf{p}$ expansion and $H_{\mathbf{k}}^{\text{SOC}}$ is a first-order contribution resultant from spin-orbit coupling effects.

For this reason, the Hamiltonian is now spin-dependent, where s denotes the spin index — $s=+1$ for spin up and $s=-1$ for spin down states. As usual, λ denotes the conduction ($\lambda=+1$) and valence ($\lambda=-1$) bands.

The first-order contribution represents the linear contributions:

$$\begin{aligned} H_{\mathbf{k}}^{(1)}(\xi,t) &= \begin{pmatrix} \frac{\Delta}{2} & a\gamma_0(\xi\pi_x - i\pi_y) \\ a\gamma_0(\xi\pi_x + i\pi_y) & -\frac{\Delta}{2} \end{pmatrix} \\ &= \begin{pmatrix} \frac{\Delta}{2} & \xi a\gamma_0|\boldsymbol{\pi}_{\mathbf{k}}|e^{-i\xi\theta_{\mathbf{k}}} \\ \xi a\gamma_0|\boldsymbol{\pi}_{\mathbf{k}}|e^{i\xi\theta_{\mathbf{k}}} & -\frac{\Delta}{2} \end{pmatrix} \end{aligned} \tag{6.2.5}$$

The Hamiltonian of Eq. (6.2.5) can be written in the compact form:

$$H_{\mathbf{k}}^{(1)}(\xi,t) = a\gamma_0\boldsymbol{\sigma}(\xi)\cdot\boldsymbol{\pi}_{\mathbf{k}} + \frac{\Delta}{2}\sigma_z \tag{6.2.6}$$

where $\boldsymbol{\sigma}(\xi) = (\xi\sigma_x, \sigma_y)$ and $\xi\pi_x - i\pi_y = \xi|\boldsymbol{\pi}_{\mathbf{k}}|e^{-i\xi\theta_{\mathbf{k}}}$ was used.

This is nothing more than what was developed so far in the previous sections, where the usual first-order Hamiltonian can be retrieved with the identification of the Fermi velocity as $v_{\text{F}} \equiv a\gamma_0/\hbar$. and a nonzero gap Δ.

The spin-orbit coupling (SOC) effects are considered up to first-order. Its effect, in this effective two-band model, is to split the valence bands between spin up and spin down states. Its corresponding Hamiltonian is therefore valley and spin-dependent:

$$H_{\mathbf{k}}^{\text{SOC}}(\xi,s) = \begin{pmatrix} 0 & 0 \\ 0 & \xi s\gamma_{\text{SOC}} \end{pmatrix} = \frac{\xi s\gamma_{\text{SOC}}}{2}\left[\mathbb{I} - \sigma_z\right] \tag{6.2.7}$$

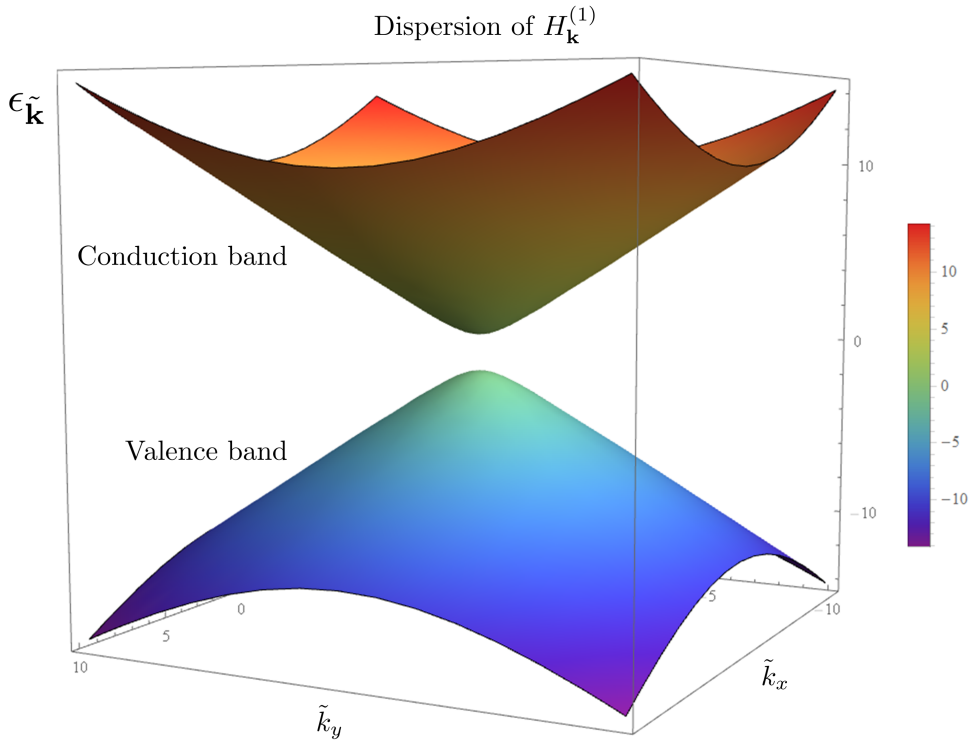

Figure 6.2: Dispersion of the first-order contribution to the full Hamiltonian. The parameter γ_0 sets the Fermi velocity of the carriers as $v_{\mathrm{F}} = a\gamma_0/\hbar$ and is therefore a measure of the slope of the Dirac cones. Δ denotes the usual energy gap and renders the dispersion hyperbolic.

The second-order $\mathbf{k}\cdot\mathbf{p}$ contribution adds three further parameters and can be written in the form:

$$\begin{aligned} H_{\mathbf{k}}^{(2)}(\xi,t) &= a^2 \begin{pmatrix} \gamma_1|\boldsymbol{\pi}_{\mathbf{k}}|^2 & \gamma_3(\xi\pi_x + i\pi_y)^2 \\ \gamma_3(\xi\pi_x - i\pi_y)^2 & \gamma_2|\boldsymbol{\pi}_{\mathbf{k}}|^2 \end{pmatrix} \\ &= a^2|\boldsymbol{\pi}_{\mathbf{k}}|^2 \begin{pmatrix} \gamma_1 & \gamma_3 e^{2i\xi\theta_{\mathbf{k}}} \\ \gamma_3 e^{-2i\xi\theta_{\mathbf{k}}} & \gamma_2 \end{pmatrix} \end{aligned} \tag{6.2.8}$$

which can be written in the compact notation:

$$H_{\mathbf{k}}^{(2)}(\xi,t) = a^2\left(\gamma_3(\boldsymbol{\sigma}(\xi)\cdot\boldsymbol{\pi}_{\mathbf{k}})^*\sigma_x(\boldsymbol{\sigma}(\xi)\cdot\boldsymbol{\pi}_{\mathbf{k}})^* + \frac{|\boldsymbol{\pi}_{\mathbf{k}}|^2}{2}\left[(\gamma_1+\gamma_2)\mathbb{I} + (\gamma_1-\gamma_2)\sigma_z\right]\right) \tag{6.2.9}$$

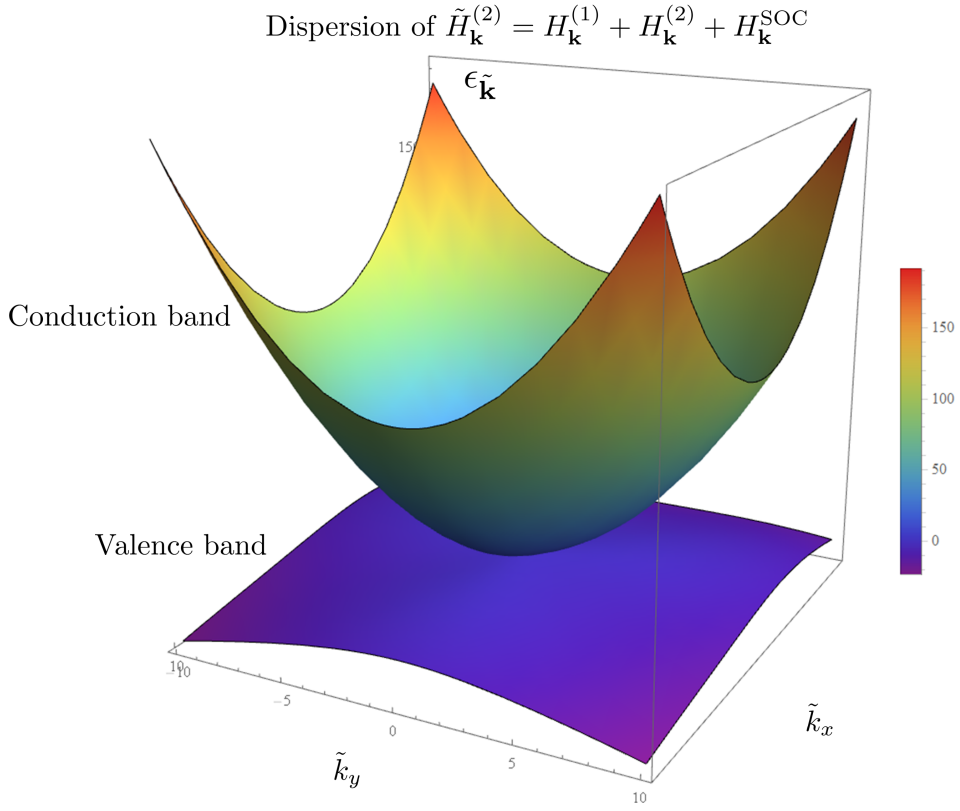

Figure 6.3: Dispersion of the cumulative Hamiltonian $\tilde{H}^2_{\mathbf{k}}$. The asymmetry parameters γ_1 and γ_2 render both bands inequivalent. Furthermore, an angular modulation on the valence band can be seen through the peaks and troughs. The exact locations are shown in the dispersion contours in Fig. 6.6(c).

The overall effect of the parameters so far introduced may be seen in the Fig. 6.2, where the dispersion of the Hamiltonian $\tilde{H}^{(2)}_{\mathbf{k}} = H^{(1)}_{\mathbf{k}} + H^{(2)}_{\mathbf{k}} + H^{\mathrm{SOC}}_{\mathbf{k}}$ is plotted. In it, it can be seen that both bands have different curvature profiles. The term proportional to γ_3 in Eq. (6.2.8) is rotating at three times the frequency of its counterpart in $H^{(1)}_{\mathbf{k}}$, the term proportional to γ_0 and leads to what is known as *trigonal warping*, which will be discussed in more detail.

Finally, the third-order contribution to the Hamiltonian reads:

$$\begin{aligned} H_{\mathbf{k}}^{(3)}(\xi,t) &= a^3 \begin{pmatrix} \xi\gamma_4\pi_x(\pi_x^2-3\pi_y^2) & \gamma_6|\boldsymbol{\pi}_{\mathbf{k}}|^2(\xi\pi_x - i\pi_y) \\ \gamma_6|\boldsymbol{\pi}_{\mathbf{k}}|^2(\xi\pi_x + i\pi_y) & \xi\gamma_5\pi_x(\pi_x^2-3\pi_y^2) \end{pmatrix} \\ &= \xi a^3|\boldsymbol{\pi}_{\mathbf{k}}|^3 \begin{pmatrix} \gamma_4\cos(3\theta_{\mathbf{k}}) & \gamma_6 e^{-i\xi\theta_{\mathbf{k}}} \\ \gamma_6 e^{i\xi\theta_{\mathbf{k}}} & \gamma_5\cos(3\theta_{\mathbf{k}}) \end{pmatrix} \end{aligned} \tag{6.2.10}$$

Where $\pi_x(\pi_x^2-3\pi_y^2) = |\boldsymbol{\pi}_{\mathbf{k}}|^3\left(\cos^3\theta_{\mathbf{k}} - 3\sin^2\theta_{\mathbf{k}}\cos\theta_{\mathbf{k}}\right) = |\boldsymbol{\pi}_{\mathbf{k}}|^3\cos(3\theta_{\mathbf{k}})$ was used, leading to:

$$H_{\mathbf{k}}^{(3)}(\xi,t) = a^3\left(\gamma_6|\boldsymbol{\pi}_{\mathbf{k}}|^2\boldsymbol{\sigma}(\xi)\cdot\boldsymbol{\pi}_{\mathbf{k}} + \frac{\xi}{2}|\boldsymbol{\pi}_{\mathbf{k}}|^3\cos(3\theta_{\mathbf{k}})\left[(\gamma_4+\gamma_5)\mathbb{I} + (\gamma_4-\gamma_5)\sigma_z\right]\right) \tag{6.2.11}$$

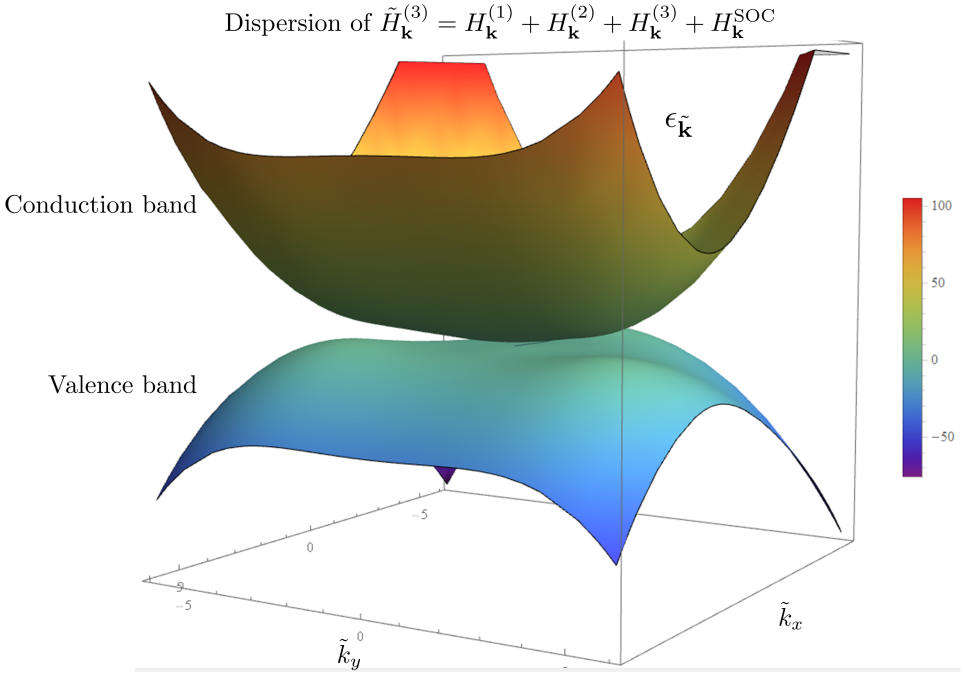

Figure 6.4: Dispersion of the full Hamiltonian $H_{\mathbf{k}}$. A similar modulation in the valence band as seen in Fig. 6.2 is also found, oriented differently as will be shown in Fig 6.6.

In order to simplify any further calculation, the full Hamiltonian will be written in the most general form that ensures hermicity: with the aid of real-valued functions $f_{\mathbf{k}}, r_{\mathbf{k}}$

and $g_{\mathbf{k}}$, the full Hamiltonian in Eq. (6.2.4) can be written in the following form:

$$\begin{aligned} H_{\mathbf{k}}(\xi,s,t) &= \sum_{i=1}^{3} H_{\mathbf{k}}^{(i)}(\xi,t) + H_{\mathbf{k}}^{\mathrm{SOC}}(\xi,s,t) \\ &= \begin{pmatrix} f_{\mathbf{k}}(\xi,t) & e^{-i\xi(\theta_{\mathbf{k}}(t)-\nu_{\mathbf{k}}(t))}g_{\mathbf{k}}(\xi,t) \\ e^{i\xi(\theta_{\mathbf{k}}(t)-\nu_{\mathbf{k}}(t))}g_{\mathbf{k}}(\xi,t) & r_{\mathbf{k}}(\xi,s,t) \end{pmatrix} \end{aligned} \tag{6.2.12}$$

In particualr for MoS_2, these amplitudes take the functional form [1] :

$$f_{\mathbf{k}}(\xi,t) = \frac{\Delta}{2} + \gamma_1 a^2|\boldsymbol{\pi}_{\mathbf{k}}|^2 + \xi\gamma_4\cos(3\theta_{\mathbf{k}})a^3|\boldsymbol{\pi}_{\mathbf{k}}|^3 \tag{6.2.13}$$

$$r_{\mathbf{k}}(\xi,s,t) = -\frac{\Delta}{2} + s\xi\gamma_{\mathrm{SOC}} + \gamma_2 a^2|\boldsymbol{\pi}_{\mathbf{k}}|^2 + \xi\gamma_5\cos(3\theta_{\mathbf{k}})a^3|\boldsymbol{\pi}_{\mathbf{k}}|^3 \tag{6.2.14}$$

$$\begin{aligned} g_{\mathbf{k}}^2(\xi,t) = {} & \xi^2\gamma_0^2 a^2|\boldsymbol{\pi}_{\mathbf{k}}|^2 + 2\xi\gamma_0\gamma_3\cos(3\theta_{\mathbf{k}})a^3|\boldsymbol{\pi}_{\mathbf{k}}|^3 + (\gamma_3^2 + 2\gamma_0\gamma_6)a^4|\boldsymbol{\pi}_{\mathbf{k}}|^4 \\ & + 2\xi\gamma_3\gamma_6\cos(3\theta_{\mathbf{k}})a^5|\boldsymbol{\pi}_{\mathbf{k}}|^5 + \gamma_6^2 a^6|\boldsymbol{\pi}_{\mathbf{k}}|^6 \end{aligned} \tag{6.2.15}$$

The factor ξ^2 is left so the correct branch of the radical is obtained when reducing the full Hamiltonian to the first-order contribution.

The aggregate difference between the corresponding frequency of the anti-diagonal (hopping) terms from the second and third order contributions leads to the appearance of a new valley-dependent phase in the full Hamiltonian, which will be termed the *warping phase* $\nu_{\mathbf{k}}(\xi,t)$:

$$\nu_{\mathbf{k}}(\xi,t) = \arctan\left[\frac{\gamma_3\sin(3\theta_{\mathbf{k}})a|\boldsymbol{\pi}_{\mathbf{k}}|}{\xi\gamma_0 + \gamma_3\cos(3\theta_{\mathbf{k}})a|\boldsymbol{\pi}_{\mathbf{k}}| + \xi\gamma_6 a^2|\boldsymbol{\pi}_{\mathbf{k}}|^2}\right] \tag{6.2.16}$$

From now on, the dependence on the degrees of freedom is dropped unless they must be emphasized.

In the notation just introduced, the full dispersion of the two bands is easily obtained through solving $|H_{\mathbf{k}}(\xi,s,t) - \epsilon_{\mathbf{k}}(\xi,s,\lambda,t)| = 0$. Due to the minimal substitution, it is also time-dependent. Unlike for both gapped and ungapped graphene, it is now

valley and spin-dependent:

$$\epsilon_{\lambda,\mathbf{k}} = \frac{1}{2}\left(f_{\mathbf{k}} + r_{\mathbf{k}} + \lambda\sqrt{(f_{\mathbf{k}} - r_{\mathbf{k}})^2 + 4g_{\mathbf{k}}^2}\right) \tag{6.2.17}$$

The functional form of the dispersion allows for a useful separation: the contributions to the dispersion's asymmetry are more easily captured by rewriting Eq. (6.2.17) as:

$$\epsilon_{\mathbf{k}}(\xi, s, \lambda, t) = \epsilon_{\mathbf{k}}^{a}(\xi, s, t) + \lambda\epsilon_{\mathbf{k}}^{b}(\xi, s, t) \tag{6.2.18}$$

In this fashion, the asymmetry and the hopping (bulk) contributions — respectively denoted by $\epsilon_{\mathbf{k}}^{a}$ and $\epsilon_{\mathbf{k}}^{b}$ — are explicitly given by:

$$\epsilon_{\mathbf{k}}^{a} = \frac{1}{2}\left(f_{\mathbf{k}} + r_{\mathbf{k}}\right) \qquad \epsilon_{\mathbf{k}}^{b} = \sqrt{\left(\frac{f_{\mathbf{k}} - r_{\mathbf{k}}}{2}\right)^2 + g_{\mathbf{k}}^2} \tag{6.2.19}$$

An auxiliary variable $z_{\mathbf{k}}$ is defined now. It will be seen to define the relative strength of many contributions:

$$z_{\mathbf{k}} \equiv \frac{r_{\mathbf{k}} - \epsilon_{\mathbf{k}}^{a}}{\epsilon_{\mathbf{k}}^{b}} \tag{6.2.20}$$

To obtain the functional form of the dispersion, the $\mathbf{k}\cdot\mathbf{p}$ expansion can be used to construct both asymmetry and bulk contributions. Given the introduction of the canonical momentum, these are collected by powers of $|\boldsymbol{\pi}_{\mathbf{k}}|$:

$$\epsilon_{\mathbf{k}}^{a}(\xi, s, t) = \sum_{i=0}^{3} \alpha_{\mathbf{k}}^{(i)}(\xi, s, t)|\boldsymbol{\pi}_{\mathbf{k}}|^i \tag{6.2.21}$$

$$\epsilon_{\mathbf{k}}^{b}(\xi, s, t) = \sqrt{\sum_{i=0}^{6} \beta_{\mathbf{k}}^{(i)}(\xi, s, t)|\boldsymbol{\pi}_{\mathbf{k}}|^i} \tag{6.2.22}$$

The asymmetry term $\epsilon^a_{\mathbf{k}}(\xi, s, t)$ evaluates to:

$$\begin{aligned}
\alpha^{(0)}_{\mathbf{k}} &= \frac{1}{2}\xi s\gamma_{\mathrm{SOC}} \\
\alpha^{(2)}_{\mathbf{k}} &= \frac{1}{2}(\gamma_1+\gamma_2)a^2 \\
\alpha^{(3)}_{\mathbf{k}} &= \frac{1}{2}\xi(\gamma_4+\gamma_5)\cos(3\theta_{\mathbf{k}})a^3
\end{aligned} \tag{6.2.23}$$

and can thus be seen to vanish whenever $\gamma_1+\gamma_2=\gamma_4+\gamma_5=0$ and $\gamma_{\mathrm{SOC}}=0$.
As for the coefficients of the bulk of the dispersion $\beta^{(i)}_{\mathbf{k}}$, they take the form:

$$\begin{aligned}
\beta^{(0)}_{\mathbf{k}} &= \left(\frac{\Delta-\xi s\gamma_{\mathrm{SOC}}}{2}\right)^2 \\
\beta^{(2)}_{\mathbf{k}} &= \frac{1}{2}\left[2\gamma_0^2+(\gamma_1-\gamma_2)(\Delta-\xi s\gamma_{\mathrm{SOC}})\right]a^2 \\
\beta^{(3)}_{\mathbf{k}} &= \frac{1}{2}\xi\cos(3\theta_{\mathbf{k}})\left[(\gamma_4-\gamma_5)(\Delta-\xi s\gamma_{\mathrm{SOC}})+4\gamma_0\gamma_3\right]a^3 \\
\beta^{(4)}_{\mathbf{k}} &= \left(\left(\frac{\gamma_1-\gamma_2}{2}\right)^2+\gamma_3^2+2\gamma_0\gamma_6\right)a^4 \\
\beta^{(5)}_{\mathbf{k}} &= \frac{1}{2}\xi\cos(3\theta_{\mathbf{k}})\left[(\gamma_1-\gamma_2)(\gamma_4-\gamma_5)+4\gamma_3\gamma_6\right]a^5 \\
\beta^{(6)}_{\mathbf{k}} &= \left[\left(\frac{\gamma_4-\gamma_5}{2}\right)^2\cos^2(3\theta_{\mathbf{k}})+\gamma_6^2\right]a^6
\end{aligned} \tag{6.2.24}$$

With the remaining coefficients vanishing: $\alpha^{(1)}_{\mathbf{k}}=\beta^{(1)}_{\mathbf{k}}=0$.

The contribution of all the parameters just introduced to the dispersion in each band is more easily visualised through the contour profile of the dispersion of the cumulative Hamiltonians. In this fashion, particular orders in the expansion may reveal which new features are introduced. These can be visualised in Fig. 6.6, where the left insets show the cumulative dispersions in the valence band and the right insets the same quantity but in the conduction band.
The angular symmetry of the dispersion of the first-order Hamiltonian $\tilde{H}^{(1)}_{\mathbf{k}}=H^{(1)}_{\mathbf{k}}+$

$H_{\mathbf{k}}^{\mathrm{SOC}}$ is manifestly present in the contour plots of both bands, as can be seen in (a)-(b). Physically, the parameters γ_1 and γ_2 break the symmetry of the bands. Unless $\gamma_1 + \gamma_2 = 0$, they create a $\mathbf{k}$-dependent vertical shift between the bands.

The parameter γ_3 is responsible for *trigonal warping*, an effect which induces a distortion of the dispersion shape, leading to a breaking of the angular symmetry, as can be appreciated in Fig. 6.6(a).

The warping is more intense for low-momentum states, monotonically decreasing until it becomes rotationally symmetric. The contours of the valence band show distortion features wherein the stretch is more visible along the lines $\phi_{\tilde{\mathbf{k}}} = 0, \pi/3$ and $2\pi/3$. The distortion is less severe in the conduction band, shown in (d), where a slight departure from the concentric circles found in (b), caused by the asymmetry terms γ_1 and γ_2.

Once the full Hamiltonian is considered, up to third order, it can be seen that the valence band, in (e) has three maxima, with angles $\phi_{\tilde{\mathbf{k}}} = 0, \pi/3$ and $2\pi/3$. For momenta around $|\mathbf{k}| < 1$, the dispersion is, not surprisingly, similar to $H_{\mathbf{k}}^{(1)}$. The full conduction band in (f) shows a severely distorted contour profile, exacerbated by the asymmetry coefficients γ_4 and γ_5.

The effect of the spin-orbit coupling contribution $H_{\mathbf{k}}^{\mathrm{SOC}}$ in the full dispersion may be explicitly seen in Fig. 6.5, along $\phi_{\mathbf{k}} = 0$, i.e. with $k_y = 0$. There are now $2(\text{ on } \lambda) \times 2(\text{ on } \xi) \times 2(\text{ on } s) = 8$ bands across the entire Brillouin zone. The upper window shows the four bands (λ, s) at the $\mathbf{K}$ valley whereas the lower window shows the same bands in the $\mathbf{K}'$ valley. As can be seen, the conduction bands at either valley remain spin degenerate. The spin-orbit coupling has the effect of splitting the valence bands by a small amount γ_{SOC}, which is a mere 8% of the gap. It may seen that both valleys are vertically symmetrical. This can be understood with regards to the symmetry $p_x \mapsto -p_x$ which enters the definition of the valley-dependent pseudospin $\boldsymbol{\sigma}(\xi) = (\xi\sigma_x, \sigma_y)$

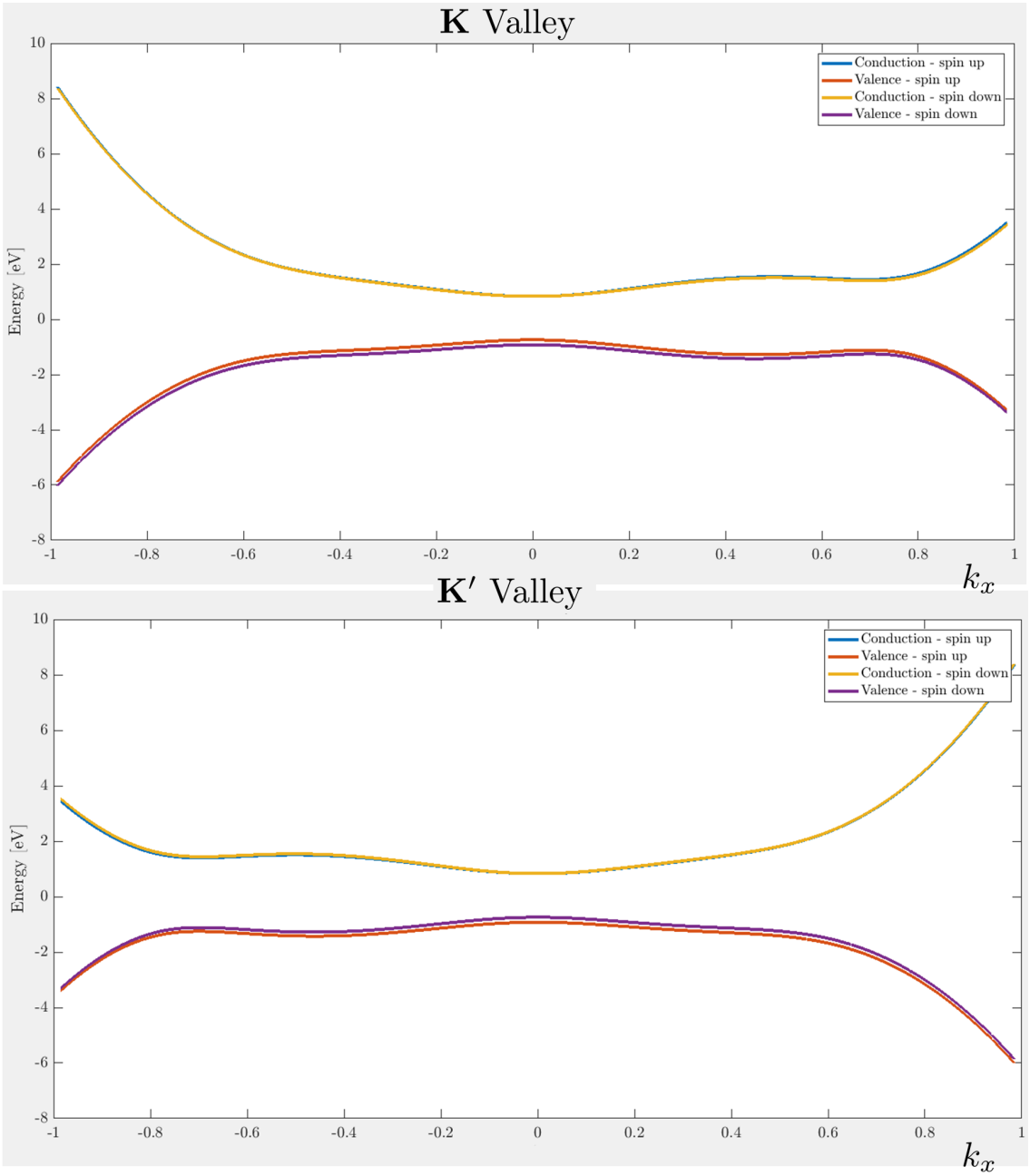

Figure 6.5: Plot of the four bands (λ, s) at the **K** valley (upper window) and at the **K**′ valley (lower window), using the effective parameters of Table 6.1.

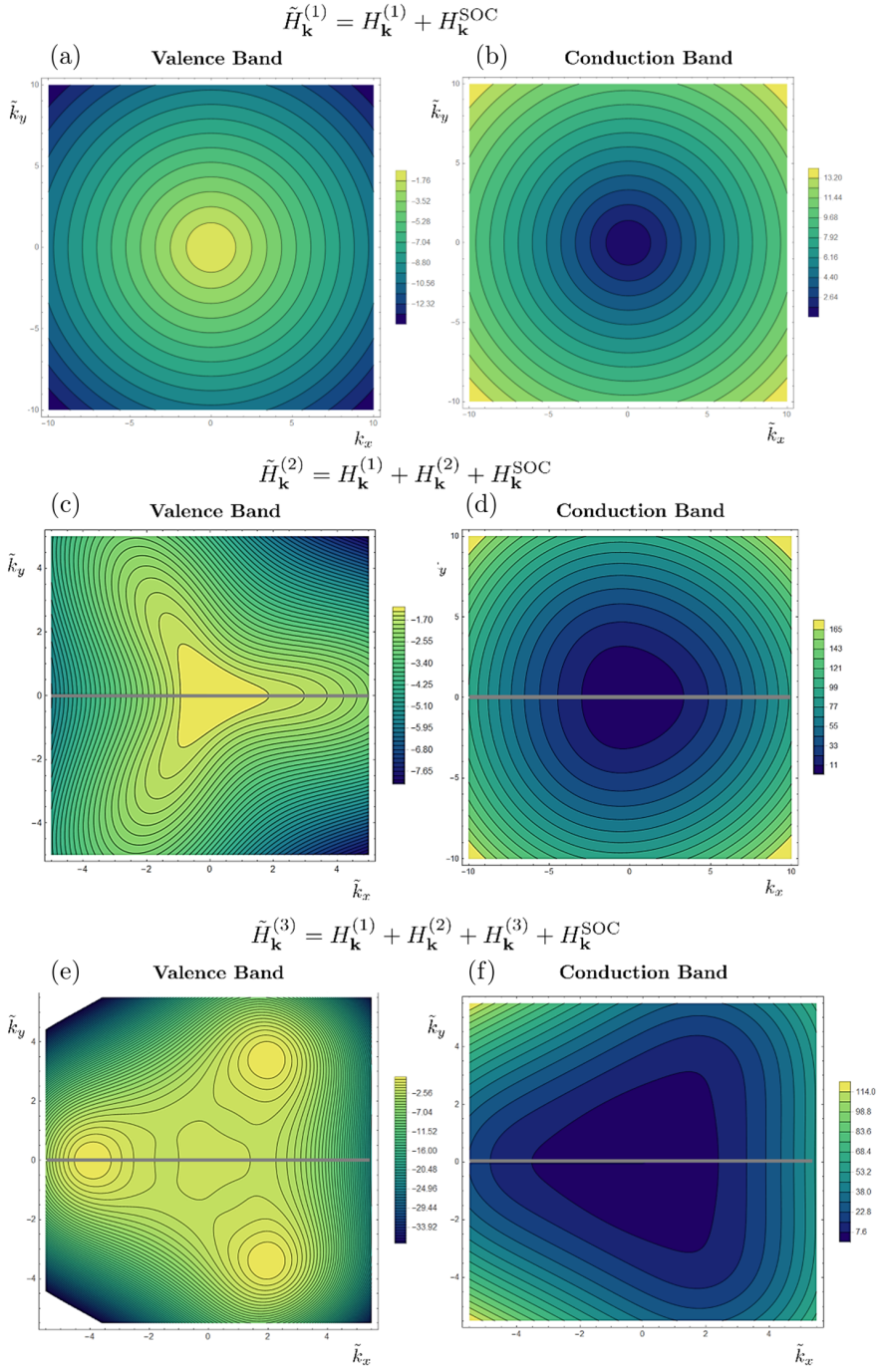

Figure 6.6: Contour plots of the dispersion of cumulative Hamiltonians $\tilde{H}^i_{\mathbf{k}} = \sum_{j=1}^{i} H^i_{\mathbf{k}} + H^{\mathrm{SOC}}_{\mathbf{k}}$ in momentum space, in the absence of an electric field. (a), (c) and (e) show respectively the valence band dispersion of the first, second and third-order cumulative dispersions. (b),(d) and (f) show respectively the same dispersions in the conduction band.

Instantaneous Eigenstates

The general instantaneous eigenstate of the full Hamiltonian, denoted by $|u_{\mathbf{k}}(\xi, s, \lambda, t)\rangle$, with components:

$$|u_{\mathbf{k}}(\xi, s, \lambda, t)\rangle \equiv \begin{pmatrix} \varphi_{\mathbf{k}}(\xi, s, \lambda, t) \\ \chi_{\mathbf{k}}(\xi, s, \lambda, t) \end{pmatrix} \tag{6.2.25}$$

may now be obtained by solving:

$$H_{\mathbf{k}}(\xi, s, t)\,|u_{\mathbf{k}}(\xi, s, \lambda, t)\rangle = \epsilon_{\mathbf{k}}(\xi, s, \lambda, t)\,|u_{\mathbf{k}}(\xi, s, \lambda, t)\rangle \tag{6.2.26}$$

The spinor components are seen to be related to one another as:

$$\varphi_{\mathbf{k}}(\xi, s, \lambda, t) = \left(\frac{\epsilon_{\mathbf{k}}(\xi, s, \lambda, t) - r_{\mathbf{k}}(\xi, s, t)}{g_{\mathbf{k}}(\xi, t)}\right) e^{-i\xi(\theta_{\mathbf{k}}(t) - \nu_{\mathbf{k}}(\xi, t))} \chi_{\mathbf{k}}(\xi, s, \lambda, t) \tag{6.2.27}$$

As usual, with the choice to fix the lower component to a spin-free field $\chi_{\mathbf{k}}(\xi, \lambda, t) \equiv \lambda e^{i\xi(\theta_{\mathbf{k}}(t) - \nu_{\mathbf{k}}(\xi, t)/2}$ and applying instantaneous orthonormality (i.e. $\langle u_{\mathbf{k}}(\xi, s, \lambda, t) | u_{\mathbf{k}}(\xi, s, \lambda', t)\rangle = \delta_{\lambda\lambda'}$), the normalised spinor takes the form:

$$\begin{aligned} |u_{\mathbf{k}}(\xi, s, \lambda, t)\rangle &= \left(\frac{\lambda g_{\mathbf{k}}}{\sqrt{(\epsilon_{\mathbf{k}} - r_{\mathbf{k}})^2 + g_{\mathbf{k}}^2}}\right) \begin{pmatrix} \left(\frac{\epsilon_{\mathbf{k}} - r_{\mathbf{k}}}{g_{\mathbf{k}}}\right) e^{-i\xi(\theta_{\mathbf{k}} - \nu_{\mathbf{k}})/2} \\ e^{i\xi(\theta_{\mathbf{k}} - \nu_{\mathbf{k}})/2} \end{pmatrix} \\ &= \left(\frac{g_{\mathbf{k}}}{\epsilon_{\mathbf{k}}^b \sqrt{2(1 - \lambda z_{\mathbf{k}})}}\right) \begin{pmatrix} \left(\frac{\epsilon_{\mathbf{k}}^b}{g_{\mathbf{k}}}\right)(1 - \lambda z_{\mathbf{k}}) e^{-i\xi(\theta_{\mathbf{k}} - \nu_{\mathbf{k}})/2} \\ \lambda e^{i\xi(\theta_{\mathbf{k}} - \nu_{\mathbf{k}})/2} \end{pmatrix} \end{aligned} \tag{6.2.28}$$

Berry Phase

Not surprisingly, the inclusion of the new contributions leads to intricate dynamics of the Berry phase, which is now valley and spin-dependent. Its derivative may be

found to be:

$$\begin{aligned}\dot{\eta}_{\mathbf{k}}(\xi,s,\lambda,t) &\equiv i\left\langle u_{\mathbf{k}}(\xi,s,\lambda,t)|\dot{u}_{\mathbf{k}}(\xi,s,\lambda,t)\right\rangle \\ &= \xi\left(\frac{1}{2}-\frac{g_{\mathbf{k}}^2}{g_{\mathbf{k}}^2+[\epsilon_{\mathbf{k}}-r_{\mathbf{k}}]^2}\right)(\dot{\theta}_{\mathbf{k}}-\dot{\nu}_{\mathbf{k}}) \\ &= -\frac{\xi\lambda z_{\mathbf{k}}}{2}(\dot{\theta}_{\mathbf{k}}-\dot{\nu}_{\mathbf{k}}) \\ &\equiv -\frac{\xi\lambda}{2}\dot{\Lambda}_{\mathbf{k}}(\xi,s,t)\end{aligned} \tag{6.2.29}$$

Considering only $H_{\mathbf{k}}^{(1)}$, the functions reduce to $r_{\mathbf{k}}=-\Delta/2$ and $\epsilon_{\mathbf{k}}^a=0$, yielding the derivative is:

$$\dot{\eta}_{\mathbf{k}}=\lambda\xi\frac{\Delta\dot{\theta}_{\mathbf{k}}}{4\epsilon_{\mathbf{k}}^b} \tag{6.2.30}$$

as previously calculated in Eq. (5.3.7).

Electric Dipole Moment

In this generalised system, once the DBEs modelling the TMDs are obtained, it will be seen that the matrix element $\langle u_{\mathbf{k}}^{\lambda}|\dot{u}_{\mathbf{k}}^{-\lambda}\rangle$ is related to the electric dipole moment of electron and hole states in the two-band model. Essentially, the electric dipole moment $\mu_{\mathbf{k}}(\xi,s,t)$ is interpreted as the field which, in the driving term for $q_{\mathbf{k}}$ in Eq. (6.3.17) complies with the Bloch form i.e.:

$$i\mu_{\mathbf{k}}(\xi,s,t)E(t)=-\left\langle u_{\mathbf{k}}^{(+)}|\dot{u}_{\mathbf{k}}^{(-)}\right\rangle \tag{6.2.31}$$

It is nonetheless more convenient to think of the coupling (matrix) element as opposed to the dipole moment since, given the complicated nature of the new variables and their derivatives, separating the field explicitly does not bring insight or simplicity of notation. The matrix element may be calculated as:

$$\langle u_{\lambda,\mathbf{k}}|\dot{u}_{-\lambda,\mathbf{k}}\rangle=-i\xi\frac{g_{\mathbf{k}}}{2\epsilon_{\mathbf{k}}^b}(\dot{\theta}_{\mathbf{k}}-\dot{\nu}_{\mathbf{k}})+\lambda\frac{\epsilon_{\mathbf{k}}^b}{2g_{\mathbf{k}}}\dot{z}_{\mathbf{k}} \tag{6.2.32}$$

Rather importantly, these matrix elements may be seen to be anti-Hermitian in the band index λ, meaning:

$$\langle u_{\mathbf{k}}^{(-)} | \dot{u}_{\mathbf{k}}^{(+)} \rangle = - \langle u_{\mathbf{k}}^{(+)} | \dot{u}_{\mathbf{k}}^{(-)} \rangle^{*} \tag{6.2.33}$$

The real part of the matrix element induces an imaginary part of the dipole moment, just like was obtained for the case of gapped graphene. This quantity naturally converges to the dipole in gapped graphene, i.e. when considering only $H_{\mathbf{k}}^{(1)}$.

6.3 The Generalised Dirac-Bloch Equations

Given the generality of the Hamiltonian in question, the same tools as used when calculating the DBEs for gapped and ungapped graphene are used to obtain a solution to the equation:

$$i\hbar \, |\dot{\Psi}_{\mathbf{k}}(\xi, s, t)\rangle = H_{\mathbf{k}}(\xi, s, t) \, |\Psi_{\mathbf{k}}(\xi, s, t)\rangle \tag{6.3.1}$$

Just as was done previously, the general wavefunction is taken as a linear superposition of the band wavefunctions $|\psi_{\mathbf{k}}(\xi, s, \lambda, t)\rangle$

$$|\psi_{\mathbf{k}}(\xi, s, \lambda, t)\rangle = |u_{\mathbf{k}}(\xi, s, \lambda, t)\rangle \, e^{-i\Omega_{\mathbf{k}}(\xi,s,\lambda,t)} e^{i\eta_{\mathbf{k}}(\xi,s,\lambda,t)} \tag{6.3.2}$$

These are simply the instantaneous eigenstate shifted by the dynamical phase $\Omega_{\mathbf{k}}(\xi, s, \lambda, t)$:

$$\Omega_{\mathbf{k}}(\xi, s, \lambda, t) = (1/\hbar) \int_{-\infty}^{t} \epsilon_{\mathbf{k}}(\xi, s, \lambda, t') dt' \tag{6.3.3}$$

and the instantaneous Berry phase $\eta_{\mathbf{k}}(\xi, s, \lambda, t)$

$$\eta_{\mathbf{k}}(\xi, s, \lambda, t) = \int_{-\infty}^{t} \dot{\eta}_{\mathbf{k}}(\xi, s, \lambda, t') dt' \tag{6.3.4}$$

whose derivative is given in Section (6.2). Moreover, note that both quantities are still valley and spin-dependent until explicit symmetries are exploited. The ansatz that

solves the Dirac equation is now obtained by expanding through the instantaneous basis:

$$|\Psi_{\mathbf{k}}\rangle = \sum_{\lambda} c_{\mathbf{k}}^{\lambda} |u_{\mathbf{k}}^{\lambda}\rangle \, e^{i(\eta_{\mathbf{k}}^{\lambda} - \Omega_{\mathbf{k}}^{\lambda})} \tag{6.3.5}$$

Inserting the ansatz of Eq. (6.3.5) in Eq. (6.3.1) leads to:

$$i\hbar \, |\dot{\Psi}_{\mathbf{k}}\rangle = \sum_{\lambda} \left[i\hbar \dot{c}_{\mathbf{k}}^{\lambda} |u_{\mathbf{k}}^{\lambda}\rangle + i\hbar c_{\mathbf{k}}^{\lambda} |\dot{u}_{\mathbf{k}}^{\lambda}\rangle - \hbar c_{\mathbf{k}}^{\lambda} |u_{\mathbf{k}}^{\lambda}\rangle \, (\dot{\eta}_{\mathbf{k}}^{\lambda} - \dot{\Omega}_{\mathbf{k}}^{\lambda}) \right] e^{i(\eta_{\mathbf{k}}^{\lambda} - \Omega_{\mathbf{k}}^{\lambda})} \tag{6.3.6}$$

$$H_{\mathbf{k}} \, |\Psi_{\mathbf{k}}\rangle = \sum_{\lambda} c_{\mathbf{k}}^{\lambda} \epsilon_{\mathbf{k}}^{\lambda} |u_{\mathbf{k}}^{\lambda}\rangle \, e^{i(\eta_{\mathbf{k}}^{\lambda} - \Omega_{\mathbf{k}}^{\lambda})} \tag{6.3.7}$$

Using the condition $\hbar \dot{\Omega}_{\mathbf{k}}^{\lambda} = \epsilon_{\mathbf{k}}^{\lambda}$, pre-multiplying both sides by $\langle u_{\mathbf{k}}^{\lambda'}|$, the following condition is obtained:

$$\sum_{\lambda} \left[\langle u_{\mathbf{k}}^{\lambda'} | u_{\mathbf{k}}^{\lambda} \rangle \, \dot{c}_{\mathbf{k}}^{\lambda} + \left(\langle u_{\mathbf{k}}^{\lambda'} | \dot{u}_{\mathbf{k}}^{\lambda} \rangle + i\dot{\eta}_{\mathbf{k}}^{\lambda} \, \langle u_{\mathbf{k}}^{\lambda'} | u_{\mathbf{k}}^{\lambda} \rangle \right) c_{\mathbf{k}}^{\lambda} \right] e^{i(\eta_{\mathbf{k}}^{\lambda} - \Omega_{\mathbf{k}}^{\lambda})} = 0 \tag{6.3.8}$$

Up to this point, the DBEs can in principle be obtained for a n level system. In the effective two-band model, the sum over $\lambda \in \{-\lambda', \lambda'\}$ is applied.

With the aid of the orthonormality condition $\langle u_{\mathbf{k}}^{\lambda'} | u_{\mathbf{k}}^{\lambda} \rangle = \delta_{\lambda'\lambda}$ and the definition of the Berry phase in Eq. (6.2.29), a dummy variable reassignment $\lambda' \mapsto \lambda$ leads to the condition:

$$\dot{c}_{\mathbf{k}}^{\lambda} = - \langle u_{\mathbf{k}}^{\lambda} | \dot{u}_{\mathbf{k}}^{-\lambda} \rangle \, e^{i\left((\eta_{\mathbf{k}}^{-\lambda} - \eta_{\mathbf{k}}^{\lambda}) - (\Omega_{\mathbf{k}}^{-\lambda} - \Omega_{\mathbf{k}}^{\lambda}) \right)} c_{\mathbf{k}}^{-\lambda} \tag{6.3.9}$$

i.e.

$$\begin{aligned} \dot{c}_{\mathbf{k}}^{(+)} + \langle u_{\mathbf{k}}^{(+)} | \dot{u}_{\mathbf{k}}^{(-)} \rangle \, e^{i\left((\eta_{\mathbf{k}}^{(-)} - \eta_{\mathbf{k}}^{(+)}) - (\Omega_{\mathbf{k}}^{(-)} - \Omega_{\mathbf{k}}^{(+)}) \right)} c_{\mathbf{k}}^{(+)} = 0 \\ \dot{c}_{\mathbf{k}}^{(-)} + \langle u_{\mathbf{k}}^{(-)} | \dot{u}_{\mathbf{k}}^{(+)} \rangle \, e^{-i\left((\eta_{\mathbf{k}}^{(-)} - \eta_{\mathbf{k}}^{(+)}) - (\Omega_{\mathbf{k}}^{(-)} - \Omega_{\mathbf{k}}^{(+)}) \right)} c_{\mathbf{k}}^{(-)} = 0 \end{aligned} \tag{6.3.10}$$

With the energy definition of Eq. (6.2.18):

$$\begin{aligned} [\Omega_{\mathbf{k}}^{(-)} - \Omega_{\mathbf{k}}^{(+)}](t) &= \frac{1}{\hbar} \int_{-\infty}^{t} [(\epsilon_{\mathbf{k}}^{a} - \epsilon_{\mathbf{k}}^{b}) - (\epsilon_{\mathbf{k}}^{a} + \epsilon_{\mathbf{k}}^{b})](t') dt' \\ &= -\frac{2}{\hbar} \int_{-\infty}^{t} \epsilon_{\mathbf{k}}^{b}(t') dt' \equiv -2\Omega_{\mathbf{k}}^{b}(t) \end{aligned} \tag{6.3.11}$$

Consequently, the dynamical angle depends only on its bulk part and not on the asymmetry contributions, $\epsilon^a_{\mathbf{k}}$. As for and the Berry phase, the separation of the degrees of freedom variables in Eq. (6.2.29) gives:

$$\begin{aligned}[\eta^{(-)}_{\mathbf{k}} - \eta^{(+)}_{\mathbf{k}}](t) &= \int_{-\infty}^{t} [\dot{\eta}^{(-)}_{\mathbf{k}} - \dot{\eta}^{(+)}_{\mathbf{k}}](t')dt' \\ &= -\frac{\xi}{2}\int_{-\infty}^{t} (-2)\dot{\Lambda}_{\mathbf{k}}(t')dt' = \xi\Lambda_{\mathbf{k}}(t)\end{aligned} \tag{6.3.12}$$

The anti-Hermicity of the coupling element of Eq. (6.2.32) can now be used to rewrite the two differential equations that resulted from Eq. (6.3.9) in a differential matrix equation of the form $\dot{\mathbf{c}} = \mathbf{M}\mathbf{c}$, where $\mathbf{c}$ is a vector whose components are the spinor coefficients and $\mathbf{M}$ is the coefficient matrix, dictating the time evolution of the coefficients:

$$\begin{pmatrix} \dot{c}^{(+)}_{\mathbf{k}} \\ c^{(-)}_{\mathbf{k}} \end{pmatrix} = \begin{pmatrix} 0 & -\langle u^{(+)}_{\mathbf{k}} | \dot{u}^{(-)}_{\mathbf{k}} \rangle \, e^{i\left(\xi\Lambda_{\mathbf{k}} + 2\Omega^b_{\mathbf{k}}\right)} \\ \langle u^{(+)}_{\mathbf{k}} | \dot{u}^{(-)}_{\mathbf{k}} \rangle^* \, e^{-i\left(\xi\Lambda_{\mathbf{k}} + 2\Omega^b_{\mathbf{k}}\right)} & 0 \end{pmatrix} \begin{pmatrix} c^{(+)}_{\mathbf{k}} \\ c^{(-)}_{\mathbf{k}} \end{pmatrix} \tag{6.3.13}$$

The fact that this matrix has vanishing diagonal entries is due to the explicit separation of the Berry phase in the definition of the band wavefunctions $|\psi_{\mathbf{k}}(\xi, s, \lambda, t\rangle$ in Eq. (6.3.5).

For a general coefficient matrix $\mathbf{M}$ satisfying:

$$\begin{pmatrix} \dot{c}^{(+)}_{\mathbf{k}} \\ \dot{c}^{(-)}_{\mathbf{k}} \end{pmatrix} = \begin{pmatrix} \alpha & \beta \\ \gamma & \delta \end{pmatrix} \begin{pmatrix} c^{(+)}_{\mathbf{k}} \\ c^{(-)}_{\mathbf{k}} \end{pmatrix} \tag{6.3.14}$$

and considering the form of the derivatives of the inversion and microscopic polarisation, found in Eq. (4.2.19), the DBEs can generally be constructed thus:

$$\dot{q}_{\mathbf{k}} = \left(\alpha + \delta^* + i(\omega_0 - 2\dot{\Omega}^b_{\mathbf{k}})\right) q_{\mathbf{k}} + \gamma^* w_{\mathbf{k}} e^{i(\omega_0 t - 2\Omega^b_{\mathbf{k}})} \tag{6.3.15}$$

$$\dot{w}_{\mathbf{k}} = \mathrm{Re}(\alpha)(w_{\mathbf{k}}+1) + \mathrm{Re}(\delta)(w_{\mathbf{k}}-1) + 2\mathrm{Re}\left((\beta^*-\gamma)q_{\mathbf{k}}e^{-i(\omega_0 t - 2\Omega^b_{\mathbf{k}})}\right) \tag{6.3.16}$$

Notably, $\beta = -\gamma^*$. Finally, inserting the coefficients found in Eq. (6.3.13), the Dirac-Bloch equations for a general two band relativistic carrier are:

$$\begin{aligned} \dot{q}_{\mathbf{k}} - i\left(\omega_0 - 2\dot{\Omega}_b\right) q_{\mathbf{k}} - \langle u^{(+)}_{\mathbf{k}} | \dot{u}^{(-)}_{\mathbf{k}} \rangle \, e^{i(\omega_0 t + \xi\Lambda_{\mathbf{k}})} w_{\mathbf{k}} = 0 \\ \dot{w}_{\mathbf{k}} + 4\mathrm{Re}\left(\langle u^{(+)}_{\mathbf{k}} | \dot{u}^{(-)}_{\mathbf{k}} \rangle^* \, e^{-i(\omega_0 t + \xi\Lambda_{\mathbf{k}})} q_{\mathbf{k}}\right) = 0 \end{aligned} \tag{6.3.17}$$

Without dephasing mechanisms, these generalised DBEs naturally encapsulate a probability conservation law, conserving the quantity $4|q_{\mathbf{k}}|^2 + w^2_{\mathbf{k}}$. This can be shown by considering its derivative:

$$\begin{aligned} \frac{d}{dt}\left(4|q_{\mathbf{k}}|^2 + w^2_{\mathbf{k}}\right) &= 4(\dot{q}_{\mathbf{k}} q^*_{\mathbf{k}} + q_{\mathbf{k}} \dot{q}^*_{\mathbf{k}}) + 2w_{\mathbf{k}} \dot{w}_{\mathbf{k}} \\ &= 4\left(2w_{\mathbf{k}} \mathrm{Re}\left(\langle u^{(+)}_{\mathbf{k}} | \dot{u}^{(-)}_{\mathbf{k}} \rangle^* \, e^{-i(\omega_0 t + \xi\Lambda_{\mathbf{k}})} q_{\mathbf{k}}\right)\right) \\ &\quad + 2w_{\mathbf{k}}\left(-4\mathrm{Re}\left(\langle u^{(+)}_{\mathbf{k}} | \dot{u}^{(-)}_{\mathbf{k}} \rangle^* \, e^{-i(\omega_0 t + \xi\Lambda_{\mathbf{k}})} q_{\mathbf{k}}\right)\right) \\ &= 0 \end{aligned} \tag{6.3.18}$$

where the derivatives were obtained by substitution from the generalised DBEs.

6.4 Currents

The philosophy underlying the calculation of the current from the generalised DBEs remains the same as applied in previous sections, although the expressions reveal much more complexity.

In general, the μ component of the microscopic current operators is still proportional to the derivative in the momentum variable of the full Hamiltonian $H_{\mathbf{k}}$, i.e.

$$\hat{j}_{\mu,\mathbf{k}}(\xi, s, t) = -\frac{e}{\hbar}\partial_{k_\mu} H_{\mathbf{k}}(\xi, s, t) \tag{6.4.1}$$

By the linearity of the derivative operators, the full current density operator can be expressed additively by the order of their expansion index (i) $\hat{j}_{\mu,\mathbf{k}}(\xi,s,t) = \sum_i \hat{j}^{(i)}_{\mu,\mathbf{k}}(\xi,s,t)$, where each order has an associated operator $\hat{j}^{(i)}_{\mu,\mathbf{k}}(\xi,s,t) \equiv -\frac{e}{\hbar}\frac{\partial}{\partial k_\mu} H^{(i)}_{\mathbf{k}}(\xi,s,t)$. Using the ansatz of Eq. (6.3.5), the current expectation of order i is:

$$\begin{aligned}
\langle \Psi_{\mathbf{k}} | \hat{j}^{(i)}_{\mu,\mathbf{k}} | \Psi_{\mathbf{k}} \rangle &= \sum_{\lambda,\lambda'} (c^{\lambda}_{\mathbf{k}})^* c^{\lambda'}_{\mathbf{k}} e^{i((\eta^{\lambda'}_{\mathbf{k}} - \eta^{\lambda}_{\mathbf{k}}) - (\Omega^{\lambda'}_{\mathbf{k}} - \Omega^{\lambda}_{\mathbf{k}})} \langle u^{\lambda}_{\mathbf{k}} | \hat{j}^{(i)}_{\mu,\mathbf{k}} | u^{\lambda'}_{\mathbf{k}} \rangle \\
&= \sum_{\lambda,\lambda'} (c^{\lambda}_{\mathbf{k}})^* c^{\lambda'}_{\mathbf{k}} e^{-i(\lambda'-\lambda)\left(\frac{\xi}{2}\Lambda_{\mathbf{k}} + \Omega^b_{\mathbf{k}}\right)} \langle u^{\lambda}_{\mathbf{k}} | \hat{j}^{(i)}_{\mu,\mathbf{k}} | u^{\lambda'}_{\mathbf{k}} \rangle \\
&= \sum_{\lambda} \left[|c^{\lambda}_{\mathbf{k}}|^2 \langle u^{\lambda}_{\mathbf{k}} | \hat{j}^{(i)}_{\mu,\mathbf{k}} | u^{\lambda}_{\mathbf{k}} \rangle + (c^{\lambda}_{\mathbf{k}})^* c^{-\lambda}_{\mathbf{k}} e^{i\lambda(\xi\Lambda_{\mathbf{k}} + 2\Omega^b_{\mathbf{k}})} \langle u^{\lambda}_{\mathbf{k}} | \hat{j}^{(i)}_{\mu,\mathbf{k}} | u^{-\lambda}_{\mathbf{k}} \rangle \right]
\end{aligned} \tag{6.4.2}$$

After the valence current is subtracted, following the discussion in Section 4.4, intraband and interband terms can be split. This regularisation term is incorporated in the intraband contributions, leading to the full current in time domain:

$$\begin{aligned}
j_{\mu,\mathbf{k}}(\xi,s,t) &= \sum_i \left[\langle \Psi_{\mathbf{k}} | \hat{j}^{(i)}_{\mu,\mathbf{k}} | \Psi_{\mathbf{k}} \rangle - \langle u^{(-)}_{\mathbf{k}} | \hat{j}^{(i)}_{\mu,\mathbf{k}} | u^{(-)}_{\mathbf{k}} \rangle \right] \\
&= \underbrace{\sum_i j^{\text{intra(i)}}_{\mu,\mathbf{k}}(t)}_{j^{\text{intra}}_{\mu,\mathbf{k}}(t)} + \underbrace{\sum_i j^{\text{inter(i)}}_{\mu,\mathbf{k}}(\xi,t)}_{j^{\text{inter}}_{\mu,\mathbf{k}}(t)}
\end{aligned} \tag{6.4.3}$$

In this fashion, the role of the expansion on intraband or interband features is easily revealed. By re-expressing the coefficients $c^{\lambda}_{\mathbf{k}}$ in terms of the dynamical variables, each order provides to each current contribution in the following way:

$$j^{\text{intra(i)}}_{\mu,\mathbf{k}}(t) = |c^{(+)}_{\mathbf{k}}|^2 \langle u^{(+)}_{\mathbf{k}} | \hat{j}^{(i)}_{\mu,\mathbf{k}} | u^{(+)}_{\mathbf{k}} \rangle + \left(|c^{(-)}_{\mathbf{k}}|^2 - 1 \right) \langle u^{(-)}_{\mathbf{k}} | \hat{j}^{(i)}_{\mu,\mathbf{k}} | u^{(-)}_{\mathbf{k}} \rangle \tag{6.4.4}$$

$$j^{\text{inter(i)}}_{\mu,\mathbf{k}}(t) = q_{\mathbf{k}} e^{-i(\omega_0 t + \xi\Lambda_{\mathbf{k}})} \langle u^{(-)}_{\mathbf{k}} | \hat{j}^{(i)}_{\mu,\mathbf{k}} | u^{(+)}_{\mathbf{k}} \rangle + q^*_{\mathbf{k}} e^{i(\omega_0 t + \xi\Lambda_{\mathbf{k}})} \langle u^{(+)}_{\mathbf{k}} | \hat{j}^{(i)}_{\mu,\mathbf{k}} | u^{(-)}_{\mathbf{k}} \rangle \tag{6.4.5}$$

The definitions so far covered are general. In order to consider a TMD monolayer, the current density operators must be obtained. It is clear that $H^{\text{SOC}}_{\mathbf{k}}$ does not contribute

to the current as it is not $\mathbf{k}$ dependent. As for the remaining contributions, this task can be completed if the terms containing $\boldsymbol{\sigma}(\xi)\cdot\boldsymbol{\pi}_{\mathbf{k}}$ in the operator form of $H^{(i)}_{\mathbf{k}}(\xi)$ are expanded. Given this form, it is more convenient to denote them as $H^{(i)}_{\mathbf{k}}(\pi_x,\pi_y)$. These will naturally be explicitly spin and valley-dependent. The newly-rewritten Hamiltonians now take the following forms, respectively given by their order:

$$H^{(1)}_{\mathbf{k}}(\pi_x,\pi_y) = a\gamma_0(\xi\pi_x\sigma_x + \pi_y\sigma_y) + \frac{\Delta}{2}\sigma_z \tag{6.4.6}$$

$$H^{(2)}_{\mathbf{k}}(\pi_x,\pi_y) = a^2\Bigg(\gamma_3\left[(\pi_x^2-\pi_y^2)\sigma_x - 2\xi\pi_x\pi_y\sigma_y\right] + \frac{\pi_x^2+\pi_y^2}{2}\left[(\gamma_1+\gamma_2)\mathbb{I} + (\gamma_1-\gamma_2)\sigma_z\right]\Bigg) \tag{6.4.7}$$

$$H^{(3)}_{\mathbf{k}}(\pi_x,\pi_y) = a^3\Bigg(\gamma_6\left[\xi(\pi_x^3+\pi_y^2\pi_x)\sigma_x + (\pi_x^2\pi_y+\pi_y^3)\sigma_y\right] + \frac{\xi}{2}(\pi_x^3-3\pi_y^2\pi_x)\left[(\gamma_4+\gamma_5)\mathbb{I} + (\gamma_4-\gamma_5)\sigma_z\right]\Bigg) \tag{6.4.8}$$

With these, the definition in Eq. (6.4) allows the current density operators for both Cartesian components to be obtained, for any order. For the first-order, the $\mathbf{k}$-independent operators used in graphene are retrieved:

$$\hat{j}^{(1)}_{x,\mathbf{k}} = -\frac{\xi e\gamma_0 a}{\hbar}\sigma_x \tag{6.4.9}$$

$$\hat{j}^{(1)}_{y,\mathbf{k}} = -\frac{e\gamma_0 a}{\hbar}\sigma_y \tag{6.4.10}$$

As for the second-order current operators, they become momentum-dependent, now also depending on the transverse momentum component:

$$\begin{aligned}\hat{j}^{(2)}_{x,\mathbf{k}}(\pi_x,\pi_y) &= -\frac{ea^2}{\hbar}\left(2\gamma_3(\pi_x\sigma_x - \xi\pi_y\sigma_y) + \pi_x\left[(\gamma_1+\gamma_2)\mathbb{I} + (\gamma_1-\gamma_2)\sigma_z\right]\right)\\ &= -\frac{ea^2|\boldsymbol{\pi}_\mathbf{k}|}{\hbar}\Bigg(2\gamma_3\cos\theta_\mathbf{k}\sigma_x - 2\xi\gamma_3\sin\theta_\mathbf{k}\sigma_y\\ &\qquad + (\gamma_1+\gamma_2)\cos\theta_\mathbf{k}\mathbb{I} + (\gamma_1-\gamma_2)\cos\theta_\mathbf{k}\sigma_z\Bigg)\end{aligned} \tag{6.4.11}$$

$$\begin{aligned}\hat{j}^{(2)}_{y,\mathbf{k}}(\pi_x,\pi_y) &= -\frac{ea^2}{\hbar}\left(-2\gamma_3(\pi_y\sigma_x + \xi\pi_x\sigma_y) + \pi_y\left[(\gamma_1+\gamma_2)\mathbb{I} + (\gamma_1-\gamma_2)\sigma_z\right]\right)\\ &= -\frac{ea^2|\boldsymbol{\pi}_\mathbf{k}|}{\hbar}\Bigg(-2\gamma_3\sin\theta_\mathbf{k}\sigma_x - 2\xi\gamma_3\cos\theta_\mathbf{k}\sigma_y +\\ &\qquad (\gamma_1+\gamma_2)\sin\theta_\mathbf{k}\mathbb{I} + (\gamma_1-\gamma_2)\sin\theta_\mathbf{k}\sigma_z\Bigg)\end{aligned} \tag{6.4.12}$$

where the last equality was obtained by rewriting the momentum components as polars. For the third-order contributions:

$$\begin{aligned}\hat{j}^{(3)}_{x,\mathbf{k}}(\pi_x,\pi_y) &= -\frac{ea^3}{\hbar}\Bigg(\gamma_6\left[\xi(3\pi_x^2+\pi_y^2)\sigma_x + 2\pi_x\pi_y\sigma_y\right]\\ &\qquad + \frac{3\xi}{2}(\pi_x^2-\pi_y^2)\left[(\gamma_4+\gamma_5)\mathbb{I} + (\gamma_4-\gamma_5)\sigma_z\right]\Bigg)\\ &= -\frac{ea^3|\boldsymbol{\pi}_\mathbf{k}|^2}{\hbar}\Bigg(\xi\gamma_6(\cos 2\theta_\mathbf{k}+2)\sigma_x + 2\gamma_6\cos\theta_\mathbf{k}\sin\theta_\mathbf{k}\sigma_y\\ &\qquad + \frac{3\xi}{2}\cos 2\theta_\mathbf{k}\left[(\gamma_4+\gamma_5)\mathbb{I} + \frac{3\xi}{2}(\gamma_4-\gamma_5)\sigma_z\right]\Bigg)\end{aligned} \tag{6.4.13}$$

$$\hat{j}^{(3)}_{y,\mathbf{k}}(\pi_x,\pi_y) = -\frac{ea^3}{\hbar}\Bigg(\gamma_6\left[2\xi\pi_x\pi_y\sigma_x + (\pi_x^2+3\pi_y^2)\sigma_y\right] - 3\xi\pi_x\pi_y\left[(\gamma_4+\gamma_5)\mathbb{I} + (\gamma_4-\gamma_5)\sigma_z\right]\Bigg)$$
$$= -\frac{ea^3|\boldsymbol{\pi}_\mathbf{k}|^2}{\hbar}\Bigg(2\gamma_6\xi\cos\theta_\mathbf{k}\sin\theta_\mathbf{k}\sigma_x - \gamma_6(\cos 2\theta_\mathbf{k}-2)\sigma_y - 3\xi\cos\theta_\mathbf{k}\sin\theta_\mathbf{k}\left[(\gamma_4+\gamma_5)\mathbb{I} + (\gamma_4-\gamma_5)\sigma_z\right]\Bigg) \tag{6.4.14}$$

where the inequalities $3\cos^2(x)+\sin^2(x) \equiv \cos(2x)+2$, $\cos^2(x)-\sin^2(x)\equiv\cos(2x)$ were used to simplify.

At this stage, with the knowledge of the current density operators and the instantaneous eigenstates, the current elements can be obtained.
From the form of $\hat{j}^{(i)}_\mathbf{k}$, it can be seen that the matrix set $\{\mathbb{I},\sigma_x,\sigma_y,\sigma_z\}\equiv\sigma_\nu$, $(\nu = 0,1,2,3)$ generates any i^{th}-order microscopic current in the sense that all current elements can always be written in the form

$$\langle u^\lambda_\mathbf{k}|\hat{j}^{(i)}_{\mu,\mathbf{k}}|u^{\lambda'}_\mathbf{k}\rangle = \sum_\nu a^{(i)}_{\mu,\nu}\langle u^\lambda_\mathbf{k}|\sigma_\nu|u^{\lambda'}_\mathbf{k}\rangle \tag{6.4.15}$$

where $a^{(i)}_{\mu,\nu}(\xi,t)$ are coefficients which can be read off the operators just obtained. Upon insertion of the instantaneous eigenstates of Eq. (6.2.28) into the elements $\langle u^\lambda_\mathbf{k}|\sigma_\nu|u^{\lambda'}_\mathbf{k}\rangle$, one obtains:

$$\langle u^\lambda_\mathbf{k}|\sigma_0|u^{\lambda'}_\mathbf{k}\rangle = \delta_{\lambda\lambda'} \tag{6.4.16}$$

$$\langle u^\lambda_\mathbf{k}|\sigma_x|u^{\lambda'}_\mathbf{k}\rangle = \left(g_\mathbf{k}\frac{2\lambda\lambda'(\epsilon^a_\mathbf{k}-r_\mathbf{k})\cos(\theta_\mathbf{k}-\nu_\mathbf{k}) + \epsilon^b_\mathbf{k}\left(\lambda' e^{i\xi(\theta_\mathbf{k}-\nu_\mathbf{k})} + \lambda e^{-i\xi(\theta_\mathbf{k}-\nu_\mathbf{k})}\right)}{\sqrt{(g^2_\mathbf{k}+(\epsilon^\lambda_\mathbf{k}-r_\mathbf{k})^2)(g^2_\mathbf{k}+(\epsilon^{\lambda'}_\mathbf{k}-r_\mathbf{k})^2)}}\right)$$
$$= \begin{cases} \lambda\frac{g_\mathbf{k}}{\epsilon^b_\mathbf{k}}\cos(\theta_\mathbf{k}-\nu_\mathbf{k}) & \text{for } \lambda'=\lambda \text{ (intraband)} \\ z_\mathbf{k}\cos(\theta_\mathbf{k}-\nu_\mathbf{k}) - i\lambda\xi\sin(\theta_\mathbf{k}-\nu_\mathbf{k}) & \text{for } \lambda'=-\lambda \text{ (interband)} \end{cases} \tag{6.4.17}$$

$$\langle u_{\mathbf{k}}^{\lambda}|\sigma_y|u_{\mathbf{k}}^{\lambda'}\rangle = \left(g_{\mathbf{k}}\frac{2\xi\lambda\lambda'(\epsilon_{\mathbf{k}}^{a}-r_{\mathbf{k}})\sin(\theta_{\mathbf{k}}-\nu_{\mathbf{k}})+i\epsilon_{\mathbf{k}}^{b}\left(\lambda e^{-i\xi(\theta_{\mathbf{k}}-\nu_{\mathbf{k}})}-\lambda' e^{i\xi(\theta_{\mathbf{k}}-\nu_{\mathbf{k}})}\right)}{\sqrt{(g_{\mathbf{k}}^2+(\epsilon_{\mathbf{k}}^{\lambda}-r_{\mathbf{k}})^2)(g_{\mathbf{k}}^2+(\epsilon_{\mathbf{k}}^{\lambda'}-r_{\mathbf{k}})^2)}}\right)$$
$$= \begin{cases} \lambda\xi\frac{g_{\mathbf{k}}}{\epsilon_{\mathbf{k}}^{b}}\sin(\theta_{\mathbf{k}}-\nu_{\mathbf{k}}) & \text{for } \lambda'=\lambda \text{ (intraband)} \\ \xi z_{\mathbf{k}}\sin(\theta_{\mathbf{k}}-\nu_{\mathbf{k}})+i\lambda\cos(\theta_{\mathbf{k}}-\nu_{\mathbf{k}}) & \text{for } \lambda'=-\lambda \text{ (interband)} \end{cases} \tag{6.4.18}$$

$$\langle u_{\mathbf{k}}^{\lambda}|\sigma_z|u_{\mathbf{k}}^{\lambda'}\rangle = -\lambda\lambda'\frac{g_{\mathbf{k}}^2-(r_{\mathbf{k}}-\epsilon_{\mathbf{k}}^{\lambda})(r_{\mathbf{k}}-\epsilon_{\mathbf{k}}^{\lambda'})}{\sqrt{(g_{\mathbf{k}}^2+(r_{\mathbf{k}}-\epsilon_{\mathbf{k}}^{\lambda})^2)(g_{\mathbf{k}}^2+(r_{\mathbf{k}}-\epsilon_{\mathbf{k}}^{\lambda'})^2)}}$$
$$= \begin{cases} -\lambda z_{\mathbf{k}} & \text{for } \lambda'=\lambda \text{ (intraband)} \\ \frac{g_{\mathbf{k}}}{\epsilon_{\mathbf{k}}^{b}} & \text{for } \lambda'=-\lambda \text{ (interband)} \end{cases} \tag{6.4.19}$$

Intraband Currents

Using the expansion of Eq. (6.4.15) on the intraband current of Eq. (6.4.4), the i^{th} contribution may be written as:

$$j_{\mu,\mathbf{k}}^{\text{intra(i)}} = \sum_{\nu} a_{\mu,\nu}^{(i)}\left(\left|c_{\mathbf{k}}^{+}\right|^2\langle u_{\mathbf{k}}^{(+)}|\sigma_\nu|u_{\mathbf{k}}^{(+)}\rangle + \left(|c_{\mathbf{k}}^{-}|^2-1\right)\langle u_{\mathbf{k}}^{(-)}|\sigma_\nu|u_{\mathbf{k}}^{(-)}\rangle\right) \tag{6.4.20}$$

It can be seen that the intraband current generators have the symmetry/antisymmetry properties:

$$\langle u_{\mathbf{k}}^{\lambda}|\sigma_\nu|u_{\mathbf{k}}^{\lambda}\rangle + \langle u_{\mathbf{k}}^{-\lambda}|\sigma_\nu|u_{\mathbf{k}}^{-\lambda}\rangle = 0 \quad \text{for} \quad \nu=1,2,3 \tag{6.4.21}$$

$$\langle u_{\mathbf{k}}^{\lambda}|\sigma_0|u_{\mathbf{k}}^{\lambda}\rangle - \langle u_{\mathbf{k}}^{-\lambda}|\sigma_0|u_{\mathbf{k}}^{-\lambda}\rangle = 0 \quad \text{for} \quad \nu=0 \tag{6.4.22}$$

Since $|c_{\mathbf{k}}^{+}|^2+|c_{\mathbf{k}}^{-}|^2=1$, the latter contribution is null in Eq. (6.4.20). The intraband current of any correction order is thus:

$$j_{\mu,\mathbf{k}}^{\text{intra(i)}}(\xi,t) = \sum_{\nu=1}^{3} a_{\mu,\nu}^{(i)}\langle u_{\mathbf{k}}^{(+)}|\sigma_\nu|u_{\mathbf{k}}^{(+)}\rangle\,(w_{\mathbf{k}}+1) \tag{6.4.23}$$

The microscopic intraband currents in time domain, may now be obtained. The first-order has the simple coefficients $a^{(1)}_{\mu,\nu} = 0$ for $\nu \neq \mu$ and is therefore:

$$j^{\text{intra}(1)}_{x,\mathbf{k}} = -\frac{\xi e a \gamma_0 g_{\mathbf{k}}}{\hbar \epsilon^b_{\mathbf{k}}} \cos(\theta_{\mathbf{k}} - \nu_{\mathbf{k}})(w_{\mathbf{k}} + 1) \tag{6.4.24}$$

$$j^{\text{intra}(1)}_{y,\mathbf{k}} = -\frac{\xi e a \gamma_0 g_{\mathbf{k}}}{\hbar \epsilon^b_{\mathbf{k}}} \sin(\theta_{\mathbf{k}} - \nu_{\mathbf{k}})(w_{\mathbf{k}} + 1) \tag{6.4.25}$$

This expression reduces to the current previously calculated for $H^{(1)}_{\mathbf{k}}$ by setting $g_{\mathbf{k}} = \xi a \gamma_0 |\boldsymbol{\pi}_{\mathbf{k}}|$, $\nu_{\mathbf{k}} = 0$ and $v_{\text{F}} = a\gamma_0/\hbar$, leading to the factor assignment $-\frac{e\xi\gamma_0 g_{\mathbf{k}}}{\hbar\epsilon^b_{\mathbf{k}}} \mapsto -e v_{\text{F}} \frac{v_{\text{F}} \boldsymbol{\pi}_{\mathbf{k}}}{\epsilon_{\mathbf{k}}}$.

As for the second-order intraband current:

$$j^{\text{intra}(2)}_{x,\mathbf{k}} = -\frac{e a^2 |\boldsymbol{\pi}_{\mathbf{k}}|}{\hbar} \left(\frac{2\gamma_3 g_{\mathbf{k}}}{\epsilon^b_{\mathbf{k}}} \cos(2\theta_{\mathbf{k}} - \nu_{\mathbf{k}}) - (\gamma_1 - \gamma_2) z_{\mathbf{k}} \cos\theta_{\mathbf{k}} \right) (w_{\mathbf{k}} + 1) \tag{6.4.26}$$

$$j^{\text{intra}(2)}_{y,\mathbf{k}} = -\frac{e a^2 |\boldsymbol{\pi}_{\mathbf{k}}|}{\hbar} \left(-\frac{2\gamma_3 g_{\mathbf{k}}}{\epsilon^b_{\mathbf{k}}} \sin(2\theta_{\mathbf{k}} - \nu_{\mathbf{k}}) - (\gamma_1 - \gamma_2) z_{\mathbf{k}} \sin\theta_{\mathbf{k}} \right) (w_{\mathbf{k}} + 1) \tag{6.4.27}$$

where the equalities $\cos(x)\cos(x-y) - \sin(x)\sin(x-y) \equiv \cos(2x-y)$ and $\sin(x)\cos(x-y) + \cos(x)\sin(x-y) \equiv \sin(2x-y)$ were used. The third-order contribution is obtained as:

$$\begin{aligned} j^{\text{intra}(3)}_{x,\mathbf{k}} = -\frac{\xi e a^3 |\boldsymbol{\pi}_{\mathbf{k}}|^2}{\hbar} \Bigg(& \frac{\gamma_6 g_{\mathbf{k}}}{\epsilon^b_{\mathbf{k}}} \left(3\cos\theta_{\mathbf{k}} \cos\nu_{\mathbf{k}} + \sin\theta_{\mathbf{k}} \sin\nu_{\mathbf{k}}\right) \\ & - \frac{3(\gamma_4 - \gamma_5)}{2} z_{\mathbf{k}} \cos 2\theta_{\mathbf{k}} \Bigg) (w_{\mathbf{k}} + 1) \end{aligned} \tag{6.4.28}$$

$$\begin{aligned} j^{\text{intra}(3)}_{y,\mathbf{k}} = -\frac{\xi e a^3 |\boldsymbol{\pi}_{\mathbf{k}}|^2}{\hbar} \Bigg(& \frac{\gamma_6 g_{\mathbf{k}}}{\epsilon^b_{\mathbf{k}}} \left(2\sin(\theta_{\mathbf{k}} - \nu_{\mathbf{k}}) + \sin(\theta_{\mathbf{k}} + \nu_{\mathbf{k}})\right) \\ & + \frac{3(\gamma_4 - \gamma_5)}{2} z_{\mathbf{k}} \sin 2\theta_{\mathbf{k}} \Bigg) (w_{\mathbf{k}} + 1) \end{aligned} \tag{6.4.29}$$

where the identities $\cos(2x)\cos(x-y)+2\cos(x-y)+2\sin(x)\cos(x)\sin(x-y) \equiv 3\cos(x)\cos(y)+\sin(x)\sin(y)$ was used.

Interband currents

The general form of the i^{th} contribution to the interband current is now obtained, by using the expansion of Eq. (6.4.15) on the interband current of Eq. (6.4.4):

$$j^{\text{inter(i)}}_{\mu,\mathbf{k}} = \sum_{\nu} a^{(i)}_{\mu,\nu} \left(q_{\mathbf{k}} e^{-i(\xi\Lambda_{\mathbf{k}}+\omega_0 t)} \langle u^{(-)}_{\mathbf{k}} | \sigma_\nu | u^{(+)}_{\mathbf{k}} \rangle + q^*_{\mathbf{k}} e^{i(\xi\Lambda_{\mathbf{k}}+\omega_0 t)} \langle u^{(+)}_{\mathbf{k}} | \sigma_\nu | u^{(-)}_{\mathbf{k}} \rangle \right) \tag{6.4.30}$$

Importantly, given the anti-Hermicity of the elements in the band index λ:

$$\langle u^{\lambda}_{\mathbf{k}} | \sigma_\nu | u^{-\lambda}_{\mathbf{k}} \rangle = \langle u^{-\lambda}_{\mathbf{k}} | \sigma_\nu | u^{\lambda}_{\mathbf{k}} \rangle^* \quad \text{for} \quad \nu = 0,1,2,3 \tag{6.4.31}$$

Furthermore, since $a^{(i)}_{\mu,\nu} \in \mathbb{R}$, one has

$$\langle u^{\lambda}_{\mathbf{k}} | \hat{j}^{(i)}_{\mu,\mathbf{k}} | u^{-\lambda}_{\mathbf{k}} \rangle = \langle u^{-\lambda}_{\mathbf{k}} | \hat{j}^{(i)}_{\mu,\mathbf{k}} | u^{\lambda}_{\mathbf{k}} \rangle^* \tag{6.4.32}$$

and the interband current of any correction order becomes:

$$\begin{aligned} j^{\text{inter(i)}}_{\mu,\mathbf{k}} &= \sum_{\nu} 2a^{(i)}_{\mu,\nu} \text{Re}\left(q_{\mathbf{k}} e^{-i(\xi\Lambda_{\mathbf{k}}+\omega_0 t)} \langle u^{(-)}_{\mathbf{k}} | \sigma_\nu | u^{(+)}_{\mathbf{k}} \rangle \right) \\ &= \left(\sum_{\nu=1}^{3} 2a^{(i)}_{\mu\nu} \mathcal{S}^{\text{R}}_{\nu} \right) \text{Re}\left(q_{\mathbf{k}} e^{-i(\xi\Lambda_{\mathbf{k}}+\omega_0 t)} \right) - \left(\sum_{\nu=1}^{2} 2a^{(i)}_{\mu\nu} \mathcal{S}^{\text{I}}_{\nu} \right) \text{Im}\left(q_{\mathbf{k}} e^{-i(\xi\Lambda_{\mathbf{k}}+\omega_0 t)} \right) \end{aligned} \tag{6.4.33}$$

where $\langle u^{(-)}_{\mathbf{k}} | \sigma_\nu | u^{(+)}_{\mathbf{k}} \rangle \equiv \mathcal{S}^{\text{R}}_{\nu} + i\mathcal{S}^{\text{I}}_{\nu,}$ has been split in its real and imaginary part and $\text{Re}(ix) = -\text{Im}(x)$ has been used. Regarding the sum limits, these have been restricted

since, by Eq. (6.4.19):

$$\mathrm{Re}\,\langle u_{\mathbf{k}}^{(-)}|\sigma_0|u_{\mathbf{k}}^{(+)}\rangle = \mathrm{Im}\,\langle u_{\mathbf{k}}^{(-)}|\sigma_0|u_{\mathbf{k}}^{(+)}\rangle = \mathrm{Im}\,\langle u_{\mathbf{k}}^{(-)}|\sigma_z|u_{\mathbf{k}}^{(+)}\rangle = 0 \tag{6.4.34}$$

All is left is for the sums to be evaluated. The first-order contributions has $a_{\mu,\nu}^{(1)} = 0$ for $\nu \neq \mu$ and consequently:

$$j_{x,\mathbf{k}}^{\mathrm{inter}(1)} = -\frac{2\xi e\gamma_0 a}{\hbar}\left(z_{\mathbf{k}}\cos(\theta_{\mathbf{k}}-\nu_{\mathbf{k}})\mathrm{Re}\left(q_{\mathbf{k}}e^{-i(\xi\Lambda_{\mathbf{k}}+\omega_0 t)}\right) - \xi\sin\theta_{\mathbf{k}}\mathrm{Im}\left(q_{\mathbf{k}}e^{-i(\xi\Lambda_{\mathbf{k}}+\omega_0 t)}\right)\right) \tag{6.4.35}$$

$$j_{y,\mathbf{k}}^{\mathrm{inter}(1)} = -\frac{2e\gamma_0 a}{\hbar}\left(\xi z_{\mathbf{k}}\sin(\theta_{\mathbf{k}}-\nu_{\mathbf{k}})\mathrm{Re}\left(q_{\mathbf{k}}e^{-i(\xi\Lambda_{\mathbf{k}}+\omega_0 t)}\right) + \cos\theta_{\mathbf{k}}\mathrm{Im}\left(q_{\mathbf{k}}e^{-i(\xi\Lambda_{\mathbf{k}}+\omega_0 t)}\right)\right) \tag{6.4.36}$$

Naturally, this expression reduces to the current predicted for $H_{\mathbf{k}}^{(1)}$ by setting $g_{\mathbf{k}} = \xi a\gamma_0|\boldsymbol{\pi}_{\mathbf{k}}|$, $r_{\mathbf{k}} = -\Delta/2$, $\nu_{\mathbf{k}} = 0$, $z_{\mathbf{k}} = -\frac{\Delta}{2\epsilon_{\mathbf{k}}^b}$.

As for the second-order:

$$j_{x,\mathbf{k}}^{\mathrm{inter}(2)} = -\frac{2ea^2\boldsymbol{\pi}_{\mathbf{k}}}{\hbar}\left(\left(2\gamma_3 z_{\mathbf{k}}\cos(2\theta_{\mathbf{k}}-\nu_{\mathbf{k}}) + (\gamma_1-\gamma_2)\frac{g_{\mathbf{k}}}{\epsilon_{\mathbf{k}}^b}\cos\theta_{\mathbf{k}}\right)\mathrm{Re}\left(q_{\mathbf{k}}e^{-i(\xi\Lambda_{\mathbf{k}}+\omega_0 t)}\right) - 2\gamma_3\xi\sin(2\theta_{\mathbf{k}}-\nu_{\mathbf{k}})\mathrm{Im}\left(q_{\mathbf{k}}e^{-i(\xi\Lambda_{\mathbf{k}}+\omega_0 t)}\right)\right) \tag{6.4.37}$$

$$j_{y,\mathbf{k}}^{\mathrm{inter}(2)} = -\frac{2ea^2\boldsymbol{\pi}_{\mathbf{k}}}{\hbar}\left(\left(-2\gamma_3 z_{\mathbf{k}}\sin(2\theta_{\mathbf{k}}-\nu_{\mathbf{k}}) + (\gamma_1-\gamma_2)\frac{g_{\mathbf{k}}}{\epsilon_{\mathbf{k}}^b}\sin\theta_{\mathbf{k}}\right)\mathrm{Re}\left(q_{\mathbf{k}}e^{-i(\xi\Lambda_{\mathbf{k}}+\omega_0 t)}\right) - 2\gamma_3\xi\cos(2\theta_{\mathbf{k}}-\nu_{\mathbf{k}})\mathrm{Im}\left(q_{\mathbf{k}}e^{-i(\xi\Lambda_{\mathbf{k}}+\omega_0 t)}\right)\right) \tag{6.4.38}$$

Similarly, the third-order interband current is obtained as:

$$j^{\text{inter}(3)}_{x,\mathbf{k}} = -\frac{ea^3|\boldsymbol{\pi}_{\mathbf{k}}|^2}{\hbar}\Bigg(-2\gamma_6(\sin\theta_{\mathbf{k}}\cos\nu_{\mathbf{k}} - 3\cos\theta_{\mathbf{k}}\sin\nu_{\mathbf{k}})\text{Im}\left(q_{\mathbf{k}}e^{-i(\xi\Lambda_{\mathbf{k}}+\omega_0 t)}\right)$$
$$+\left(2\xi\gamma_6 z_{\mathbf{k}}(3\cos\theta_{\mathbf{k}}\cos\nu_{\mathbf{k}} + \sin\theta_{\mathbf{k}}\sin\nu_{\mathbf{k}}) + 3\xi(\gamma_4-\gamma_5)\frac{g_{\mathbf{k}}}{\epsilon^b_{\mathbf{k}}}\cos 2\theta_{\mathbf{k}}\right)\text{Re}\left(q_{\mathbf{k}}e^{-i(\xi\Lambda_{\mathbf{k}}+\omega_0 t)}\right)\Bigg) \tag{6.4.39}$$

$$j^{\text{inter}(3)}_{y,\mathbf{k}} = -\frac{ea^3|\boldsymbol{\pi}_{\mathbf{k}}|^2}{\hbar}\Bigg(2\gamma_6(\cos\theta_{\mathbf{k}}\cos\nu_{\mathbf{k}} + 3\sin\theta_{\mathbf{k}}\sin\nu_{\mathbf{k}})\text{Im}\left(q_{\mathbf{k}}e^{-i(\xi\Lambda_{\mathbf{k}}+\omega_0 t)}\right)$$
$$+\left(2\xi\gamma_6 z_{\mathbf{k}}(2\sin(\theta_{\mathbf{k}}-\nu_{\mathbf{k}}) + \sin(\theta_{\mathbf{k}}+\nu_{\mathbf{k}})) - 3\xi(\gamma_4-\gamma_5)\frac{g_{\mathbf{k}}}{\epsilon^b_{\mathbf{k}}}\sin 2\theta_{\mathbf{k}}\right)\text{Re}\left(q_{\mathbf{k}}e^{-i(\xi\Lambda_{\mathbf{k}}+\omega_0 t)}\right)\Bigg) \tag{6.4.40}$$

The physical current may be retrieved at this stage by appropriately taking all momentum contributions of both valleys and spin into account. In the continuum limit, it is:

$$\mathbf{J}(t) = \frac{1}{d(2\pi)^2}\sum_{\xi,s}\int \mathbf{j}_{\mathbf{k}}(\xi,s,t)d\mathbf{k}, \tag{6.4.41}$$

where d is the thickness of the monolayer, $d\mathbf{k} = kdkd\phi$ is the 2-dimensional differential in momentum space. The usual degeneracy of $g_s g_v = 4$ may not be assumed given that each contribution may not produce the same microscopic current.

6.5 Simulations

The theory developed in this chapter is meant to fully describe the dynamics of a general two-band model system whose dynamics is dictated by the Dirac equation. The methods applied and the choice of physical mechanisms define the functional form of the Hamiltonian parameters (the functions $f_{\mathbf{k}}, r_{\mathbf{k}}, g_{\mathbf{k}}$ and $\nu_{\mathbf{k}}$) of the system

and can thus be changed accordingly.

In particular for this chapter, the optical behaviour of a MoS_2 monolayer is studied. The dispersion plots were in fact obtained by considering effective parameters that have been reported to model TMDs accurately across the Brillouin zone and can be found in Table 6.1.

k · p Order	**Hamiltonian**	**Parameter**	**Value (eV)**	**Dimensionless**
First	$H_{\mathbf{k}}^{(1)}$	γ_0	1.003	1.2307
First	$H_{\mathbf{k}}^{(1)}$	Δ	1.63	2
Second	$H_{\mathbf{k}}^{(2)}$	γ_1	1.1196	1.3737
Second	$H_{\mathbf{k}}^{(2)}$	γ_2	-0.065	-0.0798
Second	$H_{\mathbf{k}}^{(2)}$	γ_3	-0.248	-0.3043
Third	$H_{\mathbf{k}}^{(3)}$	γ_4	0.163	0.2
Third	$H_{\mathbf{k}}^{(3)}$	γ_5	-0.094	-0.1153
Third	$H_{\mathbf{k}}^{(3)}$	γ_6	-0.232	-0.2847
First	$H_{\mathbf{k}}^{\mathrm{SOC}}$	γ_{SOC}	0.073	0.0896

Table 6.1: Effective energy parameters for the two-band $\mathbf{k} \cdot \mathbf{p}$ model for a MoS_2 monolayer as calculated in Appendix C of Ref.[1]. The dimensionless values are obtained with the energy scaling given in Table A.2, for a photon energy $\hbar\omega_0 = 1.63$ eV.

In order to simulate the generalised DBE, the same numerical recipe was used as in last chapters, namely a fourth-order Runge-Kutta algorithm. To probe the monolayer, a sech pulse of electric field intensity $\psi_0 = 2$, central pulse frequency $\Omega_0 = 15$. The photon energy is matched with the gap i.e. $\hbar\omega_0 = 1.6$ eV. This leads to the dimensionless energy parameters in the rightmost column of Table 6.1.

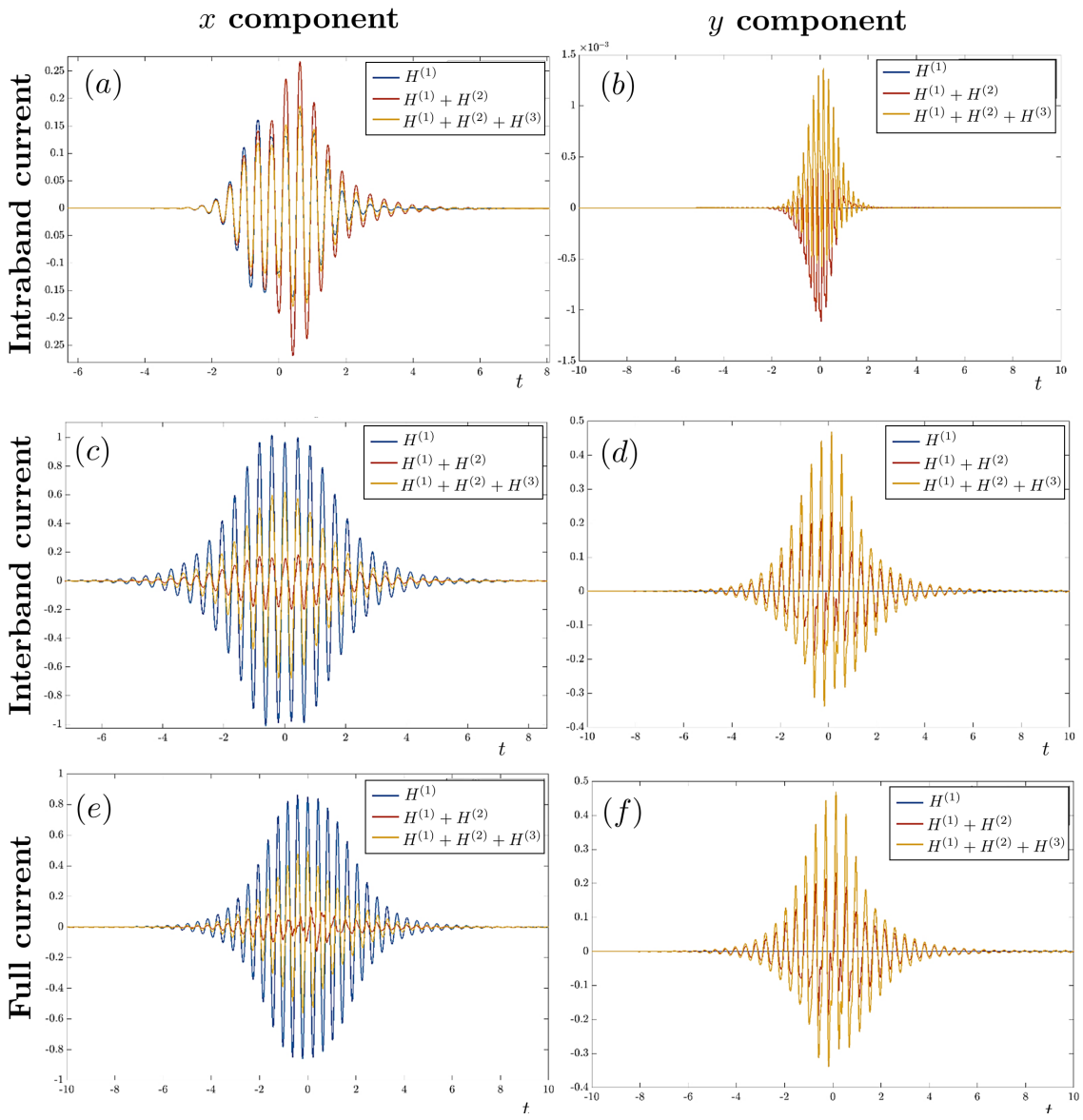

Figure 6.7: Plot of the total macroscopic current generated in a MoS_2 monolayer. In particular (a, b) shows the intraband current, (c, d) interband current and (e, f) the full current. The first column,(a, c, e), show the x component of such currents, whereas the second column, (b, d, f), shows the y component of the same currents.

In order to see the effect of each Hamiltonian term in the generation and current and related harmonic composition, the cumulative Hamiltonians are considered separately i.e. by considering only first-order, first and second-order and finally the full Hamiltonian up to third-order. Given the considerations that lead to the conclusion that no current contributions arise explicitly due to spin-orbit effects, it is expectable that its effect is rather small and hence not considered separately but always accounted for in any cumulative Hamiltonian.

The field is assumed linearly polarised in the $\hat{x}$ direction and the directional angle is thus $\Theta = 0$. The macroscopic current, containing the four spin and valley contributions, is shown in Fig. 6.7. In it, the first line, (a, b), shows the intraband current, the second line, (c, d), shows the interband current and the third line, (e, f), shows the full current, composed of both contributions. The first column, (a, c, e), show the x component of such currents, whereas the second column, (b, d, f), shows the y component of the same currents.

By analysing (f), it is clear that a non-vanishing J_y^{full} current is produced, attaining a significant amplitude, of roughly half the amplitude of J_x^{full}, shown in (e), even after averaging over the degeneracies. Upon inspection of (b) and (d), this current is created through interband processes, given the exceedingly small amplitude ($\approx 10^{-3}$) of the intraband current J_y^{intra}. The appearance of such a current is mostly likely due to the anisotropy of the underlying dispersion. This property is introduced when considering second and third-order contributions and it can be seen in (b) and (d) that only for those instances does the y component produces non-vanishing currents. In particular, the inclusion of both $H_{\mathbf{k}}^{(2)}$ and $H_{\mathbf{k}}^{(3)}$ further exacerbates the effect.

The x component still clearly dominates over its y counterpart, given the optical polarisation setup. Through the decomposition of the contributions, the interband current (c) positively makes up most of the full current shown in (e). This is not

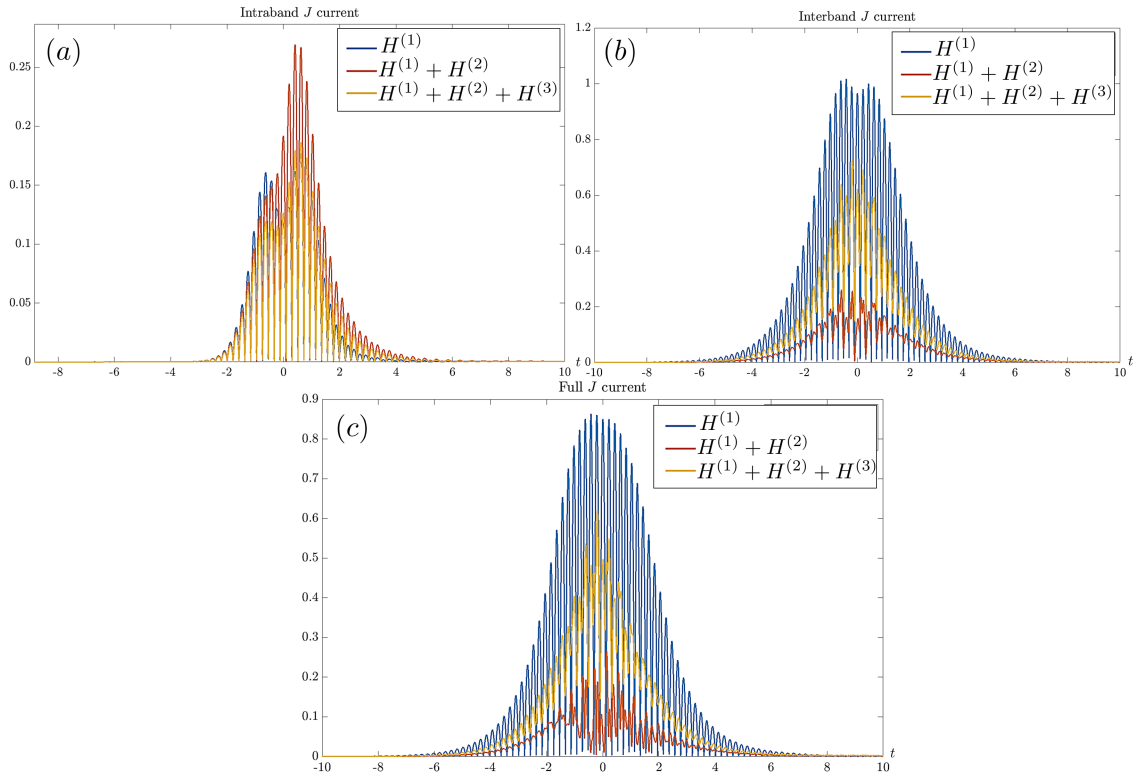

Figure 6.8: Plot of currents generated by considering different cumulative Hamiltonians up to first (blue), second (red) and third-order (yellow) terms, showing (a) the intraband current, (b) the interband current and (c) the full current.

surprising given that the sample is excited in resonant conditions. As was seen in 5.6.1, the amplitude of the interband current attains its maximum in such conditions. The inclusion of the second-order contributions leads to an appreciable suppression of current, of around 80% of the centrosymmetric model prediction. This suppression leads to the intraband (a) and interband (c) contributions to be of comparable amplitude and, due to the fact these contributions are not in phase, to a rather non-trivial modulation that results in the red line of (e). Third-order corrections make interband contributions dominate again. These, as will be shortly seen in Fig. 6.9 to further enhance the second-order nonlinearities.

For an appropriate analysis of the current generated, both components must be con-

sidered simultaneously. A total current $J(t)$ is then simply:

$$J(t) = \sqrt{J_x^2(t) + J_y^2(t)} \tag{6.5.1}$$

Fig 6.8 shows such total currents, again split in interband (a), interband (b) and full (c). The behaviour of the total intraband current is dictated mostly by the x component, as previously explained. Furthermore, the predictions when considering the contributions of first-order only and up to third-order lead to roughly the same intraband output. In (b), it is seen that the amplitude of the total interband current predicted by $\tilde{H}_{\mathbf{k}}^{(3)}$ is roughly four times greater than its intraband counterpart and thus, as expected, determines the total full current in (c).

With an understanding of how each expansion order affects the production of current in the sample, their respective spectra may now be inspected in Fig. 6.9. The total full spectrum, taking both components and contributions, indeed shows a second-harmonic peak greater than the third-harmonic peak whenever the centrosymmetry is broken, as seen by the red and yellow plots. Given the logarithmic scale of the plots, it may be deduced that the full Hamiltonian, accounting for additional terms breaking the centrosymmetry, yield a stronger SHG peak. Otherwise, the centrosymmetric Hamiltonian, whose output is shown in blue, does not show such harmonic, given its SHG peak well bellow its counterparts. Moreover, the third-harmonic peak is enhanced very considerably by centrosymmetry breaking terms.

In order to understand the origin of such a SHG enhancement, the intraband (a) and interband (b) current spectra are separately plotted. Peaks are found when $\omega/\omega_0 = 2$ in both contributions. However, the peaks in (a) are exceedingly small and do not change much when considering higher-order terms. The enhancement is clearly observed in the interband spectrum in (b), where the addition of such terms leads to a very significant increase. Again, given the resonant conditions of the excitation, the

harmonic profile of the full current is heavily defined by the interband contributions alone.

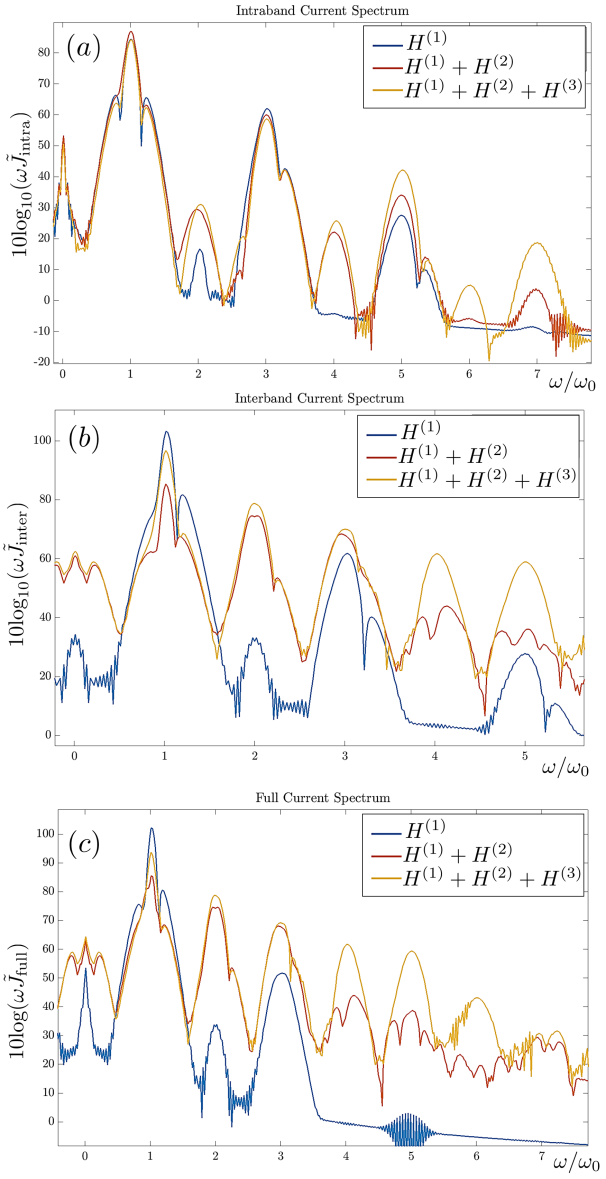

Figure 6.9: Plot of spectra in dB generated by considering different cumulative Hamiltonians up to first (blue), second (red) and third-order (yellow) terms, showing (a) the intraband spectrum, (b) the interband spectrum and (c) the full spectrum.

These results show that explicit non-centrosymmetric lattice structures show a rather high even-harmonic generation and the peaks, unlike the previous case in graphene where odd-harmonic generation dominated over its even counterparts, show a mono-

tonic decrease as the harmonic order is increased. In particular, the fourth and fifth-order peaks are remarkably large. For these observations. By comparing Fig. 6.9(a) and (b), it is clear that the contribution to even-harmonic generation certainly originates from interband currents. This is not surprising, given the resonant conditions of excitation and the consequent dominance of interband over intraband terms. The inclusion of Coulomb interactions in the carriers is expected to further enhance some nonlinearities of the system but, given the considerations in Section 6.1, presents some numerical challenges. In fact, the numerical implementation of the generalised DBEs is challenging. Nonetheless, these results provide a starting point to understand the dynamics of the carriers in such a complex system. The hope is, of course, to improve the methods and finesse of the model so the DBE formalism may be used as a means to study a variety of other materials which may be modelled as Dirac fermions.

Another interesting feature that may be studied in more detail is related to the effect of the anisotropy in the generation of such harmonics. This can be done by simulating the macroscopic current in different configurations of the direction angle Θ and by considering the effect of switching on and off the warping phase $\nu_{\mathbf{k}}$.

Chapter 7

Conclusion & Outlook

In summary, this work is concerned with models and methodologies that allow accurate light-matter interactions occurring in two-dimensional quasirelativistic materials to be understood. As the name implies, the carriers in such media are not actually relativistic in the sense that they do not travel at speeds close to the speed of light. However, their dynamics may be described by equations that resemble fully relativistic systems, namely the Dirac equation. The carriers in graphene are thus described by massless Dirac fermions.

Essentially, the work presented in this thesis tries to address the question of whether this description of the carriers yields fundamentally different optical features than "usual" carriers in lattices, described by the Schrödinger equation.

In particular, such interactions probed when the field is both intense and ultrashort vary qualitatively from their linear counterparts. Usual perturbative methods are used to express the nonlinear polarisation in powers of the field. By employing methods developed by Koch, Knorr, Östreich, Bowden, Agrawal (to name a few), a generalisation of the Optical Bloch Equations, equations that model the dynamics of a quantum-mechanical two-level system in the presence of a driving field to the realms of Condensed Matter Physics lead to extraordinary progress and insights into

the optoelectronic properties of a variety of semiconductors. Such methods resulted in the establishment of the *Semiconductor Bloch Equations* (SBEs).

Upon the discovery of fabrication methods of graphene, the research community was bewildered by the potential this material could have on many fronts. Despite the lack of a gap, an essential feature that allows many electronic phenomena in semiconductors, graphene was soon found to possess remarkable nonlinear properties.

In an effort to not only understand the principles underlying such phenomena but also to obtain proof of concept, with eventual ramifications into engineering, industry and technology at large, graphene became an intensely studied topic.

Since their first invention, the SBEs have been fantastically successful in the description of the dynamics of interband transitions in semiconductors, exciton and exciton-polariton formation and spectra, and the semiconductor laser. Immediately after the explosion of graphene research in recent years, the SBEs adapted to the graphene dispersion have been routinely applied to study the interaction between linear and nonlinear pulses with massless Dirac electrons.

However, the suitability of the SBEs to model graphene is not granted, given its different nature. To this end, Ishikawa derived and proposed a new set of equations modelling the carriers in graphene from first-principles. This lead to a generalisation of the SBEs, the *Dirac-Bloch Equations* (DBEs). In Chapter 4, it is proved that the DBEs consider further contributions than the SBEs, namely through the inclusion of the electromagnetic vector potential, as opposed to the exclusive inclusion of the electric field that couples to the electric dipole moment of the carriers.

This realisation is vital in understanding the disparities found in the predictions of both models, the SBEs and DBEs, when the optical excitation reaches a nonlinear regime. In particular, the inclusion of such potential allows the conical dispersion of graphene to oscillate and thus yields time-dependent frequency and electric dipole moment on the carriers. This phenomenon is conceptualised in a proposed mechanism

termed "*dynamical centrosymmetry breaking mechanism*", where the centrosymmetry of the medium is temporarily broken. If the pulse is illuminated at normal incidence ,with respect to the graphene monolayer, previously-forbidden even harmonics are allowed to be generated in the sample. Upon comparison of the output spectra, the SBEs, not having such mechanism explicit in its formalism, indeed fail to show any even-harmonic generation. They also overestimate the extent of which third harmonic radiation is generated. Even though many methods allowing second harmonic generation have been both proposed and experimentally realised, this result is novel given the normal incidence conditions that were assumed. For this reason, the SBEs are not a good model to study graphene in this regime.

Despite this observation, both models are in very good agreement in the linear regime. This observation can be rationalised in terms of the dynamical centrosymmetry breaking mechanism, since the time-dependent dispersion shift, provided by the vector potential, is negligible if the intensity of the field is also small. In this regime, both models accurately predict the law of universal absorption of graphene, a thoroughly observed phenomenon where the layer absorbs the incoming light with the same efficiency across all frequencies, independently of the light intensity.

In realistic samples, however, the massless description of the carriers somewhat loses its validity. Many intrinsic properties of laboratory-grown samples, such as imperfections, vacancies, defects, termination profiles and most importantly, substrate depositing, have been observed to introduce a small gap in the otherwise gapless dispersion of suspended, pristine graphene monolayers. This realisation lead to the generalisation of the DBEs to include the effects of such a gap in the generation of currents in the sample, and these are termed *Massive Dirac-Bloch equations*.

The nonlinear, non-perturbative current is consequently also generalised and shows rich dynamics. In particular, the spectrum generated by it shows rather robust odd-harmonic generation. The addition of the gap suppresses them as the gap is increased.

Since the gap does not break the centrosymmetry of the dispersion, even-harmonic generation is again expected to be absent. However, the massive DBEs predict that, if the sample is excited in ultrashort and intense conditions, a phenomenon previously reported in the context of Extreme Optics by the name of "*third harmonic generation in disguise of second harmonic generation*" takes place. This is observed in precise conditions, namely when the photon energy is appropriately tuned to the energy gap. Consequently, the output current spectra can show signatures of enhancement at the desired harmonic order. These are seen to originate from interband currents. This is to be contrasted with the origins of the second harmonic peak found in gapless graphene, which are related to the generation of intraband currents.

The Berry phase is also seen to impact the interband current dynamics. In particular, odd-harmonic generation is significantly suppressed in the presence of such a phase.

For these reasons, the massive DBEs that were proposed in this work can be extended to other realms of Condensed Matter Physics in the future. In fact, this treatment is not strictly dependent on graphene itself and may be modified to accommodate for a range of other two-dimensional hexagonal relativistic-like semiconductors.

Of particular interest, the opening of a gap should lead to non-negligible contributions of Coulomb interactions across the entire layer. The renormalisation of the Fermi velocity, which is gap-dependent, should give insight into mechanisms present in exciton physics and, in particular, to their role on harmonic generation. A natural extension of the model would thus revolve around the inclusion a Coulomb potential in the equations. This step would lead to serious challenges in their underlying numerical implementation, since the dynamics of each two-level system would be coupled to all others. In the absence of a gap, such normalisation should yield marginal differences when contrasted with its carrier-free treatment, as was discussed in Section 3.5.1.

One may generalise the description of the carriers even further. Fuelled by an ever-growing interest in "exotic" materials with particular and unusual properties, a wide

range of semiconducting two-dimensional crystals known as *transition metal dichalcogenides* (TMDs) are reported to have excellent nonlinear optical properties and additionally direct band gaps. This is a rather new subject and an ongoing effort to understand and model these materials has still not yielded a firm conceptual understanding of them. Optically, many novel mechanisms have been proposed, namely through the possibility of using the valley degree of freedom to exploit many physical processes. In an analogous way to what has been proposed through *spintronics*, *valleytronics* has lead to interesting insights into the nontrivial way the carriers in such media couple to light.

As a starting point, the DBE formalism was applied to such materials. For this endeavour, the DBEs were generalised to accommodate for any effective two-band model that is described by the Dirac equation. Furthermore, the role of the spin in spin-orbit coupling interactions may also be accounted for. By doing this, new features are found, namely a time-dependent Berry phase and a warping phase, responsible for anisotropic features of the dispersion.

If the Hamiltonian is considered up to third-order in its $\mathbf{k}\cdot\mathbf{p}$ expansion, the dispersion can be mimicked very well across the entire Brillouin zone. The inclusion of the second and third-order terms in such expansion lead to an explicit breaking of the lattice centrosymmetry. This fact accounts for a massive increase of the second-order nonlinearity in such media, eventually overcoming the usually-dominant third-harmonic peak of nonlinear centrosymmetric media.

The anisotropy present in these layers invariably leads to the creation of current in the transverse direction of optical excitation, sometimes of comparable amplitude to the longitudinal component. A natural follow-up to this consideration would be to determine which polarisation conditions maximise the generation of particular harmonics. To this end, the role of the directional angle Θ in the equations should be able provide such a link. Given the particular optical selection rules dictated by the

physics in TMDs, it would be interesting to excite the sample with circularly-polarised light and see the effect on the generated current. In particular, such a polarisation configuration should yield heavily valley-dependent contributions to the current.

Given the flexibility the generalised DBEs allow, other materials that can be modelled in the same quasirelativistic picture could also be analysed in this framework. The rather large second harmonic generation in TMDs predicted by the DBEs is already an exciting result that somewhat validates this treatment in light-matter interactions modelling. Further verification when probing different media would of course reinforce the methods outlined in this work as insightful and trustworthy.

Appendix A

The Dimensionless Scaling of the SBEs and DBEs

In this appendix, a scaling of all the dimensions is performed so that the dynamical equations discussed in each chapter may be simulated in dimensionless units.

A.1 SBEs, DBEs & Massive DBEs

The *Semiconductor Bloch Equations* (SBEs) of Eqs. (3.4.7)-(3.4.8), the *Dirac-Bloch Equations* (DBEs) modelling gapless graphene through Eqs. (4.2.20)-(4.2.21) and the *Massive Dirac-Bloch Equations* expressed in Eqs. (5.4.6)-(5.4.7), modelling a gapped Dirac-like spectrum may be simulated using the following scaling:

Quantity	**Assignment**	**Scaling**	**Scaling Factor**
Time	$t \mapsto \tau$	$t = t_0\tau$	t_0
Frequency	$\omega \mapsto \tilde{\omega}$	$\omega = f_0\tilde{\omega}$	$f_0 = \frac{1}{t_0}$
Energy	$\epsilon \mapsto \tilde{\epsilon}$	$\epsilon = \epsilon_0\tilde{\epsilon}$	$\epsilon_0 = \frac{\hbar\omega_0}{2}$
Momentum	$\mathbf{p} \mapsto \tilde{\mathbf{p}}$	$\mathbf{p} = P_0\tilde{\mathbf{p}}$	$P_0 = \frac{\hbar\omega_0}{2v_\mathrm{F}}$
Electric Field	$\mathbf{E} \mapsto \boldsymbol{\psi}$	$\mathbf{E} = \psi_0\boldsymbol{\psi}$	$\psi_0 = \frac{2\hbar\omega_0}{ev_\mathrm{F}t_0}$
Vector Potential	$\mathbf{A} \mapsto \mathbf{a}$	$\mathbf{A} = A_0\mathbf{a}$	$A_0 = ct_0\psi_0$

Table A.1: Scaling of necessary quantities in the SBEs, DBEs and Massive DBEs. The variable assignment is meant to be understood as "physical $\mapsto$ dimensionless".

The dimensionless time derivatives are obtained via the operator:

$$\frac{d}{dt} = \frac{d\tau}{dt}\frac{d}{d\tau} = \frac{1}{t_0}\frac{d}{d\tau} \tag{A.1.1}$$

where $\mathring{q}_\mathbf{k} \equiv \frac{d}{d\tau}q_\mathbf{k}$.

The dimensionless pulse frequency is $\Omega_0 \equiv \omega_0 t_0$,

Massive Dirac-Bloch Equations

This scaling results in the dimensionless instantaneous energy:

$$\tilde{\epsilon}(\tau) = \sqrt{\left(\tilde{p}_x + 4a(\tau)\right)^2 + \tilde{p}_y^2 + \left(\frac{\tilde{\Delta}}{2}\right)^2} \tag{A.1.2}$$

and dimensionless canonical momentum: The dimensionless momentum $\tilde{\pi}$ is:

$$\tilde{\pi}(\tau) = \sqrt{\left(\tilde{p}_x + 4a(\tau)\right)^2 + \tilde{p}_y^2} \tag{A.1.3}$$

Importantly, the minimal substitution is performed on the **momentum**.

Otherwise stated, the samples are excited with a pulse whose electric field and electromagnetic vector potential are the respective dimensionless

$$\begin{aligned} A(t) \mapsto a(\tau) &= -\tfrac{\psi_0}{\Omega_0}\mathrm{sech}(\tau)\sin(\Omega_0\tau) \\ E(t) \mapsto \psi(\tau) &= \psi_0\mathrm{sech}(\tau)\cos(\Omega_0\tau) - \left(\tfrac{\psi_0}{\Omega_0}\right)\mathrm{sech}(\tau)\mathrm{tanh}(\tau)\sin(\Omega_0\tau) \end{aligned} \tag{A.1.4}$$

The dimensionless massive DBEs are:

Inversion $w_{\mathbf{k}}^{\xi}$

$$\begin{aligned} \mathring{w}_{\tilde{\mathbf{k}}}(\tau) - 4\psi(\tau)\Bigg(\frac{\tilde{\Delta}}{\tilde{\epsilon}(\tau)^2}\cos\theta_{\tilde{\mathbf{k}}}(\tau)\mathrm{Re}\left(q_{\tilde{\mathbf{k}}}^{\xi}(\tau)e^{-i\Omega_0\tau}\right) \\ + 2\xi\frac{\sin\theta_{\tilde{\mathbf{k}}}(\tau)}{\tilde{\epsilon}(\tau)}\mathrm{Im}\left(q_{\tilde{\mathbf{k}}}^{\xi}(\tau)e^{-i\Omega_0\tau}\right)\Bigg) = 0 \end{aligned} \tag{A.1.5}$$

Polarisation $q_{\tilde{\mathbf{k}}}^{\xi}$

$$\begin{aligned} \mathring{q}_{\tilde{\mathbf{k}}}(\tau) + i\left(\Omega_0(\tilde{\epsilon}(\tau)-1) - 2\xi\frac{\tilde{\Delta}\tilde{p}_y\psi(\tau)}{\tilde{\epsilon}(\tau)|\tilde{\pi}(\tau)|^2}\right)q_{\tilde{\mathbf{k}}}^{\xi}(\tau) \\ + \psi(\tau)\left(\frac{\tilde{\Delta}}{\epsilon(\tau)^2}\cos\theta(\tau) + \frac{2\xi i\sin\theta_{\tilde{\mathbf{k}}}(\tau)}{\tilde{\epsilon(\tau)}}\right)e^{i\Omega_0\tau}w_{\tilde{\mathbf{k}}}^{\xi}(\tau) = 0 \end{aligned} \tag{A.1.6}$$

To simulate the graphene DBEs, $\Delta = 0$.

A.2 Generalised DBEs

The *generalised* Dirac-Bloch equations expressed in Eqs. (6.3.17) use the following scaling:

Quantity	**Assignment**	**Scaling**	**Scaling Factor**
Time	$t \mapsto \tau$	$t = t_0\tau$	t_0
Frequency	$\omega \mapsto \tilde{\omega}$	$\omega = f_0\tilde{\omega}$	$f_0 = \frac{1}{t_0}$
Energy	$\epsilon \mapsto \tilde{\epsilon}$	$\epsilon = \epsilon_0\tilde{\epsilon}$	$\epsilon_0 = \frac{\hbar\omega_0}{2}$
Wavevector	$\mathbf{k} \mapsto \tilde{\mathbf{k}}$	$\mathbf{k} = k_0\tilde{\mathbf{k}}$	$k_0 = \frac{\epsilon_0}{a\gamma_0}$
Electric Field	$\mathbf{E} \mapsto \boldsymbol{\psi}$	$\mathbf{E} = \psi_0\boldsymbol{\psi}$	$\psi_0 = \frac{4\hbar k_0}{et_0}$
Vector Potential	$\mathbf{A} \mapsto \mathbf{a}$	$\mathbf{A} = A_0\mathbf{a}$	$A_0 = ct_0\psi_0$
Current Density	$\mathrm{j} \mapsto \tilde{j}$	$j = j_0\tilde{j}$	$j_0 = -\frac{ea\gamma_0}{\hbar}$

Table A.2: Scaling of necessary quantities in the generalised DBEs. The variable assignment is meant to be understood as "physical $\mapsto$ dimensionless".

Note that the current densities scaling in the generalised DBEs is the negative of its counterpart in the DBEs and massive DBEs.

The scaling leads the momentum to be defined as:

$$\begin{aligned} \theta_{\mathbf{k}}(t) \mapsto \tilde{\theta}_{\tilde{\mathbf{k}}}(\tau) &= \arctan\left[\frac{\tilde{k}_y + 4a_y(\tau)}{\tilde{k}_x + 4a_x(\tau)}\right] \\ |\boldsymbol{\pi}_{\mathbf{k}}(t)| \mapsto |\tilde{\boldsymbol{\pi}}_{\tilde{\mathbf{k}}}(\tau)| &= \sqrt{(\tilde{k}_x + 4a_x(\tau))^2 + (\tilde{k}_y + 4a_y(\tau))^2} \end{aligned} \tag{A.2.1}$$

where the minimal substitution is now performed on the **wavevector** i.e. $\tilde{\mathbf{k}}$ is a wavevector, unlike previous sections. The functions $f_{\mathbf{k}}, r_{\mathbf{k}}$ and $g_{\mathbf{k}}$ defined in Eq. (6.2.13) can be scaled to dimensionless quantities $\tilde{f}_{\tilde{\mathbf{k}}}, \tilde{r}_{\tilde{\mathbf{k}}}$ and $\tilde{g}_{\tilde{\mathbf{k}}}$, respectively

given by:

$$\tilde{f}_{\tilde{\mathbf{k}}}(\xi,\tau)=\tfrac{\tilde{\Delta}}{2}+\tfrac{\tilde{\gamma}_1}{\tilde{\gamma}_0^2}|\tilde{\boldsymbol{\pi}}_{\tilde{\mathbf{k}}}|^2+\xi\tfrac{\tilde{\gamma}_4}{\tilde{\gamma}_0^3}\cos(3\theta_{\tilde{\mathbf{k}}})|\tilde{\boldsymbol{\pi}}_{\tilde{\mathbf{k}}}|^3$$

$$\tilde{r}_{\tilde{\mathbf{k}}}(\xi,s,\tau)=-\tfrac{\tilde{\Delta}}{2}+s\xi\tilde{\gamma}_{\mathrm{SOC}}+\tfrac{\tilde{\gamma}_2}{\tilde{\gamma}_0^2}|\tilde{\boldsymbol{\pi}}_{\tilde{\mathbf{k}}}|^2+\xi\tfrac{\tilde{\gamma}_5}{\tilde{\gamma}_0^3}\cos(3\theta_{\tilde{\mathbf{k}}})|\tilde{\boldsymbol{\pi}}_{\tilde{\mathbf{k}}}|^3$$

$$\tilde{g}^2_{\tilde{\mathbf{k}}}(\xi,\tau)=\xi^2|\tilde{\boldsymbol{\pi}}_{\tilde{\mathbf{k}}}|^2+2\xi\tfrac{\tilde{\gamma}_3}{\tilde{\gamma}_0^2}\cos(3\theta_{\tilde{\mathbf{k}}})|\tilde{\boldsymbol{\pi}}_{\tilde{\mathbf{k}}}|^3+\left(\tfrac{\tilde{\gamma}_3^2+2\tilde{\gamma}_0\tilde{\gamma}_6}{\tilde{\gamma}_0^4}\right)|\tilde{\boldsymbol{\pi}}_{\tilde{\mathbf{k}}}|^4+2\xi\tfrac{\tilde{\gamma}_3\tilde{\gamma}_6}{\tilde{\gamma}_0^5}\cos(3\theta_{\tilde{\mathbf{k}}})|\tilde{\boldsymbol{\pi}}_{\tilde{\mathbf{k}}}|^5+\tfrac{\tilde{\gamma}_6^2}{\tilde{\gamma}_0^6}|\tilde{\boldsymbol{\pi}}_{\tilde{\mathbf{k}}}|^6 \tag{A.2.2}$$

and the dimensionless warping phase to be:

$$\nu_{\mathbf{k}}(t)\mapsto\tilde{\nu}_{\tilde{\mathbf{k}}}(\tau)=\arctan\left[\frac{\tilde{\gamma}_3\sin(3\theta_{\tilde{\mathbf{k}}}(\tau))|\boldsymbol{\pi}_{\mathbf{k}}(\tau)|}{\xi\tilde{\gamma}_0^2+\tilde{\gamma}_3\cos(3\theta_{\tilde{\mathbf{k}}}(\tau))|\boldsymbol{\pi}_{\mathbf{k}}(\tau)|+\xi\frac{\tilde{\gamma}_6}{\tilde{\gamma}_0}|\boldsymbol{\pi}_{\mathbf{k}}(\tau)|^2}\right] \tag{A.2.3}$$

A.2.1 Spectral Parameters

The dimensionless spectrum is written as:

$$\tilde{\epsilon}^a_{\tilde{\mathbf{k}}}(\xi,s,\tau)=\sum_{i=0}^{3}\tilde{\alpha}^{(i)}_{\tilde{\mathbf{k}}}(\xi,s,\tau)|\tilde{\boldsymbol{\pi}}_{\tilde{\mathbf{k}}}(\tau)|^i\quad\tilde{\epsilon}^b_{\tilde{\mathbf{k}}}(\xi,s,\tau)=\sqrt{\sum_{i=0}^{6}\tilde{\tilde{k}}^{(i)}_{\tilde{\mathbf{k}}}(\xi,s,\tau)|\tilde{\boldsymbol{\pi}}_{\tilde{\mathbf{k}}}(\tau)|^i} \tag{A.2.4}$$

The asymmetry spectrum coefficients $\alpha^{(i)}_{\mathbf{k}}$of Eq. (6.2.21) are rescaled as $\alpha^{(i)}_{\mathbf{k}}=\left(\frac{\epsilon_0}{k_0^i}\right)\tilde{\alpha}^{(i)}_{\tilde{\mathbf{k}}}=\epsilon_0\tilde{\gamma}_0^i a^i\tilde{\alpha}^{(i)}_{\tilde{\mathbf{k}}}$:

$$\begin{aligned}\tilde{\alpha}^{(0)}_{\tilde{\mathbf{k}}}&=\tfrac{1}{2}\xi s\tilde{\gamma}_{\mathrm{SOC}}\\ \tilde{\alpha}^{(2)}_{\tilde{\mathbf{k}}}&=\tfrac{1}{2}\left(\tfrac{\tilde{\gamma}_1+\tilde{\gamma}_2}{\tilde{\gamma}_0^2}\right)\\ \tilde{\alpha}^{(3)}_{\tilde{\mathbf{k}}}&=\tfrac{1}{2}\xi\left(\tfrac{\tilde{\gamma}_4+\tilde{\gamma}_5}{\tilde{\gamma}^3}\right)\cos(3\theta_{\tilde{\mathbf{k}}})\end{aligned} \tag{A.2.5}$$

whereas the bulk spectrum coefficients $\tilde{k}^i_{\mathbf{k}}$ of Eq. (6.2.21) are rescaled as $\tilde{k}^{(i)}_{\tilde{\mathbf{k}}}=\left(\frac{\epsilon_0^2}{k_0^i}\right)\tilde{\tilde{k}}^{(i)}_{\tilde{\mathbf{k}}}=\epsilon_0^2\tilde{\gamma}_0^i a^i\tilde{\tilde{k}}^{(i)}_{\tilde{\mathbf{k}}}$:

$$
\begin{aligned}
\tilde{\tilde{k}}^{(0)}_{\tilde{\mathbf{k}}} &= \left(\tfrac{\tilde{\Delta}-\xi s\tilde{\gamma}_{\mathrm{SOC}}}{2}\right)^2 \\
\tilde{\tilde{k}}^{(2)}_{\tilde{\mathbf{k}}} &= \left[1+\tfrac{1}{2}\left(\tfrac{\tilde{\gamma}_1-\tilde{\gamma}_2}{\tilde{\gamma}_0^2}\right)(\tilde{\Delta}-\xi s\tilde{\gamma}_{\mathrm{SOC}})\right] \\
\tilde{\tilde{k}}^{(3)}_{\tilde{\mathbf{k}}} &= \tfrac{1}{2}\xi\cos(3\theta_{\tilde{\mathbf{k}}})\left[\left(\tfrac{\tilde{\gamma}_4-\tilde{\gamma}_5}{\tilde{\gamma}_0^3}\right)(\tilde{\Delta}-\xi s\tilde{\gamma}_{\mathrm{SOC}})+4\tfrac{\tilde{\gamma}_0\tilde{\gamma}_3}{\tilde{\gamma}_0^3}\right] \\
\tilde{\tilde{k}}^{(4)}_{\tilde{\mathbf{k}}} &= \left(\tfrac{\tilde{\gamma}_1-\tilde{\gamma}_2}{2\tilde{\gamma}_0^2}\right)^2+\left(\tfrac{\tilde{\gamma}_3}{\tilde{\gamma}_0^2}\right)^2+2\tfrac{\tilde{\gamma}_0\tilde{\gamma}_6}{\tilde{\gamma}_0^4} \\
\tilde{\tilde{k}}^{(5)}_{\tilde{\mathbf{k}}} &= \tfrac{1}{2}\xi\cos(3\theta_{\tilde{\mathbf{k}}})\left[\tfrac{(\tilde{\gamma}_1-\tilde{\gamma}_2)(\tilde{\gamma}_4-\tilde{\gamma}_5)}{\tilde{\gamma}_0^5}+4\tfrac{\tilde{\gamma}_3\tilde{\gamma}_6}{\tilde{\gamma}_0^5}\right] \\
\tilde{\tilde{k}}^{(6)}_{\tilde{\mathbf{k}}} &= \left(\tfrac{\tilde{\gamma}_4-\tilde{\gamma}_5}{2\tilde{\gamma}_0^3}\right)^2\cos^2(3\theta_{\tilde{\mathbf{k}}})+\tfrac{\tilde{\gamma}_6^2}{\tilde{\gamma}_0^6}
\end{aligned}
\tag{A.2.6}
$$

A.2.2 Dirac-Bloch Equations

The dimensionless generalised Dirac-Bloch Equations take the form:

$$
\begin{aligned}
&\mathring{q}_{\tilde{\mathbf{k}}}(\tau)-i\Omega_0\left(1-\tilde{\epsilon}^b_{\tilde{\mathbf{k}}}(\tau)\right)q_{\tilde{\mathbf{k}}}(\tau)-\langle u^{(+)}_{\tilde{\mathbf{k}}}(\tau)|\mathring{u}^{(-)}_{\tilde{\mathbf{k}}}(\tau)\rangle\, e^{i(\Omega_0\tau+\xi\Lambda_{\tilde{\mathbf{k}}}(\tau))}w_{\tilde{\mathbf{k}}}(\tau)=0 \\
&\mathring{w}_{\tilde{\mathbf{k}}}(\tau)+4\mathrm{Re}\left(\langle u^{(+)}_{\tilde{\mathbf{k}}}(\tau)|\mathring{u}^{(-)}_{\mathbf{k}}(\tau)\rangle^*\, e^{-i(\Omega_0\tau+\xi\Lambda_{\tilde{\mathbf{k}}}(\tau))}q_{\tilde{\mathbf{k}}}(\tau)\right)=0
\end{aligned}
\tag{A.2.7}
$$

A.2.3 Microscopic Currents

Intraband Currents

$$
\begin{aligned}
\tilde{j}^{\mathrm{intra}(1)}_{x,\tilde{\mathbf{k}}} &= \xi\tfrac{\tilde{g}_{\tilde{\mathbf{k}}}}{\tilde{\epsilon}^b_{\tilde{\mathbf{k}}}}\cos(\theta_{\tilde{\mathbf{k}}}-\nu_{\tilde{\mathbf{k}}})(w_{\tilde{\mathbf{k}}}+1) \\
\tilde{j}^{\mathrm{intra}(1)}_{y,\tilde{\mathbf{k}}} &= \xi\tfrac{\tilde{g}_{\tilde{\mathbf{k}}}}{\tilde{\epsilon}^b_{\tilde{\mathbf{k}}}}\sin(\theta_{\tilde{\mathbf{k}}}-\nu_{\tilde{\mathbf{k}}})(w_{\tilde{\mathbf{k}}}+1)
\end{aligned}
\tag{A.2.8}
$$

(Second-Order)

$$
\begin{aligned}
\tilde{j}^{\mathrm{intra}(2)}_{x,\tilde{\mathbf{k}}} &= \tfrac{|\tilde{\pi}_{\tilde{\mathbf{k}}}|}{\tilde{\gamma}_0^2}\left(2\tilde{\gamma}_3\tfrac{\tilde{g}_{\tilde{\mathbf{k}}}}{\tilde{\epsilon}^b_{\tilde{\mathbf{k}}}}\cos(2\theta_{\tilde{\mathbf{k}}}-\nu_{\tilde{\mathbf{k}}})-(\tilde{\gamma}_1-\tilde{\gamma}_2)z_{\tilde{\mathbf{k}}}\cos\theta_{\tilde{\mathbf{k}}}\right)(w_{\tilde{\mathbf{k}}}+1) \\
j^{\mathrm{intra}(2)}_{y,\mathbf{k}} &= \tfrac{|\tilde{\pi}_{\tilde{\mathbf{k}}}|}{\tilde{\gamma}_0^2}\left(-2\tilde{\gamma}_3\tfrac{\tilde{g}_{\tilde{\mathbf{k}}}}{\tilde{\epsilon}^b_{\tilde{\mathbf{k}}}}\sin(2\theta_{\tilde{\mathbf{k}}}-\nu_{\tilde{\mathbf{k}}})-(\tilde{\gamma}_1-\tilde{\gamma}_2)z_{\tilde{\mathbf{k}}}\sin\theta_{\tilde{\mathbf{k}}}\right)(w_{\mathbf{k}}+1)
\end{aligned}
\tag{A.2.9}
$$

(Third-Order)

$$\tilde{j}^{\text{intra(3)}}_{x,\tilde{\mathbf{k}}} = \xi \frac{|\tilde{\pi}_{\tilde{\mathbf{k}}}|^2}{\tilde{\gamma}_0^3}\left(\tilde{\gamma}_6 \frac{\tilde{g}_{\tilde{\mathbf{k}}}}{\tilde{\epsilon}^b_{\tilde{\mathbf{k}}}}\left(3\cos\theta_{\tilde{\mathbf{k}}}\cos\nu_{\tilde{\mathbf{k}}} + \sin\theta_{\tilde{\mathbf{k}}}\sin\nu_{\tilde{\mathbf{k}}}\right) - \frac{3(\tilde{\gamma}_4-\tilde{\gamma}_5)}{2} z_{\tilde{\mathbf{k}}}\cos 2\theta_{\tilde{\mathbf{k}}}\right)(w_{\tilde{\mathbf{k}}}+1)$$
$$\tilde{j}^{\text{intra(3)}}_{y,\tilde{\mathbf{k}}} = \xi \frac{|\tilde{\pi}_{\tilde{\mathbf{k}}}|^2}{\tilde{\gamma}_0^3}\left(\tilde{\gamma}_6 \frac{\tilde{g}_{\tilde{\mathbf{k}}}}{\tilde{\epsilon}^b_{\tilde{\mathbf{k}}}}\left(2\sin(\theta_{\tilde{\mathbf{k}}}-\nu_{\tilde{\mathbf{k}}}) + \sin(\theta_{\tilde{\mathbf{k}}}+\nu_{\tilde{\mathbf{k}}})\right) + \frac{3(\tilde{\gamma}_4-\tilde{\gamma}_5)}{2} z_{\tilde{\mathbf{k}}}\sin 2\theta_{\tilde{\mathbf{k}}}\right)(w_{\tilde{\mathbf{k}}}+1) \tag{A.2.10}$$

Interband Currents

(First-Order)

$$\tilde{j}^{\text{inter(1)}}_{x,\tilde{\mathbf{k}}} = 2\xi\left[z_{\tilde{\mathbf{k}}}\cos(\theta_{\tilde{\mathbf{k}}}-\nu_{\tilde{\mathbf{k}}})\text{Re}\left(q_{\tilde{\mathbf{k}}}e^{-i(\xi\Lambda_{\tilde{\mathbf{k}}}+\Omega_0\tau)}\right) - \xi\sin\theta_{\tilde{\mathbf{k}}}\text{Im}\left(q_{\tilde{\mathbf{k}}}e^{-i(\xi\Lambda_{\tilde{\mathbf{k}}}+\Omega_0\tau)}\right)\right]$$
$$\tilde{j}^{\text{inter(1)}}_{y,\tilde{\mathbf{k}}} = 2\left[\xi z_{\tilde{\mathbf{k}}}\sin(\theta_{\tilde{\mathbf{k}}}-\nu_{\tilde{\mathbf{k}}})\text{Re}\left(q_{\tilde{\mathbf{k}}}e^{-i(\xi\Lambda_{\tilde{\mathbf{k}}}+\Omega_0\tau)}\right) + \cos\theta_{\tilde{\mathbf{k}}}\text{Im}\left(q_{\tilde{\mathbf{k}}}e^{-i(\xi\Lambda_{\tilde{\mathbf{k}}}+\Omega_0\tau)}\right)\right] \tag{A.2.11}$$

(Second-Order)

$$\tilde{j}^{\text{inter(2)}}_{x,\tilde{\mathbf{k}}} = 2\frac{|\tilde{\pi}_{\tilde{\mathbf{k}}}|}{\tilde{\gamma}_0^2}\left[\tilde{\Upsilon}_{x,\tilde{\mathbf{k}}}\text{Re}\left(q_{\tilde{\mathbf{k}}}e^{-i(\xi\Lambda_{\tilde{\mathbf{k}}}+\Omega_0\tau)}\right) - 2\tilde{\gamma}_3\xi\sin(2\theta_{\tilde{\mathbf{k}}}-\nu_{\tilde{\mathbf{k}}})\text{Im}\left(q_{\tilde{\mathbf{k}}}e^{-i(\delta\eta_{\mathbf{k}}+\Omega_0\tau)}\right)\right]$$
$$\tilde{j}^{\text{inter(2)}}_{y,\tilde{\mathbf{k}}} = 2\frac{\tilde{\pi}_{\tilde{\mathbf{k}}}}{\tilde{\gamma}_0^2}\left[\tilde{\Upsilon}_{y,\tilde{\mathbf{k}}}\text{Re}\left(q_{\tilde{\mathbf{k}}}e^{-i(\xi\Lambda_{\tilde{\mathbf{k}}}+\Omega_0\tau)}\right) - 2\tilde{\gamma}_3\xi\cos(2\theta_{\tilde{\mathbf{k}}}-\nu_{\tilde{\mathbf{k}}})\text{Im}\left(q_{\tilde{\mathbf{k}}}e^{-i(\xi\Lambda_{\tilde{\mathbf{k}}}+\Omega_0\tau)}\right)\right] \tag{A.2.12}$$

With

$$\begin{aligned}\tilde{\Upsilon}_{x,\tilde{\mathbf{k}}} &= 2\tilde{\gamma}_3 z_{\tilde{\mathbf{k}}}\cos(2\theta_{\tilde{\mathbf{k}}}-\nu_{\tilde{\mathbf{k}}}) + (\tilde{\gamma}_1-\tilde{\gamma}_2)\frac{\tilde{g}_{\tilde{\mathbf{k}}}}{\tilde{\epsilon}^b_{\tilde{\mathbf{k}}}}\cos\theta_{\tilde{\mathbf{k}}} \\ \tilde{\Upsilon}_{y,\tilde{\mathbf{k}}} &= -2\tilde{\gamma}_3 z_{\tilde{\mathbf{k}}}\sin(2\theta_{\tilde{\mathbf{k}}}-\nu_{\tilde{\mathbf{k}}}) + (\tilde{\gamma}_1-\tilde{\gamma}_2)\frac{\tilde{g}_{\tilde{\mathbf{k}}}}{\tilde{\epsilon}^b_{\tilde{\mathbf{k}}}}\sin\theta_{\tilde{\mathbf{k}}}\end{aligned} \tag{A.2.13}$$

(Third-Order)

$$\begin{aligned}
\tilde{j}^{\text{inter}(3)}_{x,\tilde{\mathbf{k}}} &= \frac{|\tilde{\pi}_{\tilde{\mathbf{k}}}|^2}{\tilde{\gamma}_0^3}\Bigg[\tilde{\Phi}_{x,\tilde{\mathbf{k}}}\text{Re}\left(q_{\tilde{\mathbf{k}}}e^{-i(\xi\Lambda_{\tilde{\mathbf{k}}}+\Omega_0\tau)}\right) \\
&\qquad - 2\tilde{\gamma}_6(\sin\theta_{\tilde{\mathbf{k}}}\cos\nu_{\tilde{\mathbf{k}}} - 3\cos\theta_{\tilde{\mathbf{k}}}\sin\nu_{\tilde{\mathbf{k}}})\text{Im}\left(q_{\tilde{\mathbf{k}}}e^{-i(\xi\Lambda_{\tilde{\mathbf{k}}}+\Omega_0\tau)}\right)\Bigg] \\
\tilde{j}^{\text{inter}(3)}_{y,\tilde{\mathbf{k}}} &= \frac{|\tilde{\pi}_{\tilde{\mathbf{k}}}|^2}{\tilde{\gamma}_0^3}\Bigg[\tilde{\Phi}_{y,\tilde{\mathbf{k}}}\text{Re}\left(q_{\tilde{\mathbf{k}}}e^{-i(\xi\Lambda_{\tilde{\mathbf{k}}}+\Omega_0\tau)}\right) \\
&\qquad + 2\tilde{\gamma}_6(\cos\theta_{\tilde{\mathbf{k}}}\cos\nu_{\tilde{\mathbf{k}}} + 3\sin\theta_{\tilde{\mathbf{k}}}\sin\nu_{\tilde{\mathbf{k}}})\text{Im}\left(q_{\tilde{\mathbf{k}}}e^{-i(\xi\Lambda_{\tilde{\mathbf{k}}}+\Omega_0\tau)}\right)\Bigg]
\end{aligned} \tag{A.2.14}$$

with:

$$\begin{aligned}
\tilde{\Phi}_{x,\tilde{\mathbf{k}}} &= 2\xi\tilde{\gamma}_6 z_{\tilde{\mathbf{k}}}(3\cos\theta_{\tilde{\mathbf{k}}}\cos\nu_{\tilde{\mathbf{k}}} + \sin\theta_{\tilde{\mathbf{k}}}\sin\nu_{\tilde{\mathbf{k}}}) + 3\xi(\tilde{\gamma}4 - \tilde{\gamma}_5)\frac{\tilde{g_{\tilde{\mathbf{k}}}}}{\epsilon\tilde{\epsilon^b_{\mathbf{k}}}}\cos 2\theta_{\tilde{\mathbf{k}}} \\
\tilde{\Phi}_{y,\tilde{\mathbf{k}}} &= 2\xi\tilde{\gamma}_6 z_{\tilde{\mathbf{k}}}(2\sin(\theta_{\tilde{\mathbf{k}}} - \nu_{\tilde{\mathbf{k}}}) + \sin(\theta_{\tilde{\mathbf{k}}} + \nu_{\tilde{\mathbf{k}}})) - 3\xi(\tilde{\gamma}_4 - \tilde{\gamma}_5)\frac{\tilde{g_{\tilde{\mathbf{k}}}}}{\tilde{\epsilon^b_{\mathbf{k}}}}\sin 2\theta_{\tilde{\mathbf{k}}}
\end{aligned} \tag{A.2.15}$$

Bibliography

[1] Gui-Bin Liu, Wen-Yu Shan, Yugui Yao, Wang Yao, and Di Xiao. Three-band tight-binding model for monolayers of group-vib transition metal dichalcogenides. *Physical Review B*, 88(8):085433, 2013.

[2] AH Castro Neto, Francisco Guinea, Nuno MR Peres, Kostya S Novoselov, and Andre K Geim. The electronic properties of graphene. *Reviews of modern physics*, 81(1):109, 2009.

[3] R. R. Nair, P. Blake, A. N. Grigorenko, K. S. Novoselov, T. J. Booth, T. Stauber, N. M. R. Peres, and A. K. Geim. Fine structure constant defines visual transparency of graphene. *Science*, 320(5881):1308–1308, 2008. doi: 10.1126/science.1156965.

[4] K. S. Novoselov, A. K. Geim, S. V. Morozov, D. Jiang, Y. Zhang, S. V. Dubonos, I. V. Grigorieva, and A. A. Firsov. Electric field effect in atomically test thin carbon films. *Science*, 306(5696):666–669, 2004. doi: 10.1126/science.1102896.

[5] Philip Richard Wallace. The band theory of graphite. *Physical Review*, 71(9): 622, 1947.

[6] LD Landau. Zur theorie der phasenumwandlungen ii. *Phys. Z. Sowjetunion*, 11 (545):26–35, 1937.

[7] RE Peierls. Quelques proprietes typiques des corpses solides. *Ann. IH Poincare*, 5:177–222, 1935.

[8] N David Mermin. Crystalline order in two dimensions. *Physical Review*, 176 (1):250, 1968.

[9] K. S. Novoselov and A. K. Geim. Two-dimensional gas of massless dirac fermions in graphene. *Nature*, 438:197–200, 2005. doi: 10.1038/nature04233.

[10] L Wu, HS Chu, WS Koh, and EP Li. Highly sensitive graphene biosensors based on surface plasmon resonance. *Optics express*, 18(14):14395–14400, 2010.

[11] Ahmet Avsar, Tsung-Yeh Yang, Sukang Bae, Jayakumar Balakrishnan, Frank Volmer, Manu Jaiswal, Zheng Yi, Syed Rizwan Ali, Gernot Guntherodt, Byung Hee Hong, et al. Toward wafer scale fabrication of graphene based spin valve devices. *Nano letters*, 11(6):2363–2368, 2011.

[12] Changgu Lee, Xiaoding Wei, Jeffrey W Kysar, and James Hone. Measurement of the elastic properties and intrinsic strength of monolayer graphene. *science*, 321(5887):385–388, 2008.

[13] CWJ Beenakker. Colloquium: Andreev reflection and klein tunneling in graphene. *Reviews of Modern Physics*, 80(4):1337, 2008.

[14] MI Katsnelson. Zitterbewegung, chirality, and minimal conductivity in graphene. *The European Physical Journal B-Condensed Matter and Complex Systems*, 51(2):157–160, 2006.

[15] Shou-cheng Zhang. Topological states of quantum matter. *Physics*, 1:6, 2008.

[16] Charles L Kane and Eugene J Mele. Z 2 topological order and the quantum spin hall effect. *Physical review letters*, 95(14):146802, 2005.

[17] Yuanbo Zhang, Yan-Wen Tan, Horst L Stormer, and Philip Kim. Experimental observation of the quantum hall effect and berry's phase in graphene. *nature*, 438(7065):201, 2005.

[18] Yuan Cao, Valla Fatemi, Shiang Fang, Kenji Watanabe, Takashi Taniguchi, Efthimios Kaxiras, and Pablo Jarillo-Herrero. Unconventional superconductivity in magic-angle graphene superlattices. *Nature*, 556(7699):43, 2018.

[19] Sanju Gupta and Avadh Saxena. Importance of topology in materials science. In *The Role of Topology in Materials*, pages 3–33. Springer, 2018.

[20] Zhijun Wang, Yan Sun, Xing-Qiu Chen, Cesare Franchini, Gang Xu, Hongming Weng, Xi Dai, and Zhong Fang. Dirac semimetal and topological phase transitions in a 3 bi (a= na, k, rb). *Physical Review B*, 85(19):195320, 2012.

[21] Sergey Borisenko, Quinn Gibson, Danil Evtushinsky, Volodymyr Zabolotnyy, Bernd Büchner, and Robert J Cava. Experimental realization of a three-dimensional dirac semimetal. *Physical review letters*, 113(2):027603, 2014.

[22] AA Burkov and Leon Balents. Weyl semimetal in a topological insulator multilayer. *Physical review letters*, 107(12):127205, 2011.

[23] Alexey A Soluyanov, Dominik Gresch, Zhijun Wang, QuanSheng Wu, Matthias Troyer, Xi Dai, and B Andrei Bernevig. Type-ii weyl semimetals. *Nature*, 527 (7579):495, 2015.

[24] Huaqing Huang, Shuyun Zhou, and Wenhui Duan. Type-ii dirac fermions in the ptse 2 class of transition metal dichalcogenides. *Physical Review B*, 94(12): 121117, 2016.

[25] GE Volovik and K Zhang. Lifshitz transitions, type-ii dirac and weyl fermions, event horizon and all that. *Journal of Low Temperature Physics*, 189(5-6): 276–299, 2017.

[26] F. Bonaccorso, Z. Sun, T. Hasan, and A. C. Ferrari. Graphene photonics and optoelectronics. *Nature Photonics*, 4:611–622, 2005. doi: 10.1038/nphoton.2010.186.

[27] T. Mueller, F. Xia, and P. Avouris. Graphene photodetectors for high-speed optical communications. *Nature Photonics*, 4:297 – 301, 2010. doi: 10.1038/nphoton.2010.40.

[28] M. Liu, X. Yin, E. Ulin-Avila, B. Geng, T. Zentgraf, L. Ju, F. Wang, and X. Zhang. A graphene-based broadband optical modulator. *Nature*, 474:64 – 67, 2011. doi: 10.1038/nature10067.

[29] A. Marini, I. Silveiro, and F.J. García de Abajo. Molecular sensing with tunable graphene plasmons. *ACS Photonics*, 2:876–882, 2015. doi: 10.1021/acsphotonics.5b00067.

[30] M. Gullans, D. E. Chang, F. H. L. Koppens, F. J. García de Abajo, and M. D. Lukin. Single-photon nonlinear optics with graphene plasmons. *Phys. Rev. Lett.*, 111:247401, 2013. doi: 10.1103/PhysRevLett.111.247401.

[31] D.A. Smirnova, I.V. Shadrivov, A.I. Smirnov, and Y.S. Kivshar. Dissipative plasmon-solitons in multilayer graphene. *Laser & Photonics Reviews*, 8:291–296, 2014. doi: 10.1002/lpor.201300173.

[32] S. A. Mikhailov. Non-linear electromagnetic response of graphene. *EPL (Europhysics Letters)*, 79(2):27002, 2007.

[33] Q. Bao, H. Zhang, Y. Wang, Z. Ni, Y. Yan, Z.X. Shen, K.P. Loh, and D.Y. Tang. Atomic-layer graphene as a saturable absorber for ultrafast pulsed lasers. 19:3077–3083, 2009. doi: 10.1002/adfm.200901007.

[34] Z. Sun, T. Hasan, F. Torrisi, D. Popa, G. Privitera, F. Wang, F. Bonaccorso, D.M. Basko, and A.C. Ferrari. Graphene mode-locked ultrafast laser. *ACS Nano*, 4:803–810, 2010. doi: 10.1021/nn901703e.

[35] N. M. Peres, Y. V. Bludov, J. E. Santos, A. Jauho, and M. I. Vasilevskiy. Optical bistability of graphene in the terahertz range. *Phys. Rev. B*, 90:125425, 2014. doi: 10.1103/PhysRevB.90.125425.

[36] S. A. Mikhailov. Quantum theory of third-harmonic generation in graphene. *Phys. Rev. B*, 90:241301, 2014. doi: 10.1103/PhysRevB.90.241301.

[37] Jean-Noel Fuchs and Mark Oliver Goerbig. Introduction to the physical properties of graphene. *Lecture notes*, 2008.

[38] Paul AM Dirac. The quantum theory of the electron. *Proc. R. Soc. Lond. A*, 117(778):610–624, 1928.

[39] Mikhail I Katsnelson. Graphene: carbon in two dimensions. *Materials today*, 10(1-2):20–27, 2007.

[40] Charles Kittel. Introduction to solid state physics. 1953.

[41] JP Hobson and WA Nierenberg. The statistics of a two-dimensional, hexagonal net. *Physical Review*, 89(3):662, 1953.

[42] Wright A. The electronic and optical properties of graphene.

[43] Aiping Zhou and Weidong Sheng. Van hove singularities in graphene nanoflakes. *Journal of Applied Physics*, 112(9):094313, 2012.

[44] María AH Vozmediano. Renormalization group aspects of graphene. *Philosophical Transactions of the Royal Society of London A: Mathematical, Physical and Engineering Sciences*, 369(1946):2625–2642, 2011.

[45] Samuel Leverte McCall and Erwin L Hahn. Self-induced transparency by pulsed coherent light. *Physical Review Letters*, 18(21):908, 1967.

[46] Robert W Boyd. *Nonlinear optics*. Academic press, 2003.

[47] Yuen-Ron Shen. The principles of nonlinear optics. *New York, Wiley-Interscience, 1984, 575 p.*, 1984.

[48] Marlan O Scully and M Suhail Zubairy. *Quantum optics*. Cambridge university press, 1997.

[49] H. Haug and S. W. Koch. *Quantum Theory of the Opti- cal and Electronic Properties of Semiconductors*. World Scientific, 5 edition, 2009.

[50] Wilfried Schäfer and Martin Wegener. *Semiconductor optics and transport phenomena*. Springer Science & Business Media, 2013.

[51] Igor F Herbut and Vieri Mastropietro. Universal conductivity of graphene in the ultrarelativistic regime. *Physical Review B*, 87(20):205445, 2013.

[52] LA Falkovsky. Optical properties of graphene. In *Journal of Physics: Conference Series*, volume 129, page 012004. IOP Publishing, 2008.

[53] Kin Fai Mak, Matthew Y Sfeir, Yang Wu, Chun Hung Lui, James A Misewich, and Tony F Heinz. Measurement of the optical conductivity of graphene. *Physical review letters*, 101(19):196405, 2008.

[54] Peter D Drummond and Mark Hillery. *The quantum theory of nonlinear optics*. Cambridge University Press, 2014.

[55] Leslie Allen and Joseph H Eberly. *Optical resonance and two-level atoms*, volume 28. Courier Corporation, 1975.

[56] M. Lindberg and S. W. Koch. Effective bloch equations for semiconductors. *Phys. Rev. B*, 38:3342–3350, 1988. doi: 10.1103/PhysRevB.38.3342.

[57] A Knorr, R Binder, M Lindberg, and SW Koch. Theoretical study of resonant ultrashort-pulse propagation in semiconductors. *Physical Review A*, 46(11): 7179, 1992.

[58] A Girndt, A Knorr, M Hofmann, and SW Koch. Theory of coherent phenomena in pump-probe excitation of semiconductor amplifiers. *Journal of applied physics*, 78(5):2946–2954, 1995.

[59] Charles M Bowden and Jonathan P Dowling. Near–dipole-dipole effects in dense media: Generalized maxwell-bloch equations. *Physical Review A*, 47(2): 1247, 1993.

[60] Charles M Bowden and Govind P Agrawal. Maxwell-bloch formulation for semiconductors: Effects of coherent coulomb exchange. *Physical Review A*, 51 (5):4132, 1995.

[61] Th Östreich and A Knorr. Various appearances of rabi oscillations for 2π-pulse excitation in a semiconductor. *Physical Review B*, 48(24):17811, 1993.

[62] Th Östreich and A Knorr. Nonperturbative scaling behavior of the coherent semiconductor bloch equations in the low-density regime. *Physical Review B*, 50(8):5717, 1994.

[63] ME Crenshaw, M Scalora, and Ch M Bowden. Ultrafast intrinsic optical switching in a dense medium of two-level atoms. *Physical review letters*, 68(7):911, 1992.

[64] B Meziane. Instability hierarchies in self-pulsing lasers. *Physical Review A*, 48 (3):2346, 1993.

[65] S Hughes, A Knorr, and SW Koch. Interplay of optical dephasing and pulse propagation in semiconductors. *JOSA B*, 14(4):754–760, 1997.

[66] E. Malic and A. Knorr. *Graphene and Carbon Nanotubes*. Wiley-VCH, 2013.

[67] Jozef Gruska. *Quantum computing*, volume 2005. McGraw-Hill London, 1999.

[68] Dietrich Leibfried, Brian DeMarco, Volker Meyer, David Lucas, Murray Barrett, Joe Britton, Wayne M Itano, B Jelenković, Chris Langer, Till Rosenband, et al. Experimental demonstration of a robust, high-fidelity geometric two ion-qubit phase gate. *Nature*, 422(6930):412, 2003.

[69] Isidor Isaac Rabi. Space quantization in a gyrating magnetic field. *Physical Review*, 51(8):652, 1937.

[70] F Arecchi and R Bonifacio. Theory of optical maser amplifiers. *IEEE Journal of Quantum Electronics*, 1(4):169–178, 1965.

[71] Heinz-Peter Breuer and Francesco Petruccione. *The theory of open quantum systems*. Oxford University Press on Demand, 2002.

[72] J González, F Guinea, and MAH Vozmediano. Electron-electron interactions in graphene sheets. *Physical Review B*, 63(13):134421, 2001.

[73] J. Hofmann, E. Barnes, and S. das Sarma. Why does graphene behave as a weakly interacting system? *Phys. Rev. Lett.*, 113:105502, Sep 2014. doi: 10.1103/PhysRevLett.113.105502.

[74] Valeri N Kotov, Bruno Uchoa, Vitor M Pereira, F Guinea, and AH Castro Neto. Electron-electron interactions in graphene: Current status and perspectives. *Reviews of Modern Physics*, 84(3):1067, 2012.

[75] DC Elias, RV Gorbachev, AS Mayorov, SV Morozov, AA Zhukov, P Blake, LA Ponomarenko, IV Grigorieva, KS Novoselov, F Guinea, et al. Dirac cones reshaped by interaction effects in suspended graphene. *Nature Physics*, 7(9): 701, 2011.

[76] Isabella Gierz, Matteo Mitrano, Jesse C Petersen, Cephise Cacho, IC Edmond Turcu, Emma Springate, Alexander Stöhr, Axel Köhler, Ulrich Starke, and Andrea Cavalleri. Population inversion in monolayer and bilayer graphene. *Journal of Physics: Condensed Matter*, 27(16):164204, 2015.

[77] T Winzer and E Malic. The impact of pump fluence on carrier relaxation dynamics in optically excited graphene. *Journal of Physics: Condensed Matter*, 25(5):054201, 2013.

[78] Weng W Chow and Stephan W Koch. *Semiconductor-laser fundamentals: physics of the gain materials*. Springer Science & Business Media, 2013.

[79] David N Carvalho, Andrea Marini, and Fabio Biancalana. Dynamical centrosymmetry breaking—a novel mechanism for second harmonic generation in graphene. *Annals of Physics*, 378:24–32, 2017.

[80] David N Carvalho, Fabio Biancalana, and Andrea Marini. Monolayer graphene can emit shg waves. *Optical Data Processing and Storage*, 3(1):47–53, 2017.

[81] K. L. Ishikawa. Nonlinear optical response of graphene in time domain. *Phys. Rev. B*, 82:201402, 2010. doi: 10.1103/PhysRevB.82.201402.

[82] K. L. Ishikawa. Electronic response of graphene to an ultrashort intense terahertz radiation pulse. *New Journal of Physics*, 15(5):055021, 2013.

[83] E. Malic, T. Winzer, E. Bobkin, and A. Knorr. Microscopic theory of absorption and ultrafast many-particle kinetics in graphene. *Phys. Rev. B*, 84:205406, 2011. doi: 10.1103/PhysRevB.84.205406.

[84] M. M. Glazov. Second harmonic generation in graphene. *JETP Letters*, 93(7): 366–371, 2011. doi: 10.1134/S0021364011070046.

[85] MM Glazov and SD Ganichev. High frequency electric field induced nonlinear effects in graphene. *Physics Reports*, 535(3):101–138, 2014.

[86] Yong Q An, Florence Nelson, Ji Ung Lee, and Alain C Diebold. Enhanced optical second-harmonic generation from the current-biased graphene/sio2/si (001) structure. *Nano letters*, 13(5):2104–2109, 2013.

[87] JL Cheng, N Vermeulen, and JE Sipe. Second order optical nonlinearity of graphene due to electric quadrupole and magnetic dipole effects. *Scientific reports*, 7:43843, 2017.

[88] T.O. Wehling, A.M. Black-Schaffer, and A.V. Balatsky. Dirac materials. *Advances in Physics*, 63(1):1–76, 2014. doi: 10.1080/00018732.2014.927109.

[89] JE Sipe and Ed Ghahramani. Nonlinear optical response of semiconductors in the independent-particle approximation. *Physical Review B*, 48(16):11705, 1993.

[90] Kung-Hsuan Lin, Shao-Wei Weng, Po-Wei Lyu, Tsong-Ru Tsai, and Wei-Bin Su. Observation of optical second harmonic generation from suspended single-layer and bi-layer graphene. *Applied Physics Letters*, 105(15):151605, 2014.

[91] Frank Schwierz. Graphene transistors. *Nature nanotechnology*, 5(7):487–496, 2010.

[92] Thomas G Pedersen, Antti-Pekka Jauho, and Kjeld Pedersen. Optical response and excitons in gapped graphene. *Physical Review B*, 79(11):113406, 2009.

[93] Leone Di Mauro Villari, Ian Galbraith, and Fabio Biancalana. Coulomb effects in the absorbance spectra of two-dimensional dirac materials (submitted). 2018.

[94] David N Carvalho, Andrea Marini, and Fabio Biancalana. The nonlinear optical effects of opening a gap in graphene. *arXiv preprint arXiv:1710.04581*, 2017.

[95] S Yi Zhou, G-H Gweon, AV Fedorov, PN First, WA De Heer, D-H Lee, F Guinea, AH Castro Neto, and A Lanzara. Substrate-induced bandgap opening in epitaxial graphene. *Nature materials*, 6(10):770–775, 2007.

[96] Joongoo Kang, Junhyeok Bang, Byungki Ryu, and KJ Chang. Effect of atomic-scale defects on the low-energy electronic structure of graphene: Perturbation theory and local-density-functional calculations. *Physical Review B*, 77(11): 115453, 2008.

[97] Zhen Hua Ni, Ting Yu, Yun Hao Lu, Ying Ying Wang, Yuan Ping Feng, and Ze Xiang Shen. Uniaxial strain on graphene: Raman spectroscopy study and band-gap opening. *ACS nano*, 2(11):2301–2305, 2008.

[98] Eduardo V Castro, KS Novoselov, SV Morozov, NMR Peres, JMB Lopes Dos Santos, Johan Nilsson, F Guinea, AK Geim, and AH Castro Neto. Biased bilayer graphene: semiconductor with a gap tunable by the electric field effect. *Physical review letters*, 99(21):216802, 2007.

[99] Xiaolin Li, Xinran Wang, Li Zhang, Sangwon Lee, and Hongjie Dai. Chemically derived, ultrasmooth graphene nanoribbon semiconductors. *Science*, 319(5867): 1229–1232, 2008.

[100] Philip Shemella and Saroj K Nayak. Electronic structure and band-gap modulation of graphene via substrate surface chemistry. *Applied Physics Letters*, 94 (3):032101, 2009.

[101] Yong-Ju Kang, Joongoo Kang, and KJ Chang. Electronic structure of graphene and doping effect on sio 2. *Physical Review B*, 78(11):115404, 2008.

[102] M. I. Katsnelson. *Graphene - Carbon in Two Dimensions*. Cambridge University Press, 2012.

[103] Max Born and Vladimir Fock. Beweis des adiabatensatzes. *Zeitschrift für Physik*, 51(3-4):165–180, 1928.

[104] Dariusz Chruscinski and Andrzej Jamiolkowski. *Geometric phases in classical and quantum mechanics*, volume 36. Springer Science & Business Media, 2012.

[105] Pierre Carmier and Denis Ullmo. Berry phase in graphene: Semiclassical perspective. *Physical Review B*, 77(24):245413, 2008.

[106] Martin Wegener. *Extreme nonlinear optics: an introduction*. Springer Science & Business Media, 2005.

[107] T Tritschler, OD Mücke, M Wegener, U Morgner, and FX Kärtner. Evidence for third-harmonic generation in disguise of second-harmonic generation in extreme nonlinear optics. *Physical review letters*, 90(21):217404, 2003.

[108] Di Xiao, Gui-Bin Liu, Wanxiang Feng, Xiaodong Xu, and Wang Yao. Coupled spin and valley physics in monolayers of mos 2 and other group-vi dichalcogenides. *Physical Review Letters*, 108(19):196802, 2012.

[109] Antti Säynätjoki, Lasse Karvonen, Habib Rostami, Anton Autere, Soroush Mehravar, Antonio Lombardo, Robert A Norwood, Tawfique Hasan, Nasser Peyghambarian, Harri Lipsanen, et al. Ultra-strong nonlinear optical processes and trigonal warping in mos 2 layers. *Nature communications*, 8(1):893, 2017.

[110] John R. Schaibley, Hongyi Yu, Genevieve Clark, Pasqual Rivera, Jason S. Ross, Kyle L. Seyler, Wang Yao, and Xiaodong Xu. Valleytronics in 2d materials. *Nature Reviews Materials*, 1, 2016. doi: 2016/08/23/online.

[111] Xiaodong Xu, Wang Yao, Di Xiao, and Tony F. Heinz. Spin and pseudospins in layered transition metal dichalcogenides. *Nature Physics*, 10:343–350, 2014. doi: 10.1038/nphys2942.

[112] Fengnian Xia, Han Wang, Di Xiao, Madan Dubey, and Ashwin Ramasubramaniam. Two-dimensional material nanophotonics. *Nature Photonics*, 8(12): 899–907, 2014.

[113] Martin Gmitra, Denis Kochan, Petra Högl, and Jaroslav Fabian. Trivial and inverted dirac bands and the emergence of quantum spin hall states in graphene on transition-metal dichalcogenides. *Physical Review B*, 93(15):155104, 2016.

[114] Andor Kormányos, Viktor Zólyomi, Neil D. Drummond, Péter Rakyta, Guido Burkard, and Vladimir I. Fal'ko. Monolayer mos_2: Trigonal warping, the Γ valley, and spin-orbit coupling effects. *Phys. Rev. B*, 88:045416, Jul 2013. doi: 10.1103/PhysRevB.88.045416.

[115] A Säynätjoki, L Karvonen, H Rostami, A Autere, S Mehravar, A Lombardo, RA Norwood, T Hasan, N Peyghambarian, H Lipsanen, et al. Ultra-strong nonlinear optical processes and trigonal warping in mos $_2$ layers. *arXiv preprint arXiv:1608.04101*, 2016.

[116] Hanzhe Liu, Yilei Li, Yong Sing You, Shambhu Ghimire, Tony F Heinz, and David A Reis. High-harmonic generation from an atomically thin semiconductor. *Nature Physics*, 2016.

[117] Hongyi Yu, Gui-Bin Liu, Pu Gong, Xiaodong Xu, and Wang Yao. Dirac cones and dirac saddle points of bright excitons in monolayer transition metal dichalcogenides. *Nature communications*, 5, 2014.

[118] Edward McCann and Mikito Koshino. The electronic properties of bilayer graphene. *Reports on Progress in Physics*, 76(5):056503, 2013.

[119] Edward McCann and Vladimir I Fal'ko. Landau-level degeneracy and quantum hall effect in a graphite bilayer. *Physical Review Letters*, 96(8):086805, 2006.

[120] Alexander V Kolobov and Junji Tominaga. *Two-Dimensional Transition-Metal Dichalcogenides*, volume 239. Springer, 2016.

[121] PN Romanets and FT Vasko. Rabi oscillations under ultrafast excitation of graphene. *Physical Review B*, 81(24):241411, 2010.

[122] Ermin Malic, Torben Winzer, Evgeny Bobkin, and Andreas Knorr. Microscopic theory of absorption and ultrafast many-particle kinetics in graphene. *Physical Review B*, 84(20):205406, 2011.

[123] AA Kozikov, AK Savchenko, BN Narozhny, and AV Shytov. Electron-electron interactions in the conductivity of graphene. *Physical Review B*, 82(7):075424, 2010.

[124] Jun Yao, Govind P Agrawal, Philippe Gallion, and Charles M Bowden. Semiconductor laser dynamics beyond the rate-equation approximation. *Optics communications*, 119(1-2):246–255, 1995.

[125] DSL Abergel, V Apalkov, J Berashevich, K Ziegler, and Tapash Chakraborty. Properties of graphene: a theoretical perspective. *Advances in Physics*, 59(4): 261–482, 2010.

[126] T Stroucken, JH Grönqvist, and SW Koch. Excitonic resonances as fingerprint of strong coulomb coupling in graphene. *JOSA B*, 29(2):A86–A94, 2012.

[127] P.A.M. Dirac. The lorentz transformation and absolute time. *Physica*, 19(1-–12):888–896, 1953. doi: 10.1016/S0031-8914(53)80099-6.

[128] R.P Feynman and F.L Vernon Jr. The theory of a general quantum system interacting with a linear dissipative system. *Annals of Physics*, 24:118–173, 1963. doi: 10.1016/0003-4916(63)90068-X.

[129] Q Bao and K.P. Loh. Graphene photonics, plasmonics, and broadband optoelectronic devices. *ACS Nano*, 6:3677–94, 2012. doi: 10.1021/nn300989g.

[130] F. J. García de Abajo. Graphene plasmonics: Challenges and opportunities. *ACS Photonics*, 1:135—-152, 2014. doi: 10.1021/ph400147y.

[131] T. Stroucken, J.H. Grönqvist, and S.W. Koch. Optical response and ground state of graphene. *Phys. Rev. B*, 84:205445, 2011. doi: 10.1103/PhysRevB.84.205445.

[132] P.L. Voss Z. Zhang. Full-band quantum-dynamical theory of saturation and four-wave mixing in graphene. *Optics Letters*, 36(23):4569–4571, 2011. doi: 10.1364/OL.36.004569.

[133] Y. Li, J. Deslippe, C.H. Park, M.L. Cohen, and S. G. Louie. Excitonic effects on the optical response of graphene and bilayer graphene. *Phys. Rev. Lett.*, 103: 186802, 2009. doi: 10.1103/PhysRevLett.103.186802.

[134] E. G. Mishchenko. Minimal conductivity in graphene: Interaction corrections and ultraviolet anomaly. *EPL (Europhysics Letters)*, 83, 2008.

[135] M. V. Entin, L. I. Magarill, and D. L. Shepelyansky. Theory of resonant photon drag in monolayer graphene. *Phys. Rev. B*, 81:165441, 2010. doi: 10.1103/PhysRevB.81.165441.

[136] Tineke Stroucken and Stephan W Koch. Optically bright p-excitons indicating strong coulomb coupling in transition-metal dichalcogenides. *Journal of Physics: Condensed Matter*, 27(34):345003, 2015.

[137] Olaf MJ Van't Erve, Aubrey T Hanbicki, Adam L Friedman, Kathleen M McCreary, Enrique Cobas, Connie H Li, Jeremy T Robinson, and Berend T Jonker. Graphene and monolayer transition-metal dichalcogenides: properties and devices. *Journal of Materials Research*, 31(07):845–877, 2016.

[138] Prasenjit Dey, Jagannath Paul, Zefang Wang, CE Stevens, Cunming Liu, AH Romero, Jie Shan, DJ Hilton, and Denis Karaiskaj. Optical coherence in atomic-monolayer transition-metal dichalcogenides limited by electron-phonon interactions. *Physical review letters*, 116(12):127402, 2016.

[139] Kin Fai Mak and Jie Shan. Photonics and optoelectronics of 2d semiconductor transition metal dichalcogenides. *Nature Photonics*, 10(4):216–226, 2016.

[140] Zhiming M Wang. *MoS2: materials, physics, and devices*, volume 21. Springer Science & Business Media, 2013.

[141] A. Giuliani, V. Mastropietro, and M. Porta. Absence of interaction corrections in the optical conductivity of graphene. *Phys. Rev. B*, 83:195401, 2011. doi: 10.1103/PhysRevB.83.195401.

[142] David N Carvalho, Fabio Biancalana, and Andrea Marini. A study of the nonlinear optics of transition metal dichalcogenides with the dirac-bloch equations (in preparation for submission).